Quantum Simulation of Quantum Field Theories

Anthony Ciavarella

A dissertation
submitted in partial fulfillment of the
requirements for the degree of

Doctor of Philosophy

University of Washington

2023

Reading Committee:

Martin J. Savage, Chair

David B. Kaplan

Lukasz Fidkowski

Program Authorized to Offer Degree:
Physics

University of Washington

Abstract

Quantum Simulation of Quantum Field Theories

Anthony Ciavarella

Chair of the Supervisory Committee:
Professor and Senior INT Fellow Martin J. Savage

The theory of quantum chromodynamics (QCD) describes the nuclear forces that bind quarks into nucleons and nucleons into nuclei. The dynamics in the non-perturbative regime of QCD are of relevance for understanding inelastic hadron scattering, the behavior of quark-gluon plasma in the early universe and matter inside of extreme enviroments such as supernovae. The discretization of QCD onto a spacial lattice gives a formalism that can be used to study the non-perturbative aspects of the theory and quantum simulation offers the promise of being able to probe real time dynamics directly.

The research presented in this dissertation contributes to the development of quantum simulation techniques for quantum field theory. This dissertation is organized into two parts. The first part discusses digital quantum simulation techniques which can be implemented on a universal quantum computer. This part begins with an encoding of SU(3) gauge fields onto quantum computer and a discussion of how to simulate time evolution on a quantum computer. Variational methods are then used to prepare ground states on quantum hardware. The similarity renormalization group is used to derive improved Hamiltonians that mitigate the effects of truncating the gauge fields. As a step towards simulating lattice QCD with dynamical fermions on quantum computers, a study of algorithms that can be used to simulate time evolution of a system of fermions interacting through a Coulomb interaction is performed. An algorithm is introduced to study the decay of unstable particles and total cross sections. The techniques in this section lay out a path for computing scattering observables on a quantum computer. In the second part, techniques are developed for analog quantum simulation of the O(3) non-linear σ model on cold atoms. This part begins with the development of a method to simulate Heisenberg interactions on cold atom systems. This method is then extended to an adiabatic state preparation technique. This part concludes with a proposal for an analog simulation of the asymptotically free region of the O(3) non-linear σ model that should be possible on currently existing cold atom quantum simulators. With the combination of long term algorithm design and near term implementation, the research in this disseration has contributed to the development of quantum simulations of quantum field theories.

TABLE OF CONTENTS

LIST OF FIGURES

LIST OF TABLES

ACKNOWLEDGMENTS

My scientific journey has benefited from interactions with so many people and while I may thank a few of them here, this is only a small sampling of people who have had an impact on me.

I would like to begin by thanking my advisor Martin Savage for his continuous support in helping me grow as a scientist and as a person. Martin's willingness to go after ambitious problems and commitment to doing good science has been a source of inspiration. I hope to reach the same level of curiosity about the world and integrity that Martin has continuously demonstrated.

My time at the University of Washington has also benefited from interactions with all of the other members of IQuS. My scientific and personal life has been forever enriched through conversations with Stephan Caspar, Marc Illa Subina, Hersh Singh, Francesco Turro, Ramya Bhaskar, Ivan Chernyshev, Roland Farrell, Henry Froland, Jeremy Hartse, Nikita Zemlevskiy, Fabio Anza, Alessandro Roggero, Dorota Grabowska, Niklas Mueller and Xiaojun Yao. I would also like to thank Natalie Klco and Jesse Stryker for helping to point me in the right direction as I began to do research. David Kaplan and Stephen Sharpe also both provided guidance during my first year at the University of Washington that helped me begin to do research. It was an absolute pleasure to share an office with Ibrahim Abdurrahman for a few years. I would like to thank Nathan Wiebe for his willingness to explain any quantum algorithm I was confused about. I would also like to thank Pavel Lougovksi for his good humor and honest feedback when attempting to perform neutral atom simulations. Of course, none of the work presented in this thesis would have been possible without support staff like Katie Hennessey who keeps IQuS running and Catherine Provost guiding graduate students throughout their time at UW.

A special thanks goes out to Jared Canright, Josh Labounty, Alex Kato, Audrey Silliman, Daniel Woodrich, and Anna Shepherd. A global pandemic shutting down society is not how any of us would have chosen to spend 2020, but I am glad to have had all of you to go through it with.

I would also like to thank my parents, Monica and Nicolas, and my brother Alec for their support as I've been working on the other side of the country.

My time at Ohio State University as an undergraduate was filled with mentors that set me on the path I'm on now. I am grateful for Robert Perry and Dick Furnstahl for showing me just how interesting nuclear and computational physics can be. During my time working with him, Harris Kagan continuously encouraged me to question everything I was being told and pushed me towards being a better scientist. I am grateful for Gregory Kilcup introducing me to a number of interesting physics problems and pointing me towards people to talk to when I arrived at the University of Washington. I would also like to thank Vitaly Bergelson in the OSU Math department for helping me to develop my presentation skills during the What is..? seminar series he ran.

Financially, work in this dissertation was supported by the Institute for Nuclear Theory's U.S. Department of Energy Grant No. DE-FG02-00ER41132, in part by the U.S. Department of Energy Grant No. DE-SC0019478, the DOE QuantISED program through the theory consortium "Intersections of QIS and Theoretical Particle Physics" at Fermilab through Fermi National Accelerator Laboratory PO No. 652197, and the U.S. Department of Energy, Office of Science, Office of Nuclear Physics, InQubator for Quantum Simulation (IQuS) under Award Number DOE (NP) Award DE-SC0020970 through the Quantum Horizons: QIS Research and Innovation for Nuclear Science Initiative. We acknowledge the use of IBM Quantum services for this work. The views expressed are those of the author, and do not reflect the official policy or position of IBM or the IBM Quantum team. This work was facilitated through the use of advanced computational, storage, and networking infrastructure provided by the Hyak supercomputer system at the University of Washington. This work also made use of AWS EC-2 compute instances through the generous support of AWS Programs for Research and Education. I would also like to acknowledge UAW 4121 for negotiating the terms of my employment and for providing worker protections throughout my time at the University of Washington.

DEDICATION

To the beauty hidden throughout nature

Part I

INTRODUCTION

The development of quantum mechanics in the 20^{th} century revolutionized humanity's understanding of nature. The deterministic classical mechanics assumed to describe nature was replaced with a fundamentally probabilistic framework. In the framework of quantum mechanics, systems exist in a superposition of different states until measured by an external observer. The correlation between systems can also exist in superposition and this allows for a form of correlation that goes beyond classical probability theory known as quantum entanglement. Attempts to understand entanglement led to the development of quantum information science.

Alongside these advances in fundamental physics, the 20^{th} century also saw the development of digital computers. This allowed for calculations to be performed that were previously unimaginable. Using computers to solve problems also required problems to be reformulated such that a computer could be useful. These reformulations often led to new insights into problems. For example, the attempts to use computers to simulate fluid mechanics led to developments in the field of chaos theory. In addition to new insights into classical problems, attempts to utilize computers also led to insights into new physics. For example, Ken Wilson's studies into how to use a computer to perform quantum field theory calculations led to the development of lattice methods which has provided a non-perturbative definition of a quantum field theory that can be used for practical calculation [1].

However, attempts to use computers to simulate quantum systems ran into fundamental limitations. As realized by Feynman [2], these limitations are a consequence of it not being possible to efficiently describe entanglement on a computer based on classical laws of nature. Feynman's argument assumes that a computer can only have local interactions between its parts and considers a successful simulation one where the resources scale linearly with the spacetime volume being simulated. If a classical computer could simulate quantum systems under these restrictions, then it would be mathematically equivalent to writing quantum mechanics in terms of a system of local hidden classical variables (which may or may not be probabilistic). However as the Bell inequalities have shown, this is not possible due to the existence of entanglement. Therefore, Feynman suggested that efficient simulations of quantum systems would require the construction of computers that directly utilize quantum effects. Experimental control over quantum systems has advanced to the point where quantum computers are being constructed.

Quantum computers offer the possibility of directly simulating the evolution of quantum systems. This is expected to enable new insights into fundamental physics. Simulations of the Standard Model are of relevance to a number of physical systems. The strong force sector of the Standard Model is described by quantum chromodynamics (QCD) [3, 4, 5, 6]. In QCD, matter is described by excitations of quark fields that interact by exchanging gluons. Due to the strength of this interaction, quarks are confined inside bound states such as mesons and baryons. The interaction in QCD is also strong enough that it cannot be studied perturbatively. Non-perturbative aspects of QCD can be studied on a computer by mapping the theory onto a lattice in a formalism known as lattice QCD [1]. However as argued by Feynman, a classical computer will be limited in simulating the dynamics of a quantum system. The dynamics of QCD are relevant to a number of physical systems such as quark gluon plasma in the early universe, inelastic hadron collisions at particle accelerators, and supernovae. Quantum computers offer the ability to directly simulate QCD in these systems and make theoretical predictions from first principles.

Setting up a quantum simulation of lattice QCD requires the development of new theoretical tools. Quantum computers require the use of a Hamiltonian formulation unlike lattice QCD calculations on classical computers which work directly with a path integral. Once a formulation has been chosen, a physically relevant state must be prepared on the quantum computer. This could be the vacuum state or a system of hadrons depending on the physics that one wishes to study. Then the time evolution operator must be approximated on the quantum computer to evolve the system in time. How this is done depends on the nature of the simulation being performed. On a digital quantum computer, the computer's time evolution is broken into discrete operations known as gates that act on small numbers of the computer's degrees of freedom. In principle, an arbitrary unitary time evolution operator can be constructed on a digital quantum computer using an appropriate set of gates. In an analog quantum simulation, a quantum system is engineered to have a Hamiltonian that matches the one being simulated. This framework is limited what theories can be simulated, but requires less experimental control over the quantum computer which can make it useful in the near term. Regardless of the method, once the simulation has been evolved in time, measurements must be performed to extract physics from the simulation. The observables used in practice will vary depending on what type of physics is being simulated. To develop the theoretical tools to perform these calculations, it is helpful to study simplified toy models such as QCD in one spatial dimension or other asymptotically free theories such as the O(3) non-linear σ model.

In addition to the theoretical challenges in setting up the theory, quantum simulations will have to contend with the effects of noise on the quantum computer. Digital quantum computers are not able to implement gates without imperfections. Additionally as calculations are performed, the computer will become entangled with its environment and will decohere. Fortunately, these effects can be corrected for. Once the error rate in gates drops below a threshold, it becomes possible to implement error correcting codes and systematically reduce these errors. Even if gate errors are not low enough for error correction, error mitigation techniques can be used to reduce the size of errors. These techniques have enabled calculations to be performed that would otherwise be outside the reach of present day quantum computers.

This dissertation contributes to the development of quantum simulation of field theories with a focus towards performing quantum simulation of lattice QCD. Part II focuses on developing techniques for digital quantum simulation. In part III, techniques for performing an analog quantum simulation of the O(3) non-linear σ model on an analog cold atom quantum simulator are introduced.

In chapter 1, a mapping of SU(3) gauge fields onto qubit degrees of freedom is performed. This is used to perform quantum simulations of the real time evolution for SU(3) Yang Mills gauge theory on some small lattices. Methods are proposed to extend these calculations to larger lattices. This work was done in collaboration with N. Klco and M.J. Savage and was published in *Physical Review D* 103 (9), 094501.

In chapter 2, variational state preparation for SU(3) lattice gauge theory using the basis introduced in chapter 1 is studied. Bayesian optimization and gradient descent are both studied for optimizing the circuit on quantum hardware. The ground state of one and two plaquettes systems are prepared on IBM's quantum processors. Methods for constructing circuits for larger lattices are introduced and tensor network calculations are performed to demonstrate their scalability. This work was done in collaboration with I. Chernyshev and was published in *Physical Review D* 105 (7), 074504.

In chapter 3, improved Hamiltonians are derived to correct for the effects of gauge field truncation. It is shown in $1+1D$ that this enables low chromo-electric field truncations to quantitatively reproduce features of the untruncated theory over a range of couplings and quark masses. In $3+1D$, an improved Hamiltonian is derived for lattice QCD with staggered massless fermions. It is shown in the strong coupling limit that the spectrum qualitatively reproduces aspects of two flavor QCD and simulations of a small system are performed. This work is drawn from arXiv:2307.05593.

In chapter 4, algorithms for performing time evolution in effective quantum electrodynamics are developed. An analysis is performed to rigorously upper bound the worst case performance for these algorithms. Explicit circuits are introduced to implement these algorithms. These techniques are expected to be of relevance for implementing circuits to perform time evolution of the fermionic piece of the QCD Hamiltonian. This work was done in collaboration with T. Stetina and N. Wiebe and was published in *Quantum* 6, 622.

In chapter 5, an algorithm for computing the decay rate of unstable particles is introduced. A calculation is performed on IBM's quantum processor for a theory of two scalar fields. The finite volume errors are quantified and the scalability of the algorithm is determined. This work was published in *Physical Review D* 102 (9), 094505.

In chapter 6, methods for performing an analog quantum simulation of the Heisenberg model on a number of different hardware platforms is introduced. It is shown that above a critical drive strength, the Heisenberg model can be successfully simulated with perturbatively controlled errors. The breakdown of this controlled simulation is shown to be associated with a dynamical quantum phase transition. This work was done in collaboration with S. Caspar, H. Singh, M.J. Savage, and P. Lougovski and is drawn from arXiv:2207.09438.

In chapter 7, it is demonstrated that the Heisenberg model and the Ising model with a strong external field in an appropriate direction share eigenstates up to perturbative corrections. This is used to develop a proposal for preparation of the Heisenberg model ground state on analog quantum simulators. The feasibility of this method on cold atoms and superconducting qubit platforms is investigated. This work was done in collaboration with S. Caspar, M. Illa, and M.J. Savage and was published in *Quantum* 7, 970.

In chapter 8, the D-theory regularization of the O(3) non-linear σ model is mapped onto a cold atom quantum simulator. A new definition of the renormalized coupling, suitable for use with open boundary conditions, is introduced to show that this regularization correctly reproduces the O(3) non-linear σ model in the asymptotically free region with modest system sizes. Tensor network methods are used to show that the state preparation method introduced in chapter 7 can be used on cold atom systems to quantitatively reproduce the O(3) model's step scaling curve with experimentally realizable laser strengths and coherence times. This work was done in collaboration with S. Caspar, H. Singh, and M.J. Savage and was published in *Physical Review A* 107 (4), 042404.

0.0.1 Lattice Quantum Chromodynamics

Quantum chromodynamics is the fundamental theory describing nuclear physics in terms of fundamental particles. The theory is formulated in terms of spin $\frac{1}{2}$ Dirac fermions known as quarks coupled to SU(3) gauge fields that describe gluons. The theory is defined by the action

$$S_{QCD} = \int d^4x \; i \sum_f \bar{\psi}_f \gamma^\mu D_\mu \psi_f - m_f \bar{\psi}_f \psi_f - \frac{1}{4} G^a_{\mu\nu} G^{\mu\nu}_a \quad , \tag{1}$$

where ψ_f is the quark field with flavor f, γ^μ are the Dirac gamma matrices, m_f is the mass of quarks with flavor f. D_μ is the gauge covariant derivative defined by

$$D_\mu = \partial_\mu - igT_a A_\mu^a \quad , \tag{2}$$

where g is the gauge coupling, T_a are the Gellmann matrices, and A_μ^a are the gluon fields. $G_{\mu\nu}^a$ is the gluon field strength tensor defined by

$$G_{\mu\nu}^a = \partial_\mu A_\nu^a - \partial_\nu A_\mu^a + g f^{abc} A_\mu^b A_\nu^b \quad , \tag{3}$$

where f^{abc} are the SU(3) structure constants. Aspects of this theory can be studied perturbatively in g by evaluating the path integral

$$Z = \int D\bar{\psi}_f D\psi_f D A_\mu^a e^{iS_{QCD}} \quad , \tag{4}$$

using Feynman diagrams. Due to the property of asymptotic freedom, this expansion is valid at high energies and can be used to describe fragmentation in high energy collisions such as those that occur at the LHC [7]. However at lower energies, the quarks and gluons are confined into color singlet states known as baryons and mesons and the perturbative expansion breaks down.

Non-perturbative aspects of QCD can be probed by studying the theory on a lattice [1]. In the usual path integral formulation of lattice QCD, the gluon fields are mapped onto the links between sites in a four dimensional spacetime lattice. The gluon degrees of freedom are written in terms of parallel transporters which are defined by

$$U_\mu(x) = e^{iagT_c A_\mu^c(x)} \quad , \tag{5}$$

where x is a spacetime lattice position, μ specifies the direction of the link, a is the lattice spacing, g is the strong coupling constant, T_c are the Gellman matrices, and $A_\mu^c(x)$ is a gluon field on a link connected to site x pointing in direction μ. The action for the gluon piece of lattice QCD is given by

$$S_{LQCD} = -\sum_{x,\mu,\nu} \mathrm{Re}\left(\mathrm{Tr}\{\Box_{\mu\nu}(x)\}\right) \quad , \tag{6}$$

where the plaquette term $\Box_{\mu\nu}(x)$ is defined by

$$\Box_{\mu\nu}(x) = U_\nu^\dagger(x + a\hat{\nu}) U_\mu^\dagger(x + a\hat{\mu} + a\hat{\nu}) U_\nu(x + \hat{\mu}) U_\mu(x) \quad , \tag{7}$$

where $\hat{\mu}$ and $\hat{\nu}$ are unit vectors in the μ and ν directions. Note that the quarks will also have to mapped onto the lattice to fully simulate QCD, however there are subtleties involved that will be expanded on in later chapters of this thesis. Lattice QCD can be studied in Euclidean time by using classical computers to perform Monte Carlo sampling of $e^{-\beta S_{LQCD}}$. This has enabled non-perturbative calculations of static observables in QCD such as hadron masses and form factors [1, 8, 9, 10, 11, 12].

Quantum simulations of Yang-Mills gauge theory can be performed by keeping time continuous and discretizing the gauge fields in the spatial directions using a cubic lattice of sites and defining link variables connecting adjacent sites of this underlying grid. These link variables are parallel transporters that connect, for SU(3), color vectors at one site to those at an adjacent site. The Hamiltonian is a sum over the chromo-electric and chromo-magnetic contributions, as first discussed by Kogut and Susskind [13],

$$\hat{H} = \frac{g^2}{2a^{d-2}} \sum_{b,\text{links}} |\hat{\mathbf{E}}^{(b)}|^2 \; + \; \frac{1}{2a^{4-d}g^2} \sum_{\text{plaquettes}} \left[\, 6 \; - \; \hat{\Box}(\mathbf{x}) \; - \; \hat{\Box}^{\dagger}(\mathbf{x}) \, \right] \quad , \tag{8}$$

where g is the strong coupling constant, a is the lattice spacing between adjacent sites, and d is the number of spatial dimensions. In the irrep basis of tensor indices that are labeled by (p, q), the number of (fundamental, anti-fundamental) indices with total dimension

$$\dim(p, q) = \frac{(p+1)(q+1)(p+q+2)}{2} \quad , \tag{9}$$

the electric Hamiltonian is diagonal with eigenvalues determined by the Casimir operator,

$$\sum_b |\hat{\mathbf{E}}^{(b)}|^2 \, |p, q\rangle = \frac{p^2 + q^2 + pq + 3p + 3q}{3} \, |p, q\rangle \quad . \tag{10}$$

The plaquette operator, $\hat{\Box}(\mathbf{x})$, is defined in the same way as in the path integral formulation of lattice gauge theory, i.e.

$$\hat{\Box}(\mathbf{x}) = \mathrm{Tr}\left[\, \hat{U}^{\mathbf{3}}(\mathbf{x}, \mathbf{x} + a\boldsymbol{\mu}) \; \hat{U}^{\mathbf{3}}(\mathbf{x} + a\boldsymbol{\mu}, \mathbf{x} + a\boldsymbol{\mu} + a\boldsymbol{\nu}) \; \hat{U}^{\mathbf{3}}(\mathbf{x} + a\boldsymbol{\mu} + a\boldsymbol{\nu}, \mathbf{x} + a\boldsymbol{\nu}) \; \hat{U}^{\mathbf{3}}(\mathbf{x} + a\boldsymbol{\nu}, \mathbf{x}) \, \right] \quad , \tag{11}$$

where $\hat{U}^{\mathbf{3}}(\mathbf{x}, \mathbf{y})$ are 3×3 unitary matrices, and $\boldsymbol{\mu}$ and $\boldsymbol{\nu}$ are unit vectors that define the spatial orientation of the plaquette. In the electric basis, links are defined by states of the color irrep to which they belong, $\mathbf{R}$, and the (uncorrelated) orientations in the two color spaces they connect, α and β, $|\mathbf{R}, \alpha, \beta\rangle$. The electric contribution from each link is proportional to the Casimir operator acting on the link without changing the color irrep, while the plaquette operators, $\hat{\Box} + \hat{\Box}^{\dagger}$, add color fluxes to the links in the plaquette, $\mathbf{3}$

and $\overline{\mathbf{3}}$, which change the irrep of each link, subject to Gauss's law. Constraints imposed to define physically allowed states of the system are included through additional conditions. In the absence of external color charges and quarks, Gauss's law is satisfied by the product of link irreps at each vertex combining to a color singlet. The quantum simulation of this Hamiltonian was first considered by Byrnes and Yamamoto [14] where the Hilbert space was made finite by truncating the electric field representations. This enabled the mapping of electric field basis states onto qubit states and a conceptual framework for constructing quantum circuits to prepare low energy states and simulate time evolution lattice gauge theories.

Part II

DIGITAL QUANTUM SIMULATION

Chapter 1

SU(3) GAUGE FIELDS ON A QUANTUM COMPUTER

1.1 Introduction

For the quantum simulation of lattice gauge theories, the bases that are chosen to spatially latticize the field and to digitize, or capture through finite quantum resources, the continuous local group manifold affects the processes of initialization, the complexity of the time evolution operator, creation of localized wavepackets, and the resulting distribution of information required to be captured in the final measurement process. Due to its ubiquity and potential relevance to the initialization process, the efficiency of the time evolution operator is often prioritized, and a strategy of spatially local distributions of quantum registers is employed [15, 16]. With this tactic, algorithms for the implementation of large lattices can be defined through the design of a small number of local operators, commonly acting in two conjugate bases, that, when parallelized, allow for temporal propagation of the field with computation times that are independent of the volume. Thus, constructing an algorithm for the quantum simulation of fields begins with studies of the chosen basis or mapping of the field to quantum hardware.

In this chapter, the multiplet basis utilized in the work of Byrnes and Yamamoto [14] is integrated over the local gauge space at each vertex of the lattice, reducing the Hilbert space describing the system down to the local SU(N) irreducible representations below a chosen truncation. This approach has been previously used to explore (1 + 1)-dim SU(2) lattice gauge theory [17], further implemented for a 1-dim chain of plaquettes in SU(2) lattice gauge theory [18], and is here developed for application to SU(3) lattice gauge theory.

Quantum simulations of Yang-Mills theories and QCD are in their infancy. Precision calculations of quantities that can be directly compared with experiment are far in the future, and are expected to require major advances in quantum devices, algorithms and formalism. However, in starting along the path to this ultimate objective, explorations of simple systems, establishing informative benchmarks, analyzing features of profitable mappings, observing natural structures, quantifying truncation sensitivity, and identifying amenable architectures are all important steps. We focus on understanding the behavior of simple systems, one- and two-plaquette systems, with regard to coupling, truncations in color space, the scaling of global and local basis states and operators, and the mapping of color irreps onto qubits, qutrits and qudits. We perform quantum simulations of low-truncation one- and two-plaquette systems using IBM's QExperience superconducting quantum devices. Further, we examine a framework (that appears to scale amiably) for the use of controlled-plaquette operators on qudit systems as a way to perform simulations of SU(3) Yang-Mills gauge field theory.

1.2 The SU(3) Yang-Mills Hamiltonian

1.2.1 The Plaquette Operator

In the standard formulation of Hamiltonian lattice gauge theory [13], wavefunctions carry Clebsch-Gordon (CG) factors at each vertex with the effect of enforcing local gauge invariance. Using the notation of Fig. 1.1, an example of the local vertex structure is (upper-left vertex)

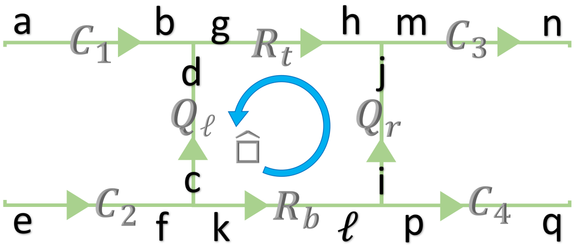

Figure 1.1: Following an arrow convention generalizable to higher dimension, the above link labels will be employed. Indices local to one end of each link represent a set of indices characterizing the local gauge space e.g., the color spin and color hypercharge in SU(3).

$$|\psi_{3pt}\rangle \sim \sum_{b,g,d,\Gamma} \langle \mathbf{C}_1, b, \overline{\mathbf{R}}_t, g | \overline{\mathbf{Q}}_\ell, d\rangle_\Gamma \; |\mathbf{C}_1, a, b\rangle |\mathbf{Q}_\ell, c, d\rangle |\mathbf{R}_t, g, h\rangle \quad , \tag{1.1}$$

where the sum is over the quantum numbers internal to the links at the vertex. The subscript, Γ, on the SU(3) CG coefficient indexes the multiplicity of combined irreps achieved through tensor contractions. An example of this multiplicity is in the product $\mathbf{8} \otimes \mathbf{8}$ that can be combined to produce the 8-dimensional irrep in two distinct ways, symmetric and antisymmetric contractions, with distinct CGs. These multiplicities mildly complicate the calculation of plaquette matrix elements, but are otherwise benign with respect to the structure of the quantum simulation.

With a truncation including only up to the single-index irreps, the vertices that contain a singlet (and are thus gauge invariant) are $\mathbf{1} \otimes \mathbf{1} \otimes \mathbf{1}$, $\mathbf{1} \otimes \overline{\mathbf{3}} \otimes \mathbf{3}$, $\mathbf{3} \otimes \mathbf{3} \otimes \mathbf{3}$, and those related under global conjugation and permutation symmetries. With a truncation including the $\mathbf{8}$

irrep, described by the two index tensor with one upper and one lower index, the number of gauge invariant vertices rises to include the $\mathbf{1} \otimes \mathbf{8} \otimes \mathbf{8}, \mathbf{3} \otimes \overline{\mathbf{3}} \otimes \mathbf{8}$ and $\mathbf{8} \otimes \mathbf{8} \otimes \mathbf{8}$.

A key role of the vertex CGs is to allow a localization of the plaquette operator, determining the magnetic Hamiltonian, as the minimal contracted loop of local link operators (directionality as in Fig. 1.1),

$$\hat{\Box} = \hat{U}^{\mathbf{3}}_{\alpha,\beta} \hat{U}^{\mathbf{3}}_{\beta,\gamma} \left(\hat{U}^{\mathbf{3}}_{\gamma,\delta} \right)^{\dagger} \left(\hat{U}^{\mathbf{3}}_{\delta,\alpha} \right)^{\dagger} \quad , \tag{1.2}$$

$$\hat{U}^{\mathbf{r}}_{\alpha,\beta} |\mathbf{R}, a, b\rangle = \sum_{\oplus \mathbf{R}', \vec{\Gamma}} \sum_{a'b'} \sqrt{\frac{\dim(\mathbf{R})}{\dim(\mathbf{R}')}} |\mathbf{R}', a', b'\rangle \ \langle \mathbf{R}, a, \mathbf{r}, \alpha | \mathbf{R}', a' \rangle_{\Gamma_1} \langle \mathbf{R}', b' | \mathbf{R}, b, \mathbf{r}, \beta \rangle_{\Gamma_2} \quad , \tag{1.3}$$

where $\mathbf{r}$ indicates the representation of the link operator, the $a(b)$ label states within an irrep in the left(right) spaces, and the primes denote final state properties generated by the application of the link operator. For SU(2), the internal state labels are naturally identified with half integers capturing the third component projection of the total angular momentum. For SU(3), these labels may be the three-component vector of color isospin(T)-hypercharge(Y) rational numbers (T, T^z, Y) with T^z, Y additive as utilized in Ref. [14] or, more abstractly, the Gelfand–Tsetlin patterns.

While this four-link operator is naively capable of producing transitions outside the gauge-invariant subspace, the vertex CGs prevent such transitions. To be concrete, consider the application of a plaquette operator impacting two links of a three-point vertex in an initial state of $\mathbf{C}_1 = \mathbf{R}_t = \mathbf{3}$ and $\mathbf{Q}_\ell = \mathbf{8}$. Schematically,

$$\hat{\Box}^{\dagger} |\mathbf{3}\rangle_{C_1} |\mathbf{8}\rangle_{Q_\ell} |\mathbf{3}\rangle_{R_t} \rightarrow$$

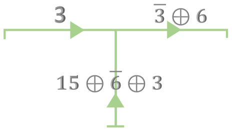

$$\rightarrow \begin{cases} |\mathbf{3}\rangle |\overline{\mathbf{6}}\rangle |\overline{\mathbf{3}}\rangle & \langle \mathbf{3}, \ , \mathbf{3}, \ |\mathbf{6}, \ \rangle \\ |\mathbf{3}\rangle |\mathbf{3}\rangle |\overline{\mathbf{3}}\rangle & \langle \mathbf{3}, \ , \mathbf{3}, \ |\overline{\mathbf{3}}, \ \rangle \\ |\mathbf{3}\rangle |\mathbf{3}\rangle |\mathbf{6}\rangle & \langle \mathbf{3}, \ , \overline{\mathbf{6}}, \ |\overline{\mathbf{3}}, \ \rangle \\ |\mathbf{3}\rangle |\mathbf{15}\rangle |\mathbf{6}\rangle & \langle \mathbf{3}, \ , \overline{\mathbf{6}}, \ |\overline{\mathbf{15}}, \ \rangle \end{cases} \quad , \tag{1.4}$$

where the right shows the physical irrep configurations populated by the plaquette operator application and the associated CGs that would appear in the vertex factor. When applying the $\hat{\Box}^{\dagger}$ operator, $\mathbf{3}$'s will be applied, according to Eq. (1.3), to $\mathbf{R}_t$ and $\mathbf{Q}_\ell$. Some combinations of the irreps generated by the plaquette operator are disallowed by Gauss's law, requiring information of the state of the neighboring link $\mathbf{C}_1$ stored in the vertex CG to maintain gauge invariance. An example of such a configuration disallowed by the neighboring link is $|\mathbf{3}\rangle_{C_1} |\mathbf{15}\rangle_{Q_\ell} |\overline{\mathbf{3}}\rangle_{R_t}$ as $\mathbf{3} \otimes \mathbf{3}$ does not produce a $\overline{\mathbf{15}}$ or, equivalently, there is no singlet present in $\mathbf{3} \otimes \mathbf{3} \otimes \mathbf{15}$ tensor product.

As detailed in Appendix .1.1, the vector components at each vertex can be captured analytically through the calculation of composite CG factors. As a result, the basis for quantum simulation can be simplified to expressing an SU(3) irrep on each link, leaving internal quantum numbers to impact the matrix elements comprising the local plaquette operator calculated classically. This formulation extends the observations previously made in SU(2) lattice gauge theory for a one-dimensional string of links [17] and plaquettes [18]. Defining notation through the 9-R symbol,

$$\begin{Bmatrix} \mathbf{A} & \mathbf{B} & \mathbf{C} \\ \mathbf{3} & \mathbf{1} & \mathbf{3} \\ \mathbf{D} & \mathbf{B} & \mathbf{E} \end{Bmatrix} = \sum \langle \mathbf{D}, y', \mathbf{B}, x | \mathbf{E}, q' \rangle_{\Gamma_1} \langle \mathbf{A}, y, \mathbf{B}, x | \mathbf{C}, q \rangle_{\Gamma_2} \langle \mathbf{A}, y, \mathbf{3}, c | \mathbf{D}, y' \rangle_{\Gamma_3} \langle \mathbf{C}, q, \mathbf{3}, c | \mathbf{E}, q' \rangle_{\Gamma_4} \quad , \tag{1.5}$$

where the sum is over all local vector and multiplicity indices, the plaquette matrix elements may be expressed as

$$\left\langle \begin{pmatrix} \mathbf{C}_1, \mathbf{R}'_t, \mathbf{C}_3 \\ \mathbf{Q}'_\ell, \mathbf{Q}'_r \\ \mathbf{C}_2, \mathbf{R}'_b, \mathbf{C}_4 \end{pmatrix} \middle| \hat{\Box} \middle| \begin{pmatrix} \mathbf{C}_1, \mathbf{R}_t, \mathbf{C}_3 \\ \mathbf{Q}_\ell, \mathbf{Q}_r \\ \mathbf{C}_2, \mathbf{R}_b, \mathbf{C}_4 \end{pmatrix} \right\rangle = \sqrt{\frac{\dim(\mathbf{R}_t)\dim(\mathbf{R}_b)}{\dim(\mathbf{R}'_t)\dim(\mathbf{R}'_b)\dim(\mathbf{Q}_\ell)\dim(\mathbf{Q}_r)\dim(\mathbf{Q}'_\ell)^3\dim(\mathbf{Q}'_r)^3}}$$
$$\begin{Bmatrix} \overline{\mathbf{R}}_t & \mathbf{C}_1 & \overline{\mathbf{Q}}_\ell \\ \mathbf{3} & \mathbf{1} & \mathbf{3} \\ \overline{\mathbf{R}}'_t & \mathbf{C}_1 & \overline{\mathbf{Q}}'_\ell \end{Bmatrix}_{\bullet\square} \begin{Bmatrix} \mathbf{R}_t & \overline{\mathbf{C}}_3 & \overline{\mathbf{Q}}_r \\ \overline{\mathbf{3}} & \mathbf{1} & \overline{\mathbf{3}} \\ \mathbf{R}'_t & \overline{\mathbf{C}}_3 & \overline{\mathbf{Q}}'_r \end{Bmatrix}_{\square\bullet} \begin{Bmatrix} \overline{\mathbf{R}}_b & \mathbf{C}_2 & \mathbf{Q}_\ell \\ \overline{\mathbf{3}} & \mathbf{1} & \overline{\mathbf{3}} \\ \overline{\mathbf{R}}'_b & \mathbf{C}_2 & \mathbf{Q}'_\ell \end{Bmatrix}_{\bullet\square} \begin{Bmatrix} \mathbf{R}_b & \overline{\mathbf{C}}_4 & \mathbf{Q}_r \\ \mathbf{3} & \mathbf{1} & \mathbf{3} \\ \mathbf{R}'_b & \overline{\mathbf{C}}_4 & \mathbf{Q}'_r \end{Bmatrix}_{\square\bullet} \quad , \tag{1.6}$$

where the subscipts on the 9-R symbols graphically denote the corresponding vertex in Fig. 1.1. The delocalization of information necessary to consider in the application of a plaquette operator, depicted in Eq. (1.4), is set at the distance of neighboring links and does not grow beyond this locality for larger lattices, nor in higher dimension. Because the simple Hilbert space structure of qubit degrees of freedom will not provide the vertex CGs necessary to retain a four-link local plaquette operator, the CGs, usually separately relegated to the vertex and the operator, have been included here in their entirety. Two methods of implementation will be explored below. In Section 1.4, the vertex CGs of Eq. (1.1) will be manually captured through symmetry-projected, global wavefunctions of the lattice mapped to quantum states of a quantum device. In Section 1.5, the vertex CGs will be captured in the structure of an eight-link operator controlled on the quantum states of the four neighboring links.

1.2.2 Connectivity in Multiplet Space

When designing operations for the implementation of dynamical processes within a Hilbert space, it is helpful to understand the natural connectivity between states. This basis-dependent feature will affect the efficiency of digital formulations of time evolution as well as their ease of implementation on quantum architectures with limited connectivity. Naturally, designing quantum hardware with connectivity matching that of the field Hilbert space (or vice versa) is expected to be advantageous.

When an SU(2) link operator in the fundamental representation acts, it is capable of raising or lowering the total angular momentum j value of the link state by $\pm\frac{1}{2}$. When the vector components of the link Hilbert space are classically incorporated into the matrix elements of the plaquette operator, as discussed above, these j values are sufficient to describe the state of the local link degree of freedom. Thus, in a basis of multiplets, the relevant connectivity of quantum states within an SU(2) gauge link is in the form of a simple ladder, as shown in Fig. 1.2. While the coefficients associated with connections

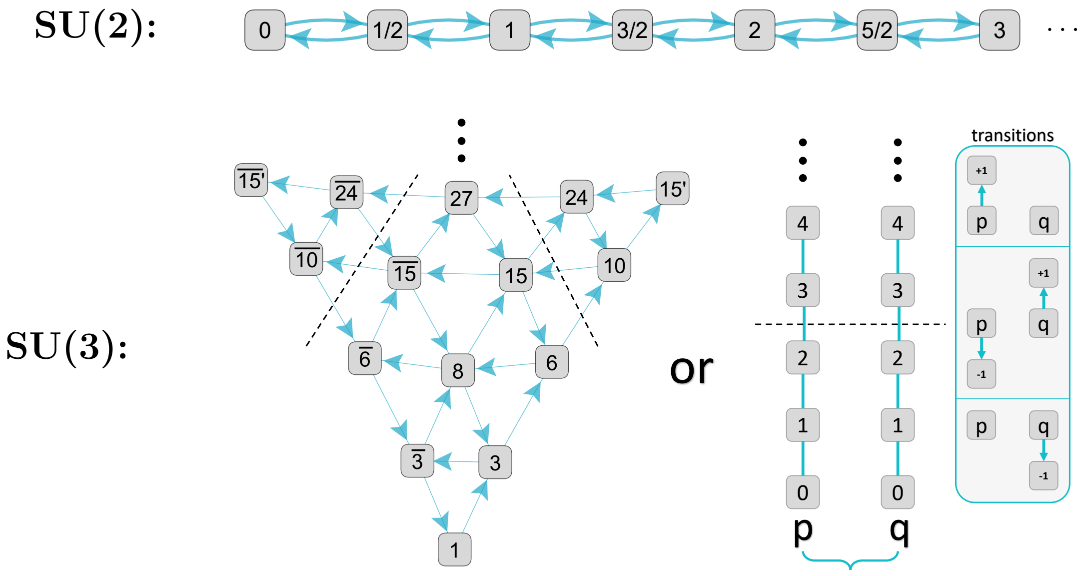

Figure 1.2: Connectivity diagrams for the low-Casimir irreps in SU(2) and SU(3) gauge theory upon application of the plaquette operator. In SU(2), connections are bidirectional. In SU(3), connections between multiplets are directional, shown here for the application of the fundamental representation. The link Hilbert space can be captured through the connectivity of a single constrained hexagonal lattice of quantum states (lower-left panel) or through a pair of correlated one dimensional lattices (lower-right panel).

between these states depend on the surrounding links and the associated local CG factors, states interact with maximally two neighboring states.

For SU(3) lattice gauge theory in the multiplet basis, the connectivity among states within the local gauge link Hilbert space is only slightly more elaborate, and is well known from group theory. For the link operator in the **3** or $\overline{\mathbf{3}}$, the tensor indices become,

$$\begin{aligned} (p,q) \otimes (1,0) &= (p+1,q) \oplus (p-1,q+1) \oplus (p,q-1) \quad , \\ (p,q) \otimes (0,1) &= (p,q+1) \oplus (p+1,q-1) \oplus (p-1,q) \quad . \end{aligned} \tag{1.7}$$

A connectivity diagram of the transitions described by Eq. (1.7) is shown at the bottom of Fig. 1.2, with black dashed lines indicating a possible truncation of irreps with up to two fundamental and two antifundamental indices. For each irrep not affected by the lower boundary of zero indices or the upper truncation, three connections exit the irrep associated with the three transitions described in Eq. (1.7). Connections into any irrep through the fundamental link operator also appear with maximal number three and along distinct paths from those exiting the irrep. In this sense, the one-dimensional nearest-neighbor locality of the SU(2) link-operator-generated gauge space is promoted in SU(3) to a two-dimensional hexagonal lattice in the bulk of high irrep truncation on each link. Importantly, these connections remain local upon the two-dimensional manifold.

1.2.3 Embeddings of the Gauge Space

Due to their role in defining the Hilbert space, the basis used to digitize gauge fields impacts many aspects of quantum simulations of gauge-field theories. It is for this reason that understanding the practical consequences of basis choice, or distributions of the field content onto the degrees of freedom, is expected to play a central role in optimizing simulations on different quantum architectures.

Before discussing the bases explored in this manuscript for the digitization of the SU(3) gauge field, it is worth pausing to reflect upon the basic assumption that continuous gauge fields be digitized at all. There is an alternative to digitizing the gauge field directly that retains a spatially local distribution of qubit degrees of freedom. Rather than implementing the gauge field continuum limit and then the thermodynamic and spatial continuum limits, it has been proposed, under the names of link models or qubit regularization, that this can be replaced with a one-step process by devising a spin system of appropriate local symmetries with a critical point in the same universality class as the field of interest [19, 20, 21, 22, 23, 24, 25]. Tuning to the lattice continuum limit at a phase transition of the latticized spin system produces an emergent relativistic field theory. One way to interpret success with this approach is through spatial blocking of the lattice producing effectively continuous field values in the continuum limit at the critical point. Just as the correlation length of the field determines the lattice volume needed to approach the thermodynamic limit for the spatial continuum with continuous fields, a second correlation length will be present in the spin lattice expressing the blocked volume necessary to capture effectively continuous fluctuations in the local field degrees of freedom. For a scalar field, it has been shown that the local digitization of the field, and the efficiency of the local quantum Fourier transform (QFT), allows the effectively continuous fluctuations in the local field degrees of freedom to be captured with double exponential convergence in local qubit number [15, 16, 26, 27]. Benefitting from this application of the Nyquist-Shannon (NS) sampling theorem, the number of qubits per site relevant to foreseeable applications is expected to be $\lesssim 5$ [26, 27]. With current methodologies, the spatial continuum of the scalar field retains polynomial lattice artifacts as the volume-sized QFT is not expected to be efficient and thus modifications to the lattice dispersion relation will appear polynomially with the lattice spacing [28, 27]. When working in a spin system, both the field continuum and the spatial continuum limits are naïvely expected to be of the latter type, allowing neither to enjoy the rapid NS convergence. It is for this reason, with an expectation that local NS convergence will retain some relevance for digitized quantum fields beyond the scalar field, that the current manuscript will focus on the local digitization of the gauge field rather than the identification of a UV completion structured as a local spin system sharing a universality class with QCD. However, the rapidly evolving quantum ecosystem and exploratory nature of current development encourages thorough investigation of all possible avenues for embedding gauge fields into controllable quantum architectures.

Multiple embeddings of the lattice Hilbert space through the basis of SU(3) irreps will be considered in the following. The first distinction that can be made is whether the embedding is *global* or *local*. A local embedding of the Hilbert space assigns a qubit register to each link of the lattice, thus storing local information of the field in locally-distributed quantum systems. Distributing qubits/qudits across the lattice in this way is not always the most efficient use of Hilbert space. In particular there are a number of symmetries present in the gauge theory creating correlations between the link states e.g., vertex gauge symmetries, spatial parity and color-parity. Being good symmetries of the Hamiltonian, a state that begins in one symmetry sector will remain within the sector throughout its dynamical evolution. Transferring to a *global* embedding allows manual projections into these symmetry sectors, as utilized in Refs. [29, 30]. The resulting efficient use of Hilbert space, beyond reducing the total qubit resource requirements of the calculation, protects the calculation from gauge-variant or symmetry-breaking errors. Each state of the quantum hardware is associated with a full lattice configuration with the desired projected symmetry. As long as an error maintains the computational basis, all errors maintain global and vertex symmetries of the lattice in the global embedding.

While the global embedding is advantageous for small lattices on noisy hardware, the classical computational demands for pre-conditioning the Hilbert space and computing symmetry-projected matrix elements scale poorly with the volume of the lattice. For this reason, we further explore two link-local embeddings of the lattice Hilbert space in the irrep basis. In the first approach, a single quantum register or qudit is used to capture the gauge space of each link, the operations of Section 1.5 describe how the internal modes must interact in order to express time evolution of a quantum state with respect to the magnetic Hamiltonian. While full connectivity has been permitted within a qudit, with rotations mixing populations between any two modes, it can be seen from Fig. 1.2 that the required mode connectivity does contain a sense of locality. In particular, the dynamical mode connectivity, reflecting that produced by the plaquette operator between irreps, will have a structure of nearest neighbor locality in a truncated and constrained two-dimensional hexagonal lattice. While this locality is an improvement over arbitrarily non-local interactions, this connectivity is potentially sub-optimal, unless a qudit architecture is designed that naturally reflects this two-dimensional structure. In particular, for a one-dimensional embedding of the irrep modes into a ladder-structured qudit, necessary mode rotations delocalize as the irrep truncation increases, reflected by the growing number of irreps per row in Fig. 1.2.

One natural way to address the growing two-dimensional link structure in gauge space, inspiring the second local embedding explored in this work, is to introduce a number of qudits on every link equal to the rank of the gauge group, two for SU(3), as introduced by Byrnes and Yamamoto [14]. These two qudits will reflect the tensor index structure of the irrep, in SU(3) denoted as (p, q) in Section 1.2 above, with one qudit specifying the value of p and the second indicating the value of q. In this local (p, q) representation of the local irreps, the p and q registers are simply integers from zero to the maximum number of tensor indices considered. The plaquette operator produces correlated transitions by $\pm 1, 0$ within the p and q qudits at each active link of a plaquette. In this way, further separating the link space into a pair of qudits naturally simplifies the two-dimensional connectivity shown in the left panel of Fig. 1.2 into a correlated pair of qudits shown in the right panel of Fig. 1.2, each requiring only a raising/lowering operator within a one-dimensional embedded space. With this splitting of the link space into two qudits, however, operators of up to 8 qudits controlled on another 8 qudits will be required for constructing the local time evolution operators for the one-dimensional plaquette string. As hardware-specific strategies evolve for implementing mode-isolated multi-qudit unitary rotations, tradeoffs in the fidelity of intra- and inter-qudit operations will inspire a decision: implementing a two-dimensional gauge space within a single qudit at each link versus implementing one-dimensional correlated gauge spaces within each of two qudits per link, or some spatially dependent combination of the two.

As will become clear, the choice of basis inspires different ways to perform the gauge field truncations, resulting in different convergence properties and resource requirements for simulation. Local truncations at the level of the representations in the link Hilbert spaces readily scale to larger systems, requiring resources that scale with the spatial volume of the simulation. While a global truncation connects well to intuition based on globally conserved quantities, the implementation of such a basis does not scale well with increasing system size. It would appear that an adaptive local truncation scheme constrained by a global truncation may be required for optimal use of available resources in future simulations, though constructing such a scheme is beyond the scope of this work.

1.3 The Single Plaquette

A single plaquette is one of the simplest gauge-invariant objects that can be constructed within a lattice gauge field theory. For Yang-Mills gauge theory, the Hamiltonian responsible for its dynamics is a special case of that given in Eq. (8), given by

$$\hat{H} = \frac{g^2}{2} \sum_{b,\text{links}} |\hat{\mathbf{E}}^{(b)}|^2 + \frac{1}{2g^2}\left(6 - \hat{\Box} - \hat{\Box}^\dagger\right) \quad , \tag{1.8}$$

where the lattice spacing is set to $a = 1$, and b is an adjoint color index. The Hilbert space of a single link has been defined previously, spanned by the eigenstates of the electric-field strength operator, $|\mathbf{R}, \alpha, \beta\rangle = |\mathbf{R}, \alpha\rangle_L |\mathbf{R}, \beta\rangle_R$. The Gauss's law constraint allows the state of the one-plaquette system to be expressed in terms of basis states of the form

$$|\mathbf{R}\rangle = \frac{1}{\dim(\mathbf{R})^2} \sum_{\alpha,\beta,\gamma,\delta} |\mathbf{R}, \alpha, \beta\rangle_1 |\mathbf{R}, \beta, \gamma\rangle_2 |\mathbf{R}, \gamma, \delta\rangle_3 |\mathbf{R}, \delta, \alpha\rangle_4 \quad , \tag{1.9}$$

where $\mathbf{R}$ is the representation of each link. The irreducible representations of $SU(3)$ with tensor representation $T^{a_1,a_2,\cdots,a_p}_{b_1,b_2,\cdots,b_q}$ can be specified by p and q, and the global basis states for the one plaquette system is conventionally denoted by $|p, q\rangle$. The electric energy of a basis state is determined by the action of the Casimir operator (Eq. (10)), and is equal to four times the value of the Casimir operator on a single link multiplied by a factor of $g^2/2$. The plaquette operator is defined in Eq. (11), and the subsequent section. For the one-plaquette system, matrix elements between basis states $\langle \mathbf{R}_f | \hat{\Box} | \mathbf{R}_i \rangle = 1$ if $\mathbf{R}_f$ is present in the decomposition of $\mathbf{R}_i \otimes \mathbf{3}$, and 0 otherwise, by the completeness of CG coefficients.

1.3.1 Color Space Truncation Errors

As any computational framework is comprised of a finite number of controllable degrees of freedom, numerical explorations of gauge theories require spatial latticization as well as a form of digitization and truncation of the continuous field. As discussed above for SU(3) gauge theory on a single plaquette, digitization will here be accomplished in a gauge invariant way by truncating the number of tensor indices (p, q) at values (Λ_p, Λ_q) with $\Lambda_p = \Lambda_q$ a choice following the natural color parity symmetry of the system. Any truncation of the field will introduce controlled, systematic errors that must be quantified. Previous explorations of digitized scalar fields on a spatial lattice found that the field-space digitization converged double-exponentially in the number of qubits per lattice site describing the local field [16, 15, 31, 26, 27]. This convergence is attributed to the Nyquist-Shannon sampling theorem when the field and conjugate momentum bases are distributed appropriately. In Appendix .1.2, it is shown analytically that the asymptotic form of the "color" space wavefunction for a single plaquette in SU(2) gauge theory is Gaussian with respect to the irrep dimensionality or number of tensor indices. In the case of 1+1 dim. SU(2) lattice gauge theory, the exponential convergence of low-lying quantities with increasing truncation has been identified previously as discussed, for example, in Ref. [32]. In this section, it is shown numerically that this Gaussian convergence is also present in the color space of an SU(3) plaquette ground state, as well as its static and dynamical observables.

Focusing upon the ground state wavefunction in a basis of irreducible representations, Fig. 1.3 shows an exponentially localized distribution of amplitudes. In the left panel of

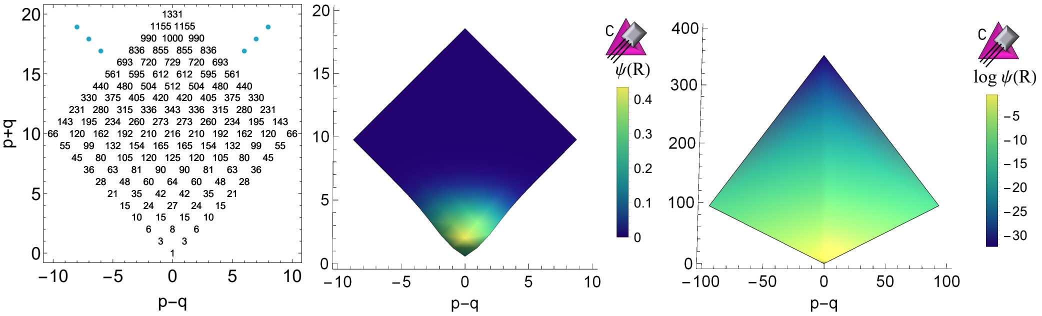

Figure 1.3: On a grid (left panel) of irreducible representations organized by their dimensionality and plaquette connectivity (as shown in Fig. 1.2), support of the the ground state wavefunction $\psi(\mathbf{R})$, shown for $g = 0.5$, is localized to low irrep dimensionalities (center panel). Conjugate irreps appear on the left half of the grid with real irreps appearing along the center vertical. The right panel shows $\log \psi(\mathbf{R})$ on a scaled quadratic grid for visual clarity of the convergence structure.

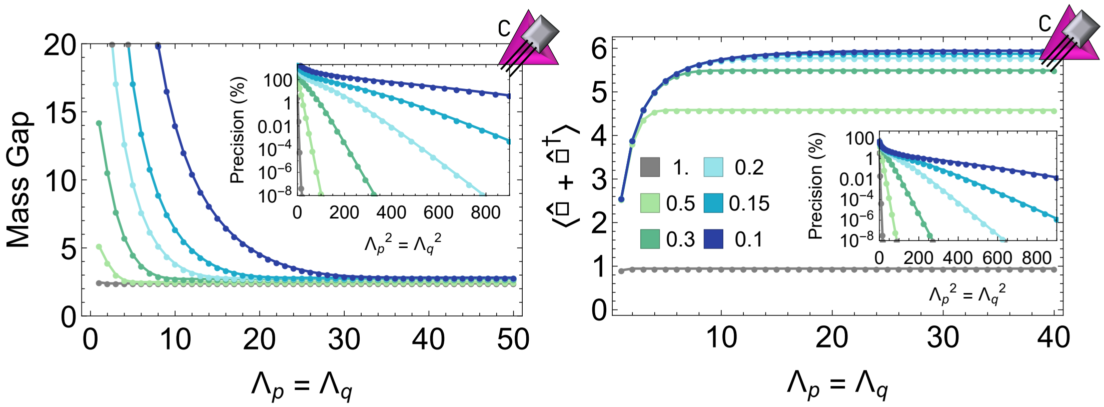

Figure 1.4: Mass gap (left panel) and vacuum expectation value of the Hermitian magnetic plaquette operator $\hat{\Box} + \hat{\Box}^\dagger$ (right panel) for one plaquette in SU(3) gauge theory as a function of Λ_p, the irrep tensor index truncation. Convergence is demonstrated for six different values of the coupling ($g = 0.1$ to 1). Inset panels show the percent deviation in observables from their values without truncation. The inset x-axes are squared for visual clarity of the convergence structure.

Fig. 1.3, a grid of irrep dimensionalities is established akin to that of Fig. 1.2. Neighboring points on this grid are connected through the magnetic plaquette operator and thus experience a sense of locality. The x-axis of this space is the difference between the number of fundamental and anti-fundamental indices in the tensor representation of each irrep, resulting in conjugate irreps residing at negative values and real irreps residing along the $p - q = 0$ axis. The dimensionalities of irreps below a truncation of $\Lambda_p = \Lambda_q = 10$ are shown explicitly, and higher index irreps would appear in the upper triangles. In this space, the ground state amplitudes of the SU(3) single plaquette wavefunction at coupling $g = 0.5$ are shown in the center and right panels. In the center panel, it is seen that support of this wavefunction is highly localized to the low-index regime. Of course, the extent of localization is g-dependent and becomes dispersed as g is lowered toward the weak coupling limit. The right panel presents the same wavefunction as in the center panel, but with logarithmic and quadratic functional distortions on the wavefunction amplitudes and the tensor indices, respectively. From this perspective, the asymptotic Gaussian structure of the irrep-space wavefunction is visually clear.

The exponential localization of the single plaquette wavefunction extends this profitable convergence also to static and dynamic observables. Figure 1.4 shows the convergence of the mass gap and the magnetic plaquette operator expectation value at a range of couplings. Static observables for the unit coupling are found to converge to 10^{-8} percent of their asymptotic values at a low irrep truncation of $\Lambda_p = 4$ up to and including tensor irreps with

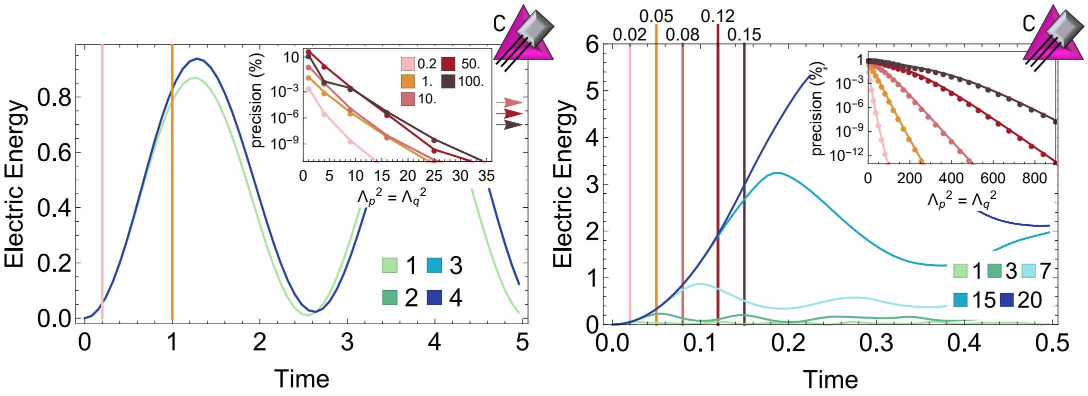

Figure 1.5: Expectation of the electric energy as a function of time for the single plaquette beginning in the strong coupling vacuum. Evolution is shown for tensor index truncations $\Lambda_p \leq 4$ (20) in the left (right) panel where $g = 1$ (0.1). Insets show the percent deviation of the electric energy from its value without truncation at fixed times indicated by vertical lines in the main panels ($t = 10, 50, 100$ are beyond the domain of left panel). The inset x-axes are squared for visual clarity of the convergence structure.

four fundamental and four anti-fundamental indices. As g is lowered and the wavefunction disperses in irrep space, truncation errors naturally become more dramatic. Interestingly, the mass gap demonstrates low g-dependence at high truncation, Λ_p, throughout the shown coupling range. The insets of Fig. 1.4 provide convergence information with tensor index truncations scaled quadratically, as in the right panel of Fig. 1.3, such that the linear trajectories experienced at large tensor index truncations express Gaussian-type convergence structure. From these insets, one can connect necessary quantum resources to the attainable precision of local observables as the weak-coupling limit is approached. For example, percent-level precision for these quantities at couplings $g \geq 0.3$ is expected to be achievable with $\Lambda_p \leq 10$ or equivalently 3-4 qubits per index register. These features are expected to apply to the link-space localization and convergence on larger lattices of SU(3) gauge theory. This suggests that SU(3) Yang-Mills simulations in a cubic spatial lattice of extent $10 \times 10 \times 10$ could be performed with $\lesssim 10^4$ qubits at this coupling.

It is important to keep in mind that our analysis has been performed in the electric basis, and requires increasing resources with decreasing lattice spacing to achieve the same level of precision for any given quantity. Therefore, there is a minimum lattice spacing (coupling) below which computations are inaccessible to the electric basis for a given quantum device and available classical computing resources. Recent work by Haase *et al* [33] has shown in the context of QED that working instead with the magnetic basis is potentially more effective in calculations at small lattice spacings, making it an interesting area for further investigations.

As a final demonstration, Fig. 1.5 shows similar exponential convergence properties also for dynamic observables. Calculating the time evolution of the electric energy as a function of time at increasing field truncations, Λ_j, similar Gaussian precision improvements are observed. Related to the fact that the $g = 1$ mass gap is well captured at low truncation, the $g = 1$ time evolution in the left panel of Fig. 1.5 is well captured at low truncations even at long times. For example, the expectation value of the electric energy at time $t = 100$ is achievable at single precision with just 3 qubits per index register. As the coupling is reduced and the wavefunction experiences reduced locality, larger truncations are demanded to achieve precise calculations of long-time observables. The right panel of Fig. 1.5 quantifies this scenario for a coupling of $g = 0.1$. Convergence calculations such as these inform estimations of resource requirements for future lattice gauge theory simulations that will be implemented at a selection of coupling strengths and extrapolated to inform the continuum limit with a complete quantification of uncertainties. In subsequent subsections, we show the results of simulations of these systems performed on IBM's superconducting architecture.

1.3.2 Global Basis for One Plaquette

8 *Truncation*

It is informative to study a simple basis truncation of $p, q \leq 1$, containing the irreps $\{\mathbf{1}, \mathbf{3}, \overline{\mathbf{3}}, \mathbf{8}\}$. These can be straightforwardly mapped to two qubits as $\{|00\rangle, |10\rangle, |01\rangle, |11\rangle\} = \{|\mathbf{1}\rangle, |\mathbf{3}\rangle, |\overline{\mathbf{3}}\rangle, |\mathbf{8}\rangle\}$. In this basis, the Hamiltonian is

$$\hat{H} = \frac{g^2}{2}\begin{pmatrix} 0 & 0 & 0 & 0 \\ 0 & \frac{16}{3} & 0 & 0 \\ 0 & 0 & \frac{16}{3} & 0 \\ 0 & 0 & 0 & 12 \end{pmatrix} + \frac{1}{g^2}\left(3\,\hat{\mathbb{I}} - \frac{1}{2}\begin{pmatrix} 0 & 1 & 1 & 0 \\ 1 & 0 & 1 & 1 \\ 1 & 1 & 0 & 1 \\ 0 & 1 & 1 & 0 \end{pmatrix}\right) \quad , \tag{1.10}$$

consistent with the results provided in Ref. [34] (when truncated at $f_1 \leq 2$ and removing the contribution from the $\mathbf{6}$ and $\overline{\mathbf{6}}$). In terms of operators acting on a two-qubit system, the electric Hamiltonian operator can be decomposed as

$$\hat{H}_E = \frac{g^2}{6}\left(17\,\hat{\mathbb{I}}\otimes\hat{\mathbb{I}} - 9\,\hat{Z}\otimes\hat{\mathbb{I}} - 9\,\hat{\mathbb{I}}\otimes\hat{Z} + \hat{Z}\otimes\hat{Z}\right) \quad , \tag{1.11}$$

where $\hat{\mathbb{I}}$ is the identity operator. The magnetic Hamiltonian can similarly be decomposed as

$$\hat{H}_B = \frac{3}{g^2}\hat{\mathbb{I}}\otimes\hat{\mathbb{I}} - \frac{1}{2g^2}\left(\hat{X}\otimes\hat{\mathbb{I}} + \hat{\mathbb{I}}\otimes\hat{X} + \frac{1}{2}\left(\hat{X}\otimes\hat{X} + \hat{Y}\otimes\hat{Y}\right)\right) \quad . \tag{1.12}$$

While there is a wide range of tactics being explored for the time evolution of quantum systems [35, 36, 37, 38, 39], the method of Trotterization [40, 41] is a qubit-efficient approach introducing zero auxiliary qubits. Focusing on this latter method, time evolution through Trotterization [42, 43, 44, 45, 46] for a time Δt of a general quantum wavefunction is approximated at first and second orders as

$$e^{-i\Delta t\sum\limits_k \hat{H}_k} \sim \prod_k e^{-i\Delta t\hat{H}_k} + O(\Delta t^2) \sim \prod_{k=N}^{1} e^{-i\frac{\Delta t}{2}\hat{H}_k}\prod_{k=1}^{N} e^{-i\frac{\Delta t}{2}\hat{H}_k} + O(\Delta t^3) \quad . \tag{1.13}$$

Neglecting terms proportional to the identity, the one-plaquette Hamiltonian can be separated into Trotterized operators, $\hat{H} = \hat{H}_1 + \hat{H}_2$, with

$$\begin{aligned}\hat{H}_1 &= \left(\frac{17g^2}{6} + \frac{3}{g^2}\right)\hat{\mathbb{I}}\otimes\hat{\mathbb{I}} - \frac{g^2}{6}\left(9\,\hat{Z}\otimes\hat{\mathbb{I}} + 9\,\hat{\mathbb{I}}\otimes\hat{Z}\right) - \frac{1}{2g^2}\left(\hat{X}\otimes\hat{\mathbb{I}} + \hat{\mathbb{I}}\otimes\hat{X}\right)\\ \hat{H}_2 &= \frac{g^2}{6}\hat{Z}\otimes\hat{Z} - \frac{1}{4g^2}\left(\hat{X}\otimes\hat{X} + \hat{Y}\otimes\hat{Y}\right) \quad .\end{aligned} \tag{1.14}$$

The matrix exponential of the first Hamiltonian contribution can be implemented with single-qubit gates, while that of the second Hamiltonian contribution can be implemented as

$$e^{i(a\hat{X}\otimes\hat{X} + b\hat{Y}\otimes\hat{Y} + c\hat{Z}\otimes\hat{Z})} =$$

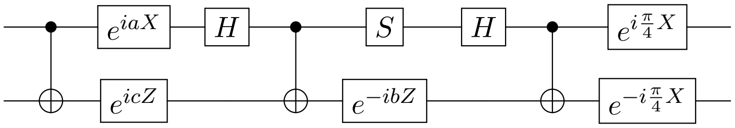

, (1.15)

using the decomposition of the SU(4) Cartan subalgebra [47, 48].

The panels of Fig. 1.6 show the probability of a single plaquette remaining in the trivial vacuum, $|00\rangle$, and its electric energy fluctuations for a color irrep basis truncated to $\{\mathbf{1}, \mathbf{3}, \overline{\mathbf{3}}, \mathbf{8}\}$. Up to four 2nd-order Trotter steps of the form,

$$\hat{U}(\Delta t) = e^{-i\frac{\Delta t}{2}\hat{H}_1}e^{-i\Delta t\hat{H}_2}e^{-i\frac{\Delta t}{2}\hat{H}_1} \quad , \tag{1.16}$$

are implemented for a coupling of $g = 1$. Beyond this number, it is found that the increased gate fidelity and coherence demands of the extended quantum circuit do not allow controlled mitigation of noise. The dashed curves correspond to exact classical calculations of each Trotterization, with the limit of continuous time evolution shown by the solid black curve.

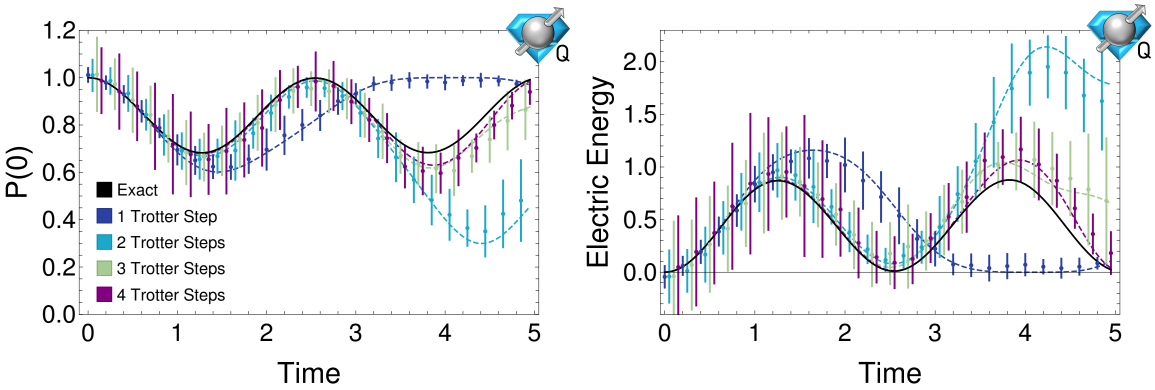

Figure 1.6: The (trivial-) vacuum-to-vacuum persistence probability $|\langle 00|\ \hat{U}(t)\ |00\rangle|^2$ (left panel) and the energy in the electric field (right panel) of the one-plaquette system derived from the Hamiltonian given in Eq. (1.10) for color irreps $\mathbf{1}, \mathbf{3}, \overline{\mathbf{3}}, \mathbf{8}$. Dashed lines correspond to the exact results for 2nd-order Trotterization given in Eq. (1.16) with $\Delta t = t, t/2, t/3, t/4, 0$. Points correspond to quadratic extrapolations of results obtained from IBM's `Athens` quantum processor, with systematic and statistical uncertainties combined in quadrature.

The data points correspond to results of the circuits discussed above implemented on IBM's `Athens` quantum processor [49], a superconducting qubit system in the lineage of IBM's devices using Qiskit [50]. The connectivity of this device is linear across five superconducting qubits [49] and two of the middle qubits were used to store the wavefunction of the truncated SU(3) plaquette.

The largest sources of systematic uncertainty in simulating with current quantum devices are measurements and CNOT gates, with the former dominating by a factor of ~ 3 in basic benchmarking of the `Athens` device. To account for systematic errors associated with CNOT gates, previously employed extrapolation procedures [51, 52] have been utilized. Mitigation of this CNOT-gate error combines the results obtained by replacing each CNOT in a circuit with an odd number, r (for r $= 3, 5, 7$), of CNOTs and extrapolating to $r = 0$ (as CNOT.CNOT$= \hat{\mathbb{I}}$). Linear and quadratic extrapolations to $r = 0$ in the number of CNOTs-per-circuit-CNOT were performed, and $\frac{1}{2}|O(\text{linear}) - O(\text{quadratic})|$ was used as an estimate of the systematic uncertainty in the extrapolation of a quantity O. In many cases, the linear fit was of relatively poor quality and gate fidelity limited the reliable extraction of sufficient samples in r to estimate the systematic uncertainty at a comparison of higher polynomials. Hence, this comparison provides only an estimate and should not be considered a complete quantification of CNOT errors.

Measurement errors were mitigated in two ways. The first was implementing Qiskit's `measurement filter` subroutine [53] during production, which removes the leading order measurement errors by optimizing an approximate inverse of the calculated all-to-all measurement matrix. When the error introduced by application of a single CNOT gate is small compared to those of the measurement procedure, it is viable to mitigate measurement errors through the use of auxiliary qubits by implementing a majority- or unanimous-vote for the measurement result. In this democratic approach, each auxiliary qubit is connected as the CNOT target controlled on a qubit in the plaquette Hilbert space and provides one correlated measurement to inform post-selected voting. After calibration, the typical single qubit measurement error rate on the `Athens` processor is approximately 3% and the typical CNOT error rate is approximately 0.9% [49]. As a result, the unanimous voting criterion provides an improvement that is found in some cases to be comparable to that of the measurement filter, with degradation for circuits implemented at times distant from a calibration procedure. The initially positive results observed in this work, along with the scalability of the voting procedure, inspire future exploration of the device-dependent tuning necessary to optimize this measurement error mitigation strategy.

In addition to a choice of measurement error mitigation, the calculation shown in Fig. 1.6 was implemented with both a 3- and 4-CNOT gate version of $e^{i\left(a\hat{X}\otimes\hat{X}+b\hat{Y}\otimes\hat{Y}+c\hat{Z}\otimes\hat{Z}\right)}$, the time evolution of the Cartan subalgebra. In the absence of noise, these two implementations should give the same results. While additional noise would be reasonably expected for the 4-CNOT calculations, temporal fluctuations in error rates of the device instead produced lower noise fluctuations for the 4-CNOT calculations. Thus, in order to express most accurately the uncertainties associated with this calculation on quantum hardware, the four implementations (3-CNOT Cartan subalgebra with unanimous voting, 4-CNOT Cartan subalgebra with the measurement filter, and others) after r-extrapolation have been combined. The uncertainty is a quadrature combination of the extrapolation errors and standard deviations of the four implementations. As a result, the uncertainties presented in Fig. 1.6 and throughout this manuscript are not statistical confidence intervals, but also capture the systematic errors associated with gate fidelities and temporal fluctuations of the device between calibrations that produce dominant error contributions.

6 *Truncation*

The next lowest-lying irreps beyond the $\{\mathbf{1},\mathbf{3},\bar{\mathbf{3}},\mathbf{8}\}$ to be included in the one-plaquette basis are the $\mathbf{6}$ and $\bar{\mathbf{6}}$. With six basis states, three qubits are required with two remaining unphysical states in the Hilbert space. As was leveraged in Ref. [18], the freedom of gauge-variant completion allows couplings and interactions within the unphysical subspace to be chosen to simplify the implementation of the Hamiltonian on the quantum device. The one-plaquette basis can be embedded into the Hilbert space of three qubits with the encoding, $\{|0\rangle,|1\rangle,|2\rangle,|3\rangle,|4\rangle,|7\rangle\} = \{|\mathbf{1}\rangle, |\mathbf{3}\rangle, |\bar{\mathbf{3}}\rangle, |\mathbf{8}\rangle, |\mathbf{6}\rangle, |\bar{\mathbf{6}}\rangle\}$, leaving the states $|101\rangle$ and $|110\rangle$ to be unphysical. With this mapping, the Hamiltonian can be gathered into seven terms, $\hat{H} = \sum_{i=0}^{7} \hat{H}_i$, with

$$\begin{aligned}
\hat{H}_0 &= g^2 \left(\frac{14}{3} \hat{\mathbb{I}} \otimes \hat{\mathbb{I}} \otimes \hat{\mathbb{I}} - \frac{11}{6} \hat{Z} \otimes \hat{\mathbb{I}} \otimes \hat{\mathbb{I}} - \frac{3}{2} \hat{\mathbb{I}} \otimes \hat{\mathbb{I}} \otimes \hat{Z} - \frac{3}{2} \hat{Z} \otimes \hat{Z} \otimes \hat{\mathbb{I}} + \frac{1}{6} \hat{\mathbb{I}} \otimes \hat{Z} \otimes \hat{Z} \right) \quad , \\
\hat{H}_1 &= -\frac{1}{4g^2} \hat{\mathbb{I}} \otimes \hat{\mathbb{I}} \otimes \hat{X} \quad , \\
\hat{H}_2 &= -\frac{1}{4g^2} \left(\hat{\mathbb{I}} + \hat{Z} \right) \otimes \hat{X} \otimes \hat{\mathbb{I}} \quad , \\
\hat{H}_3 &= -\frac{1}{4g^2} \left(\hat{\mathbb{I}} \otimes \hat{X} \otimes \hat{X} + \hat{\mathbb{I}} \otimes \hat{Y} \otimes \hat{Y} \right) \quad , \\
\hat{H}_4 &= -\frac{1}{4g^2} \left(\hat{X} \otimes \hat{\mathbb{I}} \otimes \hat{X} + \hat{Z} \otimes \hat{\mathbb{I}} \otimes \hat{X} \right) \quad , \\
\hat{H}_5 &= -\frac{1}{4g^2} \hat{Y} \otimes \hat{Z} \otimes \hat{Y} \quad , \\
\hat{H}_6 &= -\frac{1}{2g^2} \left(\hat{b}^\dagger \otimes \hat{b} \otimes \hat{b} + \hat{b} \otimes \hat{b}^\dagger \otimes \hat{b}^\dagger \right) \quad , \\
\hat{H}_7 &= -\frac{1}{8g^2} \hat{X} \otimes \left(\hat{\mathbb{I}} - \hat{Z} \right) \otimes \left(\hat{\mathbb{I}} - \hat{Z} \right) \quad , \qquad (1.17)
\end{aligned}$$

where $\hat{b} = (\hat{X} + i\hat{Y})/2$.

Middle qubits on the `Athens` quantum processor were chosen to represent the state of the system, while the two remaining qubits were used to mitigate the measurement errors of the second and fourth qubits when employing voting protocols for measurement error mitigation. A single application of the Trotterized time evolution operator acted on the trivial vacuum $|000\rangle$, and the CNOT error extrapolation procedure described in Sec. 1.3.2 was applied. Due to the nearest neighbor couplings of the device, the Trotterized time evolution operator is decomposed into 38 CNOT gates and 37 single qubit gates. However, many of the CNOT gates in the circuit were required to compensate for the linear nearest neighbor coupling of qubits; on a device with all-to-all couplings between the qubits, this Trotterized time evolution operator could be implemented with 20 CNOT gates.

Unfortunately, implementation of this three-qubit calculation is found to exceed the capabilities of the `Athens` architecture with controllable systematic errors. The $r \geq 3$ measurements show clear signs of coherence time saturation and the $r = 1$ experiences already large deviations. This combination results in an inability to perform an r extrapolation and thus an inability to mitigate the CNOT gate errors. It is possible that an extrapolation at fractional r, introducing error-exacerbating CNOT pairs at stochastically-chosen fractions of the CNOTs in the circuit as implemented in Ref. [18], could be reliably implemented, though the errors experienced already at $r = 1$ remain daunting anchors for extrapolation.

An additional interesting quantity to inform development is the survival probability in the physical subspace. As gauge theories are commonly designed for quantum simulation by embedding locally-interacting gauge-invariant spaces within larger Hilbert spaces, maintaining symmetry subspaces to high fidelity will be an important property of future quantum devices. These subspace fidelity demands also reside at the heart of many quantum error correction protocols with the space of logical quantum information embedded non-locally in a low-energy Hilbert space satisfying local symmetries. In Ref. [18], a gauge invariant survival probability of approximately 40% was calculated for a physical/unphysical Hilbert space ratio of 4/12 at the peak of the first oscillation in the electric energy of two plaquettes in SU(2) lattice gauge theory utilizing a circuit of 6 CNOTs on the IBM `Tokyo` 20-qubit quantum device. In the current application, a physical/unphysical Hilbert space ratio of 6/2 was explored with a time evolution operator of 38 CNOTs, demonstrating a survival probability of approximately 90% at the minimum of the first oscillation in the electric energy of the SU(3) global basis plaquette. While the latter represents a possible improvement in survival probability per CNOT, the former, being within both the coherence time and gate-fidelity coherence time of the device, was found to allow reliable extrapolation to a survival probability of approximately 60% and accurately capture the time evolution of electric-basis observables at the accuracy of a single Trotter step. These observations further support the necessity of multi-dimensional optimization in the design of quantum architectures. In the next subsection, the flexibility of the global basis is leveraged to perform a projection into the color parity symmetric space respected by the SU(3) Hamiltonian that is shown to allow reliable exploration of the $\{\mathbf{1}, \mathbf{3}, \overline{\mathbf{3}}, \mathbf{8}, \mathbf{6}, \overline{\mathbf{6}}\}$ dynamics through reduction onto two qubits with no unphysical subspace.

1.3.3 Color Parity Bases

To simulate the time evolution of the trivial electric vacuum, only states that are connected by repeated applications of the Hamiltonian are required to be included in the simulated basis. Observing the structure of the plaquette operator, color parity is a symmetry of SU(3) lattice Hamiltonian. Thus, time evolution will only couple states of positive color parity,

$$\left|R^{+}\right\rangle = \frac{1}{\sqrt{2}}\left[\ |R\rangle + |\bar{R}\rangle\ \right] \quad , \tag{1.18}$$

to the electric strong-coupling vacuum. By including only states of the form of $|R^{+}\rangle$ in the basis, the evolution of the trivial electric vacuum can be simulated with a reduced Hilbert space, or a higher precision calculation can be performed using the same quantum register.

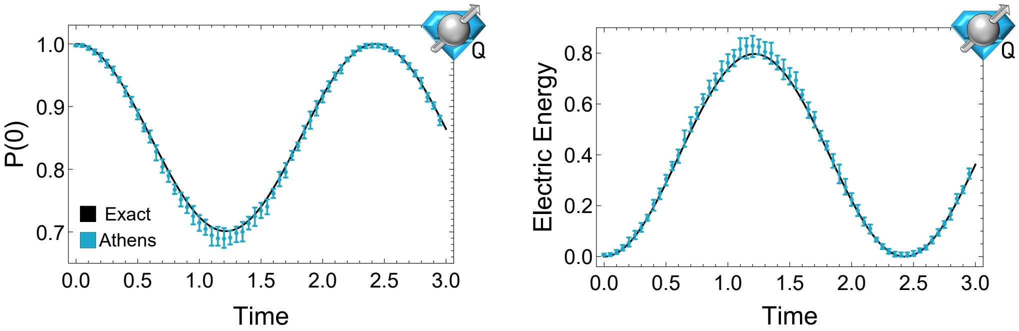

Figure 1.7: The (trivial-) vacuum-to-vacuum persistence probability $|\langle 00|\,\hat{U}(t)\,|00\rangle|^2$ (left panel) and the energy in the electric field (right panel) of the one-plaquette system in the color parity basis truncated at $\mathbf{3}^+$ evolved according to the Hamiltonian in Eq. (1.19). The points correspond to the average value and the maximal extent of 68% binomial confidence intervals across four implementations on IBM's `Athens` quantum processor, expressing both statistical and systematic uncertainties.

$(\mathbf{1}, \mathbf{3}^+)$

The lowest non-trivial truncation in the color parity basis consists of the states $|\mathbf{1}\rangle$ and $|\mathbf{3}^+\rangle = \frac{1}{\sqrt{2}}(|\mathbf{3}\rangle + |\bar{\mathbf{3}}\rangle)$. This can be mapped onto a single qubit with the basis choice $|0\rangle = |\mathbf{1}\rangle$ and $|1\rangle = |\mathbf{3}^+\rangle$, and the Hamiltonian becomes,

$$\hat{H} = \left(\frac{4}{3}g^2 + \frac{11}{4g^2}\right)\hat{\mathbb{I}} + \left(-\frac{4}{3}g^2 + \frac{1}{4g^2}\right)\hat{Z} - \frac{1}{\sqrt{2}g^2}\hat{X} \quad . \tag{1.19}$$

With the availability of arbitrary single qubit gates, the associated time evolution can be implemented with a single unitary rotation without Trotterization. Figure 1.7 shows the results of performing the $\mathbf{3}^+$ time evolution on the `Athens` quantum processor with $g = 1$ beginning in the electric vacuum. The combinations of measurement error and CNOT extrapolations have been employed as described in Sec. 1.3.2. As this calculation does not require CNOT gates, there is significantly less noise relative to the associated two-qubit calculation performed in the global basis without color parity projection.

$(\mathbf{1}, \mathbf{3}^+, \mathbf{8}, \mathbf{6}^+)$

With two qubits, the color parity basis can be extended to include the $|\mathbf{8}\rangle$ and $|\mathbf{6}^+\rangle$ states in a basis encoding of the form $\{|00\rangle, |01\rangle, |10\rangle, |11\rangle\} = \{|\mathbf{1}\rangle, |\mathbf{3}^+\rangle, |\mathbf{6}^+\rangle, |\mathbf{8}\rangle\}$, leading to a

Hamiltonian of the form,

$$\begin{aligned}\hat{H} = {} & g^2\left(\frac{23}{6}\hat{\mathbb{I}}\otimes\hat{\mathbb{I}} - \frac{5}{2}\hat{Z}\otimes\hat{\mathbb{I}} - \frac{1}{2}\hat{\mathbb{I}}\otimes\hat{Z} - \frac{5}{6}\hat{Z}\otimes\hat{Z}\right) \\ & -\frac{1}{2g^2}\left(\sqrt{2}\,\hat{\mathbb{I}}\otimes\hat{X} + \sqrt{2}\,\hat{X}\otimes\left(\frac{\hat{\mathbb{I}}-\hat{Z}}{2}\right) + \frac{1}{2}\hat{X}\otimes\hat{X} + \frac{1}{2}\hat{Y}\otimes\hat{Y} + \frac{1}{4}\left(\hat{\mathbb{I}}+\hat{Z}\right)\otimes\left(\hat{\mathbb{I}}-\hat{Z}\right) - 6\,\hat{\mathbb{I}}\otimes\hat{\mathbb{I}}\right) \quad .\end{aligned} \tag{1.20}$$

To Trotterize, the single qubit terms can be grouped together, and the Cartan subalgebra $(\hat{X}\otimes\hat{X}, \hat{Y}\otimes\hat{Y}, \hat{Z}\otimes\hat{Z})$ can be implemented as in the case of the global basis **8**-truncation above. When including the **6** irrep in the color parity projected basis, there is an additional $\hat{X}\otimes\hat{Z}$ term in the Hamiltonian whose Trotterized time evolution can be decomposed with the following circuit,

$$e^{i\alpha\hat{X}\otimes\hat{Z}} = \tag{1.21}$$

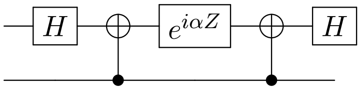

Explicitly, the first order Trotterized time evolution operator is chosen to be implemented as $\hat{U}(t) = e^{-i\hat{H}_3 t}e^{-i\hat{H}_2 t}e^{-i\hat{H}_1 t}$ with

$$\begin{aligned}\hat{H}_1 &= \left(\frac{23g^2}{6} + \frac{23}{8g^2}\right)\hat{\mathbb{I}}\otimes\hat{\mathbb{I}} - \left(\frac{5g^2}{2} + \frac{1}{8g^2}\right)\hat{Z}\otimes\hat{\mathbb{I}} - \left(\frac{g^2}{2} - \frac{1}{8g^2}\right)\hat{\mathbb{I}}\otimes\hat{Z} - \frac{1}{2\sqrt{2}g^2}\hat{X}\otimes\hat{\mathbb{I}} - \frac{1}{\sqrt{2}g^2}\hat{\mathbb{I}}\otimes\hat{X} \quad , \\ \hat{H}_2 &= \frac{1}{2\sqrt{2}g^2}\hat{X}\otimes\hat{Z} \quad , \\ \hat{H}_3 &= -\frac{1}{4g^2}\hat{X}\otimes\hat{X} - \frac{1}{4g^2}\hat{Y}\otimes\hat{Y} - \left(\frac{5}{6}g^2 - \frac{1}{8g^2}\right)\hat{Z}\otimes\hat{Z} \quad .\end{aligned} \tag{1.22}$$

Implementing this Trotterized time evolution employs 10 single qubit gates and 6 CNOT gates. The accuracy of the simulation can be improved by using a second order Trotterized time evolution operator of the form,

$$\hat{U}(t) = e^{-i\hat{H}_1\frac{t}{2}}e^{-i\hat{H}_2\frac{t}{2}}e^{-i\hat{H}_3 t}e^{-i\hat{H}_2\frac{t}{2}}e^{-i\hat{H}_1\frac{t}{2}} \quad , \tag{1.23}$$

which employs 15 single qubit gates and 8 CNOT gates. Because the second order Trotter step requires fewer gates than performing two first order Trotter steps, higher order Trotterizations may be capable of improving the calculation.

Implementation of these two forms of Trotterization are presented in Fig. 1.8. Due to the extra $\hat{X}\otimes\hat{Z}$ term in the Hamiltonian, the time evolution circuit requires more CNOT gates and the additional gates in the circuit causes noise to dominate the calculation earlier than when using the global basis truncated at **8**. Adding a majority choice mitigation of the

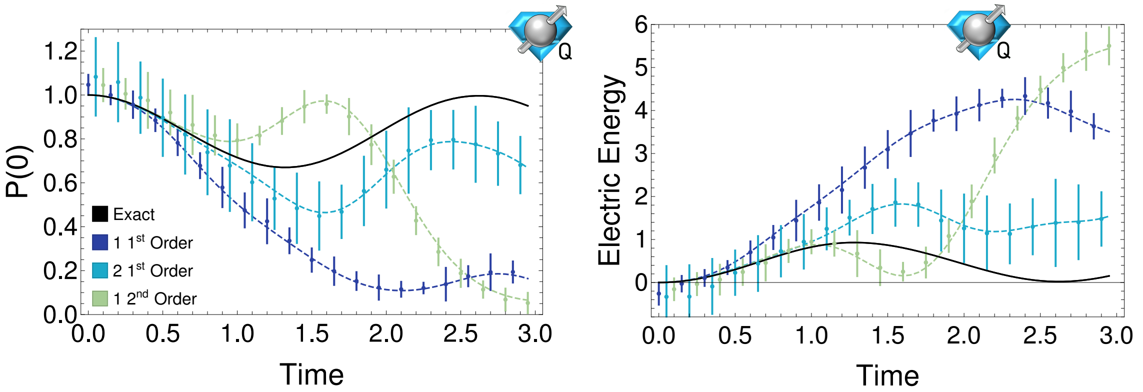

Figure 1.8: The (trivial-) vacuum-to-vacuum persistence probability $|\langle 00|\ \hat{U}(t)\ |00\rangle|^2$ (left panel) and the energy in the electric field (right panel) of the one-plaquette system derived from the Hamiltonian given in Eq. (1.20) in the color parity basis truncated at $\mathbf{6}^+$. The different curves correspond to the exact results for 1$^{\text{st}}$-order Trotterizations with $\Delta t = t, t/2$ and for a single step of 2$^{\text{nd}}$-order Trotterization with $\Delta t = t$. The points correspond to quadratic extrapolations of results obtained from IBM's `Athens` quantum processor, with systematic and statistical uncertainties combined in quadrature.

measurement error in addition to the measurement filter does not significantly improve the results, indicating that the breakdown in the calculation is due to noise in the circuit rather than the measurement process. As a result, only two steps of the 1$^{\text{st}}$-order and one step of the 2$^{\text{nd}}$ order Trotterizations were found to be reliable compared to the four 2$^{\text{nd}}$ order steps achievable for the **8**-truncated global basis. This two qubit calculation of the **6**-truncated single plaquette contains all of the states coupled to the vacuum present in the three qubit global basis calculation above 1.3.2. However, due to the more efficient mapping, reliable time evolution is achievable with the added color parity projection.

1.3.4 Rudimentary Single Plaquette Benchmarks

While the performance of many-body dynamics cannot be captured in a single metric, benchmarks for scientific application can provide useful information toward the simulation of dynamical lattice gauge theories as quantum devices develop. Near term benchmarks are likely too rudimentary to survive into the production era, but may provide helpful guidance in the near term NISQ era. Given the exacerbated noise experienced by many quantum devices at local extrema of time evolved observables, a succinct, yet meaningful, quantity expressing device performance in this area is the extrema of the electric energy fluctuations for a single plaquette of an SU(3) lattice. Analogously to the array of hardware calibrations used to capture the high-dimensional optimization affecting the quality of operations and measurements across devices, the peaks and troughs in the fluctuation of the electric energy focuses on one informative aspect of the time evolution.

The left (right) panel of Fig. 1.9 shows the values of the first minimum (maximum) in the electric energy time evolution performed on the `Athens` quantum processor. Numerical values for the data appearing in Fig. 1.9 can be found in Tables 4 and 3 of Appendix .1.3. Being a single-qubit calculation and thus requiring no Trotterization, the data of the $\mathbf{3}^+$ truncation is well controlled as seen in Fig. 1.7. Increasing the irreps included in the basis moving to the right also increases the number of qubits necessary to capture the Hilbert space. Within a sub-panel at fixed irrep truncation, the number of Trotter steps used to time evolve to the local extrema is increased moving to the right, increasing the gate fidelity and coherence demanded of the quantum device. Thus, from left to right each panel of Fig. 1.9 trades the impact of theoretical approximations for the impact of hardware noise. Ideally, this type of figure will show *windows*, in which Trotter errors are reduced and hardware noise has not yet overwhelmed the calculation, for an array of irrep truncations in order to inform a systematic extrapolation to the limit of infinite truncation.

As discussed in Subsection 1.3.1, the exploration of decreasing coupling increases the required Hilbert space of the ground state wavefunction in the basis of electric multiplets. While the convergence of observables at fixed g is subsequently exponential in the irrep truncation, finite computational resources, both in quantity and quality, will limit the parameter regime that can be controllably explored with extrapolation to infinite Λ irrep cut off. This relationship has been visually translated in Fig. 1.9 to the presence of *windows*, with the smallest g reliably accessible being that for which a set of windows relevant for extrapolation are achievable. In this preliminary exploration, reliable extraction of results with increasing gauge field truncation was limited to $\Lambda_p = 1$ with the $\{\mathbf{1}, \mathbf{3}, \overline{\mathbf{3}}, \mathbf{8}\}$ basis, where Fig. 1.9 shows a crossing between the regime dominated by Trotter errors to the regime dominated by hardware noise with little extended intermediate window. For this reason, a coupling of $g = 1$ was chosen for presentation, expressing the limited Hilbert space delocalization that can be accurately captured. However, the implemented quantum circuits experience only modified rotation angles for different couplings. For this reason, it is expected that uncertainties associated with the implementation of alternate g values will be commensurate with those presented, though the angle dependence of current hardware performance supports a more thorough exploration.

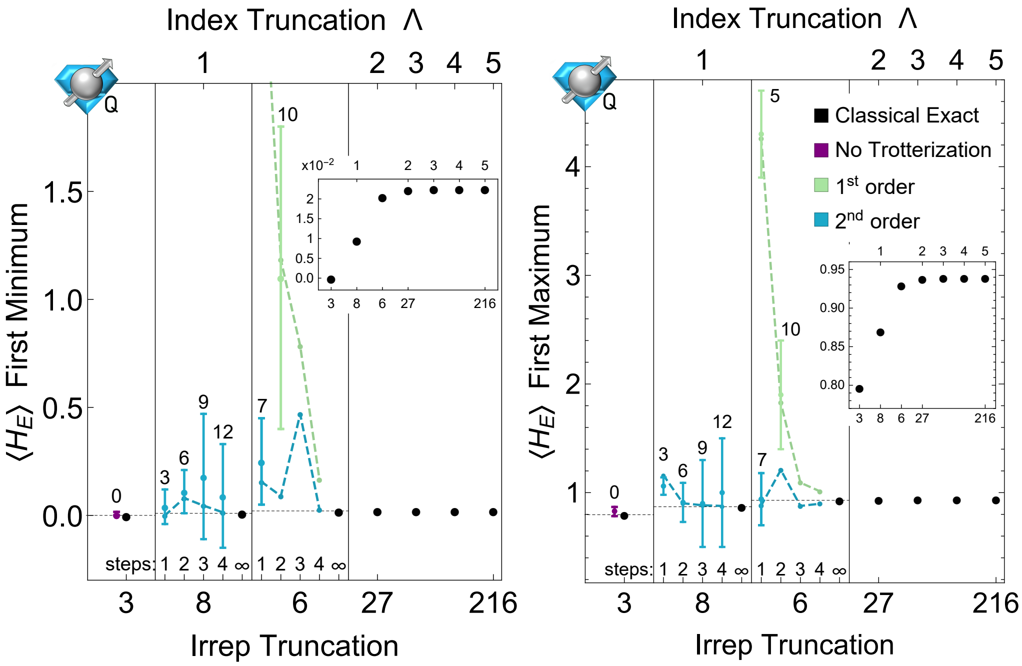

Figure 1.9: Calculation of the first local minimum and maximum in the temporal fluctuations of the electric energy for one irrep-truncated SU(3) plaquette at unit coupling on the `Athens` quantum processor beginning from the strong coupling vacuum state. Expected theoretical approximations from Trotterization are shown as dashed lines. Insets provide the exact values at each truncation with smaller vertical axis scale for perspective. The irrep truncation of **8** was calculated in the global basis while the **3** and **6** were evaluated in color parity projected global bases. Numbers associated with each point indicate the relevant number of CNOT gates.

1.3.5 Single Plaquette Operator Scalability

While exploring Pauli decompositions of operators are important first steps for lattice gauge theory time evolution on quantum architectures, construction of relevant operators can quickly become treacherous as the color space truncation is raised. This was experienced in the quantum simulation of SU(2) lattice gauge theory and is seen to arise also in SU(3). For this reason, exploring alternate compilation protocols for the representation of plaquette operators amenably for hardware implementation is of vital significance. In this subsection, an approach based on a decomposition into two-level unitaries will be presented for the single plaquette global basis and similar methods will be used to describe the local plaquette operator for extended lattices in Section 1.5.

As discussed in Subsection 1.2.3, the further splitting of the local irrep basis into two registers per link representing the fundamental and antifundamental indices is likely to be practically advantageous in requiring only nearest neighbor connectivity within the two Hilbert spaces representing the link as shown at the right of Fig. 1.2. Because the Hilbert space of the single plaquette lattice satisfying the local Gauss's law is structurally similar to that of one (unconstrained) link of a larger lattice, the one plaquette system can be represented in a global $|p,q\rangle$ basis with p and q digitized in a binary encoding on two separate qubit registers. With this encoding, the operators capturing the p and q index values are diagonal,

$$\hat{p} = \sum_{k=0}^{n-1} 2^k \frac{\mathbb{I} - \hat{Z}_{p,k}}{2} \quad , \quad \hat{q} = \sum_{k=0}^{n-1} 2^k \frac{\mathbb{I} - \hat{Z}_{q,k}}{2} \quad , \tag{1.24}$$

where the subscripts on Z specify which register and qubit the operator acts upon. With this representation, the electric term in the Hamiltonian becomes a sum over one- and two-qubit Pauli-Z operators as the Casimir of Eq. (10) is quadratic.

Because the connectivity of both the p- and q-registers is nearest neighbor, it is convenient to consider the (non-unitary) operator, $\hat{B}_n$ that maps $|p\rangle$ to $|p-1\rangle$ and annihilates $|p\rangle = |0\rangle$ when p is stored in the binary encoding with n qubits. The operator $\hat{B}_n$ can be constructed recursively according to

$$\hat{B}_n = \mathbb{I} \otimes \hat{B}_{n-1} + \hat{b} \bigotimes_{k=1}^{n-1} \hat{b}^\dagger \;=\; \sum_{k=0}^{n-1} \left(\bigotimes_{j=1}^{n-k-1} \mathbb{I} \right) \otimes \hat{b} \otimes \left(\bigotimes_{i=1}^{k} \hat{b}^\dagger \right) \quad , \tag{1.25}$$

expressed in n contributing terms with an increasing number of $\hat{b}^\dagger$ operators in the Hilbert spaces. The operator $\hat{b}$ has been defined previously, just below Eq. (1.17). Using n qubits to represent each of the p and q registers, the plaquette operator can be written as

$$\hat{\square} = \hat{B}_n^\dagger \otimes \mathbb{I} + \hat{B}_n \otimes \hat{B}_n^\dagger + \mathbb{I} \otimes \hat{B}_n \quad , \tag{1.26}$$

where the first and second Hilbert spaces represent the p and q registers, respectively. Note again that the single plaquette lattice shares a Hilbert space structure with that of the single (unconstrained) link of an extended lattice, leading to later connections between Eq. (1.26) and the local link operator. As an explicit example, for a $|p\rangle$ or $|q\rangle$ register of four qubits, this non-unitary lowering operator would be decomposed as

$$\hat{B}_4 = \mathbb{I}_8 \otimes \hat{b} + \mathbb{I}_4 \otimes \hat{b} \otimes \hat{b}^\dagger + \mathbb{I}_2 \otimes \hat{b} \otimes \hat{b}^\dagger \otimes \hat{b}^\dagger + \hat{b} \otimes \hat{b}^\dagger \otimes \hat{b}^\dagger \otimes \hat{b}^\dagger \quad . \tag{1.27}$$

If decomposed in the Pauli basis, the $\hat{B}_n$ operator would span $\sum_{k=1}^{n} 2^k = 2^{n+1} - 2$ unique terms. Decomposing the plaquette operator in the Pauli basis subsequently demands $2^{n+2}(2^n - 1)$ unique operators, or $\mathcal{O}(\Lambda_p \Lambda_q)$ as the index truncation is exponential in the number of qubits per register. The Pauli decomposition of the Hermitian combination $\hat{\square} + \hat{\square}^\dagger$ relevant for Trotterized time evolution presents a factor of two simplification to $2^{n+1}(2^n - 1)$ unique operators, due to the Hermiticity of the Pauli matrices. Ignoring simplifications for the implementation of terms sharing a basis, each of these exponentially numerous terms can be implemented with $\mathcal{O}(2n)$ or $\mathcal{O}(\log(\Lambda_p \Lambda_q))$ CNOT gates [54] resulting in the total number of gates to implement the plaquette operator time evolution scaling exponentially with n or polynomially in $\Lambda_{p,q}$.

While the exponential suppression of wavefunction amplitudes discussed in Subsection 1.3.1 may allow this naïve approach to be practically fruitful, it is possible to restructure the plaquette time evolution decomposition for improved scaling. Again allowing p and q to be represented by two quantum registers with n qubits each, the Hermitian combination of plaquette operators present in the magnetic Hamiltonian can be written as a sum of the form

$$\hat{\square} + \hat{\square}^\dagger = \left(\hat{B}_n + \hat{B}_n^\dagger\right) \otimes \mathbb{I} + \mathbb{I} \otimes \left(\hat{B}_n + \hat{B}_n^\dagger\right) + \hat{B}_n \otimes \hat{B}_n^\dagger + \hat{B}_n^\dagger \otimes \hat{B}_n = \sum_{j=1}^{n^2+2n} \hat{O}_j + \hat{O}_j^\dagger \quad , \tag{1.28}$$

where $\hat{O}_j$ is a tensor product operator of elements of the form $\{\mathbb{I}, \hat{b}, \hat{b}^\dagger\}^{\otimes 2n}$. For example, the $\hat{O}_j$ operators associated with the first term may consist of k identity operators, one $\hat{b}$ operator, $(n - k - 1)$ conjugate $\hat{b}$ operators, and n identity operators for the q-register. Each of these Hermitian operators, $\hat{O} + \hat{O}^\dagger$, can be identified as a two-level unitary between computational basis states dictated by the Hilbert space locations of the $\hat{b}$ and $\hat{b}^\dagger$ operators.

As discussed in Ref. [54] (4.5.2), the time evolution associated with such operators can be implemented by first transforming the basis through a Gray code [55], implementing a controlled single-qubit rotation, and then inverting the Gray code transformation. For example, implementing the time evolution associated with the last term of Eq. (1.27) in the $|p\rangle$ register, contributing to the first term of Eq. (1.28), connects the states $|1000\rangle$ and $|0111\rangle$ in the p-register for every state in the q-register. The time evolution according to this term can then be implemented with the following circuit acting on the p-register

$$e^{-i\alpha(\hat{b}\hat{b}^\dagger\hat{b}^\dagger\hat{b}^\dagger+\hat{b}^\dagger\hat{b}\hat{b}\hat{b})} =$$

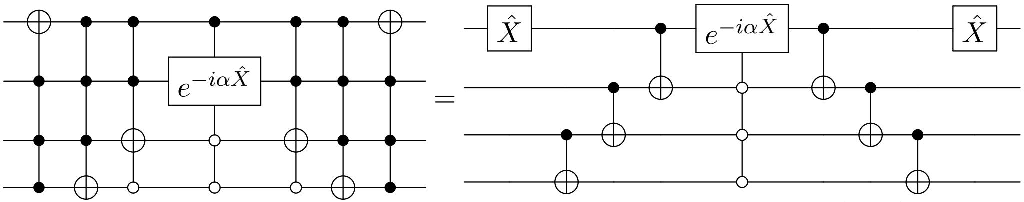

(1.29)

where α is both time and coupling dependent. The second equality emphasizes the simplifications often available in the practical application of Gray code techniques, though the generic implementation of the first equality will be momentarily convenient for the scaling discussion. At the left, a Gray code is implemented in the order 0111 → 1111 → 1110 → 1100 → 1000 through the first three multi-controlled-$\hat{X}$ operators and the location of the central controlled rotation operator. With maximal Hamming distance of $2n$ between two bit strings spanning the $\{|p\rangle, |q\rangle\}$ basis, the maximal depth of any Trotter contribution of the form $e^{-i\alpha(\hat{O}_j+\hat{O}_j^\dagger)}$ will be $2(2n)+1$ in terms of these maximally-$(2n-1)$-controlled $\hat{X}$ and rotation operators. Decomposing each of these C^kNOT operators into Toffoli, CNOT, and single qubit gates can be done with $\mathcal{O}(k)$ gates without the introduction of any auxiliary qubits [56, 54]. In practice, however, the desire to avoid the demand of exponentially precise rotation gates may inspire the use of a single auxiliary qubit. This efficiency of multi-controlled CNOT operators translates directly to an equivalent efficiency in the decomposition of the general multi-controlled SU(2) rotation at the center of this circuit [57]. With this identification of two-level unitaries treated through Gray code manipulation, the total number of gates to implement the plaquette operator time evolution is found to scale polynomially with $n = \log_2(\Lambda_p + 1)$, the number of qubits used to represent the tensor indices of irreducible representations composing the basis.

While the qubit decompositions of these two-level contributions to the plaquette time evolution are straightforward and technically efficient, later discussions in Section 1.5 of the local plaquette operator will maintain this level of abstraction due to an expectation that currently-developing qudit frameworks may provide advantageous hardware-specific approaches for the implementation of two-level rotations.

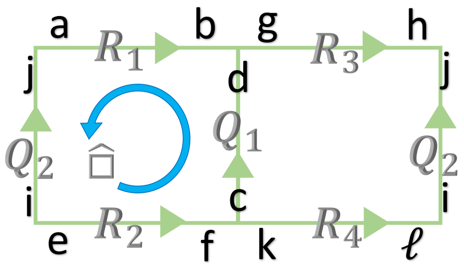

Figure 1.10: Two plaquettes with periodic boundary conditions and an arrow convention amenable to infinite extension in the two-dimensional plane. Indices local to each end of each link characterize states in SU(3) e.g., the color isospin and hypercharge indices.

1.4 Global Basis: Two Plaquettes

The results obtained for a single plaquette, detailed in Section 1.3, have provided insights into the convergence of the color-representation truncation in a simple system. Some other features that are required for QCD calculations at scale only first appear in more complex systems, such as a two-plaquette system subject to spatial periodic boundary conditions (PBCs). The SU(3) two-plaquette systems are similar to those of the SU(2) system explored in Ref. [18], but with additional structure associated with the SU(3) gauge group defining the link variables. Figure 1.10 shows the layout of the two plaquettes, along with our conventions that define the action of plaquette operators. With an eye toward an efficient mapping of the problem onto quantum hardware, we employ the techniques used in Refs. [17, 18] to “integrate over” the gauge group at each lattice site. Local gauge invariance of the theory is used to eliminate redundancies associated with the local orientations in color space, allowing the vertex amplitudes to be defined completely by the dimensionality of irreducible representations of the intersecting links. This process reduces the dimensionality of the Hilbert space and the associated resources required for quantum simulation compared with previous algorithms, for example, Ref. [14].

Similar to the methods employed for the one-plaquette system, Gauss's law can be explicitly satisfied in the global wavefunctions by construction of the basis states. Using the dimensionality of the color irrep of each link, as shown in Fig. 1.10, the basis states for the two-plaquette system are written as $|\chi(\mathbf{R_1}, \mathbf{Q_1}, \mathbf{R_2}, \mathbf{R_3}, \mathbf{Q_2}, \mathbf{R_4})\rangle$. The gauge invariant lattice wavefunction for this two-plaquette system, as discussed in greater generality in

Appendix .1.1, is

$$|\chi(\mathbf{R_1},\mathbf{Q_1},\mathbf{R_2},\mathbf{R_3},\mathbf{Q_2},\mathbf{R_4})\rangle = \frac{1}{\dim(\mathbf{Q}_1)\dim(\mathbf{Q}_2)}\sum_{all}|\mathbf{R}_1,a,b\rangle|\mathbf{Q}_1,c,d\rangle|\mathbf{R}_2,e,f\rangle|\mathbf{R}_3,g,h\rangle|\mathbf{Q}_2,i,j\rangle|\mathbf{R}_4,k,\ell\rangle$$
$$\langle\mathbf{R}_3,h,\bar{\mathbf{R}}_1,a|\bar{\mathbf{Q}}_2,j\rangle_{\Gamma_{312}}\ \langle\mathbf{R}_1,b,\bar{\mathbf{R}}_3,g|\bar{\mathbf{Q}}_1,d\rangle_{\Gamma_{131}}$$
$$\langle\mathbf{R}_4,\ell,\bar{\mathbf{R}}_2,e|\mathbf{Q}_2,i\rangle_{\Gamma_{422}}\ \langle\mathbf{R}_2,f,\bar{\mathbf{R}}_4,k|\mathbf{Q}_1,c\rangle_{\Gamma_{241}}\quad , \tag{1.30}$$

where $|\mathbf{R},a,b\rangle$ is a link-state in the electric basis and $\langle\mathbf{R}_i,f,\mathbf{R}_j,k|\mathbf{Q}_k,c\rangle_{\Gamma_{ijk}}$ are SU(3) CG coefficients.

The global wavefunctions of the two-plaquette system are formed from combinations of these basis states, consistent with the global symmetries of the system such as: color-parity symmetry resulting from the sum of $\Box + \Box^\dagger$ in the Hamiltonian, e.g., $\{\mathbf{R}_i,\mathbf{Q}_i\}\leftrightarrow\{\overline{\mathbf{R}}_i,\overline{\mathbf{Q}}_i\}$, translation invariance, and reflection symmetry. These symmetries lead to a natural block-diagonalization of the Hamiltonian in these projected bases. Quantum numbers may be assigned to the states in each block, ±1 for each of the symmetries in the case of two-plaquettes. In this section, we consider a global basis in which dynamical quantum states are mapped to symmetry-projected configurations of the full two-plaquette lattice. Two related local truncations in color space are used to explore the convergence of both local and global truncations.

1.4.1 Two-Plaquette: $\{\mathbf{1},\mathbf{3},\overline{\mathbf{3}}\}$ *Local Truncation*

In limiting the local link basis to color irreps $\{\mathbf{1},\mathbf{3},\overline{\mathbf{3}}\}$ for the two-plaquette system without constraints and symmetries, there are 3^6 independent basis states. Imposing Gauss's law at each vertex reduces this number down to 27. Further restricting to global singlet states, as is the strong coupling vacuum and preserved by the Hamiltonian, the dynamical Hilbert space becomes 9 dimensional, which decomposes into sectors of dimensions (4, 2, 2, 1) under the discrete symmetries of color parity and spatial translation. Focusing on the sector that contains the trivial vacuum, the basis states in the ++ sector are,

$$\begin{aligned}
|\psi_1^{(\mathbf{1}\mathbf{3}\overline{\mathbf{3}};++)}\rangle &= |\chi(\mathbf{1},\mathbf{1},\mathbf{1},\mathbf{1},\mathbf{1},\mathbf{1})\rangle\\
|\psi_2^{(\mathbf{1}\mathbf{3}\overline{\mathbf{3}};++)}\rangle &= \frac{1}{2}\left[\ |\chi(\mathbf{3},\overline{\mathbf{3}},\overline{\mathbf{3}},\mathbf{1},\mathbf{3},\mathbf{1})\rangle + |\chi(\overline{\mathbf{3}},\mathbf{3},\mathbf{3},\mathbf{1},\overline{\mathbf{3}},\mathbf{1})\rangle + |\chi(\mathbf{1},\mathbf{3},\mathbf{1},\mathbf{3},\overline{\mathbf{3}},\overline{\mathbf{3}})\rangle + |\chi(\mathbf{1},\overline{\mathbf{3}},\mathbf{1},\overline{\mathbf{3}},\mathbf{3},\mathbf{3})\rangle\ \right]\\
|\psi_3^{(\mathbf{1}\mathbf{3}\overline{\mathbf{3}};++)}\rangle &= \frac{1}{\sqrt{2}}\left[\ |\chi(\mathbf{3},\mathbf{1},\overline{\mathbf{3}},\mathbf{3},\mathbf{1},\overline{\mathbf{3}})\rangle + |\chi(\overline{\mathbf{3}},\mathbf{1},\mathbf{3},\overline{\mathbf{3}},\mathbf{1},\mathbf{3})\rangle\ \right]\\
|\psi_4^{(\mathbf{1}\mathbf{3}\overline{\mathbf{3}};++)}\rangle &= \frac{1}{\sqrt{2}}\left[\ |\chi(\mathbf{3},\mathbf{3},\overline{\mathbf{3}},\overline{\mathbf{3}},\overline{\mathbf{3}},\mathbf{3})\rangle + |\chi(\overline{\mathbf{3}},\overline{\mathbf{3}},\mathbf{3},\mathbf{3},\mathbf{3},\overline{\mathbf{3}})\rangle\ \right]\quad ,
\end{aligned} \tag{1.31}$$

where the superscript "++" denotes the transformation properties under color parity inversion and spatial translation, respectively. The wavefunctions in the other sectors are

$$\begin{aligned} |\psi_2^{(\mathbf{1}\mathbf{3}\bar{\mathbf{3}};-+)}\rangle &= \frac{1}{2}\left[\ |\chi(\mathbf{3},\bar{\mathbf{3}},\bar{\mathbf{3}},\mathbf{1},\mathbf{3},\mathbf{1})\rangle - |\chi(\bar{\mathbf{3}},\mathbf{3},\mathbf{3},\mathbf{1},\bar{\mathbf{3}},\mathbf{1})\rangle + |\chi(\mathbf{1},\mathbf{3},\mathbf{1},\mathbf{3},\bar{\mathbf{3}},\bar{\mathbf{3}})\rangle - |\chi(\mathbf{1},\bar{\mathbf{3}},\mathbf{1},\bar{\mathbf{3}},\mathbf{3},\mathbf{3})\rangle\ \right] \\ |\psi_3^{(\mathbf{1}\mathbf{3}\bar{\mathbf{3}};-+)}\rangle &= \frac{1}{\sqrt{2}}\left[\ |\chi(\mathbf{3},\mathbf{1},\bar{\mathbf{3}},\mathbf{3},\mathbf{1},\bar{\mathbf{3}})\rangle - |\chi(\bar{\mathbf{3}},\mathbf{1},\mathbf{3},\bar{\mathbf{3}},\mathbf{1},\mathbf{3})\rangle\ \right] \quad , \end{aligned} \tag{1.32}$$

in the $-+$ sector,

$$\begin{aligned} |\psi_2^{(\mathbf{1}\mathbf{3}\bar{\mathbf{3}};+-)}\rangle = \frac{1}{2}\Big[\ & |\chi(\mathbf{3},\bar{\mathbf{3}},\bar{\mathbf{3}},\mathbf{1},\mathbf{3},\mathbf{1})\rangle + |\chi(\bar{\mathbf{3}},\mathbf{3},\mathbf{3},\mathbf{1},\bar{\mathbf{3}},\mathbf{1})\rangle \\ & - |\chi(\mathbf{1},\mathbf{3},\mathbf{1},\mathbf{3},\bar{\mathbf{3}},\bar{\mathbf{3}})\rangle - |\chi(\mathbf{1},\bar{\mathbf{3}},\mathbf{1},\bar{\mathbf{3}},\mathbf{3},\mathbf{3})\rangle\ \Big] \quad , \end{aligned} \tag{1.33}$$

in the $+-$ sector, and

$$\begin{aligned} |\psi_2^{(\mathbf{1}\mathbf{3}\bar{\mathbf{3}};--)}\rangle &= \frac{1}{2}\left[\ |\chi(\mathbf{3},\bar{\mathbf{3}},\bar{\mathbf{3}},\mathbf{1},\mathbf{3},\mathbf{1})\rangle - |\chi(\bar{\mathbf{3}},\mathbf{3},\mathbf{3},\mathbf{1},\bar{\mathbf{3}},\mathbf{1})\rangle - |\chi(\mathbf{1},\mathbf{3},\mathbf{1},\mathbf{3},\bar{\mathbf{3}},\bar{\mathbf{3}})\rangle + |\chi(\mathbf{1},\bar{\mathbf{3}},\mathbf{1},\bar{\mathbf{3}},\mathbf{3},\mathbf{3})\rangle\ \right] \\ |\psi_4^{(\mathbf{1}\mathbf{3}\bar{\mathbf{3}};--)}\rangle &= \frac{1}{\sqrt{2}}\left[\ |\chi(\mathbf{3},\mathbf{3},\bar{\mathbf{3}},\bar{\mathbf{3}},\bar{\mathbf{3}},\mathbf{3})\rangle - |\chi(\bar{\mathbf{3}},\bar{\mathbf{3}},\mathbf{3},\mathbf{3},\mathbf{3},\bar{\mathbf{3}})\rangle\ \right] \quad , \end{aligned} \tag{1.34}$$

in the $--$ sector.

By a direct calculation of the Hamiltonian matrix elements, both the Casimir and plaquette operators, we find Hamiltonian matrices of the following form in the ++ sector,

$$\hat{H}^{(\mathbf{1}\mathbf{3}\bar{\mathbf{3}};++)} = \frac{g^2}{2}\begin{pmatrix} 0 & 0 & 0 & 0 \\ 0 & \frac{16}{3} & 0 & 0 \\ 0 & 0 & \frac{16}{3} & 0 \\ 0 & 0 & 0 & 8 \end{pmatrix} + \frac{1}{2g^2}\begin{pmatrix} 6 & -2 & 0 & 0 \\ -2 & 5 & -\frac{\sqrt{2}}{9} & -\frac{\sqrt{2}}{3} \\ 0 & -\frac{\sqrt{2}}{9} & 6 & -\frac{2}{3} \\ 0 & -\frac{\sqrt{2}}{3} & -\frac{2}{3} & 6 \end{pmatrix} \tag{1.35}$$

and in the other sectors

$$\begin{aligned} \hat{H}^{(\mathbf{1}\mathbf{3}\bar{\mathbf{3}};-+)} &= \frac{g^2}{2}\begin{pmatrix} \frac{16}{3} & 0 \\ 0 & \frac{16}{3} \end{pmatrix} + \frac{1}{2g^2}\begin{pmatrix} 7 & -\frac{\sqrt{2}}{9} \\ -\frac{\sqrt{2}}{9} & 6 \end{pmatrix} \quad , \\ \hat{H}^{(\mathbf{1}\mathbf{3}\bar{\mathbf{3}};+-)} &= \frac{g^2}{2}\,\frac{16}{3} + \frac{1}{g^2}\,\frac{5}{2} \quad , \\ \hat{H}^{(\mathbf{1}\mathbf{3}\bar{\mathbf{3}};--)} &= \frac{g^2}{2}\begin{pmatrix} \frac{16}{3} & 0 \\ 0 & 8 \end{pmatrix} + \frac{1}{2g^2}\begin{pmatrix} 7 & -\frac{\sqrt{2}}{3} \\ -\frac{\sqrt{2}}{3} & 6 \end{pmatrix} \quad . \end{aligned} \tag{1.36}$$

The eigenvalues of these sectors are shown in the left panel of Fig. 1.11 as a function of the coupling, g. The axes have been re-scaled, according to their behavior in the strong and weak coupling limits, to be g^2E vs $1/g^4$. At the left of this panel resides the strong

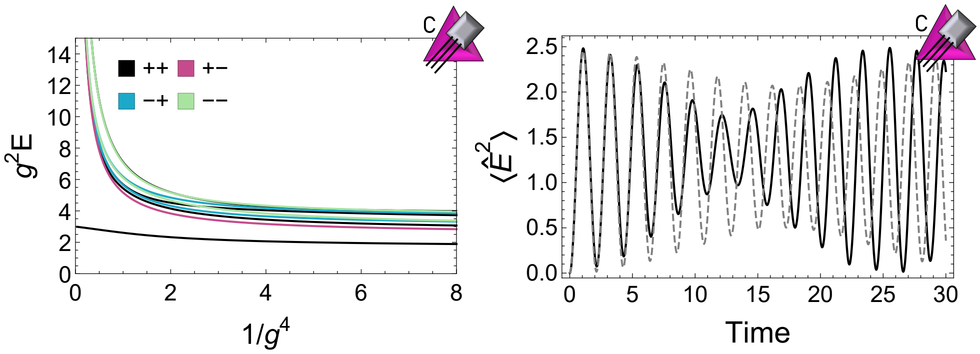

Figure 1.11: (left panel) The energy eigenvalues of the two-plaquette system as a function of coupling. The vertical axis shows the scaled energy eigenvalues, $g^2 E_i$ versus $1/g^4$, from each of the sectors, $\hat{H}^{(\mathbf{1}\mathbf{3}\overline{\mathbf{3}};++)}$ (black), $\hat{H}^{(\mathbf{1}\mathbf{3}\overline{\mathbf{3}};-+)}$ (blue), $\hat{H}^{(\mathbf{1}\mathbf{3}\overline{\mathbf{3}};+-)}$ (pink), and $\hat{H}^{(\mathbf{1}\mathbf{3}\overline{\mathbf{3}};--)}$ (green), given in Eqs. (1.35) and (1.36). (right panel) Time evolution of $\sum_a |\mathbf{E}^a|^2$ in the $++$ two-plaquette system (with PBCs) locally truncated to $\{\mathbf{1}, \mathbf{3}, \overline{\mathbf{3}}\}$ and globally truncated to basis Casimir's of $\frac{16}{3}$ (dashed gray curve) and of 8 (solid black curve) for $g = 1$. The system is initially in the trivial vacuum.

coupling limit where the electric contributions to the Hamiltonian dominate and the ground state is well separated. At the right of this panel resides the weak coupling limit where the magnetic contributions to the Hamiltonian dominate and the ground state remains gapped below excitations. For demonstration purposes, $g = 1$ is chosen in what follows, however the behavior as a function of coupling should be noted when considering the lattice continuum limit, where $ga \to 0$.

While the present basis is highly truncated, and we will explore a larger basis in subsequent sections, it is orienting to see the effect of a global truncation. In the right panel of Fig. 1.11, the time evolution of the system initially in the trivial vacuum, $|\psi_1^{(\mathbf{1}\mathbf{3}\overline{\mathbf{3}};++)}\rangle$ for a coupling $g = 1$ is displayed. From this evaluation it is seen that the lowered global cutoff at a quadratic Casimir of $\frac{16}{3}$ has an impact that increases with evolution temporal extent, a natural observation considering the low-Casimir initialization. Discrepancies first appear in magnitude at local extrema and build a significant phase shift over a few oscillations as the restricted Hilbert space of the added global truncation has effectively reduced the period. Informed by understanding of the truncation dependence of the single-plaquette wavefunction discussed in Section 1.3, it is not surprising that the presence of states at the global truncation boundary in this system are significant.

Though severely truncated to the local $\{\mathbf{1}, \mathbf{3}, \overline{\mathbf{3}}\}$ basis, this example parallels previous quantum simulations of a two plaquette SU(2) system [18] and naturally maps onto a qutrit device with each qutrit describing the color state of a link. Further, the global wavefunctions discussed above can be simulated with two qubits (embedding the four global states in the ++ sector). While current understanding indicates local bases to be advantageous at scale, global bases will continue to be valuable techniques (e.g., Refs. [58, 29, 30]) for exploring the quantum simulation capabilities of available quantum architectures.

Hardware Implementation

Mapping the ++ sector of Eq. (1.31) onto the computational basis of two qubits,

$$\left\{|\psi_1^{(\mathbf{1}\bar{\mathbf{3}};++)}\rangle, \ldots, |\psi_4^{(\mathbf{1}\bar{\mathbf{3}};++)}\rangle\right\} \to \{|0\rangle, \ldots, |3\rangle\} \quad , \tag{1.37}$$

the Hamiltonian of Eq. (1.35) is decomposed in the Pauli basis as

$$\begin{aligned} \hat{H}^{(\mathbf{1}\bar{\mathbf{3}};++)} = g^2 \left(\frac{7}{3}\hat{\mathbb{I}} \otimes \hat{\mathbb{I}} - \hat{Z} \otimes \hat{\mathbb{I}} - \hat{\mathbb{I}} \otimes \hat{Z} - \frac{1}{3}\hat{Z} \otimes \hat{Z}\right) - \frac{1}{2g^2}\left(\frac{1}{4}\left(-23\ \hat{\mathbb{I}} \otimes \hat{\mathbb{I}} + \hat{Z} \otimes \hat{\mathbb{I}} - \hat{\mathbb{I}} \otimes \hat{Z} - \hat{Z} \otimes \hat{Z}\right)\right. \\ \left. + \frac{1}{3\sqrt{2}}\hat{X} \otimes \left(\hat{\mathbb{I}} - \hat{Z}\right) + \frac{2}{3}\left(2\ \hat{\mathbb{I}} + \hat{Z}\right) \otimes \hat{X} + \frac{1}{9\sqrt{2}}\left(\hat{X} \otimes \hat{X} + \hat{Y} \otimes \hat{Y}\right)\right) \quad . \end{aligned} \tag{1.38}$$

A Trotterized time evolution can be constructed by further decomposing into a sum of three terms,

$$\begin{aligned} \hat{H}_1 &= \left(\frac{7}{3}g^2 + \frac{23}{8g^2}\right)\hat{\mathbb{I}} \otimes \hat{\mathbb{I}} - \left(\frac{1}{8g^2} + g^2\right)\hat{Z} \otimes \hat{\mathbb{I}} + \left(\frac{1}{8g^2} - g^2\right)\hat{\mathbb{I}} \otimes \hat{Z} - \frac{1}{6g^2\sqrt{2}}\hat{X} \otimes \hat{\mathbb{I}} - \frac{2}{3g^2}\hat{\mathbb{I}} \otimes \hat{X} \quad , \\ \hat{H}_2 &= \left(\frac{1}{8g^2} - \frac{g^2}{3}\right)\hat{Z} \otimes \hat{Z} - \frac{1}{18g^2\sqrt{2}}\left(\hat{X} \otimes \hat{X} + \hat{Y} \otimes \hat{Y}\right) \quad , \\ \hat{H}_3 &= \frac{1}{6g^2\sqrt{2}}\hat{X} \otimes \hat{Z} - \frac{1}{3g^2}\hat{Z} \otimes \hat{X} \quad . \end{aligned} \tag{1.39}$$

The first order Trotterized time evolution operator used in the following implementation is $\hat{U}(t) = e^{-i\hat{H}_3 t}e^{-i\hat{H}_2 t}e^{-i\hat{H}_1 t}$. Application of the first evolution contains only single qubit operators in $\hat{H}_1$, which can be implemented by single qubit quantum gates without further Trotterization, while the second evolution can be implemented using the quantum circuit in Eq. (1.15), and the third can be implemented with the following circuit relation

$$e^{i\left(\alpha\hat{Z}\otimes\hat{X}+\beta\hat{X}\otimes\hat{Z}\right)} =$$

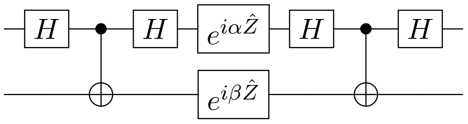

. (1.40)

The results of performing first order Trotter time steps with $g = 1$ beginning in the electric vacuum are shown in Fig. 1.12. Two middle qubits were used to store the state of the system and, when the measurement error mitigation is implemented through voting, the remaining three qubits were used to inform the post-selection described in Section 1.3.2. As the results show, three Trotter steps are capable of reproducing the first maximum and minimum in the evolution of the electric energy and calculations on the `Athens` quantum processor are in agreement with the exact calculation.

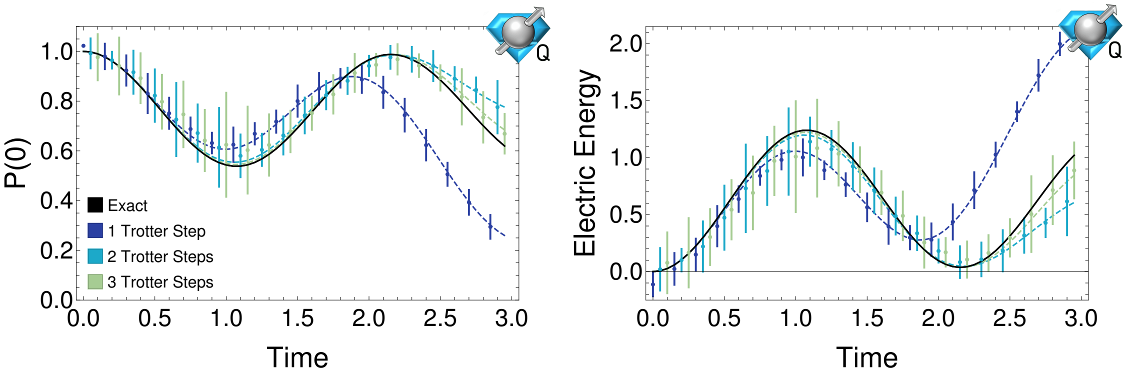

Figure 1.12: The (trivial-) vacuum-to-vacuum persistence probability $|\langle 00|\,\hat{U}(t)\,|00\rangle|^2$ (left panel) and the energy in the electric field (right panel) of the two plaquette system in the color parity basis truncated locally at $\mathbf{3}$ and $\overline{\mathbf{3}}$. Evolution is a 1st-order Trotterization of the Hamiltonian in Eq. (1.35). Points correspond to quadratic extrapolations of results obtained from IBM's `Athens` quantum processor, with systematic and statistical uncertainties combined in quadrature.

1.4.2 Two-Plaquette: $\{\mathbf{1}, \mathbf{3}, \overline{\mathbf{3}}, \mathbf{8}\}$ *Local Truncation*

To further explore global wavefunctions and also to demonstrate a further complexity in such calculations, the discussion in Subsection 1.4.1 is here extended to include the $\mathbf{8}$ in the local link basis. The construction involves an expanded basis that requires considering non-trivial multiplicities in the products of irreps, in particular in $\mathbf{8}\otimes\mathbf{8} = \mathbf{27}\oplus\mathbf{10}\oplus\overline{\mathbf{10}}\oplus\mathbf{8}\oplus\mathbf{8}\oplus\mathbf{1}$. Of the 4^6 states in this local basis, 109 of them satisfy Gauss's law. Projecting further to the global color singlet states—the global color charge being a quantum number conserved by the Hamiltonian—there are 41 distinct physical configurations potentially connected to the strong coupling vacuum.

These physical and global color singlet states combine into states with definite transformation properties under the discrete symmetries of color parity, translation, and reflection, which is no longer redundant in this larger basis as $\mathbf{3}\otimes\overline{\mathbf{3}} = \mathbf{8}\oplus\mathbf{1}$ leads to configurations that can be odd under reflection. Focusing only on the $+++$ sector, the 15 independent states are,

$$
\begin{aligned}
|\psi_1^{(\mathbf{13\bar{3}8};+++)}\rangle =& |\chi(\mathbf{1},\mathbf{1},\mathbf{1},\mathbf{1},\mathbf{1},\mathbf{1})\rangle \quad , \\
|\psi_{2a}^{(\mathbf{13\bar{3}8};+++)}\rangle =& \frac{1}{2}\left[\ |\chi(\mathbf{3},\bar{\mathbf{3}},\bar{\mathbf{3}},\mathbf{1},\mathbf{3},\mathbf{1})\rangle + |\chi(\bar{\mathbf{3}},\mathbf{3},\mathbf{3},\mathbf{1},\bar{\mathbf{3}},\mathbf{1})\rangle + |\chi(\mathbf{1},\mathbf{3},\mathbf{1},\mathbf{3},\bar{\mathbf{3}},\bar{\mathbf{3}})\rangle + |\chi(\mathbf{1},\bar{\mathbf{3}},\mathbf{1},\bar{\mathbf{3}},\mathbf{3},\mathbf{3})\rangle\ \right] \quad , \\
|\psi_{2b}^{(\mathbf{13\bar{3}8};+++)}\rangle =& \frac{1}{\sqrt{2}}\left[\ |\chi(\mathbf{3},\mathbf{1},\bar{\mathbf{3}},\mathbf{3},\mathbf{1},\bar{\mathbf{3}})\rangle + |\chi(\bar{\mathbf{3}},\mathbf{1},\mathbf{3},\bar{\mathbf{3}},\mathbf{1},\mathbf{3})\rangle\ \right] \quad , \\
|\psi_3^{(\mathbf{13\bar{3}8};+++)}\rangle =& \frac{1}{\sqrt{2}}\left[\ |\chi(\mathbf{8},\mathbf{1},\mathbf{1},\mathbf{8},\mathbf{1},\mathbf{1})\rangle + |\chi(\mathbf{1},\mathbf{1},\mathbf{8},\mathbf{1},\mathbf{1},\mathbf{8})\rangle\ \right] \quad , \\
|\psi_4^{(\mathbf{13\bar{3}8};+++)}\rangle =& \frac{1}{\sqrt{2}}\left[\ |\chi(\mathbf{3},\mathbf{3},\bar{\mathbf{3}},\bar{\mathbf{3}},\bar{\mathbf{3}},\mathbf{3})\rangle + |\chi(\bar{\mathbf{3}},\bar{\mathbf{3}},\mathbf{3},\mathbf{3},\mathbf{3},\bar{\mathbf{3}})\rangle\ \right] \quad , \\
|\psi_{5a}^{(\mathbf{13\bar{3}8};+++)}\rangle =& \frac{1}{2}\left[\ |\chi(\mathbf{3},\mathbf{1},\bar{\mathbf{3}},\mathbf{3},\mathbf{8},\bar{\mathbf{3}})\rangle + |\chi(\bar{\mathbf{3}},\mathbf{1},\mathbf{3},\bar{\mathbf{3}},\mathbf{8},\mathbf{3})\rangle + |\chi(\mathbf{3},\mathbf{8},\bar{\mathbf{3}},\mathbf{3},\mathbf{1},\bar{\mathbf{3}})\rangle + |\chi(\bar{\mathbf{3}},\mathbf{8},\mathbf{3},\bar{\mathbf{3}},\mathbf{1},\mathbf{3})\rangle\ \right] \quad , \\
|\psi_{5b}^{(\mathbf{13\bar{3}8};+++)}\rangle =& \frac{1}{2\sqrt{2}}\Big[\ |\chi(\mathbf{3},\bar{\mathbf{3}},\bar{\mathbf{3}},\mathbf{1},\mathbf{3},\mathbf{8})\rangle + |\chi(\mathbf{3},\bar{\mathbf{3}},\bar{\mathbf{3}},\mathbf{8},\mathbf{3},\mathbf{1})\rangle \\
& + |\chi(\bar{\mathbf{3}},\mathbf{3},\mathbf{3},\mathbf{1},\bar{\mathbf{3}},\mathbf{8})\rangle + |\chi(\bar{\mathbf{3}},\mathbf{3},\mathbf{3},\mathbf{8},\bar{\mathbf{3}},\mathbf{1})\rangle \\
& + |\chi(\mathbf{1},\mathbf{3},\mathbf{8},\mathbf{3},\bar{\mathbf{3}},\bar{\mathbf{3}})\rangle + |\chi(\mathbf{8},\mathbf{3},\mathbf{1},\mathbf{3},\bar{\mathbf{3}},\bar{\mathbf{3}})\rangle \\
& + |\chi(\mathbf{1},\bar{\mathbf{3}},\mathbf{8},\bar{\mathbf{3}},\mathbf{3},\mathbf{3})\rangle + |\chi(\mathbf{8},\bar{\mathbf{3}},\mathbf{1},\bar{\mathbf{3}},\mathbf{3},\mathbf{3})\rangle\Big] \quad , \\
|\psi_{6a}^{(\mathbf{13\bar{3}8};+++)}\rangle =& \frac{1}{\sqrt{2}}\left[\ |\chi(\mathbf{3},\mathbf{8},\bar{\mathbf{3}},\mathbf{3},\mathbf{8},\bar{\mathbf{3}})\rangle + |\chi(\bar{\mathbf{3}},\mathbf{8},\mathbf{3},\bar{\mathbf{3}},\mathbf{8},\mathbf{3})\rangle\ \right] \quad , \\
|\psi_{6b}^{(\mathbf{13\bar{3}8};+++)}\rangle =& \frac{1}{2}\left[\ |\chi(\mathbf{3},\bar{\mathbf{3}},\bar{\mathbf{3}},\mathbf{8},\mathbf{3},\mathbf{8})\rangle + |\chi(\bar{\mathbf{3}},\mathbf{3},\mathbf{3},\mathbf{8},\bar{\mathbf{3}},\mathbf{8})\rangle + |\chi(\mathbf{8},\mathbf{3},\mathbf{8},\mathbf{3},\bar{\mathbf{3}},\bar{\mathbf{3}})\rangle + |\chi(\mathbf{8},\bar{\mathbf{3}},\mathbf{8},\bar{\mathbf{3}},\mathbf{3},\mathbf{3})\rangle\ \right] \quad , \\
|\psi_{7a}^{(\mathbf{13\bar{3}8};+++)}\rangle =& |\chi(\mathbf{8},\mathbf{1},\mathbf{8},\mathbf{8},\mathbf{1},\mathbf{8})\rangle \quad , \\
|\psi_{7b}^{(\mathbf{13\bar{3}8};+++)}\rangle =& \frac{1}{\sqrt{2}}\left[\ |\chi(\mathbf{8},\mathbf{8},\mathbf{8},\mathbf{1},\mathbf{8},\mathbf{1})\rangle + |\chi(\mathbf{1},\mathbf{8},\mathbf{1},\mathbf{8},\mathbf{8},\mathbf{8})\rangle\ \right] \quad , \\
|\psi_{7c}^{(\mathbf{13\bar{3}8};+++)}\rangle =& \frac{1}{\sqrt{2}}\left[\ |\chi(\mathbf{1},\mathbf{8},\mathbf{8},\mathbf{8},\mathbf{8},\mathbf{1})\rangle + |\chi(\mathbf{8},\mathbf{8},\mathbf{1},\mathbf{1},\mathbf{8},\mathbf{8})\rangle\ \right] \quad , \\
|\psi_{8a}^{(\mathbf{13\bar{3}8};+++)}\rangle =& \frac{1}{\sqrt{2}}\left[\ |\chi(\mathbf{8},\mathbf{1},\mathbf{8},\mathbf{8},\mathbf{8},\mathbf{8})\rangle + |\chi(\mathbf{8},\mathbf{8},\mathbf{8},\mathbf{8},\mathbf{1},\mathbf{8})\rangle\ \right] \quad , \\
|\psi_{8b}^{(\mathbf{13\bar{3}8};+++)}\rangle =& \frac{1}{2}\left[\ |\chi(\mathbf{1},\mathbf{8},\mathbf{8},\mathbf{8},\mathbf{8},\mathbf{8})\rangle + |\chi(\mathbf{8},\mathbf{8},\mathbf{8},\mathbf{1},\mathbf{8},\mathbf{8})\rangle + |\chi(\mathbf{8},\mathbf{8},\mathbf{1},\mathbf{8},\mathbf{8},\mathbf{8})\rangle + |\chi(\mathbf{8},\mathbf{8},\mathbf{8},\mathbf{8},\mathbf{8},\mathbf{1})\rangle\ \right] \quad , \\
|\psi_9^{(\mathbf{13\bar{3}8};+++)}\rangle =& |\chi(\mathbf{8},\mathbf{8},\mathbf{8},\mathbf{8},\mathbf{8},\mathbf{8})\rangle \quad .
\end{aligned}
\tag{1.41}
$$

States have been grouped together by the value of the Casimir operator, e.g., $|\psi_{2a}^{(\mathbf{13\bar{3}8};+++)}\rangle$ and $|\psi_{2b}^{(\mathbf{13\bar{3}8};+++)}\rangle$ both have a Casimir of $\sum_a |\mathbf{E}^a|^2 = \frac{16}{3}$. The basis states associated with $\{\mathbf{1},\mathbf{3},\bar{\mathbf{3}}\}$ local truncation are, of course, found in this basis, $|\psi_1^{(\mathbf{13\bar{3}};+++)}\rangle = |\psi_1^{(\mathbf{13\bar{3}8};+++)}\rangle$, $|\psi_2^{(\mathbf{13\bar{3}};+++)}\rangle = |\psi_{2a}^{(\mathbf{13\bar{3}8};+++)}\rangle$, $|\psi_3^{(\mathbf{13\bar{3}};+++)}\rangle = |\psi_{2b}^{(\mathbf{13\bar{3}8};+++)}\rangle$, $|\psi_4^{(\mathbf{13\bar{3}};+++)}\rangle = |\psi_4^{(\mathbf{13\bar{3}8};+++)}\rangle$. Interestingly, there is a configuration with one or more of the links in the **8** that has a smaller Casimir, e.g., $|\psi_3^{(\mathbf{13\bar{3}8};+++)}\rangle$ has a smaller Casimir than $|\psi_4^{(\mathbf{13\bar{3}8};+++)}\rangle$, further emphasizing

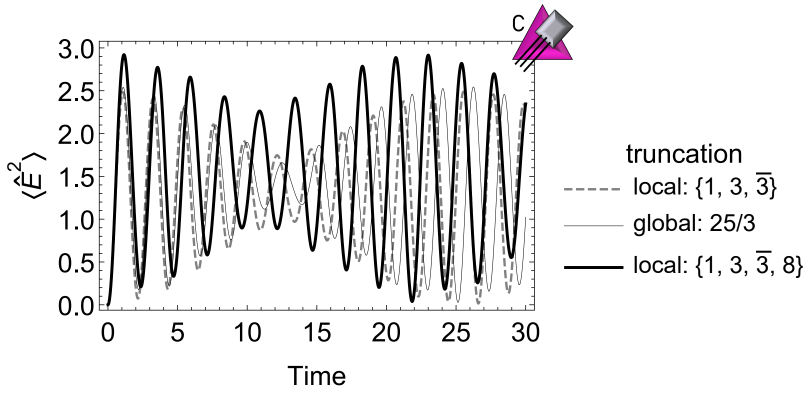

Figure 1.13: Time evolution of the electric Casimir operators $\sum_a |\mathbf{E}^a|^2$ in the symmetry-sector-(+++) two-plaquette system (with PBCs) for coupling $g = 1$ initialized in the trivial vacuum at three different truncations: a local truncation of irreps $\{\mathbf{1}, \mathbf{3}, \overline{\mathbf{3}}\}$ (gray, dashed), a global truncation to basis Casimirs of $\frac{25}{3}$ (thin solid gray line), and the local truncation of $\{\mathbf{1}, \mathbf{3}, \overline{\mathbf{3}}, \mathbf{8}\}$ expressed in Eq. (1.41) (thick black line).

a practical difference between global and local truncations. The basis states in the other sectors can be constructed straightforwardly (by inspection from the $+++$ states).

Using the same methods as described previously, the electric and magnetic matrix elements of the Kogut-Susskind Hamiltonian can be determined with this symmetry-projected basis, leading to a 15×15 dimensional matrix for the $+++$ sector. The Hamiltonian matrix containing the electric contributions is diagonal,

$$\hat{H}_E^{(\mathbf{1}\mathbf{3}\overline{\mathbf{3}}\mathbf{8};+++)} = \frac{g^2}{2} \mathrm{diag}\left(0, \frac{16}{3}, \frac{16}{3}, 6, 8, \frac{25}{3}, \frac{25}{3}, \frac{34}{3}, \frac{34}{3}, 12, 12, 12, 15, 15, 18\right) \tag{1.42}$$

while the magnetic contributions are

$$\hat{H}_{B,\alpha}^{(\mathbf{13\overline{3}8};+++)} = \frac{3}{g^2}\hat{\mathbb{I}}_{15} \quad ,$$

$$\hat{H}_{B,\beta}^{(\mathbf{13\overline{3}8};+++)} = -\frac{1}{2g^2}\begin{pmatrix} 0 & 2 & 0 & 0 & 0 & 0 & 0 & 0 & 0 & 0 & 0 & 0 & 0 & 0 & 0 \\ 2 & 1 & \frac{\sqrt{2}}{9} & 0 & \frac{\sqrt{2}}{3} & \frac{4\sqrt{2}}{9} & 0 & \frac{8\sqrt{2}}{9} & 0 & 0 & \sqrt{2} & 0 & 0 & 0 & 0 \\ 0 & \frac{\sqrt{2}}{9} & 0 & 0 & \frac{2}{3} & 0 & \frac{4\sqrt{2}}{9} & 0 & \frac{8\sqrt{2}}{9} & 0 & 0 & 0 & 0 & 0 & 0 \\ 0 & 0 & 0 & 0 & 0 & 0 & \frac{1}{\sqrt{2}} & 0 & 0 & 0 & 0 & 0 & 0 & 0 & 0 \\ 0 & \frac{\sqrt{2}}{3} & \frac{2}{3} & 0 & 0 & \frac{2}{3} & \frac{\sqrt{2}}{3} & \frac{1}{3} & \frac{1}{3\sqrt{2}} & 0 & 0 & 0 & 0 & 0 & 0 \\ 0 & \frac{4\sqrt{2}}{9} & 0 & 0 & \frac{2}{3} & 0 & -\frac{2\sqrt{2}}{9} & 0 & \frac{1}{9\sqrt{2}} & 0 & 0 & 0 & 0 & 0 & 0 \\ 0 & 0 & \frac{4\sqrt{2}}{9} & \frac{1}{\sqrt{2}} & \frac{\sqrt{2}}{3} & -\frac{2\sqrt{2}}{9} & \frac{1}{4} & \frac{1}{9\sqrt{2}} & 0 & 0 & 0 & \frac{1}{\sqrt{2}} & 0 & -\frac{1}{2\sqrt{2}} & 0 \\ 0 & \frac{8\sqrt{2}}{9} & 0 & 0 & \frac{1}{3} & 0 & \frac{1}{9\sqrt{2}} & 0 & \frac{1}{288\sqrt{2}} & 0 & 0 & 0 & 0 & 0 & 0 \\ 0 & 0 & \frac{8\sqrt{2}}{9} & 0 & \frac{1}{3\sqrt{2}} & \frac{1}{9\sqrt{2}} & 0 & \frac{1}{288\sqrt{2}} & \frac{1}{16} & \frac{1}{4} & \frac{1}{4\sqrt{2}} & 0 & -\frac{1}{4} & -\frac{1}{4\sqrt{2}} & \frac{1}{8} \\ 0 & 0 & 0 & 0 & 0 & 0 & 0 & 0 & \frac{1}{4} & 0 & 0 & 0 & 0 & 0 & 0 \\ 0 & \sqrt{2} & 0 & 0 & 0 & 0 & 0 & 0 & \frac{1}{4\sqrt{2}} & 0 & 0 & 0 & 0 & 0 & 0 \\ 0 & 0 & 0 & 0 & 0 & 0 & \frac{1}{\sqrt{2}} & 0 & 0 & 0 & 0 & 0 & 0 & 0 & 0 \\ 0 & 0 & 0 & 0 & 0 & 0 & 0 & 0 & -\frac{1}{4} & 0 & 0 & 0 & 0 & 0 & 0 \\ 0 & 0 & 0 & 0 & 0 & 0 & -\frac{1}{2\sqrt{2}} & 0 & -\frac{1}{4\sqrt{2}} & 0 & 0 & 0 & 0 & 0 & 0 \\ 0 & 0 & 0 & 0 & 0 & 0 & 0 & 0 & \frac{1}{8} & 0 & 0 & 0 & 0 & 0 & 0 \end{pmatrix} , \tag{1.43}$$

where $\mathbb{I}_n$ is the n-dimensional identity matrix, and the full Hamiltonian in the $+++$ sector is the sum $\hat{H}^{(\mathbf{13\overline{3}8};+++)} = \hat{H}_{E}^{(\mathbf{13\overline{3}8};+++)} + \hat{H}_{B,\alpha}^{(\mathbf{13\overline{3}8};+++)} + \hat{H}_{B,\beta}^{(\mathbf{13\overline{3}8};+++)}$.

The wavefunctions in Eq. (1.41) form a complete set of gauge invariant states that could be accessed through applications of the plaquette operators to the trivial vacuum with a local link truncation of $\{\mathbf{1}, \mathbf{3}, \overline{\mathbf{3}}, \mathbf{8}\}$. As previously mentioned, the smallest Casimir for any state containing an $\mathbf{8}$ is less than the maximum Casimir associated with the $\{\mathbf{1}, \mathbf{3}, \overline{\mathbf{3}}\}$ local truncation. Similarly, the smallest Casimir for a state containing a $\mathbf{6}$ or $\overline{\mathbf{6}}$ is 10, which lies below that of the Casimir of $|\psi_{6a}^{(\mathbf{13\overline{3}8};+++)}\rangle$ and higher states. Therefore, there is a fixed number of states in the global basis beyond which changes to observables from including higher-Casimir states provide an estimate of the systematic uncertainty from the local link truncation, but do not improve the fidelity of predictions. For the $\{\mathbf{1}, \mathbf{3}, \overline{\mathbf{3}}, \mathbf{8}\}$ local truncation, the basis states $1, 2a, 2b, 3, 4, 5a, 5b$ have Casimirs below that of the state with the first appearance of the $\mathbf{6}$ or $\overline{\mathbf{6}}$. Therefore computing observables from these wavefunctions provides a consistent prediction for the contribution from $\{\mathbf{1}, \mathbf{3}, \overline{\mathbf{3}}, \mathbf{8}\}$ link states. Differences between predictions from the $1, 2a, 2b, 3, 4, 5a, 5b$ states and those of part or all of the larger Hamiltonian matrix provide an estimate of the irrep truncation uncertainties, i.e. the impact of omitting the $\mathbf{6}, \overline{\mathbf{6}}, \mathbf{10}, \cdots$. Figure 1.13 shows the time dependence of the energy in the electric field for three truncations. The dashed gray curve corresponds to the truncation imposed by the $\{\mathbf{1}, \mathbf{3}, \overline{\mathbf{3}}\}$ local link truncation, the thin solid gray curve corresponds to the global truncation at a Casimir of 25/3 including the contribution from the **8** that is below the threshold for the contribution from the $(\mathbf{6},\overline{\mathbf{6}})$, and the solid black curve corresponds to the evolution from the complete matrices in Eqs. (1.42) and (1.43), locally truncated at with $\Lambda_p = \Lambda_q = 1$. The difference between the solid gray and black curves provides an estimate of the systematic uncertainty due to the truncation in color space. This parallels naive dimensional analysis that is used to estimate the systematic uncertainty introduced by the omission of counterterms in low-energy EFTs. We conclude from this analysis that the color-space truncation defined at the link level has not fully converged at $g = 1$, and inclusion of the $\mathbf{6},\overline{\mathbf{6}}$, followed by the three-index tensor representations, **10**, $\overline{\mathbf{10}}$, **15** and $\overline{\mathbf{15}}$, will be required to obtain a result that is converged at the percent level.

A technical detail related to multiplicities in products of irreps appears in calculations with the $\{\mathbf{1},\mathbf{3},\overline{\mathbf{3}},\mathbf{8}\}$ local truncated basis, but absent in the $\{\mathbf{1},\mathbf{3},\overline{\mathbf{3}}\}$ truncation. Specifically, as is well known, there are two distinct transitions to the **8** irrep in the tensor product $\mathbf{8}\otimes\mathbf{8}$: the symmetric and anti-symmetric contractions, with two distinct sets of CG coefficients that contribute to amplitudes, for example, in the fusion of states, $A_\mathbf{8} + B_\mathbf{8} \to C_\mathbf{8}$. For the calculations in this section, the high-lying states in the spectrum involving three **8** links at one vertex, require a coherent sum over amplitudes in their fusion. Modifications to the local or global basis that would denote symmetrization or antisymmetrization at relevant vertices are not required. A consistently phased set of CG coefficients used to sum over color states at each vertex is sufficient to arrive at amplitudes and matrix elements.

In the same way that time evolution in the two-plaquette global basis truncated to $\{\mathbf{1},\mathbf{3},\overline{\mathbf{3}}\}$ was performed above by mapping states of projected global symmetries to states in the quantum hardware, one can contemplate an analogous computation for the $\{\mathbf{1},\mathbf{3},\overline{\mathbf{3}},\mathbf{8}\}$ local truncation from the 15×15 matrices in Eqs. (1.42) and (1.43). The first step in developing the qubit-based quantum circuit, using the ordering of states that follows naturally from the basis of increasing global quadratic Casimir, is to project the Hamiltonian onto tensor products of Pauli and Identity operators, to give rise to coefficients of the form,

$$\hat{H} \quad\to\quad c_{ijkl}\ \hat{\sigma}^i\otimes\hat{\sigma}^j\otimes\hat{\sigma}^k\otimes\hat{\sigma}^l \quad , \tag{1.44}$$

where $\hat{\sigma}^\alpha = \{\hat{\mathbb{I}}_2, \hat{\sigma}^x, \hat{\sigma}^y, \hat{\sigma}^z\ \}$. The coefficients c_{ijkl} are

$$c_{ijkl} \quad=\quad \frac{1}{16}\,\mathrm{Tr}\left[\ \hat{H}\ \hat{\sigma}^i\otimes\hat{\sigma}^j\otimes\hat{\sigma}^k\otimes\hat{\sigma}^l\ \right] \quad , \tag{1.45}$$

where an extra row of zeros has been added to the matrices in Eqs. (1.42) and (1.43). For the plaquette operator, there are 104 non-zero c_{ijkl}. If the system is further truncated to eight states to be implemented on three qubits, then the number of non-zero coefficients is reduced to 30. While Pauli decompositions do not always utilize quantum resources optimally, as demonstrated in Section 1.3.5, the lack of uniform Hilbert space organization (as is present in the local (p, q) basis) leads to challenges in identifying scalable alternatives for global basis circuit decomposition. Even for this small system, involving only two plaquettes, the anticipated limitations of working with the global basis are becoming evident.

1.5 Local Basis: The Plaquette Operator

Unlike the space-efficient global basis, where classical pre-preprocessing identifies and isolates the physical sector of the gauge field and each symmetry projected configuration of the field is mapped onto quantum hardware, the local basis distributes local qubit registers uniformly across the lattice to express local quantum numbers of the field. In this way, an operator acting on a limited number of quantum registers (dictated by its inherent spatial locality) can be developed on small lattices while subsequently retaining relevance even in the infinite volume limit. In this section, a formulation of the local plaquette operator for the SU(3) magnetic Hamiltonian is presented in the language of digital circuit elements on an architecture comprised of a qudit (d-level quantum system) representing the gauge field on each link of a one-dimensional string of plaquettes.

As discussed in Section 1.2.1, the plaquette operator in a Hilbert space without naturally embedded CG factors will necessarily be controlled on the link registers neighboring the plaquette. Consider the case of a local qutrit representing the irreps $\{0, 1, 2\} \leftrightarrow \{\mathbf{1}, \mathbf{3}, \overline{\mathbf{3}}\}$ on each link. To define the structure of the associated magnetic time evolution operator is to characterize an approach for the evolution of an infinite volume lattice with a truncation on any local excitation of the field. For each plaquette operator interacting with 8 qutrits in this system, there are 81 physical states out of the total 3^8 that satisfy Gauss's law and contain a singlet at each vertex. In order to design an operator implementing the correct quantum dynamics, it is necessary to accurately mix these physical states among themselves as well as to assure vanishing matrix elements between these states and the unphysical Hilbert space. The remaining portion of the operator, mixing the unphysical states among themselves, is a source of flexibility for the intended scientific application of gauge theory simulation and can be optimized or chosen as desired to simplify the circuit implementation. This freedom has been referred to as *gauge variant completion* (GVC) and will be used in the following design of the plaquette time evolution operator.

Of the 81 physical states currently being considered for plaquette operator design, there are 27 unique external link configurations, as shown in Table 1.1. These 27 control sectors are grouped in rows by vertical and horizontal spatial parity as well as by global conjugation. The time evolution under the Hermitian plaquette operator can be implemented as a series

$\{\mathbf{C}_1, \mathbf{C}_2, \mathbf{C}_3, \mathbf{C}_4\}$							
			$\mathbf{1111}$				
			$\mathbf{3333}$	$\mathbf{\bar{3}\bar{3}\bar{3}\bar{3}}$			
			$\mathbf{3\bar{3}3\bar{3}}$	$\mathbf{\bar{3}3\bar{3}3}$			
			$\mathbf{3\bar{3}\bar{3}3}$	$\mathbf{\bar{3}33\bar{3}}$			
		$\mathbf{113\bar{3}}$	$\mathbf{11\bar{3}3}$	$\mathbf{3\bar{3}11}$	$\mathbf{\bar{3}311}$		
		$\mathbf{1313}$	$\mathbf{1\bar{3}1\bar{3}}$	$\mathbf{3131}$	$\mathbf{\bar{3}1\bar{3}1}$		
		$\mathbf{1331}$	$\mathbf{1\bar{3}\bar{3}1}$	$\mathbf{3131}$	$\mathbf{\bar{3}1\bar{3}1}$		
$\mathbf{13\bar{3}\bar{3}}$	$\mathbf{1\bar{3}33}$	$\mathbf{31\bar{3}\bar{3}}$	$\mathbf{\bar{3}133}$	$\mathbf{33\bar{3}1}$	$\mathbf{331\bar{3}}$	$\mathbf{\bar{3}\bar{3}13}$	$\mathbf{\bar{3}\bar{3}31}$

Table 1.1: Physical control sectors of the $\{\mathbf{1}, \mathbf{3}, \overline{\mathbf{3}}\}$-truncated SU(3) plaquette operator.

of commuting operators in the control sectors of Table 1.1,

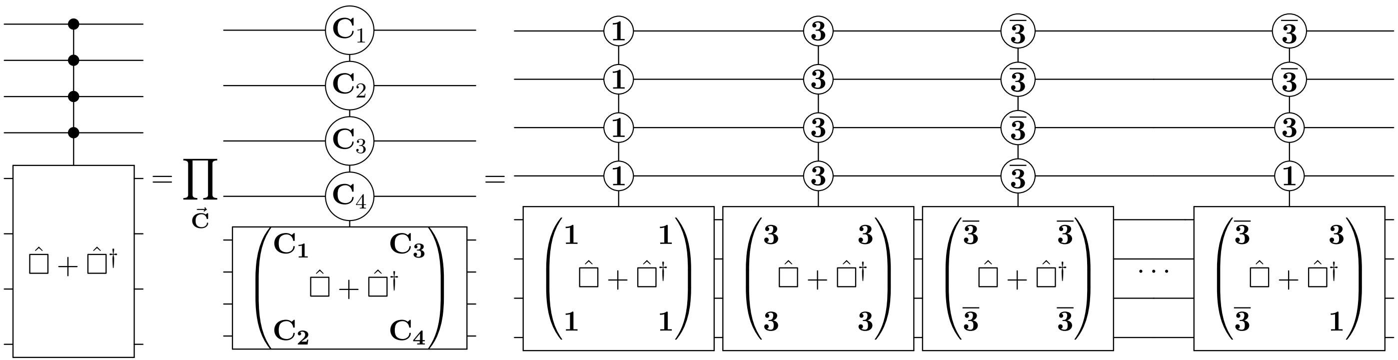

(1.46)

with a total of 27 controlled operators, mixing three physical states each, that are clearly mutually commuting.

To implement the above magnetic interaction, an architecture of qutrits is natural and amenable to generalization when higher truncations of the gauge space are designed. Consider the placement of a qutrit on each link degree of freedom. The Pauli operations in the qutrit space flip pairs of states,

$$
\begin{aligned}
X_{01} &= \begin{pmatrix} 0 & 1 & 0 \\ 1 & 0 & 0 \\ 0 & 0 & 1 \end{pmatrix} & X_{02} &= \begin{pmatrix} 0 & 0 & 1 \\ 0 & 1 & 0 \\ 1 & 0 & 0 \end{pmatrix} & X_{12} &= \begin{pmatrix} 1 & 0 & 0 \\ 0 & 0 & 1 \\ 0 & 1 & 0 \end{pmatrix} \\
Y_{01} &= \begin{pmatrix} 0 & -i & 0 \\ i & 0 & 0 \\ 0 & 0 & 1 \end{pmatrix} & Y_{02} &= \begin{pmatrix} 0 & 0 & -i \\ 0 & 1 & 0 \\ i & 0 & 0 \end{pmatrix} & Y_{12} &= \begin{pmatrix} 1 & 0 & 0 \\ 0 & 0 & -i \\ 0 & i & 0 \end{pmatrix} .
\end{aligned}
\tag{1.47}
$$

The natural rotation operator generalizing those available on current quantum architectures is the Givens rotation that transfers population between two levels within the qudit,

$$G^{\phi}_{jk}(t) = \exp\left[-it\left(e^{i\phi}|j\rangle\langle k| + e^{-i\phi}|k\rangle\langle j|\right)\right] \quad . \tag{1.48}$$

Specific rotation angles of 0 and $\pi/2$ correspond to natural extensions of the Pauli-basis rotations on qubits,

$$G^{0}_{jk}(t) = -\boxed{G^{\mathcal{X}}_{jk}(t)}- = \exp\left[-it\left(|j\rangle\langle k| + |k\rangle\langle j|\right)\right] = \exp\left[-it\mathcal{X}_{jk}\right] \quad , \tag{1.49}$$

$$G^{\frac{\pi}{2}}_{jk}(t) = -\boxed{G^{\mathcal{Y}}_{jk}(t)}- = \exp\left[-it\left(i|j\rangle\langle k| - i|k\rangle\langle j|\right)\right] = \exp\left[-it\mathcal{Y}_{jk}\right] \quad , \tag{1.50}$$

where the calligraphic $\mathcal{X}, \mathcal{Y}$ structures are Hermitian but not unitary. In terms of these operators, one GVC of the magnetic Hamiltonian in each control sector can be constructed through the following Hermitian combinations, with coefficients and transitions determined by the plaquette matrix elements discussed is Appendix .1.1. With the plaquette Hilbert space designated in the linearized basis of $|\mathbf{R}_b\rangle|\mathbf{Q}_r\rangle|\mathbf{R}_t\rangle|\mathbf{Q}_\ell\rangle$, the active space rotations are,

$$\boxed{\begin{pmatrix}\mathbf{1} & & \mathbf{1}\\ & \hat{\Box}+\hat{\Box}^\dagger & \\ \mathbf{1} & & \mathbf{1}\end{pmatrix}} = \exp\left[-i\alpha\left(\mathcal{X}_{01}\mathcal{X}_{01}\mathcal{X}_{02}\mathcal{X}_{02}+\mathcal{X}_{02}\mathcal{X}_{02}\mathcal{X}_{01}\mathcal{X}_{01}+\mathcal{X}_{12}\mathcal{X}_{12}\mathcal{X}_{12}\mathcal{X}_{12}\right)\right] \quad , \tag{1.51}$$

$$\boxed{\begin{pmatrix}\mathbf{1} & & \mathbf{3}\\ & \hat{\Box}+\hat{\Box}^\dagger & \\ \mathbf{1} & & \overline{\mathbf{3}}\end{pmatrix}} = \exp\left[-i\alpha\left(\frac{1}{3}\mathcal{X}_{02}\mathcal{X}_{01}\mathcal{X}_{01}\mathcal{X}_{01}+\frac{1}{\sqrt{3}}\mathcal{X}_{01}\mathcal{X}_{12}\mathcal{X}_{02}\mathcal{X}_{02}+\frac{1}{\sqrt{3}}\mathcal{X}_{12}\mathcal{X}_{02}\mathcal{X}_{12}\mathcal{X}_{12}\right)\right] \quad , \tag{1.52}$$

$$\boxed{\begin{pmatrix}\mathbf{1} & & \mathbf{1}\\ & \hat{\Box}+\hat{\Box}^\dagger & \\ \mathbf{3} & & \mathbf{3}\end{pmatrix}} = \exp\left[-i\alpha\left(\frac{1}{3}\mathcal{X}_{01}\mathcal{X}_{02}\mathcal{X}_{01}\mathcal{X}_{01}+\frac{1}{\sqrt{3}}\mathcal{X}_{12}\mathcal{X}_{01}\mathcal{X}_{02}\mathcal{X}_{02}+\frac{1}{\sqrt{3}}\mathcal{X}_{02}\mathcal{X}_{12}\mathcal{X}_{12}\mathcal{X}_{12}\right)\right] \quad , \tag{1.53}$$

$$\boxed{\begin{pmatrix}\mathbf{1} & & \mathbf{3}\\ & \hat{\Box}+\hat{\Box}^\dagger & \\ \mathbf{3} & & \mathbf{1}\end{pmatrix}} = \exp\left[-i\alpha\left(\frac{1}{3}\mathcal{X}_{01}\mathcal{X}_{01}\mathcal{X}_{01}\mathcal{X}_{01}-\frac{1}{\sqrt{3}}\mathcal{X}_{12}\mathcal{X}_{12}\mathcal{X}_{02}\mathcal{X}_{02}-\frac{1}{\sqrt{3}}\mathcal{X}_{02}\mathcal{X}_{02}\mathcal{X}_{12}\mathcal{X}_{12}\right)\right] \quad , \tag{1.54}$$

$$\boxed{\begin{pmatrix}\mathbf{1} & & \overline{\mathbf{3}}\\ & \hat{\Box}+\hat{\Box}^\dagger & \\ \mathbf{3} & & \overline{\mathbf{3}}\end{pmatrix}} = \exp\left[-i\alpha\left(-\frac{1}{3}\mathcal{X}_{01}\mathcal{X}_{12}\mathcal{X}_{01}\mathcal{X}_{01}-\frac{1}{3}\mathcal{X}_{12}\mathcal{X}_{02}\mathcal{X}_{02}\mathcal{X}_{02}+\frac{1}{3}\mathcal{X}_{02}\mathcal{X}_{01}\mathcal{X}_{12}\mathcal{X}_{12}\right)\right] \quad , \tag{1.55}$$

$$\boxed{\begin{pmatrix}\mathbf{3} & & \mathbf{3}\\ & \hat{\Box}+\hat{\Box}^\dagger & \\ \mathbf{3} & & \mathbf{3}\end{pmatrix}} = \exp\left[-i\alpha\left(\frac{1}{3\sqrt{3}}\mathcal{X}_{01}\mathcal{X}_{02}\mathcal{X}_{12}\mathcal{X}_{01}+\frac{1}{3\sqrt{3}}\mathcal{X}_{12}\mathcal{X}_{01}\mathcal{X}_{01}\mathcal{X}_{02}+\frac{1}{3}\mathcal{X}_{02}\mathcal{X}_{12}\mathcal{X}_{02}\mathcal{X}_{12}\right)\right] \quad , \tag{1.56}$$

$$\boxed{\begin{pmatrix}\mathbf{3} & & \mathbf{3}\\ & \hat{\Box}+\hat{\Box}^\dagger & \\ \overline{\mathbf{3}} & & \overline{\mathbf{3}}\end{pmatrix}} = \exp\left[-i\alpha\left(\frac{1}{3}\mathcal{X}_{12}\mathcal{X}_{02}\mathcal{X}_{12}\mathcal{X}_{01}+\frac{1}{9}\mathcal{X}_{02}\mathcal{X}_{01}\mathcal{X}_{01}\mathcal{X}_{02}+\frac{1}{3}\mathcal{X}_{01}\mathcal{X}_{12}\mathcal{X}_{02}\mathcal{X}_{12}\right)\right] \quad , \tag{1.57}$$

$$\boxed{\begin{pmatrix}\mathbf{3} & & \overline{\mathbf{3}}\\ & \hat{\Box}+\hat{\Box}^\dagger & \\ \overline{\mathbf{3}} & & \mathbf{3}\end{pmatrix}} = \exp\left[-i\alpha\left(\frac{1}{3}\mathcal{X}_{12}\mathcal{X}_{01}\mathcal{X}_{12}\mathcal{X}_{01}+\frac{1}{3\sqrt{3}}\mathcal{X}_{02}\mathcal{X}_{12}\mathcal{X}_{01}\mathcal{X}_{02}+\frac{1}{3\sqrt{3}}\mathcal{X}_{01}\mathcal{X}_{02}\mathcal{X}_{02}\mathcal{X}_{12}\right)\right] \quad , \tag{1.58}$$

where, when applied in the evolution of the Yang-Mills Hamiltonian, α will be determined by g and t. As enumerated in Table 1.1, the 27 rotations present in the decomposition of Eq. (1.46) can be determined from these 8 through basic parity and conjugation transformations. For example, the last rotation at the right of Eq. (1.46) can be defined from Eq. (1.55) through a paired horizontal and vertical parity transformations. Applying the link directionality structure of Fig. 1.1, the horizontal parity transformation affects the controls as $|\mathbf{C}_1\rangle|\mathbf{C}_2\rangle|\mathbf{C}_3\rangle|\mathbf{C}_4\rangle \rightarrow |\overline{\mathbf{C}}_3\rangle|\overline{\mathbf{C}}_4\rangle|\overline{\mathbf{C}}_1\rangle|\overline{\mathbf{C}}_2\rangle$ and affects the active space as $|\mathbf{R}_b\rangle|\mathbf{Q}_r\rangle|\mathbf{R}_t\rangle|\mathbf{Q}_\ell\rangle \rightarrow |\overline{\mathbf{R}}_b\rangle|\mathbf{Q}_\ell\rangle|\overline{\mathbf{R}}_t\rangle|\mathbf{Q}_r\rangle$. Likewise, the vertical parity transformation affects the controls as $|\mathbf{C}_1\rangle|\mathbf{C}_2\rangle|\mathbf{C}_3\rangle|\mathbf{C}_4\rangle \rightarrow |\mathbf{C}_2\rangle|\mathbf{C}_1\rangle|\mathbf{C}_4\rangle|\mathbf{C}_3\rangle$ and affects the active space as $|\mathbf{R}_b\rangle|\mathbf{Q}_r\rangle|\mathbf{R}_t\rangle|\mathbf{Q}_\ell\rangle \rightarrow |\mathbf{R}_t\rangle|\overline{\mathbf{Q}}_r\rangle|\mathbf{R}_b\rangle|\overline{\mathbf{Q}}_\ell\rangle$. For an example of the conjugation transformation, when implementing the third operator from the right-hand circuit of Eq. (1.46) in the $\overline{\mathbf{3}}^{\otimes 4}$ control sector, one employes the operator described in Eq. (1.56) but with swapped mode indices $1 \leftrightarrow 2$ performing the conjugation $\mathbf{3} \leftrightarrow \overline{\mathbf{3}}$ in both the control and active spaces. Appendix .1.5 provides an explicit enumeration of all 81 operators, transformed from those of Eqns. (1.51)-(1.58), for the $\{\mathbf{1}, \mathbf{3}, \overline{\mathbf{3}}\}$ Trotterized magnetic time evolution. Crucially, the construction of this local operator is applicable to lattices of any size when local irreps are truncated to single-index tensors.

The plaquette time evolution operator can be implemented through a collection of $e^{-i\alpha\mathcal{X}\mathcal{X}\mathcal{X}\mathcal{X}}$-type operators using the Givens rotations and a generalized CNOT operator controlling the application of a qutrit Pauli operator from Eq. (1.47) on the mode occupation of a second qutrit. When expressing the two-qutrit Givens rotation between the same two modes in each qutrit, a second rotation can be applied to the spectator mode to remove inadvertent rotation,

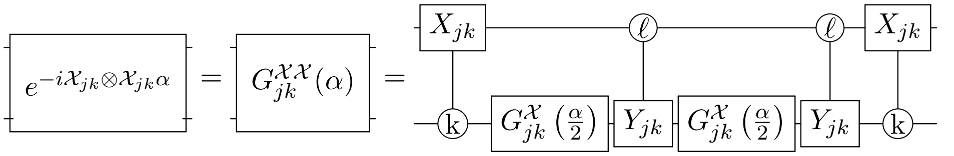

(1.59)

where ℓ is the third mode, the complement of j, k. In order to switch the relative modes acted upon in either qudit space, a pair of X operators can be used to change basis,

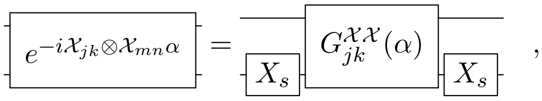

(1.60)

where X_s is the X operator necessary to bring the modes of the second qutrit in line with those of the first $\{m, n\} = \{j, k\}$ for the duration of this operator's action. This function is akin to the basis transformations commonly used in qubit implementations of multi-Pauli time evolutions. Extending the tactics of Eq. (1.59) to three qudits yields,

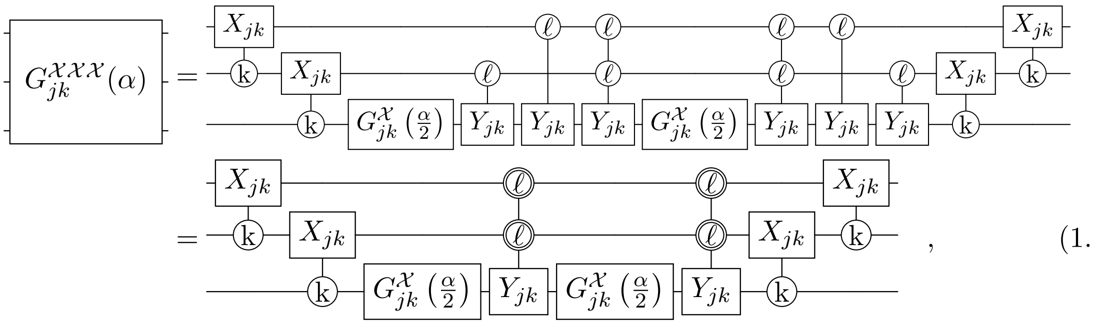

(1.61)

where the double-circled controls -ⓛ- represent the inclusive-or for multicontrols, applying the target operation if the state ℓ is populated in any of the controlled subspaces. For the $G^{\mathcal{XXXX}}$ operator, 7 ℓ-controlled operators will be used on either side to construct the inclusive-or-controlled Pauli for removal of the rotation when the third state is populated in any of the first three qutrits

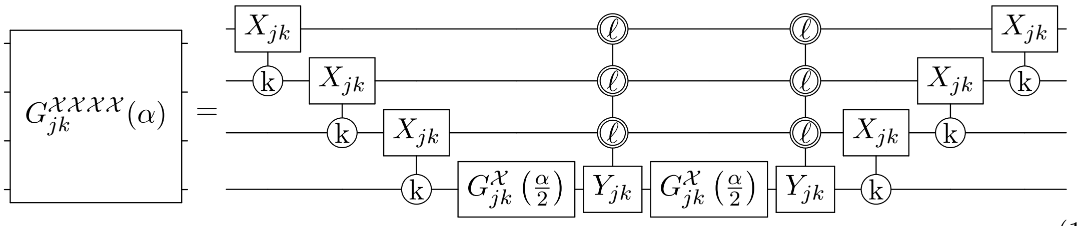

(1.62)

where one functional realization of this multi-controlled inclusive-or operation is

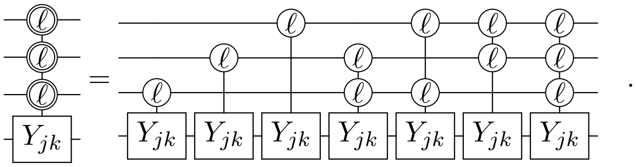

(1.63)

While this particular formulation comprised of two single-qutrit rotation operators is functionally clear and seems advantageous when considering T-costs for a potentially fault-tolerant implementation, it is entirely expected that hardware-specific variations will be made to this circuit decomposition in the course of practical implementation. Specifically, it is expected that different quantum architectures may offer unique techniques for implementing the isolated two-mode rotation when the third state is not populated in any of the four qutrits, as represents the core of this circuit decomposition. Furthermore, a qubit embedding with the common Gray-code implementation of two-level unitaries discussed in Subsection 1.3.5 may be advantageous for particular architectures.

In the above, a single qudit is used to capture the local Hilbert space of each link, demanding the two-dimensional hexagonal connectivity of Fig. 1.2 between qudit modes. Section 1.2.3 discusses the alternate opportunity to introduce two qudits per link representing the (p, q) registers of tensor indices, with the advantage that the necessary connectivity of modes in each qudit is reduced to nearest-neighbor linear, similar in form to that of a link in SU(2). The quantum circuits necessary for implementing the plaquette operator in this (p, q) basis of the local Hilbert space can be straightforwardly generalized from that above. In particular, the Hermitian combinations of Eq. (1.51)-(1.58) can be modified with the following substitutions

$$\mathcal{X}_{01} \to \mathcal{X}_{01} \otimes \mathbb{I} \qquad \mathcal{X}_{12} \to \mathcal{X}_{01} \otimes \mathcal{X}_{01} \qquad \mathcal{X}_{02} \to \mathbb{I} \otimes \mathcal{X}_{01} \tag{1.64}$$

where the $\{\mathbf{1}, \mathbf{3}, \overline{\mathbf{3}}\}$ basis within a single Hilbert space is traded for the pair of Hilbert spaces $|p\rangle \otimes |q\rangle$. In words, the last substitution in Eq. (1.64) replaces a hermitian operator mixing qudit states 0,2 (irreps $\mathbf{1}, \overline{\mathbf{3}}$) with an identity operator in the p-register and a mixing of the lowest two levels in the q-register. The plaquette operator implemented in the (p, q) basis requires only (correlated) nearest-neighbor interactions within each of the two qudits on every link. One can write a similar translation for the control operators

$$-\textcircled{\mathbf{1}}- = -\textcircled{0}- \to \begin{array}{c} -\textcircled{0}- \\ | \\ -\textcircled{0}- \end{array} \qquad -\textcircled{\mathbf{3}}- = -\textcircled{1}- \to \begin{array}{c} -\textcircled{1}- \\ | \\ -\textcircled{0}- \end{array} \qquad -\textcircled{\overline{\mathbf{3}}}- = -\textcircled{2}- \to \begin{array}{c} -\textcircled{0}- \\ | \\ -\textcircled{1}- \end{array} \tag{1.65}$$

where the two qudit lines at the right represent the $|p\rangle$ and $|q\rangle$ registers from top to bottom. While the basis with a single qudit per link demonstrated homogeneity in the type of operators, $G_{jk}^{\mathcal{X}\mathcal{X}\mathcal{X}\mathcal{X}}(t)$, necessary for a Trotterized implementation of the Hermitian combination of the plaquette operator and its conjugate, the (p, q) basis becomes a mix of operators $G_{jk}^{\mathcal{X}^{\otimes n}}(t)$ for $4 \leq n \leq 8$. These larger operators can be expressed as generalizations of Eq. (1.62). Explicit lists characterizing the set of operators for Trotterized plaquette implementation in both of these local bases are provided in Appendix .1.5.

1.5.1 Comparison Between Local and Global Bases

Subsection 1.4.1 presented results for the time evolution of the two-plaquette system computed using wavefunctions defined in a global basis truncated in color space by a local link basis of $\{\mathbf{1}, \mathbf{3}, \overline{\mathbf{3}}\}$. Above, technology was developed to address this and other systems using local controlled-plaquette operators. It is valuable to assure correspondence between results of the same quantities with these two quite different approaches.

Figure 1.14 shows the Trotterized time evolution of $\sum_a |\mathbf{E}^a|^2$ in the chromo-electric field starting from the trivial vacuum as a function of time with a local truncation of $\{\mathbf{1}, \mathbf{3}, \overline{\mathbf{3}}\}$ for

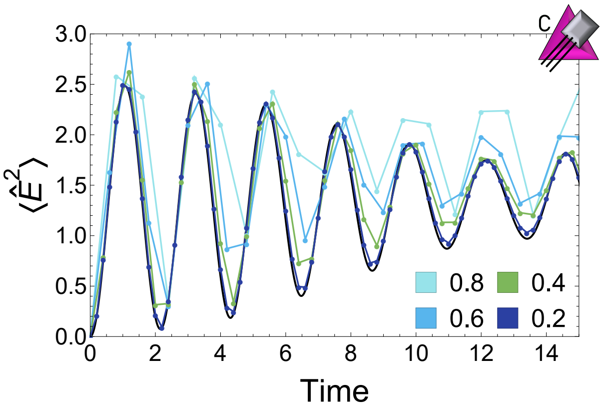

Figure 1.14: Time evolution of the Casimirs $\sum_a |\mathbf{E}^a|^2$ in the two-plaquette system (with PBCs) with each link truncated to $\{\mathbf{1}, \mathbf{3}, \overline{\mathbf{3}}\}$ for $g = 1$, initialized in the trivial vacuum. The black curve is calculated in the global ++ basis (the same curve as shown in the right panel of Fig. 1.11 and Fig. 1.13), while the points correspond to Trotter evolution of the contributing controlled-plaquette operators in the local basis.

each link. The black curve corresponds to those in the right panel of Fig. 1.11 and Fig. 1.13, obtained through the time evolution of the two-plaquette system using the four global basis states in Eqs. (1.31) and (1.41). As the quantum circuits discussed above reproduce identically the unitary evolution of each component contribution to the Hamiltonian, the same curve is recovered from the local basis through Trotterized evolution leveraging the controlled-plaquette operator. For example, the last operator in Eq. (1.58) is implemented, schematically, as the following set of three controlled Givens rotations,

$$\exp\left[-i\alpha \begin{pmatrix} \mathbf{3} & & \mathbf{3} \\ & (\hat{\square} + \hat{\square}^\dagger) & \\ \overline{\mathbf{3}} & & \overline{\mathbf{3}} \end{pmatrix}\right] \rightarrow$$
$$\left(\exp\left[-i\frac{\alpha}{3}\mathcal{X}_{12}\mathcal{X}_{02}\mathcal{X}_{12}\mathcal{X}_{01}\right] \exp\left[-i\frac{\alpha}{9}\mathcal{X}_{02}\mathcal{X}_{01}\mathcal{X}_{01}\mathcal{X}_{02}\right] \exp\left[-i\frac{\alpha}{3}\mathcal{X}_{01}\mathcal{X}_{12}\mathcal{X}_{02}\mathcal{X}_{12}\right]\right) \otimes \Lambda_1 \otimes \Lambda_2 \otimes \Lambda_1 \otimes \Lambda_2 \quad , \tag{1.66}$$

and similar decompositions apply to the other contributing controlled operators. As each unitary operator is associated with a physical transition of a plaquette, with coefficients determined from matrix elements between gauge-invariant states, the Trotterization preserves gauge invariance. As usual, however, the lack of commutativity introduces discrepancies in the evolution, analogous to the higher dimension operators in the Symanzik action describing finite lattice spacing artifacts in lattice QCD calculations.

As anticipated, Fig. 1.14 shows that the results of the Trotterized evolution in the local basis converges to a well-defined function as the Trotter step size is reduced toward zero that coincides with the result from evolution using the global basis with the same imposed color truncation. This result, and others, provides a partial validation of the controlled-plaquette local basis construction for describing QCD dynamics, and thus a framework for a scalable implementation on quantum architectures.

1.6 Technical Aspects for Simulating at Scale

The results of the previous sections inspire a discussion of technical hurdles that can be anticipated on the path to simulations of SU(3) lattice gauge theory at scale using local multiplet bases. We focus on issues related to scalability in volume, circuit depth, and gauge field truncation, to potential hardware implementations, and to extensions to three dimensional spatial lattices.

1.6.1 Scalability of Local Basis

This scalability discussion begins first with the total number of qubits required to express the gauge field; a diagrammatic notation parallel to that developed for large-N_c scaling [59, 60] is then presented to study the number of gauge invariant vertices as well as physical states and matrix elements comprising the plaquette operator. As naïvely presented above, the latter quantity can be made to directly correspond to the number of Givens rotations and thus the quantum circuit depth for the implementation of each local plaquette operator. In addition to their scaling, numerical values of these vertex and plaquette operator properties are provided to inform future practical implementations.

Qubit requirements are sensitive to the basis used to digitize and express the gauge field. The most efficient use of a hardware Hilbert space is achieved through a global basis, as discussed in Section 1.4, where the gauge variant space is removed through classical pre-processing and only the gauge invariant space is mapped onto quantum degrees of freedom. As demonstrated above, neither the classical pre-processing nor the subsequent compilation for quantum implementation are expected to be scalable in global bases. For this reason, local bases have been presented in Section 1.5, trading an expanded Hilbert space for local operators that may be optimized and implemented equivalently throughout the lattice. An initial mapping of Yang-Mills to local quantum registers, as first presented by Byrnes and Yamamoto [14], requires a large number of quantum registers to define the gauge field and include the flavor, color and Dirac degrees of freedom of the quarks. Each link would be described by $|p, q, T_L, T_L^z, Y_L, T_R, T_R^z, Y_R\rangle$ with a quantum register of qubits (or qudits) associated with each quantum number. The number of qubits for each quantum number can be determined by the cutoff, Λ_p, defining a finite (p, q) space. The compression accomplished in this work, using the methods introduced in Refs. [17, 18], significantly reduces the required qubit requirements for a given lattice. By integrating over the local color spaces, the number of registers per link is reduced from 8 to 2. For a lattice of L sites in each of D spatial directions, the number of qubits required for SU(3) Yang-Mills is estimated to be $\#\ \textit{qubits} \sim 2L^D \log_2(\Lambda_p + 1)$. For an $L = 10$ lattice in $D = 3$ dimensions truncated at $\Lambda_p = \Lambda_q = 1$ and thus restricted to color irreps $\{\mathbf{1}, \mathbf{3}, \overline{\mathbf{3}}, \mathbf{8}\}$, an estimate of ~ 2000 logical qubits are required.

In the formulation of this paper, Gauss's law is implemented explicitly by the neighboring controls associated with the action of the plaquette operator between link configurations and, in particular, the dependence on these controls of the non-vanishing matrix elements that transition between plaquette configurations. Time evolution of a Yang-Mills wavefunction defined in a local basis can be accomplished by repeated applications of these controlled-plaquette operators, parallelizable at separations of two plaquettes, and thus enjoys the volume independence of the circuit depth characteristic of locally-interacting theories [42].

To estimate the scaling of quantum resources required for the implementation of each controlled-plaquette operator as the irrep truncation is raised, it is found to be convenient to work with the (p, q) coupled register mapping. With a truncation defined by the maximum number of upper and lower indices describing the highest dimension tensor within the active color space of each link, $\Lambda_{p,q}$, it is essential to estimate the scaling as a function of increasing $\Lambda_{p,q}$. A truncation that respects color parity, $\Lambda_p = \Lambda_q$ is employed. The quasi-locality of the interactions ensures that further scaling with regard to this cutoff involves only (trivial) factors of the spacetime volume. The above analyses of the one- and two-plaquette systems indicate that, for the low-energy and low-energy-density sectors of calculations, contributions from color irreps high in the spectrum become exponentially suppressed beyond a coupling-dependent value. If this suppression is maintained for extended lattices upon raising the tensor index truncation, Λ_p, will dominate over the power-law scaling in the number of non-vanishing matrix elements defining the controlled-plaquette operators. It is anticipated that analogous arguments will be established for localized high-energy density configurations that evolve forward in time through fragmentation and hadronization (processes that are important for nuclear and high-energy physics) to configurations of low-lying final-state hadrons.

To begin to establish the scaling of the number of controlled operations that will be required for time evolution using controlled-plaquette operators acting on the local basis, it is helpful to explore and quantify the scaling of the 3-point vertex (or $2 \to 1$ fusion). This corresponds to multiplicities in the control of a single plaquette vertex. The maximum

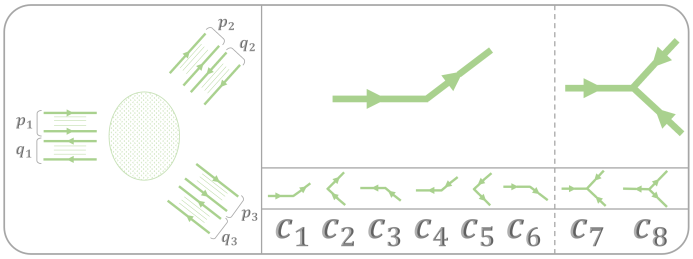

Figure 1.15: Diagrammatic representation of gauge invariant vertex contractions for the 3-pt vertex. Arrows indicate the flow of tensor indices in the fundamental and anti-fundamental and external lines are contracted to produce irreducible representations in the local (p,q) link basis.

possible growth of the Hilbert space for this three-point vertex is Λ^6, allowing a $(\Lambda+1)$-dimensional configuration space for each of the (p,q) registers detailing the irrep tensor structure on each link. However, not all vertex configurations satisfy Gauss's law, leading to a reduction to the number of physical vertices. Inspired by the diagrammatic tactics of large-N_c scaling calculations [59, 60], consider directional lines expressing propagations of fundamental or anti-fundamental indices. The left of Fig 1.15 shows the 3-point vertex characterized by p fundamental indices and q anti-fundamental indices as propagating left-right and right-left, respectively. The external lines (conventionally absent in the large-N_c analysis of color-singlet objects), can be mapped directly to irreducible representations defining the local link basis. Whether or not the chosen external lines can be connected through a center region constructed by gauge invariant index contractions determines whether the vertex is physical, or contains a singlet. All gauge invariant contractions relevant to the 3-point vertex are shown at the right of Fig. 1.15. The SU(3) structure provides two invariant tensors: the δ-function, leading to contractions labeled c_{1-6}, and the Levi-Civita, leading to contractions c_{7-8}. When implementing a local truncation in the (p,q) basis, this appears as correlated constraints between the c_i's e.g., $p_1 = c_1 + c_6 + c_7 \leq \Lambda_p$. Every integer vector $\vec{c}$ refers to a physical 3-point vertex and a unique contraction pattern. However, every unique contraction pattern does not provide a unique vertex in the local (p,q) basis, as discussed in Section 1.4. For example, the $\mathbf{8}\otimes\mathbf{8}\otimes\mathbf{8}$ vertex can be expressed by $\vec{c} = \{1,0,1,0,1,0,0,0\}, \{0,1,0,1,0,1,0,0\}$, or $\{0,0,0,0,0,0,1,1\}$ through a set of three δ-contractions or a pair of ϵ-contractions.

Using this diagrammatic approach, the algebraic tensorial decomposition methods of Coleman [61] indicating that the number of three-point vertex completions for given $(p,q)_{2,3}$

is

$$\dim(p_1, q_1)_{physical} = \sum_{i=0}^{\min(p_2,q_3)} \sum_{j=0}^{\min(p_3,q_2)} 1 + \min(p_2 - i, p_3 - j) + \min(q_2 - j, q_3 - i) \quad , \quad (1.67)$$

or evaluations through computational packages e.g., `SU-3-CG-Code` Mathematica code [62, 63], explicit calculations can be made of the unique physical vertices in the (p, q) basis.

$p, q \leq \Lambda_p$	# of singlets	$p, q \leq \Lambda_p$	# of singlets
0	1	9	182,803
1	19	10	322,621
2	165	11	542,196
3	838	12	874,483
4	3,049	13	1,361,683
5	8,865	14	2,056,971
6	22,003	15	3,026,098
7	48,514	16	4,349,413
8	97,653		

$p, q \leq \Lambda_p$	# of singlets	$p, q \leq \Lambda_p$	# of singlets
0	1	6	1,739,833
1	82	7	5,080,226
2	1967	8	13,071,135
3	19,550	9	30,436,170
4	116,929	10	65,372,321
5	504,932	11	131,352,884

Table 1.2: The number of singlets formed from three (left, 2 → 1 fusion process) and four (right, 3 → 1 fusion process) color irreps up to a cutoff in the number of upper and lower indices of Λ_p.

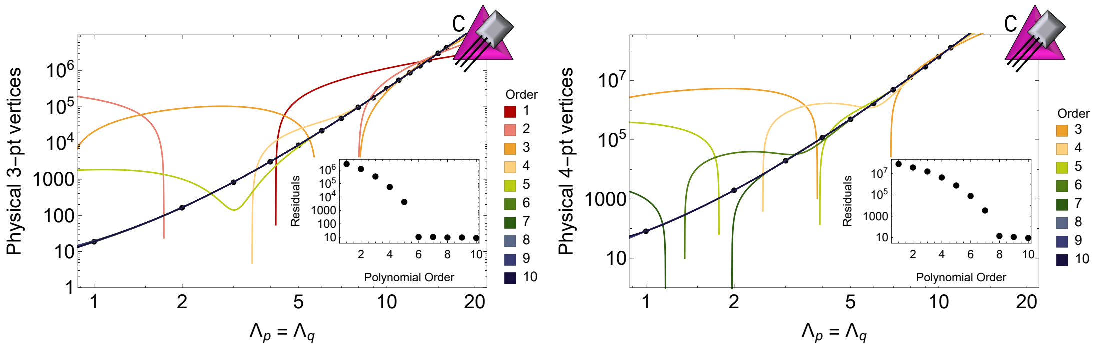

Figure 1.16: The number of singlets in the product of three (left panel) and four (right panel) color irreps as a function of the index cutoff Λ_p. The main panels show the number of singlets and polynomial fits for a range of orders, $f(x) = \sum_{n=0}^{n_{\max}} c_n x^n$ from $n_{\max} = 1$ to 10. The inset panels shows the L2 norm of residuals in the fits.

Exact values computed for the fusion of modest-sized irreps are given at the left of Table 1.2.

The left panel of Fig. 1.16 shows the results of Table 1.2 along with polynomial fits and the associated residuals. Significant reductions in fit residuals are found for polynomials up to order $n = 6$, beyond which the inclusion of terms of higher degree do not improve the quality of the (single precision) fit to the exact results. The results in Table 1.2 indicate Λ_p^6 scaling for the number of physical 3-point vertices below a local link truncation of Λ_p. This asymptotic scaling is equivalent to that of the unconstrained Hilbert space of the locally-defined vertex, indicating that satisfying Gauss's law does not modify the asymptotic polynomial scaling of the physically relevant vertices.

Another quantity whose scaling is important is the number of plaquette control sectors. This is lower bounded by the number of different products of four irreps that contains at least one singlet. The unconstrained asymptotic scaling of the associated Hilbert space is Λ_p^8. Using a similar array of techniques as those for the 3-point vertices above, explicit calculations furnish the results shown at the right of Table 1.2. As shown in the associated right panel of Fig. 1.16, the modest calculated values indicate a necessary and sufficient scaling exponent of Λ_p^8. Once again, the Gauss's law constraint does not reduce the asymptotic polynomial scaling of the number of physical vertices. The remaining stagnant residuals in both the cases of the 3-point and 4-point vertices shown in the insets of Fig. 1.16 indicate that the Gauss's law constraint does, however, add an additional non-polynomial structure to the scaling, acting to reduce the physical dimensionality from the simple $\Lambda^{6,8}$ unconstrained values. This strong scaling provides a potentially daunting backdrop to implementation on present and future quantum devices. At low Λ_p truncations, increasing the number of indices for color irreps by one in the dynamical local link basis can produce factors of ~ 10 in the number of control sectors that are required to be implemented at each Trotter step of the plaquette time evolution.

To fully understand the circuit complexity of the local controlled plaquette operator, as discussed in Section 1.5, with increasing gauge field truncation, the total number of non-vanishing matrix elements within the physical subspace needs to be considered. Explicit calculations of these properties are presented in Table 1.3. While classically capturing dimensionalities for sufficiently high truncations to numerically constrain the scaling of the physical plaquette states is nontrivial, experience with the 3- and 4-point vertices suggests that an asymptotic polynomial scaling consistent with that of the unconstrained Hilbert space is likely. This would result in a scaling of Λ_p^{16}. Additionally, a clear lower bound of Λ_p^{12} can be rationalized by the freedom of the diagonal 3-point vertices before determining physically viable values for the two remaining control links. Crucially, the final step of determining the number of non-vanishing matrix elements within the physical space (connected to the time evolution circuit depth as discussed in Section 1.5) does not contribute additional factors of Λ_p to the asymptotic scaling of the number of physical plaquette states.

$\Lambda_p = \Lambda_q$	dimensions	physical states	matrix elements	elements/states
1	$(\mathbf{1},\mathbf{3})$	81	81	1
1	$(\mathbf{1},\mathbf{3},\mathbf{8})$	529	1,018	1.92
2	$(\mathbf{1},\mathbf{3},\mathbf{8},\mathbf{6})$	5,937	19,594	3.30
2	$(\mathbf{1},\mathbf{3},\mathbf{8},\mathbf{6},\mathbf{15})$	59,737	419,316	7.02
2	$(\mathbf{1},\mathbf{3},\mathbf{8},\mathbf{6},\mathbf{15},\mathbf{27})$	139,317	1,049,931	7.54
3	$(\mathbf{1},\mathbf{3},\mathbf{8},\mathbf{6},\mathbf{15},\mathbf{27},\mathbf{10})$	509,271	4,001,111	7.86
3	$(\mathbf{1},\mathbf{3},\mathbf{8},\mathbf{6},\mathbf{15},\mathbf{27},\mathbf{10},\mathbf{24})$	2,008,297	24,648,819	12.27

Table 1.3: Properties of the plaquette operator truncated in the local index (p, q) basis and at intermediate truncations organized by dimension. The number of physical states constituting the gauge-invariant basis of the plaquette operator, as well as the number of non-zero matrix elements within the physical subspace are presented. The ratio of these two quantities is shown in the right column.

The irrep-locality of the plaquette operator produces a surface- rather than volume-type contribution to the dimension of physical states. To see this, consider the active space of the plaquette operator contracting a $\mathbf{3}$ or $\overline{\mathbf{3}}$ with the irrep at each of the four active links. As demonstrated in the connectivity diagram of Fig. 1.2, an application of the fundamental or anti-fundamental is capable of producing only local nearest-neighbor transitions in the structure of a two-dimensional hexagonal lattice. As such, the plaquette operator generates population in each of three new irreps for each link and thus a potential transition supported to $3^4 = 81$ different final states. Many of the possible states generated will not satisfy Gauss's law at the four vertices, as enforced through the plaquette operator controls. Thus, the number of non-zero matrix elements of the controlled plaquette operator is maximally a constant factor of 81 times larger than the total number of physical states. The right column of Table 1.3 indicates that in practice, for low Λ_p-truncations, this number is significantly smaller than 81, its unconstrained upper bound.

While the scaling of the number of control structures and matrix elements in the controlled-plaquette operator with cutoff in irrep space is a relatively high-order polynomial, the operator is nearly local in space, extending over just a few links. This remains the case, but involving more links, with the plethora of Hamiltonian improvements that could be implemented, for example, Refs. [28, 64, 65, 66]. Consequently, we expect that these operators can be determined using classical computing, and subsequently applied repeatedly throughout the lattice volume. With the anticipated color irrep localization of low-lying field configurations, we do not anticipate that classical computing resources will impose a limitation on defining the Trotterized time evolution operator for the relevant range of lattice spacing (a range that remains to be quantified). When increasing the gauge field truncation in this local multiplet basis, high-order polynomial quantum resources are traded for improvement in the physical convergence. The delocalization resulting from reducing the lattice spacing will require controlled extrapolations as the lattice scales are systematically removed. To understand these features more clearly, and to be able to better estimate resource requirements, even for modest-sized lattices, further calculations and simulations are required. For example, the use of binary encodings, as has been used for the single plaquette in Subsection 1.3.5, may lead to slower polynomial growth, a subject of future investigations.

The number of qubits and operations ultimately needed for a quantum simulation of lattice QCD will depend on the gauge field truncation needed to reach the continuum limit. This can be estimated by considering the size of electric fluctuations as the continuum limit is approached. Following the approach used in Ref. [67], the chromo-electric field fluctations are given by $\langle E^2 \rangle \approx \frac{\sqrt{2}}{g^2}$. The untruncated Hamiltonian should be approximated reasonably well provided the truncation on the gauge field is chosen such that the electric energy of the maximum allowed electric field is 3 times the size of the fluctuations. This gives the constraint

$$\Lambda^2 + 3\Lambda > \frac{3\sqrt{2}}{g^2} \tag{1.68}$$

where Λ is the truncation on p and q. From previous strong coupling calculations of hadron masses and the chiral condensate with the Kogut-Susskind Hamiltonian [68, 69], it can be estimated that the continuum limit can be probed with $g \approx 0.8 - 1$. This would suggest a truncation of $\Lambda = 3$ is sufficient. This is consistent with estimates of the resources required for q-deformed Kogut-Susskind Hamiltonians to approach the continuum limit [70, 71].

The convergence in color space for low-lying states suggests that a low-dimension-color-irrep EFT may exist. We conjecture that plaquettes containing "high-energy links", defined by their Casimir, can be "integrated out" of the low-dimension-color-irrep space, with their effects reproduced by higher-dimension gauge-invariant operators in the Hamiltonian with coefficients determined by matching observables. This possibility remains to be explored, and will be the subject of future work. In order to perform precision calculations at scale, developing EFT techniques, such as this and those used to make predictions from lattice QCD calculations, appear to be essential.

At this point it is worth commenting on instanton configurations that mediate transitions between distinct topological sectors in Yang-Mills theory. Far from the center of an instanton, the field strength scales as $1/r^4$ from color fields that scale as $1/r^2$, and such configurations are expected to lead to modifications to the naïve quantum resource requirements. From a scaling perspective, these configurations are anticipated to introduce power-law structure in color space. The resulting convergence in the presence of an instanton in 3-dimensional calculations is expected to be simply exponential in the number of qubits, rather than a mix of single- and double-exponential convergence for the latticization and digitization, respectively, as was found in scalar field theory [72, 15, 16, 31, 27]. Furthermore, motivated by the topological freezing effects experienced when updating gauge field configurations in Euclidean lattice QCD calculations, it will be important to understand the ability of quantum simulation time evolution and state preparation techniques to efficiently capture topological charge sectors. Observed to be influential in this aspect for classical calculations, this feature further inspires the importance of thorough explorations of boundary conditions in simulation efficiency. Reliable estimates of the impact of these configurations will only become possible when 3-dim simulations become practical. However, analysis of lattice QCD gauge-field configurations, e.g., Ref. [73], in particular in regions of topological charge density may provide helpful information.

In this work, we have focused on controlled-plaquette operators for time evolution, and have not presented an explicit formulation of a state preparation. By confinement, the connected correlation functions of the vacuum are exponentially localized with a length scale set by the mass gap. As such, the techniques associated with exponentially convergent systematically-localizable operators and fixed-point quantum circuits [74, 75] can, in principle, be implemented. Classical computations of a lattice system containing at least a correlation length can be used to tune the parameters of a link-based initialization quantum circuit, which can then be used throughout the larger volume of the quantum simulation. This is, of course, limited by the lattice spacing, which if small enough would exceed classical computing resources.

1.6.2 Hardware Implementation Exploratory Discussion

Focusing on the local controlled plaquette implementation due to its advantageous scaling, two mappings of the color space into the Hilbert space(s) associated with each link have been considered. The first, with a single quantum register or qudit per link, requires high connectivity among sets of 8 link registers and two-dimensional hexagonal connectivity within each. The second, with a pair of quantum registers or qudits per link, simplifies the connectivity internal to the link space from 2D-hexagonal to a correlated set of one-dimensional hierarchies requiring only (correlated) nearest-neighbor raising and lowering operators within each qudit. This further organization of two registers per link, one each for the upper and lower indices of the tensor describing the color irreps of the link, technically requires additional 16-register communication to implement the 8-register correlated ladder operators controlled by 8 neighboring registers.

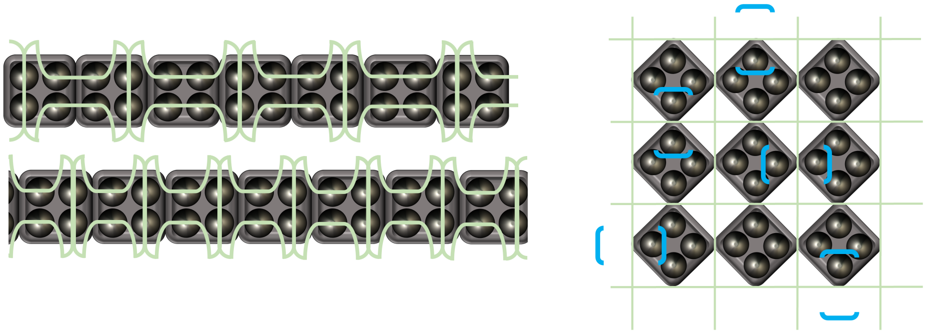

Figure 1.17: Plausible mappings of one (left panel)- and two (right panel)-dimensional SU(3) lattice gauge theory onto quad-core SRF cavities utilizing the (p, q) local basis. The light green lines indicate the lattice structure. At the left top, a one-dimensional plaquette string is illustrated in the (p, q) basis with two qudits per link. At the left bottom, the (p, q) local basis is used only for the vertical links to homogenize the quad-core operations. At the right, it is shown how an array of quad-core SRF cavities can be used to represent a two-dimensional lattice of SU(3) gauge theory in the local (p, q) basis with blue brackets indicating the cavities used to represent the (p, q) pair of qudits at local links.

While the tactics presented here can be readily implemented on qubits, qutrits, and generally qudits, they appear to be also suitable for the Superconducting Radio Frequency (SRF) cavity devices being advanced by Lawrence Livermore National Laboratory (LLNL) and Fermi National Accelerator Laboratory (FNAL) [76, 77]. Relatively large cutoffs in color irrep space could be implemented for each link, even with today's cavities. It would appear that a quantum communication fabric that connects eight nearest neighbor cavities is sufficient to simulate a chain of plaquettes using controlled-plaquette operators, as detailed in this work. The SRF cavities associated with each link and those of the four external control links would be engaged coherently. This is somewhat more complicated than the standard hypercubic communication fabric used, for example, for lattice QCD calculations.

It may be profitable to develop SRF cavity systems with sufficient cavity interconnect and/or optimized control to be able to implement simulations of one- and two-plaquette SU(3) systems using the local basis (requiring 4 and 6 cavities, respectively, or twice these numbers if trading qudits for simplified intra-qudit connectivity as in the (p, q) option of the local basis), an extended one-dimensional chain of plaquettes, and a three-dimensional cube of plaquettes (requiring 12 cavities), which would provide foundational steps toward simulations of QCD. Diagrams are provided in Fig. 1.17 to demonstrate possible lattice connectivity through the use of quad-core SRF cavity architectures for one (left panels)- and two (right panel)-dimensional SU(3) lattices. Two different embeddings for the one-dimensional plaquette string are imagined: the first with every link represented in the (p, q) local basis with two cavities per link and the second with a mixture of the (p, q) local basis on vertical links and the single-qudit local basis on horizontal links. This mixture of local bases allows unitary operators for the magnetic time evolution to be translationally invariant among the quad-core cavities, and further emphasizes the flexibility in lattice structure amenable to hardware codesign.

Crucially, by working in localized bases, the plaquette operators designed and implemented in the process of the demonstrations suggested above remain relevant even as lattices are scaled to the infinite volume limit. Looking further into the future, one could imagine $\sim 10^3$ SRF cavities with a localized communication fabric and optimized controls being used to simulate three-dimensional Yang-Mills theory on a $10 \times 10 \times 10$ spatial lattice using or adapting techniques demonstrated in this work, and their extension to higher dimensions.

Complementarily, recent advances in forming high-fidelity qudits within the hyperfine structure of trapped-ion systems, for example Ref. [78], indicate that exploratory calculations using the qutrit encodings presented above for the $\{\mathbf{1}, \mathbf{3}, \overline{\mathbf{3}}\}$ truncation may be implementable on such systems in the near future. In addition to their appealing connectivity, these systems of trapped ions are intriguingly capable of naturally generating interaction Hamiltonians that swap populations between qudit levels with a coupling constant determined by level-dependent CG sums. While the local calculation of CG coefficients is not currently foreseen to be a limiting factor, the presence of these natural interactions suggest a potential path forward for a hybrid digital-analog approach to constructing plaquette operators.

Looking forward toward future production-scale simulations, experience from classical lattice QCD calculations indicates that tuning QCD simulations, the lattice spacing and quark masses, will be required for each set of calculations. One could imagine that initial simple tunings in early productions may involve calculations of the dynamics of one- and two-plaquette systems (and higher) as benchmarks of device performance, both in execution time and fidelity.

1.6.3 Higher Spatial Dimensions

Up to this point, strings of plaquettes residing in one spatial dimension have been considered. In two spatial dimensions, four-point vertices are required, though they can be point-split into an expanded lattice of again only three-point vertices. For systems in three dimensions, vertices involve the fusion of 6 links, two in each spatial dimension. Integration over the gauge space at each vertex can be performed, and links denoted by the irrep dimensionality, as in lower dimensions. The controlled-plaquette operators will act in each of the spatial planes, controlled by the total “external” color at each vertex, as dictated by Gauss’s law. Therefore, the plaquette control structure that has been developed in this work will be applicable to three dimensions, and no further structures are required. However, at each vertex, the coherent sum over all irreps that can be formed from the external four links defines the control sectors of the operator. This is reminiscent of the function provided by point-splitting, discussed extensively in the literature for such simulations, e.g., Refs. [79, 80, 81], here applied to the controlled plaquette operator.

This is an extra layer of complexity that has to be incorporated into the quantum circuits required to analyze the system. Most of the extra layer is anticipated to be accomplished using classical computation, as it requires determining matrix elements of local objects, and does not increase in complexity with the system volume. At the level of the quantum simulation, the increase of operator structure, corresponding to an increase in the number of link projectors (and the number of orientations), the number of quantum operations scales trivially with volume.

1.7 Discussion

The quantum simulation of lattice field theories offers a path toward computing dynamical, non-equilibrium processes of importance for basic science and for advancing quantum technologies that are inaccessible to classical simulation. While classical simulations of field theories are sophisticated, with ongoing improvements to algorithms, workflows, hardware, infrastructure and community organization, quantum simulations are at their very earliest stages. Simulations of spin systems naturally map to quantum devices with quantum registers of qubits, and early real-time calculations of elastic and in-elastic processes in low-dimensions are being performed with present-day quantum devices and quantum simulators. Further, powerful formal techniques are employed, such as tensor methods, that are of benefit to both classical and quantum simulations. As three of the four fundamental forces of nature are accurately described by quantum gauge field theories—describing the interactions and dynamics of quarks, gluons, electrons, electroweak bosons, and so forth—their simulation requires the inclusion of gauge fields. Building upon a large body of work related to Hamiltonian formulations of non-Abelian quantum field theories, and somewhat recent investigations related to their implementation on quantum devices, we have investigated early steps along one of the possible paths forward (a “Trailhead”) for quantum simulations of lattice SU(3) Yang-Mills gauge theory, with an eye toward QCD. We anticipate that the results and insights gained in this work may be of benefit to the simulation of other lattice field theories where local symmetries play a central role and which are implemented, in part, through the action of plaquette operators. This includes algorithms that are relevant for quantum error correction for quantum hardware and computation.

In this work, the path toward implementation of QCD on quantum devices through the Kogut-Susskind Hamiltonian presented by Byrnes and Yamamoto [14] has been adapted to reduce the qubit (qudit) requirements through integration over the local gauge space at each lattice site. The continuous gauge field is digitized in the field conjugate representation by truncating the magnitude of the color-electric field that can be supported by any given link. These local discrete Hilbert spaces can be captured through a basis of quantum registers distributed locally across the lattice in two main ways: one using a mapping of irreps onto a qudit and one using two registers for the (p, q) values defining tensor indices of SU(3) irreps for each link. Applications of the plaquette operator then update each link in the plaquette, with amplitudes that depend upon irreps of the nearest neighbor links. In contrast, a global basis can be defined by mapping symmetry-projected link configurations of the entire lattice onto the states of a quantum device, and the action of the Hamiltonian determined. The resources required to implement local bases scale with the volume of the lattice, while those required for global bases scale super-polynomially. We examined, using classical simulation and IBM's superconducting quantum hardware, the dynamics and mappings of a single SU(3) plaquette onto a quantum device, and are encouraged by the exponential convergence of low-lying states and low-energy dynamics with increasing color-irrep cutoff. Two-plaquette systems were studied in detail using global and local bases and are the simplest systems that receive contributions from controlled-plaquette operators, the construction and implementation of which we have detailed. While the low-lying states and time evolution of the single-plaquette systems can be efficiently accommodated in a Hilbert space defined by qubits, the structure of the link color-irrep Hilbert space and the action of the controlled-plaquette operator lend themselves for embedding into qudit systems, such as qutrits or SRF cavity based systems.

The plaquette operator plays a central role in the simulation of lattice gauge theories, and the fidelity with which it can be implemented across the Hilbert space of a given quantum device is a key measure of the ultimate quantum simulation fidelity. Benchmarks for the performance of devices using both global bases and local bases may provide complementary information, the latter isolating the physical Hilbert space. In addition to the one-plaquette benchmarks above, analogous benchmarks for the two-, three-, four-plaquette and higher-dimensional systems will also be valuable, with the two-plaquette system providing a measure of the fidelity of the controlled-plaquette operator, the four-plaquette system sensitive to the point-split four-vertex interaction, and the three-dimensional systems sensitive to 6-link vertices. In near-term simulations, it is likely that a series of such benchmarks, starting from the single plaquette in the global basis, will be performed to identify preferred mappings onto device architectures and provide calibrations for simulations of larger systems. Furthermore, such calibrations are expected to begin the process of tuning simulation parameters, such as the cutoff in color irrep space, balancing theory approximations with device performance for the array of lattices and couplings that will eventually be necessary to extract continuum quantities.

At these early stages of development, there is value in considering, quantifying, and comparing all potential implementations of Yang-Mills gauge theories on quantum devices. Beyond the time evolution operator, the finite mass gap in Yang-Mills theories suggests that systematically localizable quantum circuits may be realizable to prepare the ground state and localized scattering states through the use of small-volume classical simulations. Unfortunately, the asymptotic polynomial scaling of the required matrix elements, while sub-exponential, is sufficiently significant to expect that large-scale classical resources will be required for both state preparation and design of the controlled-plaquette operators.

Building upon previous frameworks, the multiplet basis has here been further developed through local gauge-space integrations and circuit-level decomposition of local time evolution operators, showing promise for designing scalable quantum simulations of SU(3) Yang-Mills lattice gauge field theory. Early examples of the proposed strategies have been concretely demonstrated, through implementation on a superconducting quantum architecture and through explicit enumeration of relevant operators, for one- and two-plaquette systems. These simple systems are expected to guide near-term quantum simulations, inform future codesign, and provide calibration quantities for simulations at scale.

Chapter 2

PREPARATION OF THE SU(3) LATTICE YANG-MILLS VACUUM WITH VARIATIONAL QUANTUM METHODS

2.1 Introduction

To use quantum computers to study physical systems of interest, physical states, such as the vacuum of a QFT, need to be prepared. There have been a number of proposals for preparing the vacuum state of QFT. Approaches for preparing the ground state by performing imaginary time evolution on a quantum device have been explored, but computational costs scale exponentially with system size, limiting their applicability [82]. Adiabatic switching from a known ground state has also been explored and scales polynomially in system size (provided the system is gapped) [16, 83, 84]. However, the number of time steps needed to accurately simulate adiabatic switching in practice can be daunting. The Variational Quantum Eigensolver (VQE) is an algorithm suitable for near term noisy quantum computers that can be used to variationally prepare the lowest energy state of a quantum system by optimizing an ansatz circuit [85]. The application of VQE to quantum chemistry problems has been studied in great detail [85, 86, 87, 88, 89, 90, 91, 92, 93, 94, 95, 96, 97, 98]. Additionally, use of VQE in the preparation of the vacuum state for various quantum field theories, including the Abelian Higgs model with a topological θ term [99], has recently been examined. The VQE algorithm has been previously applied to find the vacuum state of small lattices for the Schwinger model [29, 100, 101]. It has also been used to prepare hadron states in an SU(2) gauge theory in 1+1 dimensions [102] and to model the force between mesons in the Schwinger model [30]. VQE requires an ansatz circuit to prepare the system's state and a classical optimizer to determine the angles in the ansatz circuit. To scale these calculations to situations with a useful quantum advantage, it will be necessary to understand how to connect these small lattice calculations to a calculation on a larger lattice and how the optimization procedure performs as system size is increased.

In this chapter, the application of VQE to pure SU(3) lattice Yang-Mills gauge theory is studied. This provides a starting point for understanding the resources required to simulate lattice QCD on a quantum computer. We performed a VQE calculation of the vacuum state for one and two plaquette systems using superconducting quantum processors. We also examine how to apply ideas from domain decomposition in lattice QCD calculations on classical computers to the construction of ansatz states for VQE of large lattices from the vacuum state of smaller lattices.

2.2 Single Plaquette Vacuum Preparation

2.2.1 Initialization

VQE is a hybrid quantum algorithm that can improve the overlap of an initial state with the vacuum state. The performance of VQE has a strong dependence on the initial state used [85, 86, 88]. In applications of VQE to electronic structure problems, Hartree-Fock states and unitary coupled cluster states computed on classical computers have been used as initial starting points for VQE. However, lattice gauge theory does not have comparable classical calculations in the Hamiltonian formulation available. As an alternative, the Lanczos algorithm can used to initialize VQE for a single plaquette.[1] The Lanczos algorithm works by constructing the Krylov subspace spanned by $\{|\psi\rangle, \hat{H}|\psi\rangle, \ldots, \hat{H}^n|\psi\rangle\}$ for some integer n and initial state $|\psi\rangle$ and diagonalizing the Hamiltonian in this subspace [103]. Quantum variations of the Lanczos algorithm have also been proposed for use in the study of state preparation [82]. The result of applying the Lanczos algorithm to a single plaquette using the electric vacuum as the initial state is shown in Fig. 2.1.[2] For a fixed coupling, the overlap with the true vacuum is shown to scale asymptotically as a Gaussian with the Krylov dimension used in the Lanczos algorithm. The dimension of the Krylov subspace needed to reach a fixed accuracy scales as $\frac{1}{g}$. This behavior can be seen to follow from the structure of the single plaquette vacuum wavefunction. The vacuum wavefunction is asymptotically Gaussian in the chromo-electric field with a width inversely proportional to g. Each time $\hat{H}$ is applied to increase the dimension of the Krylov subspace, the maximum p and q included in the Krylov subspace is increased by 1. Therefore, the size of the vacuum wavefunction components added by increasing the Krylov dimension fall off asymptotically as a Gaussian, and the Krylov dimension needed to reach a desired accuracy ϵ scales as $\frac{\log\left(\frac{1}{\epsilon}\right)}{g}$. It should be noted that an exponential convergence with field truncation has also been observed in the simulation of scalar field theories [27] and $U(1)$ gauge theories [104], and has been proven to be a rather generic property of theories involving bosonic modes [105].

The Lanczos algorithm provides approximate wavefunction components of the vacuum state that must be mapped into a quantum circuit to be useful for state preparation. The

---

[1] This application of Krylov subspaces to quantum simulation was developed in collaboration with other members of IQuS during the spring of 2020.

[2] The icons in the corners of the plots in this text were introduced in Ref. [75] and are available at `iqus.uw.edu/resources/icons/`. The pink icons indicate the calculations in the figure were performed on a classical computer and the blue icons indicate the calculations in the figure were performed on a quantum computer.

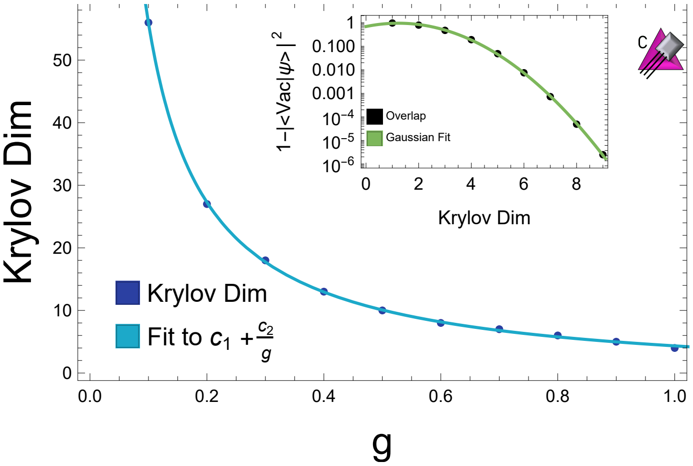

Figure 2.1: This figure shows the dimension of the Krylov subspace required for the overlap of the state prepared by the Lanczos algorithm, $|\psi\rangle$, with the true vacuum, $|\text{Vac}\rangle$, to satisfy $|\langle\psi|\text{Vac}\rangle|^2 \geq 0.999999$. The inset panel shows the overlap with the true vacuum as a function of Krylov dimension for $g = 0.5$. The true vacuum was computed numerically using Mathematica's eigensystem function.

state prepared by using a d-dimensional Krylov subspace potentially spans all basis states with $p, q < d$. Therefore, a state with nontrivial support on d^2 basis states must be prepared, which can be done using a circuit of length $O(d^2)$ using standard state preparation procedures [54]. Using the previous result on the Krylov dimension required to reach an accuracy ϵ, a quantum circuit of size

$$S = O\left(\left(\frac{\log\left(\frac{1}{\epsilon}\right)}{g}\right)^2\right) \quad , \tag{2.1}$$

can be used to prepare the vacuum of a single plaquette with coupling g on a quantum computer within an accuracy of ϵ.

2.2.2 Optimization

The VQE algorithm makes use of a classical optimizer to improve the overlap of the ansatz state with the actual vacuum. In previous work, Bayesian optimizers have been used in the VQE algorithm to prepare the ground state of the Schwinger model [29] and to prepare hadron states in an SU(2) gauge theory [102] on small lattices. Bayesian optimization minimizes an objective function by iteratively constructing an interpolator, usually a Gaussian process, from existing data and optimizing the interpolator. It is ideal for optimizations where the number of available evaluations of the objective function is limited (typically to a few hundred evaluations), the objective function is continuous, and the dimensionality of the domain is no more than 20 [106]. On existing hardware that only has a handful of qubits available, circuits that can prepare a generic ansatz state can be implemented with fewer than 20 parameters. However, as quantum computers grow in qubit count and coherence time, this will no longer be true. To reach a quantum advantage, it will be important to understand when Bayesian optimization breaks down. To test the performance of a Bayesian optimizer for lattice gauge theory, VQE was simulated without noise on a classical computer for a single SU(3) plaquette with a truncation of $p, q \leq 3$. This system can be represented using 4 qubits on a quantum processor. The vacuum state of this system lies in a 10-dimensional CP-invariant subspace which can be parametrized in spherical coordinates with 9 degrees of freedom. The details of how the Bayesian optimization was performed are available in Appendix .2.2.

The results of the simulation of VQE with a Bayesian optimizer are shown in Fig. 2.2. In these calculations, the Gaussian process used to model the energy function being minimized suffered from multicollinearity. This was mitigated with Tikohonov regularization, which in this context is equivalent to adding a small constant term λ to the covariance matrix of the energies. As this figure shows, the convergence of the Bayesian optimizer has a dependence on the regulator λ. The energy that the Bayesian optimizer converges to cannot be made arbitrarily close to the vacuum energy because at sufficiently small values of λ, multicollinearity returns and the covariance matrix cannot be inverted, causing the Bayesian optimizer to fail. The lower panels in Fig. 2.2 show the dependence of the Bayesian optimizer's convergence on the dimension of the Krylov subspace used to initialize the calculation. For certain initializations, the Bayesian optimizer is not able to improve upon the initial state's overlap with the actual vacuum. Even for this modest system size, Bayesian optimization has limitations in how close it can get to the vacuum state.

Gradient descent is an alternative classical optimizer that can be used in VQE. Gradient descent evaluates the gradient of the energy, $\boldsymbol{\nabla} f(\mathbf{x})$, at the current step's ansatz parametrization $\mathbf{x}_i$, then selects the next step's ansatz parametrization $\mathbf{x}_{i+1}$ according to

$$\mathbf{x}_{i+1} = \mathbf{x}_i - \eta \boldsymbol{\nabla} f(\mathbf{x}_i) \quad , \tag{2.2}$$

where η is a learning rate that controls the convergence of the gradient descent. Convergence to a local minimum can be guaranteed by the use of backtracking, where η is steadily decreased during the course of the calculation [107]. Alternatively, the step size can be selected by using Bayesian optimization to perform a line search [108]. In applications to VQE, the gradient can be computed on a quantum processor by making use of parameter

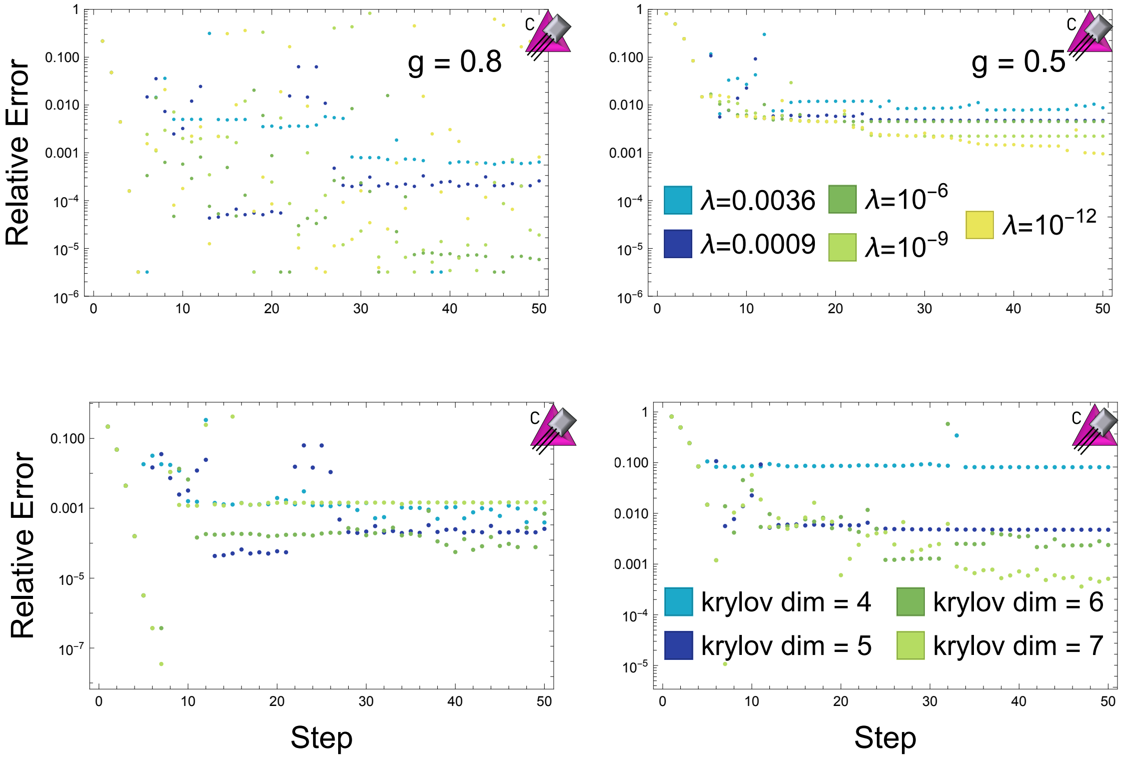

Figure 2.2: The relative error in the estimation of the vacuum energy obtained by performing a classical simulation of VQE using Bayesian optimization for a single plaquette with $p, q \leq 3$. The left panel is for $g = 0.8$ and the right panel is for $g = 0.5$. The top panel shows the results of Bayesian optimization as a function of the number of iterations of the optimization for different values of the regulator λ. Each of the calculations in the top panel was initialized with the vacuum states obtained from the Lanczos algorithm with subspace of Krylov dimension equal to 5. The bottom panel shows the result of Bayesian optimization using $\lambda = 0.0009$ with different maximum Krylov dimensions.

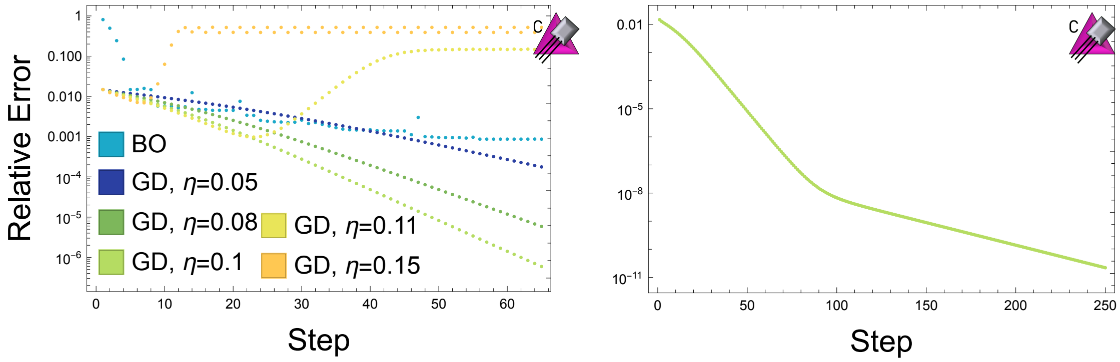

Figure 2.3: The relative error in the estimation of the vacuum energy obtained by performing a classical simulation of VQE for a single plaquette with $p, q \leq 3$. The coupling is $g = 0.5$ and the initial state was obtained from the Lanczos algorithm using a Krylov dimension of 5. The left panel shows a comparison of the results obtained by performing VQE using a Bayesian optimizer to those obtained by performing VQE using a numerical gradient descent for different learning rates η. The right panel shows the results of 250 iterations of gradient descent with $\eta = 0.1$.

shift formulas which give the gradient without discretization errors due to large shift size [109]. The use of gradient descent as the classical optimizer in VQE will require the energy of the state to be calculated on the quantum processor a number of times equal to two times the number of parameters in the circuit ansatz per step in the optimization. For comparison, Bayesian optimization only requires the energy to be computed once per step. The increase in quantum resources per step in the optimization may be offset by a faster rate of convergence and ability to converge to the actual vacuum state. As an optimizer, gradient descent also requires fewer classical resources per step than Bayesian optimization. This is because with gradient descent, the classical computer only needs to perform subtraction during gradient descent. Bayesian optimization, on the other hand, requires the computations of determinants and inverses of a matrix whose dimension is equal to the number of times the energy was previously evaluated.

Fig. 2.3 compares, for a single plaquette truncated at $p, q \leq 3$ and with $g = 0.5$, the results of using Bayesian optimization for the classical optimizer to those of using numerically-computed gradient descent. The Bayesian optimizer shown in this plot was run with $\lambda = 10^{-12}$. Both optimizers were initialized with the vacuum obtained using the Lanczos algorithm with a Krylov dimension of 5. As this plot shows, the Bayesian optimizer converges above the vacuum energy, while VQE using gradient descent with a sufficiently small η is limited only by the number of steps performed in the optimization. To understand if VQE can offer a quantum advantage, it is helpful to know how many steps in the optimizer must be performed to reach a certain level of accuracy. Fig. 2.4 shows the number of steps needed for a backtracking gradient descent to converge for a single plaquette with a truncation of $p, q \leq 31$. This truncation was chosen so that the relative error in the mass gap and the vacuum expectation of the plaquette operator due to field truncation was $\leq 1\%$ for each coupling studied. The left panel shows that as g is decreased, the number of steps needed by the gradient descent algorithm to start from the electric vacuum and reach a state $|\psi\rangle$ with $|\langle \text{Vacuum}|\psi\rangle|^2 \geq 0.999$ scales as $O(g^{-4})$. The number of steps needed to reach this level of accuracy can be decreased by beginning the optimization at a state closer to the vacuum, such as a state obtained from the Lanczos algorithm. The right panel in Fig. 2.4 shows the number of steps needed by a backtracking gradient descent to converge to $|\langle \text{Vacuum}|\psi\rangle|^2 \geq 0.999$ for a coupling $g = 0.1$ as a function of the dimension of the Krylov subspace used in the Lanczos algorithm to initialize the starting state. From the fit in the right panel, it appears that the number of steps required for the gradient descent to converge scales asymptotically as a Gaussian as a function of the Krylov dimension used. This is expected, as the discussion in the previous section showed that the error in the state obtained from the Lanczos algorithm falls off asymptotically as a Gaussian as a function of the Krylov dimension. By beginning in a state obtained from the Lanczos algorithm and performing the optimization step using gradient descent, classical simulations of the VQE algorithm are able to reach the vacuum state of a single plaquette at weak couplings that are beyond the reach of Bayesian optimization. Based on these results, Bayesian optimization will not be a practical optimizer for VQE calculations at scale, while gradient based methods have a chance of reaching the vacuum state at scale.

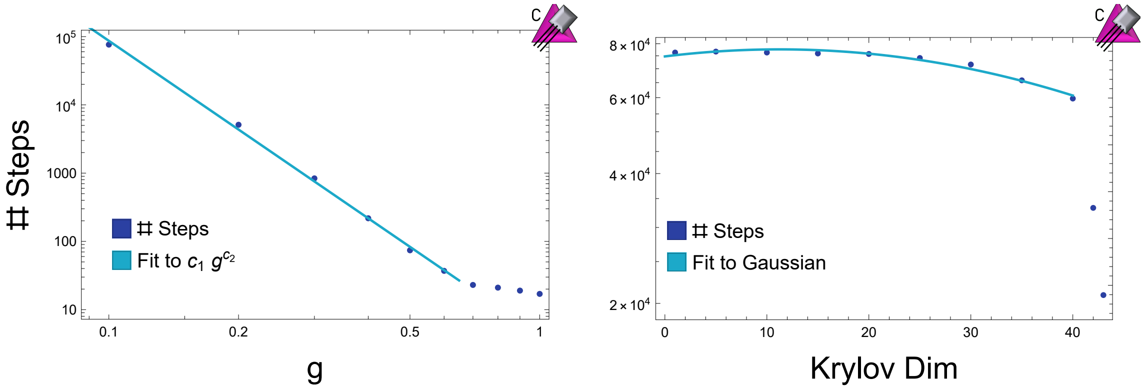

Figure 2.4: The left panel shows the number of steps needed for VQE using a backtracking gradient descent to converge to the true vacuum with an accuracy of 0.999 as a function of coupling for a single plaquette with $p, q \leq 31$. The right panel shows the number of steps needed for a backtracking gradient descent to converge to the true vacuum with an accuracy of 0.999 for $g = 0.1$ as a function of the dimension of the Krylov subspace used to obtain the initial state.

2.2.3 Hardware Implementation

The discussion in the previous section suggests that VQE should be capable of preparing the vacuum state for a single plaquette. However, existing quantum hardware suffers from the effects of noise and imperfect gate implementations. This will have an impact on how VQE performs in practice. To understand how near-term hardware will perform in the simulation of SU(3) lattice Yang-Mills theory, IBM's `Manila` superconducting quantum processor was used to perform a VQE calculation for a single plaquette [110].

The SU(3) lattice Yang-Mills Hamiltonian possesses a CP symmetry that guarantees that the amplitude of a given representation in the vacuum wavefunction will be the same as the amplitude of the conjugate representation. In principle, this symmetry can be used to restrict the state preparation circuit used in VQE which will reduce the number of free parameters. However, in the presence of noise and imperfect gate implementations, attempting to explicitly enforce the symmetry may prevent the actual state prepared on the quantum processor from respecting the symmetry. This would be the case if, hypothetically, the rotations in the circuit suffered from a constant offset error that was not corrected for. To understand if this is an issue on existing hardware, a single plaquette was simulated in the global basis truncated at a representation of **8**. The Hamiltonian is given by Eq. (14) of Ref. [111]. A VQE state preparation procedure described in Appendix .2.1 was

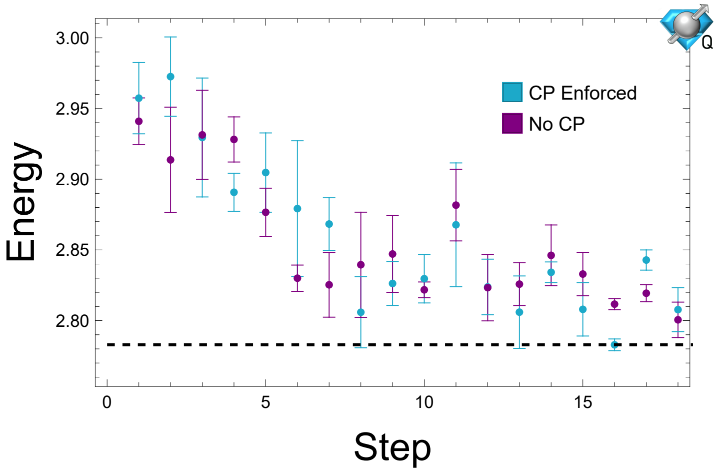

Figure 2.5: Variational state preparation of the vacuum state for a single plaquette truncated at **8** with $g = 1$ run on the `Manila` quantum processor. The blue points show the results of gradient descent with CP symmetry enforced in the rotation angles in the ansatz circuit and the purple points show the result of not explicitly enforcing CP symmetry in the state.

used to prepare the vacuum state starting from the electric vacuum and to optimize the angles using gradient descent. VQE was performed both by enforcing CP symmetry in the rotation angles in the circuit ansatz and by allowing all three of the angles to vary freely. The results of both calculations are displayed in Fig. 2.5. As this figure shows, explicitly enforcing the CP symmetry in the VQE calculation does not break the symmetry in the vacuum state prepared using VQE on this hardware. The ability to explicitly enforce CP symmetry in the ansatz circuit will be helpful when performing VQE calculations on larger systems where the number of free parameters is much greater.

As discussed in Section 2.2.1, the Lanczos algorithm can be used to obtain an initial ansatz for the VQE algorithm. At a coupling of $g = 1$, the vacuum state obtained using a two dimensional Krylov subspace has an overlap with the true vacuum within experimental errors on the `Manila` chip [110]. To accurately reproduce physics at a lower coupling, more electric field representations must be included. This can be done without increasing the qubit count by performing a calculation in the color parity basis. Using two qubits, the color parity basis allows the **6** and $\bar{\mathbf{6}}$ representations to be included, which is sufficient to accurately describe a plaquette with a coupling of $g = 0.8$. Fig. 2.6 shows the results of performing VQE for a single plaquette with $g = 0.8$ in the color parity basis, beginning both at the electric vacuum and the vacuum obtained using a Krylov subspace of dimension two. As this figure shows, pre-conditioning with the vacuum obtained using the Lanczos

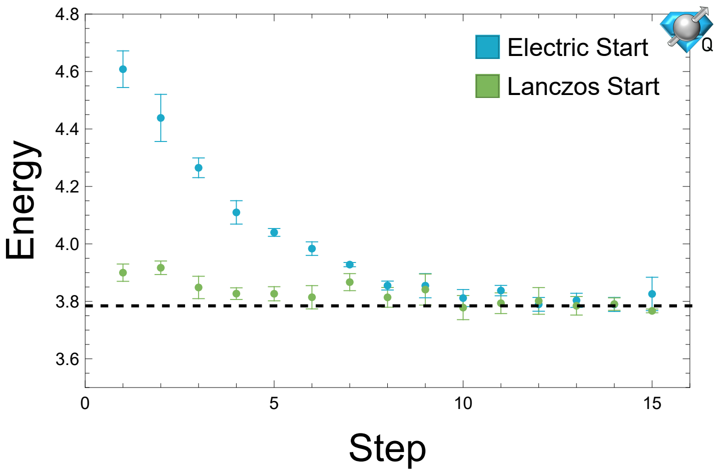

Figure 2.6: Variational state preparation of the vacuum state for a single plaquette truncated at $\mathbf{6}^+$ in the color parity basis with $g = 0.8$ run on the `Manila` quantum processor. The blue points show the result of gradient descent beginning at the electric vacuum and the green points begin at the state obtained using the Lanczos algorithm with a Krylov dimension of two.

algorithm allows one to begin closer to the actual vacuum and to converge to the true vacuum faster. Note that in both Fig. 2.5 and 2.6, the energy computed fluctuates at late steps in the gradient descent instead of converging. This is because the gradient is computed on the `Manila` chip with both statistical and systematic errors. As the optimizer approaches the vacuum state, the magnitude of the gradient vector decreases. Once the size of the gradient vector is comparable to the device errors, it can no longer be reliably computed and the updates to the circuit parameters are random noise which leads to the displayed fluctuations. This is a generic feature of having uncertainties in the computation of the gradient and will have to be considered when devising stopping criterion for VQE calculations of larger systems.

2.3 Multiple Plaquettes

The single plaquette calculations in Section 2.2 provide insight into the requirements of state preparation in a simple system. To perform calculations at scale, these insights need to be combined with features that only occur on larger lattices, such as Gauss's law constraints that can't be solved exactly without sacrificing locality. The Lanczos algorithm provides a good starting ansatz for VQE on a single plaquette, but it is inefficient on larger lattices.

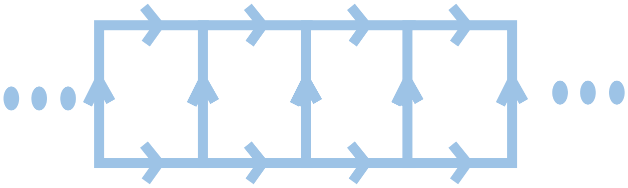

Figure 2.7: A lattice composed of a chain of plaquettes.

This can be seen by using the electric vacuum as the initial state for a chain of L plaquettes with periodic boundary conditions (PBC) as shown in Fig. 2.7. When a Krylov subspace with dimension d is used, every basis state with d plaquettes excited to have a loop of electric fields in the **3** representation will occur with equal amplitude. There are $\binom{L}{d}$ of these states and their superposition requires non-local circuits to capture the non-local correlations in the state. This leads to the circuit required to prepare the state given by the Lanczos algorithm growing exponentially in size with the Krylov dimension, and therefore no quantum advantage. An alternative approach is to use a form of domain decomposition.

In lattice QCD calculations on classical computers, a large amount of time is spent solving discretized versions of the Dirac equation. These calculations have been accelerated by making use of a domain decomposition [112, 113, 114]. Domain decomposition accelerates the calculation by solving the Dirac equation in separate sub-regions and then stitching the solutions together. Similar to solving the Dirac equation, directly preparing the vacuum state for a theory on a large lattice is difficult because the Hilbert space associated with the entire lattice is too large to efficiently work with. The ideas behind domain decomposition can be applied in a VQE calculation by splitting the lattice into separate disconnected sub-regions and preparing each sub-region in its vacuum state (note that there will be links between these regions that will remain unexcited). The vacuum state of each sub-region can be computed classically or in another VQE calculation. The VQE algorithm can then be used to excite links in-between the sub-regions and stitch together the sub-regions to form the vacuum state for the entire lattice. SU(3) Yang-Mills is a theory with spatial correlations that decay exponentially fast with distance, so it is anticipated that the domain decomposition ansatz should converge exponentially fast to the true vacuum as the domain size is increased.

Conceptually, this approach to vacuum state preparation is similar to the density matrix renormalization group (DMRG) algorithm on classical computers [115]. In DMRG, the vacuum state of a lattice is prepared, and the density matrix of a sub-region is diagonalized. The eigenstates of the density matrix with largest weight are then used as the local basis for a calculation on a larger lattice. In this manner, DMRG constructs the vacuum state for a large lattice from the vacuum state for smaller regions. This is analogous to beginning the VQE optimization in a domain-decomposed vacuum, except the calculation on the quantum computer has no need to extract eigenstates of the density matrix for subregions. Once the desired lattice length is achieved, DMRG optimizes the approximation to the vacuum state by decomposing the system into left and right blocks and using the eigenstates of the density matrix of the subregions to generate a new basis for the regions. By growing and shrinking the size of the left and right blocks, DMRG is able to converge to the true vacuum state. The process of growing and shrinking the blocks used is analogous to the stitching procedure described in this work to improve the overlap with the true vacuum, except, once again, the quantum calculation does not require the diagonalization of density matrices.

While this stitching procedure will be explicitly demonstrated for a quasi one dimensional system, it can be performed in higher dimensions as well. For a system with three spatial dimensions, the sub-regions initialized in their vacuum state will be cubes of some size. Unlike in one dimension, the number of links left unexcited between the initial subregions will scale as the surface area of the subregions. A sequence of unitary transformations acting on the individual unexcited links, controlled by their neighboring links on the two cubes they connect, can be optimized using VQE to get closer to the vacuum state of the entire lattice. By limiting the number of links each unitary acts on in this manner, the number of free parameters in the VQE ansatz circuit can be restricted to grow linearly with the surface area instead of exponentially as it could if all links were allowed to be acted on simultaneously.

2.3.1 Domain Decomposition on Plaquette Chains

A lattice composed of a chain of plaquettes as shown in Fig. 2.7 with PBC displays many of the complications inherent to larger lattices while still being tractable to simulate on classical computers. A domain decomposition of a plaquette chain can be performed by breaking up the lattice into separate sub-chains, preparing each subchain in its vacuum state and using VQE to optimize circuits that act on the boundaries and space between the domains to stitch them together.

To be useful as an initial state for VQE, a quantum circuit for the preparation of these domain-decomposed vacuums must be designed. The circuit to prepare the vacuum state for

	State 1	State 2
R_1	$\left\lvert\chi\begin{pmatrix}\mathbf{1},\mathbf{1},\mathbf{1}\\ \mathbf{1},\mathbf{1}\\ \mathbf{1},\mathbf{1},\mathbf{1}\end{pmatrix}\right\rangle$	$\left\lvert\chi\begin{pmatrix}\mathbf{1},\mathbf{3},\mathbf{1}\\ \mathbf{3},\bar{\mathbf{3}}\\ \mathbf{1},\bar{\mathbf{3}},\mathbf{1}\end{pmatrix}\right\rangle$
R_2	$\left\lvert\chi\begin{pmatrix}\mathbf{3},\mathbf{1},\mathbf{1}\\ \bar{\mathbf{3}},\mathbf{1}\\ \bar{\mathbf{3}},\mathbf{1},\mathbf{1}\end{pmatrix}\right\rangle$	$\left\lvert\chi\begin{pmatrix}\mathbf{3},\mathbf{3},\mathbf{1}\\ \mathbf{1},\bar{\mathbf{3}}\\ \bar{\mathbf{3}},\bar{\mathbf{3}},\mathbf{1}\end{pmatrix}\right\rangle$
R_3	$\left\lvert\chi\begin{pmatrix}\mathbf{3},\mathbf{1},\mathbf{1}\\ \bar{\mathbf{3}},\mathbf{1}\\ \bar{\mathbf{3}},\mathbf{1},\mathbf{1}\end{pmatrix}\right\rangle$	$\left\lvert\chi\begin{pmatrix}\mathbf{3},\bar{\mathbf{3}},\mathbf{1}\\ \mathbf{3},\bar{\mathbf{3}}\\ \bar{\mathbf{3}},\mathbf{3},\mathbf{1}\end{pmatrix}\right\rangle$
R_4	$\left\lvert\chi\begin{pmatrix}\mathbf{1},\mathbf{1},\mathbf{3}\\ \mathbf{1},\bar{\mathbf{3}}\\ \mathbf{1},\mathbf{1},\bar{\mathbf{3}}\end{pmatrix}\right\rangle$	$\left\lvert\chi\begin{pmatrix}\mathbf{1},\mathbf{3},\mathbf{3}\\ \bar{\mathbf{3}},\mathbf{1}\\ \mathbf{1},\bar{\mathbf{3}},\bar{\mathbf{3}}\end{pmatrix}\right\rangle$
R_5	$\left\lvert\chi\begin{pmatrix}\mathbf{1},\mathbf{1},\mathbf{3}\\ \mathbf{1},\bar{\mathbf{3}}\\ \mathbf{1},\mathbf{1},\bar{\mathbf{3}}\end{pmatrix}\right\rangle$	$\left\lvert\chi\begin{pmatrix}\mathbf{1},\bar{\mathbf{3}},\mathbf{3}\\ \bar{\mathbf{3}},\mathbf{3}\\ \mathbf{1},\mathbf{3},\bar{\mathbf{3}}\end{pmatrix}\right\rangle$
R_6	$\left\lvert\chi\begin{pmatrix}\mathbf{3},\mathbf{3},\mathbf{3}\\ \mathbf{1},\mathbf{1}\\ \bar{\mathbf{3}},\bar{\mathbf{3}},\bar{\mathbf{3}}\end{pmatrix}\right\rangle$	$\left\lvert\chi\begin{pmatrix}\mathbf{3},\mathbf{1},\mathbf{3}\\ \bar{\mathbf{3}},\mathbf{3}\\ \bar{\mathbf{3}},\mathbf{1},\bar{\mathbf{3}}\end{pmatrix}\right\rangle$
R_7	$\left\lvert\chi\begin{pmatrix}\mathbf{3},\bar{\mathbf{3}},\bar{\mathbf{3}}\\ \mathbf{3},\mathbf{1}\\ \bar{\mathbf{3}},\mathbf{3},\mathbf{3}\end{pmatrix}\right\rangle$	$\left\lvert\chi\begin{pmatrix}\mathbf{3},\mathbf{1},\bar{\mathbf{3}}\\ \bar{\mathbf{3}},\bar{\mathbf{3}}\\ \bar{\mathbf{3}},\mathbf{1},\mathbf{3}\end{pmatrix}\right\rangle$

Table 2.1: This table enumerates the local Givens rotations required to initialize a domain vacuum on the plaquette chain truncated at an electric field representation of **3**, (up to CP conjugates of the rotations listed here). The first column labels the rotation and the other two columns specify the basis states being rotated. R_1 excites a single plaquette loop of electric flux. R_2 through R_5 stretch the length of a loop of electric flux by one plaquette. R_6 and R_7 break a loop of electric flux into two loops. The basis labels used here were introduced in Ref. [111].

a domain of length l can be constructed recursively from the circuit to prepare the vacuum state for a domain of length $l-1$ as follows. A single plaquette state can be constructed by performing an R_1 rotation from Table 2.1 and its CP conjugate on the qubits that make up the links in the plaquette. The two plaquette state can be prepared by applying R_1 rotations on two neighboring plaquettes and then applying R_3 and R_4 rotations on one of the plaquettes. The circuit that prepares the three plaquette vacuum state can then be constructed by exciting a third plaquette (i.e. apply an R_1 rotation), stretching over the previous two plaquettes (i.e. apply R_3 and R_4 rotations to the plaquettes that have been excited), and performing a rotation on the center plaquette to de-excite it (i.e. apply R_6 and R_7 rotations to the center plaquette). In general, the circuit to prepare a domain of size l can be constructed from the circuit for a domain of size $l-1$ by exciting a neighboring plaquette, stretching it over the previous domain, and then de-exciting plaquettes in the center. In general, this approach to constructing circuits for a domain state scales exponentially with the size of the domain.

The initial domain decomposition ansatz can be improved upon by stitching together the different domains. More specifically, in the circuit that prepares the vacuum ansatz, gates R_1 through R_7, along with their CP conjugates, can be applied to the plaquettes in-between the domains and VQE can be used to optimize the rotation angles. This stitching procedure can also be used to construct the vacuum for a larger domain instead of using the generic state preparation circuit. After performing the stitching, the overlap with the true vacuum can be increased further by layering another block of gates on the original domains and optimizing the angles with VQE again. Explicitly, if the state obtained from the VQE algorithm is $S(\vec{\theta}_2)D(\vec{\theta}_1)\left|0\right\rangle$, where $D(\vec{\theta}_1)$ prepares the states on the domain and $S(\vec{\theta}_2)$ stitches the domains together, then the ansatz state

$$C(\vec{\theta}_1,\vec{\theta}_2,\vec{\theta}_3)\left|0\right\rangle = D(\vec{\theta}_3)S(\vec{\theta}_2)D(\vec{\theta}_1)\left|0\right\rangle \tag{2.3}$$

can be prepared on the quantum processor and the energy can be minimized as a function of $\vec{\theta}_1$, $\vec{\theta}_2$ and $\vec{\theta}_3$ using the VQE algorithm. Due to the exponentially decaying correlations in SU(3) Yang-Mills, the overlap with the true vacuum should increase exponentially with the number of additional gate layers stacked on the domains and their boundaries.

A plaquette chain simulated in the multiplet basis with chromo-electric fields truncated at the **3** representation will be used to test the performance of the domain decomposition ansatz. Finite and infinite plaquette chains were studied using an MPS representation of states in the TEBD algorithm as described in Appendix .2.3. Fig. 2.8 shows the results of optimizing different domain decomposition ansatzes for a chain of five plaquettes with $g=0.9$ and open boundary conditions. Fig. 2.9 shows the expectation of the electric energy

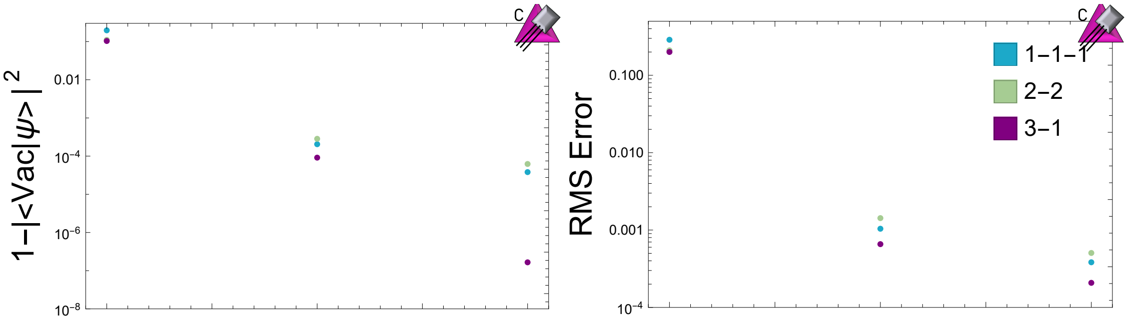

Figure 2.8: The left panel shows the overlap of different domain decompositions with the true vacuum. The right panel shows the RMS error in the expectation of the different single plaquette operators on the five plaquette lattice with open boundary conditions. The left-most points show the results for the initial domain decomposition, the middle points show the result after using VQE to stitch the boundaries of the domains together, and the right points show the results after using VQE to optimize another layer of circuits on the domains after stitching.

for the initial single plaquette ansatz and the state obtained after stitching the boundaries together with VQE. As the size of the initial domains is increased, the overlap with the actual vacuum increases. However, the improvement eventually saturates due to boundary effects. Due to the short correlation length at this coupling, even a single layer of stitching is able to achieve a high overlap with the actual vacuum.

To understand how the domain decomposition VQE ansatz performs for a large lattice, the time evolving block decimation algorithm was used to prepare the vacuum state and simulate VQE on an infinite plaquette chain as described in Appendix .2.3. VQE was performed using gradient descent as the classical optimizer. The vacuum expectation of a single plaquette operator was chosen as a test observable to study the convergence to the true vacuum. As Fig. 2.10 shows, the vacuum expectation of the plaquette operator converges exponentially fast with the domain size. A classically simulated version of VQE was used to simulate the stitching of small domains together. For domains of lengths 1-4 plaquettes, the initial domain vacuum was prepared using a generic state preparation circuit. For the initial domain of length five, the circuit to prepare the vacuum was constructed by stitching together a vacuum state preparation circuit for a domain of length three plaquettes and of length one plaquette. The circuit optimized in VQE consisted of the initial domain vacuum circuit, along with all rotations in Table 2.1 with all rotation angles allowed to vary

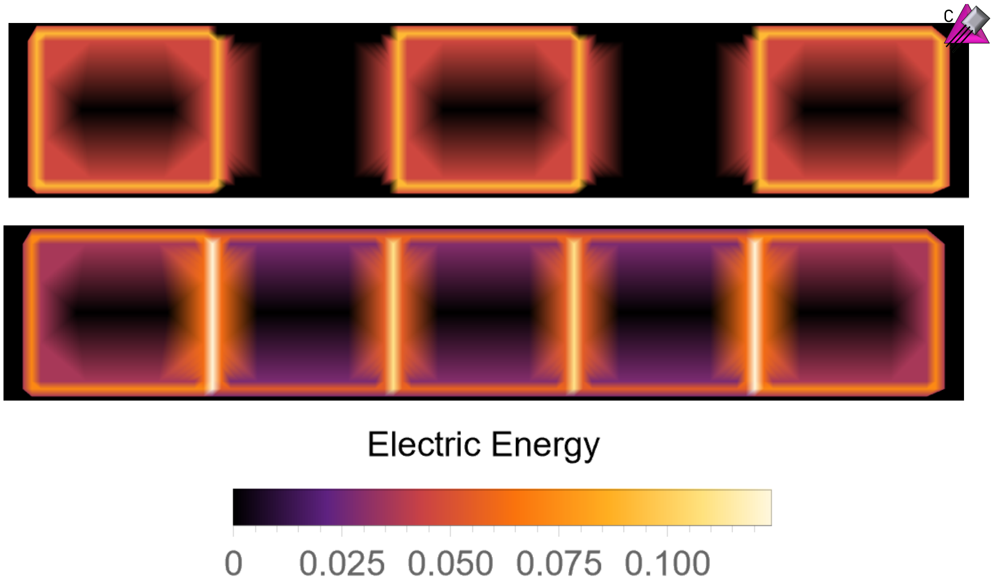

Figure 2.9: The top panel shows the expectation of the electric energy for a five plaquette chain with open boundary conditions where every other plaquette has been initialized to the single plaquette vacuum. The bottom panel shows the expectation of the electric energy after the boundaries of the initial domains have been stitched together with VQE.

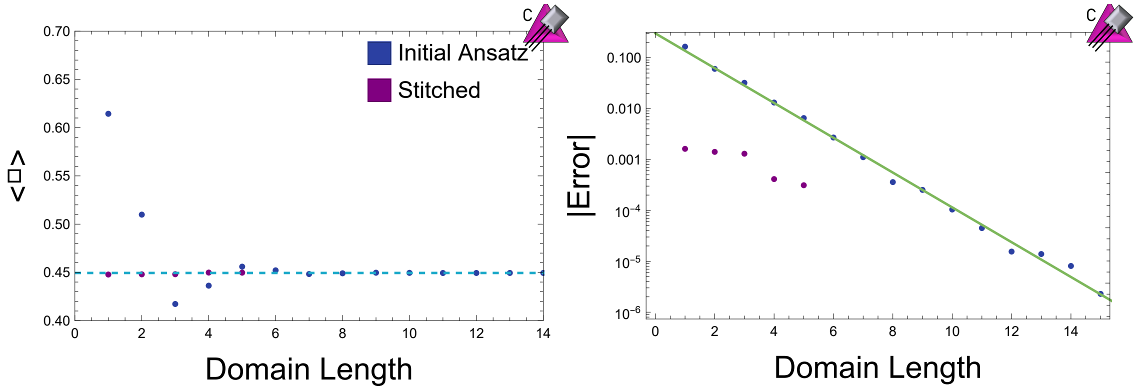

Figure 2.10: The left panel shows the expectation of a plaquette operator at the center of a domain as a function of domain length for both the initial ansatz and the state after using VQE to stitch domains together. The dashed blue line shows the vacuum expectation of a single plaquette operator on an infinite chain of plaquettes with $g = 0.9$. The right panel shows the error in the vacuum plaquette expectation as a function of the domain size.

freely. For each domain size, the optimization of the stitching improved the estimation of the vacuum plaquette expectation by at least an order of magnitude.

2.3.2 Hardware Implementation

As with the single plaquette case, it is instructive to study multiple plaquettes on existing quantum hardware. Unfortunately, simulating multiple plaquettes in a local basis as described in the previous section is beyond the reach of existing hardware. However, these techniques can be applied to state preparation in a global basis. IBM's `Manila` quantum processor was used to simulate a two plaquette system truncated at an electric field representation of **3** in the global CP invariant basis [110]. For this simple system, preparing the single plaquette vacuum is equivalent to using the vacuum state obtained using the Lanczos algorithm with a Krylov dimension of two. The results of performing VQE with the error mitigation procedures described in Appendix .2.1 are shown in Fig. 2.11. As this figure shows, the VQE algorithm is able to converge to the true vacuum energy whether it begins in the electric or single plaquette vacuum. However, by initializing the state in the single plaquette vacuum, the VQE algorithm is able to converge to the true vacuum state faster. While the two initial states converge to the same vacuum state, the uncertainties in the vacuum energy they converge to are quite different. This is due to the circuit ansatz used to initialize the state having redundancies in the angle parametrization of the state, leading to

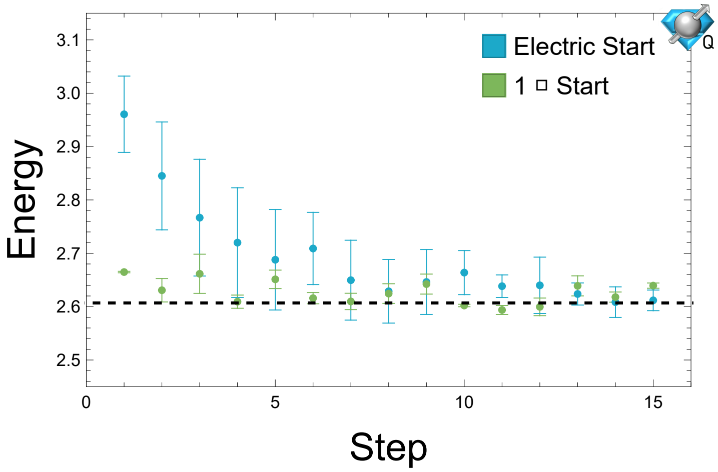

Figure 2.11: Variational state preparation of the vacuum state for a two plaquette system with $g = 1$ and PBC run on the IBM `Manila` quantum processor. The blue points show the results of performing gradient descent beginning at the electric vacuum and the green points show the results for beginning with the single plaquette vacuum.

the two initial ansatzes converging to different sets of angles describing the same state. In the absence of noise on the quantum processor, these parametrizations would be equivalent. However, existing quantum processors are noisy and there are systematic errors with angle dependence leading to the different error bars shown in Fig. 2.11.

2.4 Discussion

Achieving a quantum advantage in the simulation of lattice gauge theories requires the preparation of physically interesting states, such as the vacuum. In the NISQ era, hybrid algorithms such as VQE will be essential. To make use of VQE, an appropriate classical optimizer and ansatz circuit must be chosen. In this work, state preparation on simple SU(3) lattice gauge theories has been performed with an eye towards scalability. In the variational state preparation of single plaquette systems, we showed that Bayesian optimization suffers from convergence issues as the coupling g is decreased, while gradient descent methods suffer from no such issue. This suggests that VQE calculations at scale may need to make use of gradient descent methods in order to converge, despite the increase in computational overhead required to compute the gradient. Note that gradient based methods may converge to a local minimum instead of the true vacuum. This has not occurred for the simple systems studied in this work, but may need to be considered when performing calculations at scale.

Calculations at scale will also require appropriate ansatz circuits to perform VQE. Due to the exponential growth of the Hilbert space with lattice size, circuits capable of preparing a generic state on the lattice will not be able to go to scale. In this work, it was demonstrated that in a quasi-1D SU(3) lattice gauge theory, VQE can be used to stitch together domains in their vacuum state to prepare the vaccum state of a larger lattice. The exponential convergence with domain size on an infinite lattice suggests that even shallow circuits may be able to achieve a large overlap with the true vacuum state at scale. The calculations on IBM's `Manila` quantum processor showed that circuit ansatzes that respect a global symmetry will still respect the global symmetry on existing hardware despite the presence of noise and imperfect gates. This allows global symmetries to be used to construct circuit ansatzes that have fewer free degrees of freedom which makes them easier to optimize.

While the computations in this work are encouraging, preparing a vacuum state for QCD with VQE will require significant developments in the application of quantum algorithms to lattice gauge theories. The calculations performed in this work were for a one dimensional string of plaquettes, but QCD is a three-dimensional theory. In a 3D theory, the domains being initialized in their vacuum state will be 3D blocks and the number of circuits required to stitch them together will scale with the surface area of the domain blocks. Additionally, a QCD calculation that can be taken to the continuum limit may require more electric field representations to be included, which will increase the number of possible local rotations in the VQE stitching circuit. It is conceivable that it is possible to reach the continuum limit without increasing the field truncation, but this remains to be investigated. Regardless, as the continuum limit is approached, the correlation length of the system will diverge and more layers of circuits will be required in the VQE stitching to accurately prepare the vacuum state. Matter will also need to be included at the sites, which will complicate the integrating out of the internal gauge space. In addition to these conceptual complications, achieving a quantum advantage in the simulation of lattice QCD will require quantum hardware with more qubits and a lower error rate, in order to enable the simulation of a large lattice in a local basis. While scaling up quantum hardware is challenging, the rapid improvement in quantum hardware and recent proposals for co-design [111, 99, 116] of quantum processors suggest that it can be done in a manner that will allow the simulation of lattice QCD on quantum computers in the near future.

Chapter 3

QUANTUM SIMULATION OF LATTICE QCD WITH IMPROVED HAMILTONIANS

3.1 Introduction

The limitations of quantum hardware has limited quantum simulation of non-Abelian gauge theories to small system sizes. Theoretical studies have been performed into how to scale up these calculations to larger systems [14, 117, 118, 119, 120, 121, 70, 122, 123, 124, 125, 126, 127, 128, 129, 130, 131]. However, all these approaches to simulating gauge theories require the gauge field to be truncated and scale poorly with the gauge field truncation. Similar problems were found in the classical simulation of lattice gauge theories with the scaling of errors with lattice spacing. These problems were mitigated through the development of improved Symanzik actions with more favorable scaling of errors with lattice spacing [28]. It is expected that improved Hamiltonians can be found that mitigate the effects of truncating the gauge field as well.

In this chapter, improved Hamiltonians are derived for lattice gauge theories through the application of the similarity renormalization group (SRG). SU(3) gauge fields coupled to fermions in 1+1D are used as a case study for the improved Hamiltonians studied. Tensor network simulations are used to demonstrate that the improved Hamiltonians derived in 1+1D correctly reproduce observables on large lattices. An improved Hamiltonian for lattice QCD with two flavors is derived for 3+1D and a small simulation is performed on IBM's quantum processors.

3.2 1+1D

3.2.1 1+1D Hamiltonian

In this chapter, the SU(3) Kogut-Susskind Hamiltonian [13] with a single flavor of staggered fermions in $1+1D$ will be used as a toy model to study the effects of gauge field truncation and the performance of improved Hamiltonians. Previous one dimension quantum simulations have studied the dynamics of hadrons [102, 132, 133] and β decay [134].

The Hamiltonian describing this theory is

$$\begin{aligned}
\hat{H} &= \hat{H}_{Kin} + \hat{H}_m + \hat{H}_E \\
\hat{H}_{Kin} &= \sum_{x,a,b} \frac{1}{2} \hat{\psi}^\dagger_{x,a} \hat{U}^{a,b}_{x,x+1} \hat{\psi}_{x+1,b} + \text{h.c.} \\
\hat{H}_m &= m \sum_{x,a} (-1)^x \hat{\psi}^\dagger_{x,a} \hat{\psi}_{x,a} \\
\hat{H}_E &= \sum_{x,c} \frac{g^2}{2} \hat{E}^c_{x,x+1} \hat{E}^c_{x,x+1} \quad ,
\end{aligned} \tag{3.1}$$

where g is the gauge coupling, m is the fermion mass, $\hat{\psi}_{x,a}$ is the fermion field at site x with color a, $\hat{U}^{a,b}_{x,x+1}$ is the parallel transporter on the link between the sites $x, x+1$ and $\hat{E}^c_{x,x+1}$ is the chromo-electric field operator. By working with open boundary conditions in the axial gauge, and enforcing Gauss's law, the gauge fields in this theory can be completely integrated out yielding the Hamiltonian

$$\begin{aligned}
\hat{H} &= \hat{H}_{Kin} + \hat{H}_m + \hat{H}_E \\
\hat{H}_{Kin} &= \sum_{x,a} \frac{1}{2} \hat{\psi}^\dagger_{x,a} \hat{\psi}_{x+1,a} + \text{h.c.} \\
\hat{H}_m &= m \sum_{x,a} (-1)^x \hat{\psi}^\dagger_{x,a} \hat{\psi}_{x,a} \\
\hat{H}_E &= \sum_{x,c} \frac{g^2}{2} \left(\sum_{y<x} \hat{Q}^c_y \right) \left(\sum_{y<x} \hat{Q}^c_y \right) \quad ,
\end{aligned} \tag{3.2}$$

where $\hat{Q}^c_y$ is the chromo-electric charge at site x defined by

$$\hat{Q}^c_y = \sum_{a,b} \hat{\psi}^\dagger_{y,a} T^c_{a,b} \hat{\psi}_{y,b} \quad , \tag{3.3}$$

where $T^c_{a,b}$ are the Gell-Mann matrices. By working with this Hamiltonian, we can directly study the untruncated theory and the performance of improved Hamiltonians that correct for the gauge field truncation.

3.2.2 Strong Coupling Expansion $m = 0$

Before the Hamiltonian in Eq. (3.1) can be mapped onto a quantum computer, it must first be truncated to a finite Hilbert space. Typically, this is done by working in the basis of the chromo-electric field and truncating the field below some cutoff. It has been shown numerically for some small systems [27, 111, 70, 71] and rigorously proven in general [105] that the error induced by this truncation falls off exponentially with the truncation. The error due to gauge field truncation can be reduced even further by first performing a unitary rotation on the Hamiltonian to reduce the coupling to the higher electric field states and then truncating. In other words, there is a low-energy subspace coupled to a high-energy subspace and one would like to derive an effective field theory description of the low-energy subspace with the high-energy subspace decoupled. Previous work has explored how to perform this decoupling variationally [135, 136]. One alternative method to construct such an effective Hamiltonian is Schrieffer-Wolff perturbation theory which systematically constructs approximate unitary transformations that decouple the high-energy subspace [137, 138].

As an example, we will consider the Hamiltonian in Eq. (3.1) on two staggered sites (one physical site) with massless fermions, truncated at zero electric field. This is the harshest possible truncation that can be applied, and the only physical states left in the Hilbert space are those where sites are unoccupied or have three fermions present forming a color singlet, i.e., a baryon. At this truncation, the Hamiltonian in Eq. (3.1) is trivial, and there are no dynamics. The states kept in this truncation span the zero electric energy subspace while all states with higher electric energy are being discarded. Using the Schrieffer-Wolff perturbation theory, an effective Hamiltonian for the zero electric energy subspace at leading order is given by

$$\begin{aligned}\hat{H}_{eff} = \sum_x \frac{9}{16g^2}\hat{Z}_x\hat{Z}_{x+1} + \frac{27}{32g^4}\left(\hat{X}_x\hat{X}_{x+1} + \hat{Y}_x\hat{Y}_{x+1}\right) \\ + \mathcal{O}(g^{-6}) \quad ,\end{aligned} \tag{3.4}$$

where $\hat{X}_x$, $\hat{Y}_x$, $\hat{Z}_x$ are the corresponding Pauli matrices at site x on the lattice. In this basis, spin up states correspond to a site being unoccupied and spin down states correspond to a baryon being present on the site. The details of this derivation and how to systematically derive higher order terms are in Appendix .3. In this context, the Schrieffer-Wolff expansion corresponds to performing a strong coupling expansion around the zero electric energy subspace. Note that similar results have been derived for SU(2) lattice gauge theories and the Schwinger model with multiple flavors, showing that they are equivalent to spin systems in the strong coupling limit [139, 140, 141].

The effective Hamiltonian in Eq. (3.4) requires only a single qubit per site to be mapped onto a quantum computer. The Hamiltonian in Eq. (3.2) with gauge fields integrated out requires three qubits per site to represent the state of the system. By using this effective Hamiltonian to describe a subspace of the system, the computational resources required are reduced. However, the Schrieffer-Wolff expansion is known to have a finite radius of convergence [138], so this effective Hamiltonian should only be valid over a limited range of

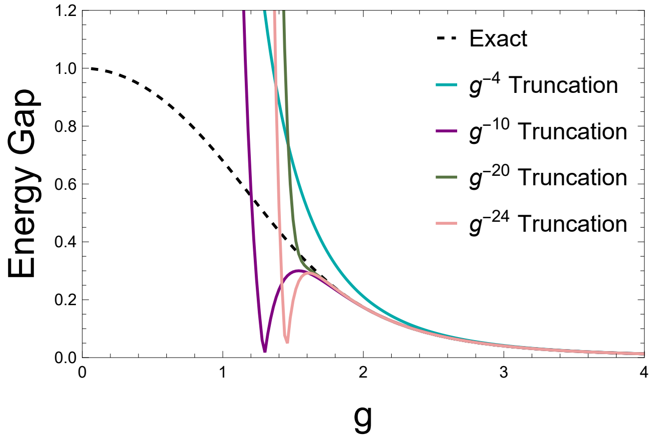

Figure 3.1: Energy gaps as a function of coupling g for the improved Hamiltonian derived with Schrieffer-Wolff perturbation theory. The black dashed curve is the energy gap of the exact Hamiltonian in Eq. (3.2) and the blue curve is the energy gap of the Hamiltonian in Eq. (3.4). The other curves correspond to including higher order terms in the Schrieffer-Wolff expansion of the improved Hamiltonian.

couplings. The energy gap for the effective Hamiltonians obtained at different orders in the Schrieffer-Wolff expansion over a range of couplings are shown in Fig. 3.1. Note that both the ground state and first excited state are in the baryon number zero sector. As this figure shows, the effective Hamiltonians obtained through the Schrieffer-Wolff expansion are only valid for strong couplings, and the expansion fails to converge at weak couplings.

3.2.3 Similarity Renormalization Group $m = 0$

The strong coupling expansion in the previous section was able to yield an improved Hamiltonian to correct for the chromo-electric field truncation for a small system. However, the performance of the improved Hamiltonian was limited by the convergence of the strong coupling expansion. An alternative approach to derive an improved Hamiltonian is the SRG. This method works by choosing a generator of unitary rotations that should decouple the high energy subspace and then continuously flowing to decouple the high energy subspace [142, 143, 144]. Explicitly the Hamiltonian being flowed is parametrized as

$$\hat{H}_s = \hat{H}_\Lambda + \hat{V}_s \quad , \tag{3.5}$$

where $\hat{H}_\Lambda$ determines the energy scales that should be decoupled, $\hat{V}_s$ is the remaining terms in the Hamiltonian and s is the flow parameter. The generator of the SRG flow is traditionally taken to be

$$\hat{\eta}_s = [\hat{H}_\Lambda, \hat{H}_s] \quad . \tag{3.6}$$

The evolution of the Hamiltonian under SRG is given by

$$\begin{aligned} \frac{d\hat{H}_s}{ds} = \frac{d\hat{V}_s}{ds} &= [[\hat{H}_\Lambda, \hat{V}_s], \hat{H}_s] \\ &= [[\hat{H}_\Lambda, \hat{V}_s], \hat{H}_\Lambda] + [[\hat{H}_\Lambda, \hat{V}_s], \hat{V}_s] \quad . \end{aligned} \tag{3.7}$$

By flowing to $s \to \infty$, the low and high energy sectors will be decoupled.

The similarity renormalization group has previously been used in low energy nuclear physics to derive low energy nuclear potentials with improved convergence properties [145]. In the following sections, it will be shown how the SRG can be used to derive improved Hamiltonians that correct for the effects of gauge field truncation.

Two Staggered Sites

Once again, the Hamiltonian in Eq. (3.1) on two staggered sites (one physical site), truncated at zero electric field will be used as an example to construct an improved Hamiltonian. The generator of the SRG flow will be chosen to decouple states with different electric energies, i.e. $\hat{H}_\Lambda = \hat{H}_E$. The SRG equations can then be solved to recover an improved Hamiltonian of the form

$$\hat{H}_{SRG} = A(g) \left(\hat{X}_1 \hat{X}_2 + \hat{Y}_1 \hat{Y}_2 \right) + B(g) \hat{Z}_1 \hat{Z}_2 \quad , \tag{3.8}$$

where $A(g)$ and $B(g)$ are constants computed numerically. Note that this Hamiltonian takes the same form as that derived in the strong coupling expansion in Eq. (3.4) except now the coefficients multiplying the operators have been determined through SRG instead of a perturbative expansion. The energy gap for this Hamiltonian as a function of the coupling is shown in Fig. 3.2. Unlike the improved Hamiltonian obtained through the strong coupling expansion, the improved Hamiltonian obtained through the SRG suffers from no convergence issues and is able to correctly reproduce the energy gap at all values of the coupling.

Larger Systems

As shown in the previous section, the SRG was capable of producing an improved Hamiltonian that correctly describes the physics of a small system. In practice, improved Hamiltonians will be needed for larger systems. The setup of the SRG used in the previous section does not scale efficiently to larger lattices. This is because as the SRG evolves, the number

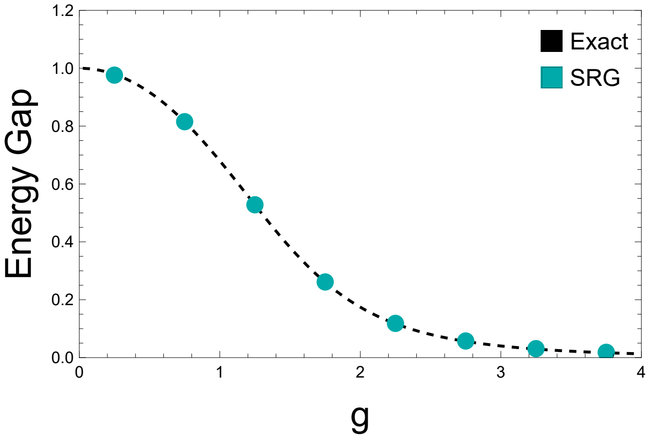

Figure 3.2: Energy gaps as a function of coupling g for the improved Hamiltonian derived with the SRG. The black dashed curve is the energy gap of the exact Hamiltonian in Eq. (3.2) and the blue points are the energy gap of the Hamiltonian in Eq. (3.8).

of operators generated can be exponential in the system size. This can be mitigated through the use of the in-medium similarity renormalization group (IMSRG) which truncates operators in the SRG flow above a certain weight [146]. The cost of performing the IMSRG scales exponentially with the size truncation. However the convergence with operator size is also exponential due to the exponential decay of correlations in low energy states.

As an explicit example, improved Hamiltonians for the zero electric field truncation will be derived with IMSRG. The smallest nontrivial operator size truncation is at two staggered sites. The improved Hamiltonian derived with IMSRG at this truncation with coupling g on L staggered sites is

$$\begin{aligned}\hat{H}_{SRG} = \sum_{x<L} & A(g)\left(\hat{X}_x\hat{X}_{x+1} + \hat{Y}_x\hat{Y}_{x+1}\right) \\ & + B(g)\hat{Z}_x\hat{Z}_{x+1} \quad .\end{aligned} \tag{3.9}$$

The accuracy of the improved Hamiltonians derived through IMSRG at this electric field truncation can be improved by computing the IMSRG flow for larger operator size truncations. In general, one would expect this method to work well when the operator size truncation used is comparable to the correlation length of the system in question. Explicitly, the form of the improved Hamiltonians obtained by truncating at operators defined on three staggered sites takes the form

$$\begin{aligned}\hat{H}_{3,SRG} =& \sum_x A_1(g)\left(\hat{X}_x\hat{X}_{x+1} + \hat{Y}_x\hat{Y}_{x+1}\right) + B_1(g)\hat{Z}_x\hat{Z}_{x+1} \\ &+ A_2(g)\left(\hat{X}_x\hat{X}_{x+2} + \hat{Y}_x\hat{Y}_{x+2}\right) + B_2(g)\hat{Z}_x\hat{Z}_{x+2}\end{aligned} \tag{3.10}$$

where $A_i(g)$, and $B_i(g)$ are constants determined from solving the SRG equations numerically. Note that this takes the same form as Eq. (3.8) just with the inclusion of next to nearest neighbor hopping. The performance of the improved Hamiltonians can be improved further by truncating the operator size at four staggered sites. The improved Hamiltonian obtained at this truncation takes the form

$$\begin{aligned}\hat{H}_{4,SRG} =& \sum_x A_1(g)\left(\hat{b}_x\hat{b}^\dagger_{x+1} + \hat{b}^\dagger_x\hat{b}_{x+1}\right) + B_1(g)\hat{Z}_x\hat{Z}_{x+1} \\ &+ A_2(g)\left(\hat{b}_x\hat{b}^\dagger_{x+2} + \hat{b}^\dagger_x\hat{b}_{x+2}\right) + B_2(g)\hat{Z}_x\hat{Z}_{x+2} \\ &+ A_3(g)\left(\hat{b}_x\hat{b}^\dagger_{x+3} + \hat{b}^\dagger_x\hat{b}_{x+3}\right) + B_3(g)\hat{Z}_x\hat{Z}_{x+3} \\ &+ C_1(g)\left(\hat{b}_x\hat{b}^\dagger_{x+1} + \hat{b}^\dagger_x\hat{b}_{x+1}\right)\hat{Z}_{x+2}\hat{Z}_{x+3} \\ &+ C_2(g)\left(\hat{b}_x\hat{b}^\dagger_{x+2} + \hat{b}^\dagger_x\hat{b}_{x+1}\right)\hat{Z}_{x+1}\hat{Z}_{x+3} \\ &+ C_2(g)\left(\hat{b}_{x+1}\hat{b}^\dagger_{x+3} + \hat{b}^\dagger_{x+1}\hat{b}_{x+3}\right)\hat{Z}_x\hat{Z}_{x+2} \\ &+ C_3(g)\left(\hat{b}_x\hat{b}^\dagger_{x+3} + \hat{b}^\dagger_x\hat{b}_{x+1}\right)\hat{Z}_{x+1}\hat{Z}_{x+2} \\ &+ C_4(g)\left(\hat{b}_{x+1}\hat{b}^\dagger_{x+2} + \hat{b}^\dagger_{x+1}\hat{b}_{x+2}\right)\hat{Z}_x\hat{Z}_{x+3} \\ &+ C_5(g)\hat{Z}_x\hat{Z}_{x+1}\hat{Z}_{x+2}\hat{Z}_{x+3} \\ &+ D_1(g)\left(b^\dagger_x b^\dagger_{x+1}b_{x+2}b_{x+3} + b_x b_{x+1}b^\dagger_{x+2}b^\dagger_{x+3}\right) \\ &+ D_2(g)\left(b^\dagger_x b_{x+1}b^\dagger_{x+2}b_{x+3} + b_x b^\dagger_{x+1}b_{x+2}b^\dagger_{x+3}\right) \\ &+ D_3(g)\left(b^\dagger_x b_{x+1}b_{x+2}b^\dagger_{x+3} + b_x b^\dagger_{x+1}b^\dagger_{x+2}b_{x+3}\right)\end{aligned} \tag{3.11}$$

where $\hat{b}_x = \frac{1}{2}\left(\hat{X}_x + i\hat{Y}_x\right)$ is a qubit annihilation operator at site x and $A_i(g)$, $B_i(g)$, $C_i(g)$, and $D_i(g)$ are constants determined from solving the SRG equations numerically.

To test the performance of the improved Hamiltonians derived through SRG, density matrix renormalization group (DMRG) calculations were performed using the C++ `iTensor` library [147, 148, 115, 149, 150] to obtain the vacuum state and the single baryon ground state of the Hamiltonian in Eq. (3.2) and the improved Hamiltonians described above for lattices with up to fifteen physical sites with open boundary conditions. Fig. 3.3 shows the

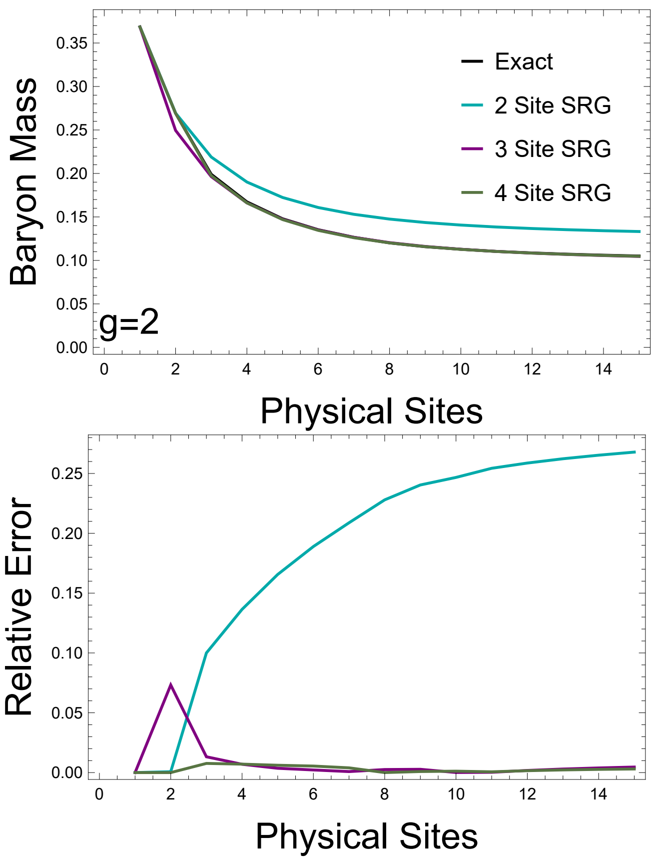

Figure 3.3: Baryon mass as a function of lattice size for $g = 2$. The black dashed curves shows the baryon mass for the Hamiltonian in Eq. (3.2). The different solid curves correspond to the baryon mass in the various improved Hamiltonians derived through the use of IMSRG with different operator size truncations.

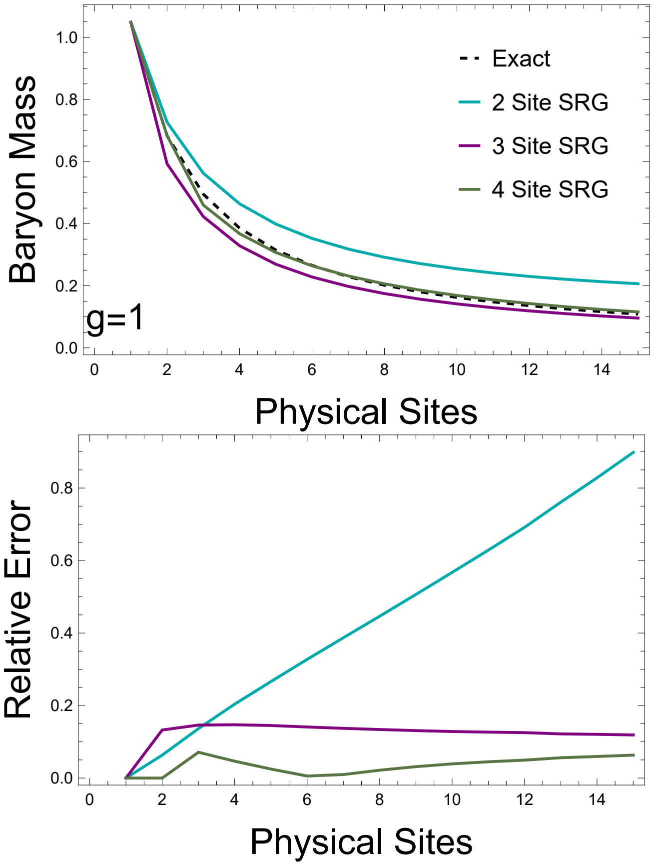

Figure 3.4: Baryon mass as a function of lattice size for $g = 1$. The black dashed curves shows the baryon mass for the Hamiltonian in Eq. (3.2). The different solid curves correspond to the baryon mass in the various improved Hamiltonians derived through the use of IMSRG with different operator size truncations.

mass of the baryon (difference of the energy of the single baryon state and vacuum state) for the full Hamiltonian and the improved Hamiltonians for the zero electric field truncation for $g = 2$. As this figure shows, the relative error in the baryon mass computed with the improved Hamiltonians grows with system size and then saturates. By using improved Hamiltonians with a larger operator size truncation in the IMSRG, the relative error in the baryon mass can be reduced down to the percent level. The baryon mass for $g = 1$ was also computed and is shown in Fig. 3.4. At this weaker coupling, the correlation length is longer and the relative error in the baryon mass grows uncontrollably with the lattice size for the improved Hamiltonian obtained by the two staggered site truncation IMSRG. However, increasing the size of the operator truncation used in the IMSRG decreases the error in the baryon mass to controllable levels.

In addition to studying the energy of different states on the lattice, the IMSRG flows of operators can be computed and their expectation values can be computed using improved Hamiltonians. As an explicit example, the SRG flow of the chromo-electric energy density was computed. The operators corresponding to the chromo-electric operators in the improved basis are the same as those that show up in the improved Hamiltonians, just with different coefficients. The vacuum expectation of the chromo-electric energy density is shown in Fig. 3.5 for $g = 1$ and $g = 2$. As before, increasing the size of the operator truncation in the IMSRG improves the accuracy of the improved Hamiltonians. Remarkably, even though the improved Hamiltonians are being truncated at zero electric field, their ground states still reproduce the electric energy density of the full untruncated theory.

3.2.4 Similarity Renormalization Group $m \neq 0$

In the previous section, IMSRG was used to derive an improved Hamiltonian that describes the dynamics of baryons in QCD in one dimension with massless quarks. The same technique can be used to setup improved Hamiltonians in the case of massive quarks as well.

In a theory with massive quarks, the piece of the Hamiltonian that should be used to generate the SRG flow is the combination of the mass and electric energy terms. At the zero electric energy truncation, the only state left after truncation is the one with matter sites empty and anti-matter sites filled. Therefore with massive quarks, there are no dynamics at this level of truncation. The next lowest truncation in the SRG flow depends on the relative size of the fermion mass m and the coupling g. If $\frac{2}{3}g^2 > m$, then the next lowest lying state in the spectrum consists of a baryon at a site. The improved Hamiltonian derived by truncating at this level takes the same form as in the previous section except with the addition of a mass term for the baryons. If instead $\frac{2}{3}g^2 < m$, then the next lowest lying state in the spectrum corresponds to a quark anti-quark pair connected by a link of electric

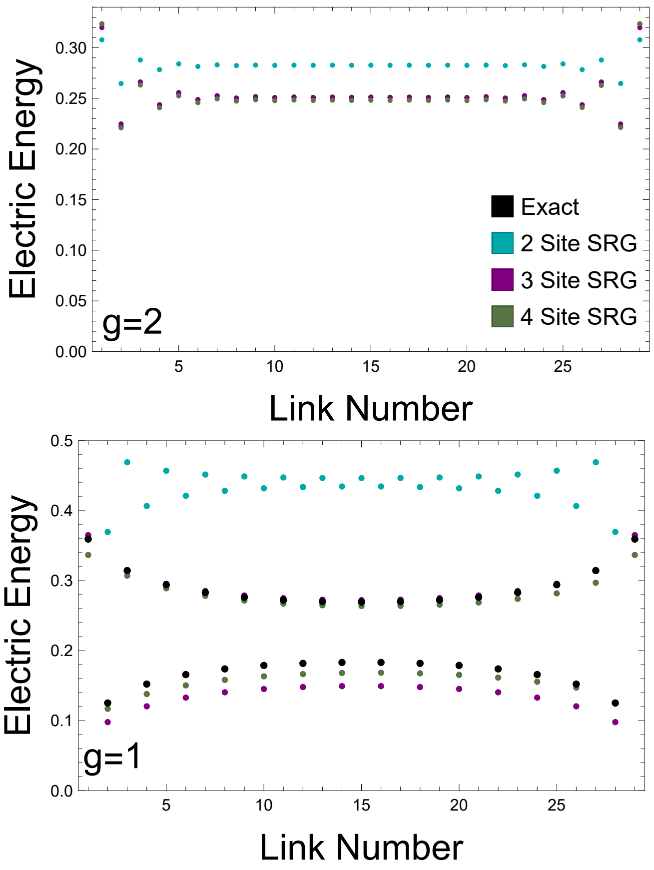

Figure 3.5: The expectation of the electric energy on each link for a lattice with 15 physical sites. The black points were computed using the Hamiltonian in Eq. (3.2). The other points were computed using the improved Hamiltonians for the zero electric field truncation computed using SRG.

flux. In the strong coupling limit, this corresponds to a meson at the excited link.

Denoting the trivial vacuum state by $|Vac\rangle$, and the state with a $q\bar{q}$ pair on link l by $|l\rangle$, the Hamiltonian obtained under IMSRG flow truncating the energy at single link excitations and the operator size at two link operators takes the form

$$\begin{aligned}\hat{H}_{SRG} &= E_0(g,m)\,|Vac\rangle\,\langle Vac| \\ &+ \sum_l h(g,m)\,(|l+1\rangle\,\langle l| + |l\rangle\,\langle l+1|) + E_1(g,m)\,|l\rangle\,\langle l| \quad ,\end{aligned} \tag{3.12}$$

where $E_0(g,m)$, $E_1(g,m)$, and $h(g,m)$ are constants determined through numerically solving the SRG flow. Note that this Hamiltonian has the same form as that of a single non-relativistic particle. The Hamiltonian in Eq. (3.12) can be viewed as a Hamiltonian for a single link excitation (or meson) and can be mapped onto a second quantized Hamiltonian to describe a system with more excited links. Explicitly, the single excitation sector of

$$\begin{aligned}\hat{H}_{SRG} = \sum_l &\frac{h(g,m)}{2}\left(\hat{X}_l\hat{X}_{l+1} + \hat{Y}_l\hat{Y}_{l+1}\right) \\ &+ \frac{E_0(g,m) - E_1(g,m)}{2}\hat{Z}_l \quad ,\end{aligned} \tag{3.13}$$

will be identical to the Hamiltonian in Eq. (3.12). This improved Hamiltonian will also be capable of describing states with multiple links excited as well. The description of these states with multiple links excited can be improved by raising the truncation of states kept after SRG flow to include states where two links are excited. By keeping these states after the SRG flow and keeping the other truncations as before, the improved Hamiltonian given by

$$\begin{aligned}\hat{H}_{SRG2} = \sum_l &\frac{h(g,m)}{2}\left(\hat{X}_l\hat{X}_{l+1} + \hat{Y}_l\hat{Y}_{l+1}\right) \\ &+ s(g,m)\hat{Z}_l\hat{Z}_{l+1} + \frac{E_0(g,m) - E_1(g,m)}{2}\hat{Z}_l \quad ,\end{aligned} \tag{3.14}$$

will have single and two excitation sectors that match the improved Hamiltonians derived through SRG. As a test of the performance of this improved Hamiltonian, the mass of the meson was computed on a lattice with two physical sites for $g = 1$ and various values of m in Fig. 3.6. Similar to the massless case, the improved Hamiltonian derived with the SRG performs well when there is a large separation in energy scales between the states being decoupled. Note that in principle, the same comparison can be done with larger lattices, however the meson is in the same baryon number sector as the vacuum which complicates the calculation of the meson mass. It is expected that this improved Hamiltonian scales to

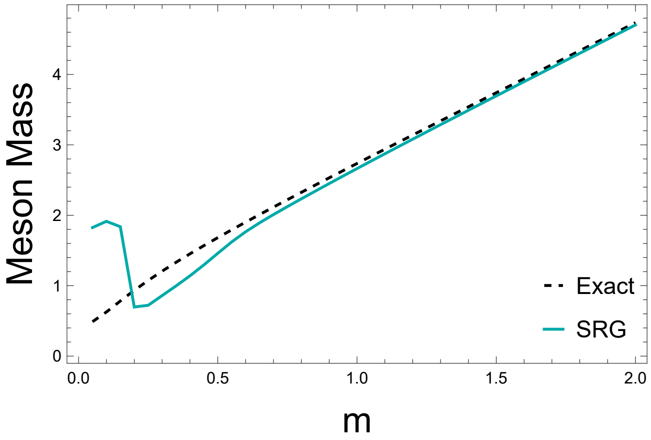

Figure 3.6: Meson mass as a function of quark mass m for $g = 1$ on a lattice of 2 physical sites (4 staggered). The black dashed curves shows the meson mass for the Hamiltonian in Eq. (3.2). The blue curve shows the meson mass for the improved Hamiltonian in Eq. (3.14).

larger lattices as in the massless case.

Quantum Simulation

As an example of how these improved Hamiltonians can be used for quantum simulation, a simulation will be performed of a meson's time evolution on three physical sites with open boundary conditions. Using the Hamiltonian in Eq. (3.2) would require a quantum computer with 18 qubits to encode the state, and non-local interactions between the qubits to implement the electric energy piece of the Hamiltonian. Using the improved Hamiltonian in Eq. (3.14) requires only 5 qubits to represent the state and only requires nearest neighbor interactions on the quantum computer to perform time evolution.

Fig. 3.7 shows the real time evolution of a single meson on three physical sites with $g = 1, m = 1$ simulated on IBM's `Perth` quantum processor [50, 151]. A meson state was prepared on the quantum processor by applying an $\hat{X}$ gate to the qubit assigned to the leftmost link. Time evolution was performed using a first order Trotter formula. Explicitly, the Hamiltonian was decomposed as $\hat{H} = \sum_{l=1}^{4} \hat{H}_l$ where

$$\hat{H}_l = \frac{h(g,m)}{2}\left(\hat{X}_l\hat{X}_{l+1} + \hat{Y}_l\hat{Y}_{l+1}\right) + s(g,m)\hat{Z}_l\hat{Z}_{l+1} \quad , \tag{3.15}$$

and the Trotterized time evolution operator was given by

$$\hat{U}(\Delta t) = e^{-i\hat{H}_2\Delta t}e^{-i\hat{H}_4\Delta t}e^{-i\hat{H}_3\Delta t}e^{-i\hat{H}_1\Delta t} \quad . \tag{3.16}$$

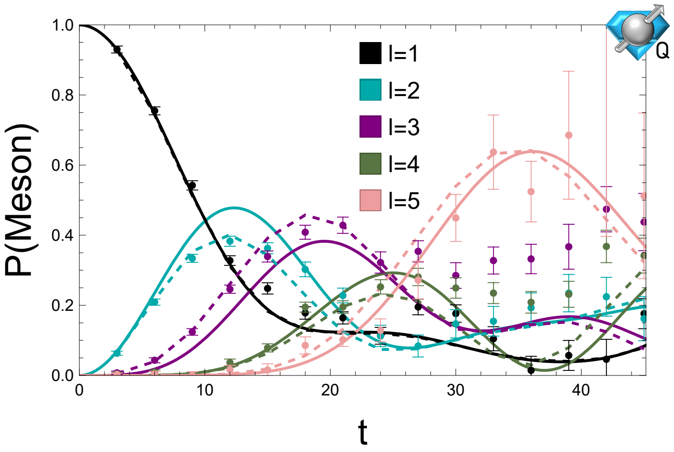

Figure 3.7: Time evolution of a single meson on 3 physical sites performed on the IBM `Perth` quantum processor. Each color corresponds to the probability of a different link being excited. The solid lines show the exact time evolution. The dashed lines show a classical simulation of the Trotterized time evolution that was implemented on the quantum processor. The data points were obtained using self-mitigating circuits on IBM `Perth`.

Each individual $e^{-i\hat{H}_l \Delta t}$ was decomposed into a circuit with 3 CNOT gates using standard techniques [47, 48]. The sum over Pauli $\hat{Z}$ operators can be ignored when performing time evolution because it commutes with the full Hamiltonian and the operators being measured. The noise in the quantum simulation was mitigated using self-mitigation combined with Pauli twirling [152, 153, 154]. For each Trotter step, 50 circuits describing the time evolution were used along with 50 circuits with $\Delta t = 0$ used to determine the strength of the depolarizing noise channel. Each circuit was sampled $10,000$ times. As Fig. 3.7 shows, the quantum hardware is able to describe the time evolution well at short times, but at long times the hardware noise begins to dominate. However, despite the presence of hardware noise at late times, the location of the peak of the wavepacket of the meson can still be located at late times.

3.3 3+1D

3.3.1 3+1D Hamiltonian

Performing a quantum simulation of lattice QCD requires a choice of Hamiltonian to be used. This choice is complicated by the phenomena of fermion doubling, where the naive discretization of the Dirac field on the lattice in d dimensions actually describes 2^d fermions. Furthermore, the Nielson-Ninomiya theorem forbids the presence of chiral symmetry on the lattice when all doublers are removed [155, 156]. In this work, staggered fermions will be used. Staggered fermions work by distributing the components of the Dirac field across different sites of the lattice. This preserves some chiral symmetry at the cost of still having some fermion doublers remain. In lattice QCD calculations on classical computers, space and time are both discretized leading to staggered fermions describing 4 types of fermions, referred to as tastes in the literature. For practical calculations, these can be reduced to a single flavor through the process of rooting [157, 158, 159, 160, 161]. In quantum simulation, time is left continuous and only space is discretized. This changes the counting of the number of tastes present. Explicitly, with three dimensions of space discretized and time left continuous, staggered fermions describe two tastes. This is a feature, not a bug for using lattice QCD to study nuclear physics as one taste can be identified as an up quark and the other can be identified as a down quark. Therefore, we would expect lattice QCD with a single staggered fermion on a quantum computer to describe two flavor QCD where both quarks have the same mass. With massless quarks, this lattice regularization should reproduce the predictions of chiral perturbation theory as the continuum limit is approached. Explicitly, the Hamiltonian that should be used for 3 + 1 dimensional two flavor massless lattice QCD on a quantum computer is

$$\begin{aligned}
\hat{H} &= \hat{H}_K + \hat{H}_E + \hat{H}_B \\
\hat{H}_K &= \sum_{\vec{r},\hat{\mu},a,b} \eta_{\vec{r},\hat{\mu}} \frac{1}{2} \hat{\psi}^{\dagger}_{\vec{r},a} \hat{U}^{a,b}_{\vec{r},\vec{r}+\hat{\mu}} \hat{\psi}_{\vec{r}+\hat{\mu},b} + \text{h.c.} \\
\hat{H}_E &= \frac{g^2}{2} \sum_{l\in\text{links},c} \hat{E}^c_l \hat{E}^c_l \\
\hat{H}_B &= -\frac{1}{2g^2} \sum_{p\in\text{plaquettes}} \Box_p \quad ,
\end{aligned} \tag{3.17}$$

where $\psi_{\vec{r},a}$ is a fermion field at site $\vec{r}$ with color a, $\hat{\mu}$ is a unit vector in the $\hat{x}$, $\hat{y}$, or $\hat{z}$ directions, $\eta_{\vec{r},\hat{\mu}}$ are the spin diagonalization phases, $\hat{U}^{a,b}_{\vec{r},\vec{r}+\hat{\mu}}$ is an SU(3) parallel transporter between sites $\vec{r}$ and $\vec{r}+\hat{\mu}$, $\hat{E}^c_l$ is the SU(3) chromo-electric field on link l and $\Box_p$ is the Hermitian component of the trace over color indices of the product of parallel transporters on plaquette p. Previous work has shown that this Hamiltonian has a discrete chiral symmetry corresponding to translation by one lattice site that is spontaneously broken and an isospin symmetry that corresponds to diagonal translations [162, 163, 69].

3.3.2 Improved Hamiltonian

As is the case for 1D QCD, mapping the Hamiltonian in Eq. (3.17) onto qubits is challenging, especially if one wishes to perform a quantum simulation with existing hardware.

Improved Hamiltonians can also be derived for performing quantum simulations of this theory. Following the discussions of the previous sections, IMSRG can be applied to this theory with a truncation in operator size. The smallest non-trivial operator size IMSRG can be applied to is a single link and the lowest electric field truncation that can be used is zero electric field. The resulting improved Hamiltonian on the 3 dimensional lattice will take the same form as in the 1D case except now the hopping terms will have phases that result from the spin diagonalization.

Explicitly, the improved Hamiltonian obtained through SRG at this truncation in operator size and electric field is

$$\begin{aligned}\hat{H}_{SRG} = \sum_{\vec{r}} & A(g)\left(\hat{\psi}^{\dagger}_{\vec{r}}\hat{\psi}_{\vec{r}+\hat{x}} + \hat{\psi}^{\dagger}_{\vec{r}+\hat{x}}\hat{\psi}_{\vec{r}}\right) \\ & + A(g)(-1)^{r_1}\left(\psi^{\dagger}_{\vec{r}}\hat{\psi}_{\vec{r}+\hat{y}} + \hat{\psi}^{\dagger}_{\vec{r}+\hat{y}}\hat{\psi}_{\vec{r}}\right) \\ & + A(g)(-1)^{r_1+r_2}\left(\hat{\psi}^{\dagger}_{\vec{r}}\hat{\psi}_{\vec{r}+\hat{z}} + \hat{\psi}^{\dagger}_{\vec{r}+\hat{z}}\hat{\psi}_{\vec{r}}\right) \\ & + B(g)\sum_{\hat{\mu}}\left(2\hat{\psi}^{\dagger}_{\vec{r}}\hat{\psi}_{\vec{r}} - 1\right)\left(2\hat{\psi}^{\dagger}_{\vec{r}+\hat{\mu}}\hat{\psi}_{\vec{r}+\hat{\mu}} - 1\right) \quad , \end{aligned} \tag{3.18}$$

where $\psi_{\vec{r}}$ is a colorless fermion field at site $\vec{r}$ and $A(g)$ and $B(g)$ are numerical constants determined through solving the SRG equations.

Note that this improved Hamiltonian only describes the QCD Hamiltonian accurately for large coupling g. At large coupling, the π meson is massive and is integrated out of this improved Hamiltonian. By increasing the chromo-electric field truncation of states kept after the SRG flow, states with quark-antiquark pairs separated by a link will be included in the low energy Hilbert space kept after truncation and will yield an improved Hamiltonian that describes meson degrees of freedom as well.

Spectrum

The improved Hamiltonian in Eq. (3.18) will describe the untruncated theory accurately in the limit of large g. While the continuum limit of lattice QCD is in the limit of $g \to 0$, large couplings can be used to study the theory at finite lattice spacing. In the limit $g \to \infty$, $A(g) \to 0$ and some qualitative features of low energy QCD are recovered. In particular, it has been shown that in the strong coupling limit this theory has an isospin symmetry and a spontaneously broken chiral symmetry [162, 163, 69]. In addition to the previously studied features of this regularization, the strong coupling limit of this Hamiltonian also reproduces the approximate SU(4) spin flavor symmetry of nuclear physics.

As an example, we will study the improved Hamiltonian in Eq. (3.18) on a single cube.

The fermionic fields will be mapped onto qubits using a Jordan-Wigner encoding. When $A(g) = 0$, the Hamiltonian in Eq. (3.18) can be rewritten in terms of Pauli matrices as

$$\hat{H}_{SRG} = \frac{9}{16g^2} \sum_{\hat{\mu}} \hat{Z}_{\vec{r}} \hat{Z}_{\vec{r}+\hat{\mu}} \quad . \tag{3.19}$$

The ground state is in the baryon number $B = 0$ sector and is a degenerate Néel state. For the rest of this discussion, we will only consider the sector that is even under reflection across the $\hat{z}$ axis. The lowest lying excited states in the $B = 0$ sector correspond to performing a SWAP operation on one of the links. Denoting the energy cost of flipping one link as $\Delta = \frac{9}{8g^2}$, this set of excited states has energy 4Δ and there are 12 of them. These 12 states should correspond to spin one and spin zero baryon anti-baryon pairs, i.e., $p\bar{p}$, $n\bar{n}$, $n\bar{p}$ and $p\bar{n}$ states.

The lowest lying energy states in the $B = 1$ sector correspond to flipping one site from the Néel state on the cube. There are four corners that can be flipped in the Néel state to end up in the $B = 1$ sector so there are four degenerate states with energy 3Δ. These correspond to the two spin modes of the proton and neutron. Note that the proton and neutron mass are degenerate which should be expected from isospin symmetry.

In the $B = 2$ sector, the lowest lying states correspond to flipping two spins in the Néel state. This results in six degenerate states with energy 6Δ. These states correspond to spin 1 pn states and spin 0 pp, pn and nn states. The fact that these states are degenerate is reflective of spin-flavor symmetry which is approximately present in low energy nuclear physics. The spin-flavor symmetry has been shown to emerge in the large N_c limit of QCD [164] and is related to the minimization of entanglement in low energy nucleon scattering [165, 166, 167, 168, 169, 170]. We also see that in the strong coupling limit, the deuteron has binding energy zero. Similar calculations can be done in the higher baryon number sectors which also show that these sectors also demonstrate spin-flavor symmetry and nuclei with binding energy = 0. It is also interesting to note that the nucleon-nucleon scattering lengths are large. As a result, the pionless EFT describing nucleon scattering is an expansion around a non-trivial fixed point where the binding energy of nuclei vanishes as is the case in this lattice regularization [171, 172, 173, 174].

Quantum Simulation

The Hilbert space describing the Hamiltonian in Eq. (3.18) consists of a single fermion mode for each site. Using the Jordan-Wigner encoding, the state of each site can be represented with a single qubit. In this encoding, a list of fermion operators $\psi_1, \hat{\psi}_2, ..., \hat{\psi}_N$ are mapped

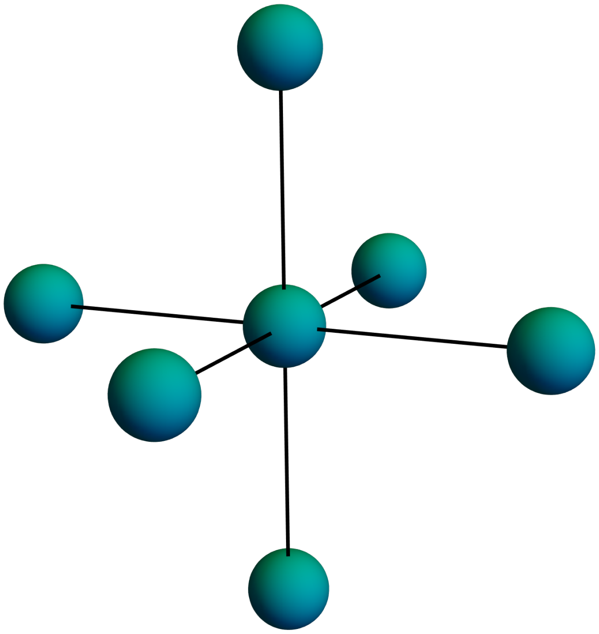

Figure 3.8: Connectivity of the system described by the improved Hamiltonian in Eq. (3.21).

onto qubit operators as

$$\hat{\psi}_n = \bigotimes_{k<n} \frac{1}{2} \hat{Z}_k \left(\hat{X}_n + i\hat{Y}_n \right) \quad . \tag{3.20}$$

For a local one dimensional fermionic theory, this fermion encoding leads to a Hamiltonian that is local in qubits. However, in higher dimensions, the operators in the Hamiltonian will include strings of Pauli $\hat{Z}$ operators that wrap around the lattice. These long range operators are necessary to enforce the anti-commutation relations of the fermionic operators and may make it difficult to practically scale to calculations on a large lattice.

As a demonstration of how this improved Hamiltonian works in practice, time evolution on six vertices connected to a single vertex at the center as shown in Fig. 3.8 will be simulated. This is the smallest non-trivial subsystem of a full three dimensional lattice that will be repeated periodically and will be useful for understanding how simulations on a larger lattice will work. Each of the seven vertices can be mapped onto a single qubit.

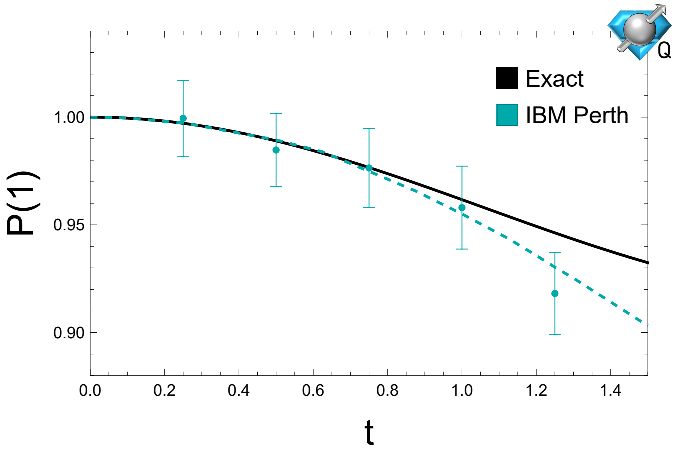

Figure 3.9: Probability of staying in the trivial vacuum state computed on the IBM `Perth` quantum processor. The solid black line shows the exact time evolution. The blue dashed line shows the probability computed using a first order Trotter step computed on a classical computer. The blue data points were obtained using self-mitigating circuits on IBM `Perth`.

The Hamiltonian describing their time evolution is given by

$$\begin{aligned}\hat{H}_{SRG} = &\sum_v A(g)\left(\hat{\psi}_0^\dagger\hat{\psi}_v + \hat{\psi}_v^\dagger\hat{\psi}_0\right)\\ &+ B(g)\sum_v\left(2\hat{\psi}_v^\dagger\hat{\psi}_v - 1\right)\left(2\hat{\psi}_0^\dagger\hat{\psi}_0 - 1\right) \quad ,\end{aligned} \tag{3.21}$$

where the 0 subscript denotes the vertex at the center and the sum is over the other vertices. The quantum processor is initialized with the center qubit in the 1 state and the remaining qubits are in the 0 state. In the staggered fermion lattice regularization, sites are alternatively identified with matter and anti-matter degrees of freedom so this state should correspond to the trivial vacuum. By evolving with the Hamiltonian in Eq. (3.21), it should be possible to observe matter anti-matter fluctuations. Note that with this initial state, a single Trotter step can be performed without having to implement CNOT gates from the Jordan-Wigner strings. A single Trotter step was implemented on IBM `Perth` with the size of the time step being varied to sample different times. Due to the connectivity of the hardware, this circuit required 28 CNOT gates. Fig. 3.9 shows the results of performing a single Trotter step for $g = 2$ on IBM `Perth`. For small times, the quantum simulation is able to describe the evolution of the system accurately, however beyond $t = 1$, the error in the single Trotter step used is large and limits the accuracy of the quantum simulation.

While the Jordan-Wigner encoding is efficient in the number of qubits used, the Hamiltonian generated has long range interactions which are necessary to preserve the anti-commutation relation of the fermions. Scaling these calculations to a larger lattice will require making use of a more efficient fermion encoding. For example, the Bravyi-Kitaev superfast encoding can be used to map fermions onto qubits [175]. In this encoding, a qubit is associated with each link on the lattice and represents the parity of the number of fermions on the link. The length of the strings of Pauli $\hat{Z}$ operators for an operator on a link extends only to neighboring links. For a large lattice, this will limit the circuit depth necessary to perform time evolution and potentially allow for larger calculations to be performed.

3.4 Discussion

In this chapter, the SRG has been used to derive improved Hamiltonians that mitigate the effects of gauge field truncation. It was demonstrated in 1+1D that the improved Hamiltonians derived this way outperform those derived through the strong coupling expansion for small systems. Tensor network calculations were performed to demonstrate that these improved Hamiltonians perform well as the system size is increased. These techniques were also applied to 3+1D giving an improved Hamiltonian capable of describing two flavour QCD on the lattice. Real time dynamics on small systems were simulated on IBM's `Perth` quantum processor.

Previous strategies for quantum simulation of lattice gauge theories improved accuracy by increasing the truncation of the gauge field. This comes at the cost of needing more qubits to represent the system and a more complicated circuit to implement the time evolution. The improved Hamiltonians introduced in this work are capable of improving accuracy only at the cost of requiring more complicated circuits to simulate.

Improved Hamiltonians have been derived for a single flavor of staggered fermions coupled to SU(3) gauge fields truncated at low electric field. This has enabled quantum simulation of systems that would otherwise be out of reach of current quantum hardware. The same approach introduced here can be used to derive improved Hamiltonians for larger electric field truncations and with more flavors of fermions. Future work will extend these methods to higher spatial dimensions with larger operator truncations where the plaquette terms will modify the SRG flow. This will enable quantum simulations of lattice gauge theories in multiple dimensions to be performed in the near term.

Chapter 4

EFFECTIVE QED ON A QUANTUM COMPUTER

In this chapter, we show that quantum computers can efficiently sample from the energy eigenvalues for an approximation to quantum electrodynamics known as eQED. This formulation of quantum electrodynamics is found from expanding the Feynman path integrals that describe quantum electrodynamics to second order from which a Hamiltonian can be derived for only the electronic and positronic degrees of freedom. We specifically provide algorithms for simulating these dynamics in both position and momentum basis both with and without an external vector potential. We then analyze the cost of performing such a simulation using Trotter-Suzuki simulation methods both theoretically and numerically for a relativistic version of the free-electron gas. The non-relativistic version of this model is known as jellium, which not only is useful for the foundations of density functional theory [176, 177] but also has become a standard benchmark problem for quantum chemistry simulation [178]. Here we will present a formulation that is appropriate for eQED which we call "rellium" in analogy to the non-relativistic jellium. While the rellium model by itself may be considered to be a toy model from an *ab initio* physics simulation perspective, we examine this model for its novel Hamiltonian terms that arise in the context of quantum simulation algorithms, that will be present in more sophisticated relativistic many-body systems. For example, the terms present in this Hamiltonian will also be present in Hamiltonian formulations of lattice QCD. Therefore, the quantum simulation techniques developed here are expected to be of use in quantum simulation of lattice QCD. In addition, we discuss how to prepare multi-reference configuration singles and doubles (MRCISD) approximations to the ground state for eQED which is necessary because the strong correlations present in systems where eQED is needed will often make elementary approximations such as Hartree-Fock inaccurate. Finally, we present a simple cost estimate for simulating a gold atom using planewaves in eQED, and context for future work involving QED and relativistic effects in quantum simulation.

4.1 Review of eQED

Quantum electrodynamics (QED) is the quantum field theory that describes the electromagnetic interactions of electrons and positrons. QED is formulated in terms of a four component fermionic spinor field, $\psi_a(x)$ that creates electrons and annihilates positrons and a 4-potential, $A_\mu(x)$, that creates and annihilates photons. It should be noted that the interpretation of $\psi_a(x)$ is not the same as the interpretation of the electron field in non-relativistic field theory. In non-relativistic field theory, applying the electron field operator to a state simply removes a single electron, but in the relativistic case, applying $\psi_a(x)$ to a state will create a superposition of a state with one less electron and a state with one more positron. For this reason, $\psi_a(x)$ can be interpreted as an operator that increases the electric charge of the state by 1. For relativistic chemical physics, the primary goal is to simulate the motion of electrons and positrons, therefore it would be convenient to have a formulation of QED without the photon degrees of freedom. In other words, the goal of effective QED is to derive a Hamiltonian H_{eQED}, such that

$$\langle\phi_f| e^{-iH_{QED}t} |\phi_i\rangle = \left\langle\tilde{\phi}_f\middle| e^{-iH_{eQED}t} \middle|\tilde{\phi}_i\right\rangle \tag{4.1}$$

where $|\phi_i\rangle$ and $|\phi_f\rangle$ are states without free photons propagating, $\left|\tilde{\phi}_i\right\rangle$ and $\left|\tilde{\phi}_f\right\rangle$ are the corresponding states with the photon field integrated out, H_{QED} is the full QED Hamiltonian, and H_{eQED} has the photon field integrated out. The effective Hamiltonian can be derived in the path integral formulation of QED with the Feynman gauge fixing procedure [7], giving

$$\begin{gathered}\langle\phi_f| e^{-iH_{QED}t} |\phi_i\rangle = \int DA_\mu(x)D\bar{\psi}(x)D\psi(x)\phi_f^*(A_\mu(x),\bar{\psi}(x),\psi(x))\phi_i(A_\mu(x),\bar{\psi}(x),\psi(x)) \\ \exp\left(i\int d^4x\left(i\bar{\psi}(x)\gamma^\mu\partial_\mu\psi(x) - m\bar{\psi}(x)\psi(x) - e\bar{\psi}(x)\gamma^\mu\psi(x)A_\mu(x) - \frac{1}{2}A^\mu(x)\Box A_\mu(x)\right)\right)\end{gathered} \tag{4.2}$$

where e is the elementary charge, $\Box = \partial_t^2 - \sum_{i=1}^3 \partial_{x_i}^2$, and $DA_\mu(x)D\bar{\psi}(x)D\psi(x)$ is the functional measure for the fields being integrated over. The repeated upper and lower indices corresponds to Einstein summation convention with a spacetime metric using the mostly negative convention ($g_{\mu\nu} = \mathrm{diag}(1,-1,-1,-1)$), i.e.

$$a^\mu b_\mu = a^0b^0 - \sum_{i=1}^3 a^ib^i \quad . \tag{4.3}$$

The γ matrices act on the Fock space that mixes the components of the particles. From this perspective, they are akin to operations such as fermionic swaps which are widely used in the quantum chemistry literature [178, 179]. The γ matrices, when seen as operators acting on the spinor of fermionic operators $[a^\dagger_{\vec{x},0}, a^\dagger_{\vec{x},1}, a^\dagger_{\vec{x},2}, a^\dagger_{\vec{x},3}]$, can be represented in the

Dirac representation as

$$\begin{aligned}\gamma^0 &= \hat{1}\otimes\hat{\sigma}_3\\ \gamma^i &= i\hat{\sigma}_2\otimes\hat{\sigma}_i\end{aligned}\tag{4.4}$$

where $\hat{\sigma}_i$ are the standard Pauli matrices with $i = 1, 2, 3$ specifying a spatial direction. In Eq. (4.2), $\bar{\psi}(x) = \psi^\dagger(x)\gamma^0$, where the summation over the spinor indices of $\psi^\dagger(x)$ and γ^0 has been suppressed. For states where the electromagnetic field is close to satisfying the classical equations of motion, an action for eQED can be obtained by performing the integral over $A_\mu(x)$ in the stationary phase approximation yielding

$$\left\langle\tilde{\phi}_f\right| e^{-iH_{eQED}t}\left|\tilde{\phi}_i\right\rangle = \int D\bar{\psi}(x)D\psi(x)\tilde{\phi}_f^*(\bar{\psi}(x),\psi(x))\tilde{\phi}_i(\bar{\psi}(x),\psi(x))$$
$$\exp\left(i\int d^4x\left(i\bar{\psi}(x)\gamma^\mu\partial_\mu\psi(x) - m\bar{\psi}(x)\psi(x) - \frac{1}{2}e^2\bar{\psi}(x)\gamma^\mu\psi(x)\Box^{-1}(x,y)\int d^4y\ \bar{\psi}(y)\gamma_\mu\psi(y)\right)\right).\tag{4.5}$$

Therefore the action for eQED is given by

$$S_{eQED} = \int d^4x\left(i\bar{\psi}(x)\gamma^\mu\partial_\mu\psi(x) - m\bar{\psi}(x)\psi(x) - \frac{1}{2}e^2\bar{\psi}(x)\gamma^\mu\psi(x)\Box^{-1}(x,y)\int d^4y\bar{\psi}(y)\gamma_\mu\psi(y)\right)\tag{4.6}$$

where $\Box^{-1}(x,y)$ is the Green's function for $\Box$.

$$\Box^{-1}(\vec{x},t',\vec{y},t) = \frac{1}{4\pi|\vec{y}-\vec{x}|}\delta(t'-t-|\vec{y}-\vec{x}|)\tag{4.7}$$

This resulting action is not local in time, which makes it unsuitable for deriving a Hamiltonian for the canonical quantization formulation of quantum mechanics. If the radiation effects are neglected (ie. the Coulomb interaction between electrons and positrons is approximated as being instantaneous), then

$$\Box^{-1}(\vec{x}',t',\vec{x},t) \approx \frac{1}{4\pi|\vec{x}'-\vec{x}|}\delta(t'-t)\tag{4.8}$$

In this approximation,

$$S_{eQED} = \int d^4x\left(i\bar{\psi}(x)\gamma^\mu\partial_\mu\psi(x) - m\bar{\psi}(x)\psi(x) - \frac{1}{2}e^2\bar{\psi}(x)\gamma^\mu\psi(x)\int d^3y\frac{1}{4\pi|\vec{x}-\vec{y}|}\bar{\psi}(y)\gamma_\mu\psi(y)\right)\tag{4.9}$$

At this point, a Legendre transform can be performed to obtain a Hamiltonian for eQED given by

$$
\begin{aligned}
H_{eQED} = \int d^3x \Bigg(& -i \sum_{j=1}^{3} \bar{\psi}(x)\gamma^j \nabla_j \psi(x) + m\bar{\psi}(x)\psi(x) \\
& + \frac{1}{2} e^2 \bar{\psi}(x)\gamma^\mu \psi(x) \int d^3y \frac{1}{4\pi|\vec{x}-\vec{y}|} \bar{\psi}(y)\gamma_\mu \psi(y) \Bigg) \; .
\end{aligned}
\tag{4.10}
$$

where ∇_j is the typical 3-space gradient operator. Note that when working in momentum space instead of position space, this issue of time nonlocality is avoided by obtaining the potentials by matching Feynman diagrams at $O(e^2)$ with QED. By performing this matching, the leading order corrections from the radiation effects neglected in the position space formulation will be included in the momentum space formulation.

4.1.1 eQED for Free Electrons

The first case that we will present is the Hamiltonian for eQED for the uniform electron gas. There are two representations that we will consider for the Hamiltonian: position space and momentum space. Both approaches have different advantages and disadvantages and without further knowledge, it is unclear which will prove to be superior for a given problem without knowing the number of lattice sites in the real-space or reciprocal-space lattice needed for the simulation.

Lattice eQED

The Hamiltonian from the previous section can be placed on a discrete cubic lattice with n_s sites and side-length L. In this discrete representation we make the identification that $\psi = a\sqrt{n_s/L^3}$ and $\bar{\psi} = a^\dagger \gamma^0 \sqrt{n_s/L^3}$ where a is the standard dimensionless fermionic annihilation operator, and n_s is the total number of lattice sites. ψ and a obey the standard fermionic anti-commutation relations

$$
\begin{aligned}
\{\psi_{\vec{x},i}, \psi_{\vec{y},j}\} &= 0 \\
\{\psi^\dagger_{\vec{x},i}, \psi_{\vec{y},j}\} &= \frac{n_s}{L^3} \delta_{\vec{x},\vec{y}} \delta_{i,j} \\
\{a_{\vec{x},i}, a_{\vec{y},j}\} &= 0 \\
\{a^\dagger_{\vec{x},i}, a_{\vec{y},j}\} &= \delta_{\vec{x},\vec{y}} \delta_{i,j}
\end{aligned}
\tag{4.11}
$$

where the first index labels the position on the lattice and the second index labels the spinor component. The discretized Hamiltonian on the lattice can then be expressed as

$$H_{eQED} = H_K + H_m + H_V$$

$$H_m = \frac{L^3}{n_s} \sum_{\vec{x}} m \bar{\psi}_{\vec{x}} \psi_{\vec{x}} = \sum_{\vec{x}} m a^\dagger_{\vec{x}} \gamma^0 a_{\vec{x}}$$

$$H_V = \frac{L^6}{n_s^2} \sum_{\vec{x} \neq \vec{y}} \sum_{\mu=0}^{3} g_{\mu\mu} \frac{e^2 n_s^{1/3}}{8\pi L |\vec{x} - \vec{y}|} (\bar{\psi}_x \gamma^\mu \psi_x)(\bar{\psi}_y \gamma^\mu \psi_y) = \sum_{\vec{x} \neq \vec{y}} \sum_{\mu=0}^{3} g_{\mu\mu} \frac{e^2 n_s^{1/3}}{8\pi L |\vec{x} - \vec{y}|} (a^\dagger_x \gamma^0 \gamma^\mu a_x)(a^\dagger_y \gamma^0 \gamma^\mu a_y) \tag{4.12}$$

Here we use the convention that $\vec{x}$, $\vec{y}$ and $\vec{p}$ are vectors of integers that index a particular fermionic mode. The state of the system can be represented by using a qubit to represent each $a^\dagger_x a_x$. This will require $4n_s$ qubits total.

A technicality emerges in choosing the correct quantization of the kinetic operator on the lattice, H_K. In particular, if a finite difference on the lattice is used as in

$$H_{\text{naïve}} = \frac{L^2}{n_s^{2/3}} \sum_{\vec{x}} -i \bar{\psi}_x \sum_{j=1}^{3} \gamma^j \frac{\psi_{x+\hat{j}} - \psi_{x-\hat{j}}}{2} \tag{4.13}$$

where $\hat{j}$ is a unit vector pointing in the j-th direction, a correct continuum limit will not be recovered [155, 156]. Consider a free electron with integer valued momentum p, in units of $2\pi/L$ in one-dimension. The electron's momentum then lies in the range $[-\frac{n_s^{1/3}}{2}, \frac{n_s^{1/3}}{2}]$where the energy is given by $E = \sqrt{m^2 + \frac{n_s^{2/3}}{L^2} \sin^2(2\pi p / n_s^{1/3})}$. Therefore with this kinetic Hamiltonian, both an electron with momentum $\frac{n_s^{1/3}}{2}$ and an electron with zero momentum have energy m. Likewise, by periodicity, at every energy there will be twice as many states as there are in the continuum limit. This doubling of states prevents this naïve choice of Hamiltonian from correctly reproducing the physics of continuum eQED. Several solutions to this fermion doubling problem have been developed in the study of lattice gauge theories [180, 13, 181, 182, 183, 184, 185]. One solution, known as SLAC fermions, solves this problem by choosing the kinetic term, H_K such that the dispersion relation agrees with the continuum limit [181, 182].

$$H_K \to H_{SLAC} := \frac{2\pi L^2}{n_s^{1/3}} \sum_{\vec{x},\vec{y},\vec{p}} \frac{e^{i 2\pi n_s^{-\frac{1}{3}} \vec{p} \cdot (\vec{x} - \vec{y})}}{n_s} \bar{\psi}_{\vec{y}} \gamma^j p_j \psi_{\vec{x}} = \frac{2\pi}{n_s^{1/3} L} \sum_{\vec{x},\vec{y},\vec{p}} e^{i 2\pi n_s^{-\frac{1}{3}} \vec{p} \cdot (\vec{x} - \vec{y})} a^\dagger_{\vec{y}} \gamma^0 \gamma^j p_j a_{\vec{x}} \tag{4.14}$$

This choice of kinetic term solves the fermion doubling at the expense of locality. The cost model we use for the simulation assumes all-to-all couplings between the qubits and can perform CNOT between such pairs as well as all single qubit Clifford operations. Therefore, the loss of locality does not represent a significant cost in this model. It should be noted that in lattice gauge theory calculations other solutions are typically used, such as Wilson's kinetic operator [180], domain wall fermions [183], and overlap fermions [184, 185]. This is because the SLAC Hamiltonian is non-local which leads to the generation of new counterterms needed to correctly renormalize the Hamiltonian as the continuum limit is approached [186, 187, 182]. This is not an issue for eQED as these counterterms are higher order in e^2 and are relevant beyond where this effective theory is valid. Additionally, the all to all connectivity of SLAC fermions presents practical problems when numerically computing fermion determinants in classical simulations of lattice gauge theories. As the purpose of this chapter is to obtain a worst case estimate for the cost of quantum simulation of relativistic fermions on the lattice, this is a feature as other formulations will likely be less computationally costly.

Momentum Space Finite Volume eQED

The momentum space formulation of a relativistic eQED Hamiltonian without an external potential can be viewed as a variant of a well known interacting electron model: jellium. We will follow similar notation to Ref. [178], where the standard non-relativistic 3 dimensional jellium Hamiltonian is defined as the following in second quantization

$$H_{jel} = \sum_{p,\sigma_1} \frac{k_p^2}{2} a^\dagger_{p,\sigma_1} a_{p,\sigma_1} + \frac{1}{2L^3} \sum_{\substack{(p,\sigma_1)\neq(q,\sigma_2) \\ \nu\neq 0}} \frac{4\pi}{k_\nu^2} a^\dagger_{p,\sigma_1} a^\dagger_{q,\sigma_2} a_{q+\nu,\sigma_2} a_{p-\nu,\sigma_1} \tag{4.15}$$

where the p, q indices are momentum space electronic planewave orbitals, L is the length of one dimension of the cubic simulation box, $\sigma_1, \sigma_2 \in [\uparrow, \downarrow]$ are the fermion spin indices, and k is the momentum. Here $\{a^\dagger_{p,\sigma_1}, a_{q,\sigma_2}\} = \delta_{p,q}\delta_{\sigma_1,\sigma_2}$ and atomic units are chosen such that the charge on the electron e, and the electron mass m_e, obeys $e = m_e = 1$ to match the standard unit choice in the literature. In non-relativistic jellium, the planewave basis is only defined for electronic and spin degrees of freedom

$$\varphi_\nu(r) = \sqrt{\frac{1}{L^3}} e^{ik_\nu \cdot r}, \qquad k_\nu = \frac{2\pi\nu}{L} \tag{4.16}$$

where $\varphi_\nu(r)$ is a single plane wave as a function of the momentum grid point $\nu \in [-N^{(1/3)}, N^{(1/3)}]^3 \subset \mathbb{Z}^3$ and distance is denoted by r. The momentum grid is the same size for both spin-up and spin-down planewaves.

In order to extend the 3D jellium Hamiltonian to a relativistic framework, we use the 4-spinor solution to the Dirac equation to build a planewave basis, and use the second order tree Feynman diagrams for eQED to compute the two particle interactions. As mentioned above, we will refer to this relativistic jellium model as ‘rellium’. In general, the planewave basis has the same form as above, but the total number of planewaves will be doubled, now that positronic degrees of freedom must be considered. The general form of the rellium Hamiltonian takes into account relativistic particle energies, and also eQED interaction amplitudes that have pair creation ($e^- \to e^- e^- e^+$) interactions in addition to the typical two body interactions ($e^- e^- \to e^- e^-$). In this form charge is conserved, but not particle number. The rellium Hamiltonian can be described in second quantization as

$$
\begin{aligned}
H_{rel} =& \sum_{p,\sigma_1} E_p a^\dagger_{p,\sigma_1} a_{p,\sigma_1} + \sum_{p,\sigma_1} E_p b^\dagger_{p,\sigma_1} b_{p,\sigma_1} \\
&+ \frac{1}{2L^3} \sum_{\substack{p,q,r \\ \sigma_1,\sigma_2,\sigma_3,\sigma_4}} \frac{\mathcal{M}^{e^-_{r,\sigma_3} e^-_{p+q-r,\sigma_4}}_{e^-_{p,\sigma_1} e^-_{p,\sigma_2}}}{\sqrt{E_p E_q E_r E_{p+q-r}}} a^\dagger_{p+q-r,\sigma_4} a^\dagger_{r,\sigma_3} a_{q,\sigma_2} a_{p,\sigma_4} \\
&+ \frac{1}{2L^3} \sum_{\substack{p,q,r \\ \sigma_1,\sigma_2,\sigma_3,\sigma_4}} \frac{\mathcal{M}^{e^+_{r,\sigma_3} e^+_{p+q-r,\sigma_4}}_{e^+_{p,\sigma_1} e^+_{q,\sigma_2}}}{\sqrt{E_p E_q E_r E_{p+q-r}}} b^\dagger_{p+q-r,\sigma_4} b^\dagger_{r,\sigma_3} b_{q,\sigma_2} b_{p,\sigma_1} \\
&+ \frac{1}{2L^3} \sum_{\substack{p,q,r \\ \sigma_1,\sigma_2,\sigma_3,\sigma_4}} \frac{\mathcal{M}^{e^-_{r,\sigma_3} e^+_{p+q-r,\sigma_4}}_{e^-_{p,\sigma_1} e^+_{q,\sigma_2}}}{\sqrt{E_p E_q E_r E_{p+q-r}}} b^\dagger_{p+q-r,\sigma_4} a^\dagger_{r,\sigma_3} b_{q,\sigma_2} a_{p,\sigma_1} \\
&+ \frac{1}{2L^3} \sum_{\substack{p,q,p_1 \\ \sigma_1,\sigma_2,\sigma_3,\sigma_4}} \frac{\mathcal{M}^{e^+_{q,\sigma_2} e^-_{p_1,\sigma_3} e^-_{p-q-p_1,\sigma_4}}_{e^-_{p,\sigma_1}}}{\sqrt{E_p E_q E_{p_1} E_{p-q-p_1}}} a^\dagger_{p-q-p_1,\sigma_4} a^\dagger_{p_1,\sigma_3} b^\dagger_{q,\sigma_2} a_{p,\sigma_1} + h.c. \\
&+ \frac{1}{2L^3} \sum_{\substack{p,q,p_1 \\ \sigma_1,\sigma_2,\sigma_3,\sigma_4}} \frac{\mathcal{M}^{e^-_{q,\sigma_2} e^+_{p_1,\sigma_3} e^+_{p-q-p_1,\sigma_4}}_{e^+_{p,\sigma_1}}}{\sqrt{E_p E_q E_{p_1} E_{p-q-p_1}}} b^\dagger_{p-q-p_1,\sigma_4} b^\dagger_{p_1,\sigma_3} a^\dagger_{q,\sigma_2} b_{p,\sigma_1} + h.c. \\
&+ \frac{1}{2L^3} \sum_{\substack{p,q,r \\ \sigma_1,\sigma_2,\sigma_3,\sigma_4}} \frac{\mathcal{M}_0^{e^-_{p,\sigma_1} e^+_{q,\sigma_2} e^-_{r,\sigma_3} e^+_{-p-q-r,\sigma_4}}}{\sqrt{E_p E_q E_r E_{-p-q-r}}} a^\dagger_{p,\sigma_1} b^\dagger_{q,\sigma_2} a^\dagger_{r,\sigma_3} b^\dagger_{-p-q-r,\sigma_4} + h.c. \\
&+ \delta m \sum_{p,\sigma_1,\sigma_2} \frac{1}{2E_p n_s} \Bigg(\bar{u}_{\sigma_1}(p) u_{\sigma_2}(p) a^\dagger_{p,\sigma_1} a_{p,\sigma_2} - \bar{v}_{\sigma_1}(p) v_{\sigma_2}(p) b^\dagger_{p,\sigma_1} b_{p,\sigma_2} \\
&+ \bar{v}_{\sigma_1}(-p) u_{\sigma_2}(p) b^\dagger_{-p,\sigma_1} a_{p,\sigma_2} + \bar{u}_{\sigma_1}(-p) v_{\sigma_2}(p) a^\dagger_{-p,\sigma_1} b_{p,\sigma_2} \Bigg) + \Lambda n_s
\end{aligned}
\tag{4.17}
$$

where the relativistic energy E_k is defined as $E_k = \sqrt{k_x^2 + k_y^2 + k_z^2 + m^2}$ where m is the electron mass, a, b are the annihilation operators corresponding to electronic and positronic degrees of freedom respectively, $\mathcal{M}$ represents the computed eQED amplitudes for the interaction, and $\sigma_1, \sigma_2, \sigma_3, \sigma_4 \in [\uparrow, \downarrow]$ are all independent spin indices. δm is the difference between the bare mass and the physical electron mass and Λ is a constant added to guarantee that the vacuum has zero energy. It is necessary to include these terms in the Hamiltonian to guarantee that the particles in this discretized theory have a mass equal to the electron mass and that the correct physics is reproduced in the continuum limit. The electron and positron operators obey the standard fermionic anti-commutation relations

$$\begin{aligned}
&\{a_{\vec{p},i}, a_{\vec{q},j}\} = 0 \\
&\{a^{\dagger}_{\vec{p},i}, a_{\vec{q},j}\} = \delta_{\vec{p},\vec{q}}\delta_{i,j} \\
&\{a_{\vec{p},i}, b_{\vec{q},j}\} = 0 \\
&\{b_{\vec{p},i}, b_{\vec{q},j}\} = 0 \\
&\{b^{\dagger}_{\vec{p},i}, b_{\vec{q},j}\} = \delta_{\vec{p},\vec{q}}\delta_{i,j}\ .
\end{aligned} \tag{4.18}$$

The helicity spinors are defined by

$$\begin{aligned}
u_1(p) &= \sqrt{E_p+m}\begin{pmatrix} 1 \\ 0 \\ \frac{p_z}{E_p+m} \\ \frac{p_x+ip_y}{E_p+m} \end{pmatrix},\ u_2(p) = \sqrt{E_p+m}\begin{pmatrix} 0 \\ 1 \\ \frac{p_x-ip_y}{E_p+m} \\ \frac{-p_z}{E_p+m} \end{pmatrix}, \\
v_1(p) &= \sqrt{E_p+m}\begin{pmatrix} \frac{p_x-ip_y}{E_p+m} \\ \frac{-p_z}{E_p+m} \\ 0 \\ 1 \end{pmatrix},\ v_2(p) = \sqrt{E_p+m}\begin{pmatrix} \frac{p_z}{E_p+m} \\ \frac{p_x+ip_y}{E_p+m} \\ 1 \\ 0 \end{pmatrix}
\end{aligned} \tag{4.19}$$

and are used in the construction of $\mathcal{M}$. The details of the amplitudes $\mathcal{M}$ are discussed in detail in Appendix .4.1. The state of the system can be represented on a quantum computer by using a qubit to represent the value of each $a^{\dagger}_{p,\sigma}a_{p,\sigma}$ and each $b^{\dagger}_{p,\sigma}b_{p,\sigma}$. Thus the total number of qubits required to encode the state of the fermionic field here is $4n_s$, in exact agreement with the number required in position space (despite the fact that in momentum basis we explicitly divide the field into a fermionic and anti-fermionic subsystem).

4.1.2 eQED with an External Potential

In the continuum, when eQED is done in the presence of an external vector potential $A^{ex}(x)$, an additional term

$$H_{ext} = -e \int d^3x \bar{\psi}(x) \gamma^\mu \psi(x) A^{ex}_\mu(x) \tag{4.20}$$

must be added to the Hamiltonian. This vector potential term is more general than the Coulomb term commonly used for external potentials in chemistry applications. In part, this is because it applies to general external electric potentials but also because this term includes the vector potential needed to describe interactions with external magnetic fields as well.

Since quantum computer simulations necessarily require discretized wave functions, it is necessary to consider discretizations of Eq. (4.20). The two natural approaches to discretize the system in a lattice are in position and momentum representations. In the position representation, the integral of the external potential can be discretized as a finite sum via

$$H_{L,ext} = -e \frac{L^3}{n_s} \sum_x \bar{\psi}_x \gamma^\mu \psi_x A^{ex}_{\mu,x}. \tag{4.21}$$

The momentum space representation can be found from the position space representation by applying the Fourier transform to the field operators. This approach is analogous to the fermionic Fourier transform used in quantum chemistry simulations [188, 178]; however, here the transform needs to be performed over all four components of the field. The transform of the vector potential operator is given by

$$A^{ex}_\mu(x) = \int \frac{d^3x}{(2\pi)^3} e^{-ipx} \tilde{A}^{ex}_\mu(p), \tag{4.22}$$

This term takes the form

$$\begin{aligned} H_{ext} = -e \sum_{\sigma_1,\sigma_2} \int \frac{d^3p d^3q}{2\sqrt{E_p E_q}} \Bigg(& \bar{u}_{\sigma_2}(q) \gamma^\mu u_{\sigma_1}(p) a^\dagger_{q,\sigma_2} a_{p,\sigma_1} \tilde{A}^{ex}_\mu(p-q) \\ & + \bar{u}_{\sigma_2}(q) \gamma^\mu v_{\sigma_1}(p) a^\dagger_{q,\sigma_2} b^\dagger_{p,\sigma_1} \tilde{A}^{ex}_\mu(-p-q) \\ & + \bar{v}_{\sigma_2}(q) \gamma^\mu u_{\sigma_1}(p) b_{q,\sigma_2} a_{p,\sigma_1} \tilde{A}^{ex}_\mu(p+q) \\ & + \bar{v}_{\sigma_2}(q) \gamma^\mu v_{\sigma_1}(p) b_{q,\sigma_2} b^\dagger_{p,\sigma_1} \tilde{A}^{ex}_\mu(q-p) \Bigg) \end{aligned} \tag{4.23}$$

in momentum space.

In the discretized momentum space simulation, the external potential term takes the form of

$$
\begin{aligned}
H_{p,ext} = & -e \sum_{\sigma_1,\sigma_2} \sum_{p,q} \frac{1}{2\sqrt{E_p E_q} L^3} \Bigg(\bar{u}_{\sigma_2}(q)\gamma^\mu u_{\sigma_1}(p) a^\dagger_{q,\sigma_2} a_{p,\sigma_1} \tilde{A}^{ex}_\mu (p-q) \\
& + \bar{u}_{\sigma_2}(q)\gamma^\mu v_{\sigma_1}(p) a^\dagger_{q,\sigma_2} b^\dagger_{p,\sigma_1} \tilde{A}^{ex}_\mu (-p-q) \\
& + \bar{v}_{\sigma_2}(q)\gamma^\mu u_{\sigma_1}(p) b_{q,\sigma_2} a_{p,\sigma_1} \tilde{A}^{ex}_\mu (p+q) \\
& + \bar{v}_{\sigma_2}(q)\gamma^\mu v_{\sigma_1}(p) b_{q,\sigma_2} b^\dagger_{p,\sigma_1} \tilde{A}^{ex}_\mu (q-p) \Bigg).
\end{aligned}
\tag{4.24}
$$

With these additional definitions, we now have a general form of the eQED Hamiltonian that we can use for cost analysis.

4.2 Trotter-Suzuki Simulations of eQED

There are many techniques that have been proposed thus far for simulating quantum dynamics. The first approach proposed for quantum simulation involves the use of Trotter-Suzuki formulas to compile quantum dynamics into a discrete sequence of gate operations [42, 43, 44, 46, 45]. These approaches are space optimal and can take advantage of properties such as locality and commutation relations that qubitization cannot. For simulations of the free electron gas, known as jellium, recent work has shown that the scaling of the time complexity of Trotter-Suzuki simulation methods and qubitization are nearly equal. For this reason, we focus on Trotter-Suzuki simulations.

Trotter-Suzuki simulations can be viewed as a method for compiling the unitary matrix e^{-iHt} as a sequence of unitary gates, U, such that $\|e^{-iHt} - U\| \leq \delta$, where the notation $\|\cdot\|$ refers to the spectral norm, and δ is a chosen error threshold. If $H = \sum_j H_j$ for a set of local Hamiltonians H_j, such that $e^{-iH_j\theta}$ can be efficiently compiled as a quantum circuit via

$$
U_2(t) := \left(\prod_{j=1}^{m} e^{-iH_j t/2}\right)\left(\prod_{j=m}^{1} e^{-iH_j t/2}\right) = e^{-iHt} + O\left(\max_{j,k,\ell} \|[H_j,[H_k,H_\ell]]\| t^3\right) \tag{4.25}
$$

then this approximation can effectively compile e^{-iHt} into a sequence of unitary operations. Here, $O(\cdot)$ refers to the standard big-O notation denoting an upper bound in the asymptotic limit. Additionally, $\widetilde{O}(\cdot)$, $\Theta(\cdot)$ denotes the asymptotic upper bound with suppressed poly-logarithmic terms, and the asymptotic tight bound respectively used throughout this manuscript. Since each H_j is assumed to be implementable using a polynomial-sized circuit, this approximation effectively compiles e^{-iHt} into a sequence of unitary operations. Higher-order variants of the Trotter-Suzuki approximation can be constructed from the symmetric Trotter formula U_2 via [189, 190]

$$\begin{aligned} U_{2k+2}(t) &:= U_{2k}^2(s_{2k}t)U_{2k}((1-4s_{2k})t)U_{2k}^2(s_{2k}t) \\ &= e^{-iHt} + O\left(\max_{j_1,\ldots,j_{2k+3}} (\|[H_{j_1},[\cdots[H_{2k+2},H_{2k+3}]\cdots]]\|)t^{2k+3}\right), \end{aligned} \tag{4.26}$$

where $s_{2k} = (4 - 4^{1/(2k+1)})^{-1}$. Such high-order Trotter-Suzuki formulas are not always superior to their lower-order brethren. This is because the number of exponentials in $U_{2k}(t)$ is in $\Theta(5^k m)$ and hence tradeoffs between the exponential improvements to accuracy yielded increasing k and the exponentially increasing costs of doing so must be made. Further, as the error in the Trotter-Suzuki approximation depends on the commutators between the Hamiltonian terms, the cost of such simulations can be better than these upper bounds suggest [191, 192, 190].

Thus in order to construct the operation $U_{2k}(t)$, for some integer value of k, we need to develop circuits for implementing each of the terms in the decomposition separately. That is to say we need to take each Hamiltonian term present in the Hamiltonian and convert them to easily simulatable Hamiltonians before using the Trotter-Suzuki approximation to compile it to a sequence of operations that can be run on a quantum computer.

The individual H_j in our representation will, similar to chemistry, be expressable as Pauli operators through the use of a Jordan-Wigner transformation. Such a transformation yields the following transformation for the fermionic creation operator $a_x^\dagger$ via

$$a_x^\dagger \mapsto \frac{(X-iY)_x(\bigotimes_{n<x} Z_n)}{2}, \tag{4.27}$$

for some arbitrary canonical ordering of the site labels. Note that it may be tempting to make this assignment to the field operators $\psi^\dagger$ and ψ but we cannot do so directly since the field operators are dimensionful. For this reason, we discuss in the following the dimensionless fermionic operators a_x and will use these operators interchangeably with their anti-particle counterparts, b_y. Other fermionic representations are possible, such as the Bravyi-Kitaev encoding [193], but here we use Jordan-Wigner for its simplicity.

One technicality that needs to be considered with the Jordan-Wigner encoding is that the pattern of Pauli-Z operations depends on the lexigraphical ordering of the site labels. In one-dimension, such orderings are straightforward, but in higher dimensions there are a multitude of natural lexigraphical orderings of the sites (orbitals) that can be chosen.

Here we focus on a simplified cost model for the simulation wherein non-Clifford operations constitute the majority of the cost. Specifically, we assume our quantum computer has all-to-all couplings between the qubits and can perform CNOT between such pairs as well as all single qubit Clifford operations (which can be formed from products of the Hadamard gate H and the phase gate $S = \sqrt{Z}$). We also assume that the $T = \sqrt{S}$ gate can be applied to each quantum bit. Further we assume that all Clifford operations can be implemented without cost and only T-gates are costly. This further motivates why we choose Jordan-Wigner representation for our problem because the additional gates needed to enforce the correct signs from the lexigraphical ordering are all Clifford operations, which we take to be without cost. Thus, within our cost model, the choice of the ordering of the labels of the sites will prove to be irrelevant.

With the Jordan-Wigner transformation in place we have all we need to compile the circuit from the Trotter-Suzuki simulation $U_{2k}(t)$ into a sequence of gates that can be executed on a quantum computer. Below, we discuss ways that exponentials of the one- and two-body terms in the Hamiltonian can be compiled into a gateset involving Clifford gates and single qubit rotations. We will discuss later what translations need to be done to convert the single qubit rotations into circuits involving H and T.

4.2.1 Quantum Circuit for the one-body operators

The free piece of the eQED Hamiltonian consists of a sum over terms of the form $\psi_p^\dagger \psi_q$, however the representation of these terms can vary depending on whether we are interested in the position or momentum basis. In the momentum basis formulation, all terms take the form $a^\dagger_{\sigma,p} a_{\sigma,p}$ and $b^\dagger_{\sigma,p} b_{s,p}$, which acts only on a single qubit register and is trivial to simulate. Therefore, evolving according to the free Hamiltonian in the momentum basis requires $4n_s$ single qubit gates. In the position space lattice formulation, the free Hamiltonian terms can take one of two more additional forms: $a_x^\dagger a_y + a_y^\dagger a_x$ and $i(a_x^\dagger a_y - a_y^\dagger a_x)$. These operators can then be converted into Pauli operators using the Jordan-Wigner transformation. Assuming without loss of generality that in the canonical ordering we choose $x < y$, the Jordan-Wigner representation of these terms takes the form

1. $a_x^\dagger a_y + a_y^\dagger a_x \xrightarrow{JW} X_y(\bigotimes_{x<n<y} Z_n)X_x + Y_y(\bigotimes_{x<n<y} Z_n)Y_x$

2. $i(a_x^\dagger a_y - a_y^\dagger a_x) \xrightarrow{JW} X_y(\bigotimes_{x<n<y} Z_n)Y_x - Y_y(\bigotimes_{x<n<y} Z_n)X_x$

While Case 1 appears in standard constructions for quantum circuits for simulating chemistry [194], Case 2 does not typically arise in existing quantum circuit constructions and so we provide optimized networks for implementing it, shown in Figure 4.2. An optimized circuit for the one-body operations in Case 1 is given in Figure 4.1

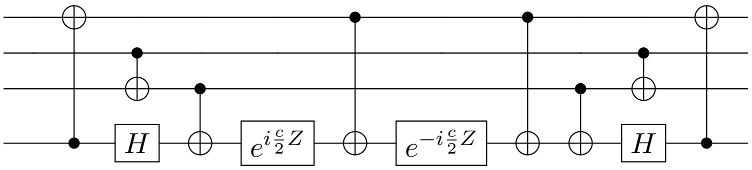

Figure 4.1: Circuit used to implement $e^{ic\left(X_y\left(\bigotimes_{x<n<y} Z_n\right)\otimes X_x + Y_y\left(\bigotimes_{x<n<y} Z_n\right)\otimes Y_x\right)}$ for $y = x + 2$.

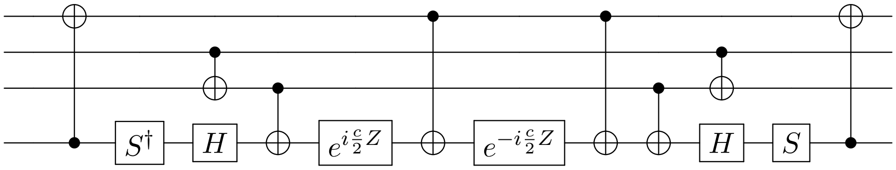

Figure 4.2: Circuit used to implement $e^{ic\left(X_y\left(\bigotimes_{x<n<y} Z_n\right)\otimes Y_x - Y_y\left(\bigotimes_{x<n<y} Z_n\right)\otimes X_x\right)}$ for $y = x + 2$.

There are $2n_s(4n_s - 1)$ couplings of this form in the Hamiltonian. Therefore, Trotter simulation of the free Hamiltonian requires

$$N_{rot} = 20n_s(4n_s - 1) \tag{4.28}$$

single qubit Z-rotations. The focus of this chapter is on fault-tolerant quantum simulation and so the cost of simulation is dominated by the number of non-Clifford operations needed to implement the rotations. Other cost models may not assume Clifford operations can be implemented without cost and the number of CNOT gates required may be of interest. Ignoring the Jordan-Wigner strings, $8n_s(4n_s - 1)$ CNOTs are needed per step. The Jordan-Wigner strings require

$$4 \sum_{n=0}^{4n_s-1} \sum_{k=0}^{n-1} k = 2 \sum_{n=0}^{4n_s-1} n(n-1) = \frac{16}{3} n_s(2n_s - 1)(4n_s - 1) \tag{4.29}$$

CNOT gates. Therefore a single Trotter step requires $\frac{8}{3}n_s(16n_s^2 - 1)$ CNOT gates for the free Hamiltonian. However, the number of CNOT operations can be reduced to $\widetilde{O}(n_s^2)$ using fermionic swap networks [178, 195, 179].

4.2.2 Interaction Circuits

As shown in the previous section, the eQED Hamiltonian potential is a sum of a 2 → 2 term that takes the same form as the non-relativistic case, and a new 1 → 3 term. New circuits will be required to simulate this 1 → 3 term which takes the form $\sum\limits_{j>k>l,m} h_{V\,j,k,l,m} a_j^\dagger a_k^\dagger a_l^\dagger a_m +$ *h.c.*. Using the Jordan-Wigner encoding, $a_j^\dagger a_k^\dagger a_l^\dagger a_m$ can take 4 different forms depending on value of m. For each case below, it is assumed that for all other sites greater than the highest site index and smaller than the lowest index, the local jth operator is simply the identity matrix I_j.

Case 1. $m < l$

$$a_j^\dagger a_k^\dagger a_l^\dagger a_m = \\ -\frac{(X-iY)_j}{2} \otimes \left(\bigotimes_{n=k+1}^{j-1} Z_n \right) \otimes \frac{(X-iY)_k}{2} \otimes \left(\bigotimes_{n=l+1}^{k-1} I_n \right) \otimes \frac{(X-iY)_l}{2} \otimes \left(\bigotimes_{n=m+1}^{l-1} Z_n \right) \otimes \frac{(X+iY)_m}{2} \tag{4.30}$$

Case 2. $m \in [l+1, k-1]$

$$a_j^\dagger a_k^\dagger a_m a_l^\dagger = \\ \frac{(X-iY)_j}{2} \otimes \left(\bigotimes_{n=k+1}^{j-1} Z_n \right) \otimes \frac{(X-iY)_k}{2} \otimes \left(\bigotimes_{n=m+1}^{k-1} I_n \right) \otimes \frac{(X+iY)_m}{2} \otimes \left(\bigotimes_{n=l+1}^{m-1} Z_n \right) \otimes \frac{(X-iY)_l}{2} \tag{4.31}$$

Case 3. $m \in [k+1, j-1]$

$$a_j^\dagger a_m a_k^\dagger a_l^\dagger = \\ -\frac{(X-iY)_j}{2} \otimes \left(\bigotimes_{n=m+1}^{j-1} Z_n \right) \otimes \frac{(X+iY)_m}{2} \otimes \left(\bigotimes_{n=k+1}^{m-1} I_n \right) \otimes \frac{(X-iY)_k}{2} \otimes \left(\bigotimes_{n=l+1}^{k-1} Z_n \right) \otimes \frac{(X-iY)_l}{2} \tag{4.32}$$

Case 4. $m > j$

$$a_m a_j^\dagger a_k^\dagger a_l^\dagger =$$

$$\frac{(X+iY)_m}{2} \otimes \left(\bigotimes_{n=j+1}^{m-1} Z_n\right) \otimes \frac{-(X-iY)_j}{2} \left(\bigotimes_{n=k+1}^{j-1} I_n\right) \otimes \frac{-(X-iY)_k}{2} \otimes \left(\bigotimes_{n=l+1}^{k-1} Z_n\right) \otimes \frac{-(X-iY)_l}{2} \tag{4.33}$$

Suppressing the chains of Z's and identities, the contribution to the Hamiltonian takes the following forms

Case 1.

$$H = -\frac{h_V + h_V^*}{16}(XXXX+XXYY+XYXY-XYYX+YXXY-YXYX-YYXX-YYYY)$$

$$-i\frac{h_V - h_V^*}{16}(XXXY-XXYX-XYXX-YXXX-XYYY-YXYY-YYXY+YYYX) \tag{4.34}$$

Case 2.

$$H = \frac{h_V + h_V^*}{16}(XXXX+XXYY-XYXY-YXXY+YXYX-YYXX+XYYX-YYYY)$$

$$+i\frac{h_V - h_V^*}{16}(-XYYY-YXYY+YYXY-YYYX-YXXX-XYXX+XXYX-XXXY) \tag{4.35}$$

Case 3.

$$H = -\frac{h_V + h_V^*}{16}(XXXX-XXYY+XYXY-YXXY-YXYX+YYXX+XYYX-YYYY)$$

$$-i\frac{h_V - h_V^*}{16}(-XXXY-XXYX+XYXX-YXXX-XYYY+YXYY-YYXY-YYYX) \tag{4.36}$$

Case 4.

$$H = \frac{h_V + h_V^*}{16}(XXXX-XXYY-XYXY+YXXY-XYYX+YXYX+YYXX-YYYY)$$

$$+i\frac{h_V - h_V^*}{16}(XYYY - YXYY - YYXY - YYYX - XXXY - XXYX - XYXX + YXXX). \tag{4.37}$$

Additionally, the eQED Hamiltonian also contains 4 creation/annhilation terms when expressed in the planewave basis. The Jordan Wigner representation of these terms is

$$a_j^\dagger a_k^\dagger a_l^\dagger a_m^\dagger =$$
$$\frac{(X-iY)_j}{2} \otimes \left(\bigotimes_{n=k+1}^{j-1} Z_n\right) \otimes \frac{(X-iY)_k}{2} \otimes \left(\bigotimes_{n=l+1}^{k-1} I_n\right) \otimes \frac{(X-iY)_l}{2} \otimes \left(\bigotimes_{n=m+1}^{l-1} Z_n\right) \otimes \frac{(X-iY)_m}{2} \tag{4.38}$$

$$H = \frac{h_V + h_V^*}{16}(XXXX - XXYY - XYXY - YXXY - XYYX - YXYX - YYXX + YYYY)$$
$$+i\frac{h_V - h_V^*}{16}(XYYY + YXYY + YYXY + YYYX - XXXY - XXYX - XYXX - YXXX). \tag{4.39}$$

From these equations, it can be seen that each term contains every possible tensor product of 4 X's and Y's. In a naïve Trotterization simulation, each term would be treated separately. However, this is suboptimal because all terms with an even number of X's and Y's commute and all terms with an odd number of X's and Y's commute. Previous work has introduced a circuit to simulate all terms with an even number of X's and Y's. It will be shown here that the same techniques can be adapted for the odd case as well. A Hamiltonian that contains all terms with odd numbers of X's and Y's can be efficiently simulated by using a circuit that will simultaneously diagonalize all terms.

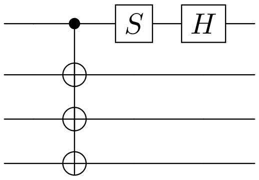

Figure 4.3: Circuit G used to diagonalize all tensor products of an odd number of X's and Y's.

The circuit G can be used to implement time evolution according to a Hamiltonian made out of a sum over the odd tensor products. For example, take

$$H = XXXY - XXYX - XYXX - YXXX - XYYY - YXYY - YYXY + YYYX. \tag{4.40}$$

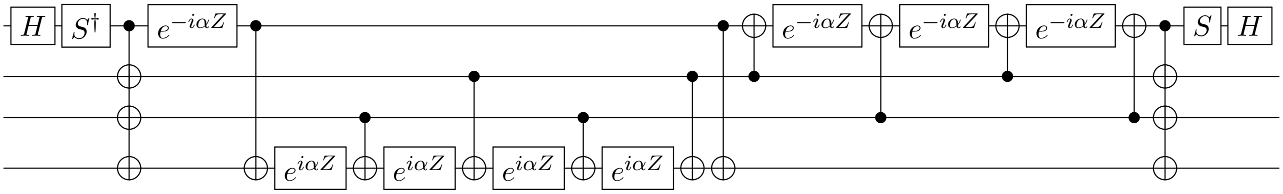

Figure 4.4: Implementation of $e^{i\alpha(XXXY-XXYX-XYXX-YXXX-XYYY-YXYY-YYXY+YYYX)}$

Then using the results in Appendix .4.2 we see that

$$H = G(ZZZZ - ZZZ1 - ZZ11 - Z111 + ZZ1Z + Z11Z + Z1ZZ - Z1Z1)G^\dagger \qquad (4.41)$$

and the resulting circuit in Fig. 4.4 can be used to implement $e^{i\alpha H}$. From Fig. 4.4, it can be seen that single term in the interaction Hamiltonian requires 12 single qubit gates to implement, and 16 CNOT gates in addition to however many CNOT gates are needed to implement the Jordan-Wigner strings. In the position space formulation, there are at most $256n_s^2$ terms and in the momentum space formulation there are at most $8192n_s^3$ terms.

4.3 Cost Estimates for eQED Simulation

The aim of this section is to provide preliminary cost estimates for simulating effective quantum electrodynamics on quantum computers using Trotter-Suzuki approximations and also provide a comparison to the asymptotic scaling expected from a naïve application of qubitization. All such cost estimates are performed within a computational model wherein Clifford gates are free but non-Clifford gates (specifically the T-gate) are not free. We will consider the cost of simulations both for lattice eQED (position space) or momentum space eQED.

4.3.1 Cost Estimates for Lattice eQED

Estimating the trotterization error for eQED requires the computation of nested commutators of terms in the Hamiltonian [196, 190]. The Hamiltonian for eQED in position space is given by

$$H = H_{SLAC} + H_m + H_{int} + H_{L,ext} \qquad (4.42)$$

where

$$H_m = \frac{L^3}{n_s}\sum_{\vec{x}} m\bar{\psi}_x\psi_x = \sum_{\vec{x}} m a_{\vec{x}}^\dagger \gamma^0 a_{\vec{x}}$$

$$H_{L,ext} = -e\frac{L^3}{n_s}\sum_x \bar{\psi}(x)\gamma^\mu\psi(x)A^{ex}_\mu(x) = -\sum_{\vec{x}} e a^\dagger_{\vec{x}}\gamma^0\gamma^\mu A^{ex}_\mu(x)a_{\vec{x}}$$

$$H_{SLAC} = \frac{2\pi}{n_s^{1/3}L}\sum_{\vec{x},\vec{y},\vec{p}} e^{i2\pi n_s^{-\frac{1}{3}}\vec{p}\cdot(\vec{x}-\vec{y})} a^\dagger_{\vec{y}}\gamma^0\gamma^j p_j a_{\vec{x}} =: \sum_{\vec{x},\vec{y}}\sum_{\mu,\mu'} T^{(\mu,\mu')}_{\vec{x},\vec{y}}\, a^\dagger_{\vec{x},\mu}a_{\vec{y},\mu'}$$

$$H_{int} = \sum_{\vec{x}\neq\vec{y}}\sum_{\mu=0}^{3} g_{\mu\mu}\frac{n_s^{1/3}e^2}{8\pi L|\vec{x}-\vec{y}|}(a^\dagger_{\vec{x}}\gamma^0\gamma^\mu a_{\vec{x}})(a^\dagger_{\vec{y}}\gamma^0\gamma^\mu a_{\vec{y}}) =: \sum_{\vec{x}\neq\vec{y}}\sum_{\mu,\mu'} h_{V\,\vec{x},\vec{y}}^{(\mu,\mu',\nu,\nu')}\, a^\dagger_{\vec{x},\mu}a_{\vec{x},\mu'}a^\dagger_{\vec{y},\nu}a_{\vec{y},\nu'}, \tag{4.43}$$

here we have taken the convention that $\vec{x}$ and $\vec{y}$ are 4-vectors of integers and that the indices μ, ν specify one of the components of the 4-vector.

Theorem 1. *Let H be the Hamiltonian of Eq.* (4.42) *with $n_s \geq 8$ sites in the cubic lattice with side-length L and external vector potential operator $A^{ex}(x)$ and let*

$$\Lambda := \max\left(m + e\max_x \|A^{ex}(x)\|, \frac{e^2 n_s}{L}, \frac{n_s^{4/3}}{L}\right) \quad . \tag{4.44}$$

Finally let $|\psi\rangle$ be an eigenstate of H such that $H|\psi\rangle = E|\psi\rangle$. The number of T-gates, N_T, needed to estimate E within error ϵ and constant failure probability less than $1/3$ obeys

$$N_T \in \left(\frac{\Lambda n_s^2}{\epsilon}\right)^{1+o(1)} .$$

Proof. In order to estimate the error in the Trotter-Suzuki approximation, we need to evaluate the commutators between all these terms. A first step towards this is to estimate the commutators between the individual terms involved.

In order to evaluate the commutator terms involving H_{SLAC} we need to estimate the magnitude of these terms. As seen above, this involves estimating an oscillating sum. This expression is symmetric with respect to exchange of x, y, z axis labels and so we will proceed by bounding the coefficient for $k = 1$ (i.e. the x component of the momentum. Further, let $\vec{\Delta} = \vec{x} - \vec{y}$, and p_k be the kth component of vector $\vec{p}$.

$$\begin{aligned} T_{\vec{x},\vec{y}}^{(1,1)} &= \frac{2\pi}{n_s^{\frac{1}{3}} L} \sum_{\vec{p}} p_1 \left(e^{i2\pi n_s^{-\frac{1}{3}} \vec{p}\cdot\vec{\Delta}} \right) \\ &= \frac{2\pi}{n_s^{\frac{1}{3}} L} \left(\sum_{p_1=-n_s^{1/3}/2+1}^{n_s^{1/3}/2} p_1 e^{i2\pi n_s^{-1/3} p_1 \Delta_1} \left(\sum_{p_2,p_3=-n_s^{1/3}/2+1}^{n_s^{1/3}/2} e^{i2\pi n_s^{-1/3}(p_2\Delta_2+p_3\Delta_3)} \right) \right) \end{aligned} \tag{4.45}$$

Next let us assume $\Delta_2 > 0$ and $\Delta_3 > 0$. In this case we have from the formula for the sum of a geometric series that under these circumstances

$$\left| \sum_{p_2=-n_s^{1/3}/2+1}^{n_s^{1/3}/2} e^{i2\pi n_s^{-1/3}(p_2\Delta_2)} \right| = 1 + O(n_s^{-1/3}). \tag{4.46}$$

Similarly, if $\Delta_2 = 0$ then

$$\left| \sum_{p_2=-n_s^{1/3}/2+1}^{n_s^{1/3}/2} e^{i2\pi n_s^{-1/3}(p_2\Delta_2)} \right| = n_s^{1/3}. \tag{4.47}$$

We then have that, for $n_s^{1/3} \geq 2$

$$\begin{aligned} |T_{\vec{x},\vec{y}}^{(1,1)}| &\leq \frac{2\pi}{n_s^{\frac{1}{3}} L} \left| \sum_{p_1=-n_s^{1/3}/2+1}^{n_s^{1/3}/2} p_1 e^{i2\pi n_s^{-1/3} p_1 \Delta_1} \left(\sum_{p_2,p_3=-n_s^{1/3}/2+1}^{n_s^{1/3}/2} e^{i2\pi n_s^{-1/3}(p_2\Delta_2+p_3\Delta_3)} \right) \right| \\ &\leq \frac{2\pi}{n_s^{\frac{1}{3}} L} \left(\sum_{p_1=-n_s^{1/3}/2+1}^{n_s^{1/3}/2} |p_1| \left| \sum_{p_2,p_3=-n_s^{1/3}/2+1}^{n_s^{1/3}/2} e^{i2\pi n_s^{-1/3}(p_2\Delta_2+p_3\Delta_3)} \right| \right) \\ &\in O\left(\frac{1}{n_s^{\frac{1}{3}} L} \left(\sum_{p_1=-n_s^{1/3}/2}^{n_s^{1/3}/2} |p_1| (1+\delta_{\Delta_2,0} n_s^{1/3})(1+\delta_{\Delta_3,0} n_s^{1/3}) \right) \right) \\ &\subseteq O\left(\frac{1}{n_s^{\frac{1}{3}} L} \left(\frac{n_s^{1/3}}{2} \left(\frac{n_s^{1/3}}{2} + 1 \right) (1+\delta_{\Delta_2,0} n_s^{1/3})(1+\delta_{\Delta_3,0} n_s^{1/3}) \right) \right) \\ &\subseteq O\left(\frac{n_s^{1/3}}{L} (1+\delta_{\Delta_2,0} n_s^{1/3})(1+\delta_{\Delta_3,0} n_s^{1/3}) \right) \end{aligned} \tag{4.48}$$

By symmetry, the exact same bound holds by permuting the labels of the indices,

$$|T_{\vec{x},\vec{y}}^{(\chi,\chi)}| \in O\left(\frac{n_s^{1/3}}{L}(1+\delta_{\Delta_{\chi+1 \bmod 3+1},0}n_s^{1/3})(1+\delta_{\Delta_{\chi+2 \bmod 3+1},0}n_s^{1/3})\right) \tag{4.49}$$

The exact same argument can be applied to find a similar expression for $|T_{\vec{x},\vec{y}}^{(\chi,\xi)}|$ for $\xi \neq \chi$. Specifically, it can be shown that for each χ, ξ there exist $f, g \in \{1,2,3\}$ such that

$$|T_{\vec{x},\vec{y}}^{(\chi,\xi)}| \in O\left(\frac{n_s^{1/3}}{L}(1+\delta_{\Delta_f,0}n_s^{1/3})(1+\delta_{\Delta_g,0}n_s^{1/3})\right) \tag{4.50}$$

Next it is straightforward to see that for each of the n_s terms in H_m, their coefficients are at most m. The situation for H_{int} is a little more complicated since the coefficients for a given term vary with the distance between $\vec{x}$ and $\vec{y}$. It is useful for us to envision a probability distribution over the possible coefficients that emerge in the expansion. Let V be a random variable drawn from a uniform distribution over upper bounds on the coefficients of T. It follows from the above discussion that there exist constants κ_1 and κ_2 such that the distribution on the upper bounds on the coefficients for the creation operators in the potential term obeys

$$P\left(V \le (\kappa_1 e^2/L)\right) \in O(1), \qquad P\left(V \ge (\kappa_2 e^2 n_s^{1/3}/L)\right) \in O(1/n_s). \tag{4.51}$$

Thus we have that the expectation value of V satisfies

$$\mathbb{E}(V) \in O\left(\frac{e^2}{L}\right) \tag{4.52}$$

Similarly, from the previous discussion it follows that if we define W to be a random variable found by sampling $T_{\vec{x},\vec{y}}^{(\chi,\xi)}$ we find that there exist constants K_1, K_2, K_3, K_4 such that the sampled upper bound on the coefficients reads

$$\begin{gathered} P\left(W \le \left(\frac{K_1 n_s^{\frac{1}{3}}}{L}\right)\right) \in O(1), \\ P\left(W \in \left[\frac{K_2 n_s^{2/3}}{L}, \frac{K_3 n_s^{2/3}}{L}\right]\right) \in O(1/n_s^{1/3}), \\ P\left(W \ge \left(\frac{K_4 n_s}{L}\right)\right) \in O(1/n_s^{2/3}) \end{gathered} \tag{4.53}$$

Hence the expectation value of W satisfies

$$\mathbb{E}(W) \in O\left(\frac{n_s^{1/3}}{L}\right). \tag{4.54}$$

Thus since $W > 0$ we have from Chebyshev's inequality that for any constant $\delta > 0$, $P(W \geq \delta\mathbb{E}(W)) \in O(1/\delta)$. Thus from the union bound for independent and identically distributed variables $W_1, \ldots, W_N$, $P(W_1 \cdots W_N \geq \delta\mathbb{E}(W)^N) \in O(N/\delta)$. Therefore taking $\delta \in \Theta(n_s^{\lambda N})$ for some constant $\lambda > 0$ yields $P(W_1 \cdots W_N \geq (n_s^{\lambda}\mathbb{E}(W))^N) \in O(N n_s^{-\lambda N})$. Thus because $W \in O(n_s/L)$ for all inputs,

$$W^N \in N\mathbb{E}(W)^{N+O(1)}. \tag{4.55}$$

The exact same reasoning implies that V^N is similarly bounded.

Now let us consider all commutators consisting of N_m mass terms, N_{ext} external potential terms, N_T kinetic terms and N_V two-body interaction terms. Each such commutator is a Lie-product between even monomials of creation and annihilation operators of degree at most 4. Each commutator at most doubles the number of terms in the polynomial and increases the degree of each monomial by at most 4. For example, we have that if $\phi_{s_1}\phi_{s_2}\phi_{s_3}\phi_{s_4}$ is a monomial taken from the set $\phi \in \{a_1^\dagger, a_1, \ldots, a_{n_s}^\dagger, a_{n_s}, 1\}$ that for any polynomial in the creation and annihilation operators of degree d, P, which can be expressed as $P = \sum_j c_j \phi_{\sigma_{j,1}} \cdots \phi_{\sigma_{j,d}}$ we have that

$$\begin{aligned}[\phi_{s_1}\phi_{s_2}\phi_{s_3}\phi_{s_4}, P] &= \sum_j c_j [\phi_{s_1}\phi_{s_2}\phi_{s_3}\phi_{s_4}, \phi_{\sigma_{j,1}} \cdots \phi_{\sigma_{j,d}}] \\ &= \sum_{j:\{\phi_s\}\bigcap\{\phi_{\sigma_{j,1}}\cdots\phi_{\sigma_{j,d}}\}\not\subseteq\{\emptyset,1\}} c_j [\phi_{s_1}\phi_{s_2}\phi_{s_3}\phi_{s_4}, \phi_{\sigma_{j,1}} \cdots \phi_{\sigma_{j,d}}]\end{aligned} \tag{4.56}$$

Therefore there exists a polynomial Q of degree at most $d+4$ in the elements of ϕ and a sequence $\Sigma_{\ell,j}$ such that

$$Q = \sum_\ell \gamma_\ell \phi_{\Sigma(\ell,1)} \cdots \phi_{\Sigma(\ell,d+4)} = [\phi_{s_1}\phi_{s_2}\phi_{s_3}\phi_{s_4}, P], \tag{4.57}$$

where $\max(|\gamma_\ell|) = \max(|c_j|)$ and $|\{\gamma_\ell\}| \leq 2|\{c_j : \{\phi_s\}\bigcap\{\phi_{\sigma_{j,1}} \cdots \phi_{\sigma_{j,d}}\} \not\subseteq \{\emptyset, 1\}\}| \leq 2|\{c_j\}|$ If we consider an initial term P_0 to be of the form $\phi_{t_1}\phi_{t_2}\phi_{t_3}\phi_{t_4}$ then it is easy to validate that for any $\phi_{s_1}\phi_{s_2}\phi_{s_3}\phi_{s_4}$, $[\phi_{t_1}\phi_{t_2}\phi_{t_3}\phi_{t_4}, c\phi_{s_1}\phi_{s_2}\phi_{s_3}\phi_{s_4}]$ is at most an eighth-order polynomial with coefficients at most c. Therefore we have by induction that for any sequence χ

$$\|[\phi_{\chi_{1,\ell}}\phi_{\chi_{2,\ell}}\phi_{\chi_{3,\ell}}\phi_{\chi_{4,\ell}},[\cdots,[\phi_{\chi_{1,2}}\phi_{\chi_{2,2}}\phi_{\chi_{3,2}}\phi_{\chi_{4,2}},\phi_{\chi_{1,1}}\phi_{\chi_{2,1}}\phi_{\chi_{3,1}}\phi_{\chi_{4,1}}]\cdots]]\| \le 2^\ell \max_j \|\phi_j\|^{4\ell} = 2^\ell \tag{4.58}$$

By setting $\ell = N_m + N_{\rm ext} + N_T + N_V$, it therefore follows that the expectation value over indices $\vec{x}, \vec{y}$, the norm of the commutators of such terms is with constant probability greater than 2/3, from the triangle inequality, Eq. (4.55) and the sub-multiplicative property of the operator norm, in

$$\begin{aligned}
&O(2^\ell \|H_m + H_{L,ext}\|^{N_m+N_{ext}}(N_T N_V)(\mathbb{E}(V))^{N_T}\mathbb{E}(W)^{N_V})\\
&\subseteq 2^{N_m+N_{ext}+N_T+N_V} N_T N_V (m + e\max_{\vec{x}}\|A^{ex}(x)\|)^{N_m+N_{ext}}(\max(\kappa_1,\kappa_2)e^2/L)^{N_T+O(1)}\\
&\qquad \times (\max(K_1,K_2,K_3,K_4)/(n_s^{1/3}L))^{N_V+O(1)})\\
&\subseteq 3^{N_m+N_{ext}+N_T+N_V}(m + e\max_{\vec{x}}\|A^{ex}(x)\|)^{N_m+N_{ext}}(\max(\kappa_1,\kappa_2)e^2/L)^{N_T+O(1)}\\
&\qquad \times (\max(K_1,K_2,K_3,K_4)/(n_s^{1/3}L))^{N_V+O(1)})
\end{aligned} \tag{4.59}$$

The maximum number of non-zero commutators that can arise in the commutator series can be bounded using the following argument. Let us consider the simplest non-trivial commutator which is of the form $[a_x^\dagger a_y, a_u^\dagger a_v]$. There are clearly $O(n_s^4)$ possible combinations. However, unless the sets $\{x,y\}$ and $\{u,v\}$ have a non-empty intersection the commutator is zero. Therefore there are actually $O(n_s^3)$ rather than $O(n_s^4)$ possible non-zero commutators of this form. Iterating this, it is clear that there are $O(n_s^4)$ non-zero commutators of the form $[a_s^\dagger a_u,[a_x^\dagger a_y, a_u^\dagger a_v]]$. In general it follows by induction that for the k-fold nested commutator (if $k \in O(1)$) that there are at most n_s^{1+k} such terms.

The situation is even more constrained with terms that arise from the external potential as well as the mass. Such terms consist of creation and annihilation operators that only act on one fermion site (and 4 potential components). Therefore for each such term introduced the site must match one of the other terms in the commutator product otherwise the commutator will be zero. Thus the number of non-zero commutators in a k-fold nested commutator series, where $k \in O(1)$, is also in $O(1)$.

Thus combining these two observations we see that the total number of non-zero commutators that can be formed from a general product is in

$$O(n_s^{1+N_V+N_T})\,. \tag{4.60}$$

Thus the sum over all terms formed by these commutators is simply the number of commutators multiplied by the expectation value of the coefficients. We can use the expression in Eq. (4.59) to estimate the sum over all commutators by simply multiplying the mean by the number of commutator terms in (4.60). This yields

$$O\left(n_s 3^{N_m+N_{ext}+N_T+N_v}\left(m+e\max_x\|A^{ex}(x)\|\right)^{N_m+N_{ext}}\left(\frac{e^2 n_s}{L}\right)^{N_T+O(1)}\left(\frac{n_s^{4/3}}{L}\right)^{N_V+O(1)}\right) \tag{4.61}$$

Next let $\Lambda := \max\left(m+e\max_x\|A^{ex}(x)\|, \frac{e^2 n_s}{L}, \frac{n_s^{4/3}}{L}\right)$. The sum of over all commutators with $N_m+N_{ext}+N_T+N_v=\ell$ is then in

$$n_s\Lambda^{\ell+O(1)}e^{O(\ell)} \tag{4.62}$$

Therefore the size of any commutator that arises from the expansion of the error in the Trotter-Suzuki formula, using time-step t, is in

$$n_s(\Lambda t)^{\ell}e^{O(\ell)} \tag{4.63}$$

It then follows from Theorem 6 of [190] that the Trotter-Suzuki error for a p^{th} order formula is therefore in

$$\Delta_{TS}(p)\in n_s(\Lambda t)^{p+1}e^{O(p)}. \tag{4.64}$$

Thus we can choose t such that the error, Δ_{TS} is at most ϵ_{TS} for

$$t\in O\left(\frac{1}{\Lambda}\left(\frac{\epsilon_{TS}}{n_s\Lambda^{O(1)}}\right)^{1/(p+1)}\right) \tag{4.65}$$

Next note that each product formula of order p consists of a product of $5^{p/2-1}$ second-order Trotter formulas. Each such product formula is composed of $O(n_s^2)$ exponentials. Therefore we have that the number of exponentials in the product formula is [44]

$$N_{\exp}=O\left(n_s^2 5^{p/2-1}\right)\ . \tag{4.66}$$

Next let $U_{\text{TS}}(t)$ be the Trotter-Suzuki formula for e^{-iHt}. If we apply phase estimation to $U_{\text{TS}}(t)$ the eigenvalues returned are, with high probability, those of Ht. Therefore if we wish to estimate the eigenvalues of H within error $O(\epsilon_{\text{TS}})$ the phase estimation protocol requires $O(1/(\epsilon_{\text{TS}}t))$ repetitions. We choose the error in the phase estimation protocol to be in $\Theta(\epsilon_{TS})$ because we want to ensure that $\epsilon_{PE}+\epsilon_{TS}\le\epsilon$ where ϵ is our total error tolerance. This can be attained by choosing $\epsilon_{PE}\in\Theta(\epsilon_{TS})$ as we do here.

The cost of performing phase estimation and estimating the energy within error $\epsilon =$

$\Theta(\epsilon_{TS} t)$ and probability of failure $\delta < 1/3$ is in

$$O\left(\frac{N_{\rm exp}}{\epsilon_{\rm TS} t}\right) \subseteq O\left(\frac{n_s^{2+1/(p+1)}\Lambda^{1+o(1)}5^{p/2}}{\epsilon_{\rm TS}^{1+1/(p+1)}}\right) . \tag{4.67}$$

In practice, however, we only guarantee that $\|e^{-iHt} - U_{\rm TS}(t)\| \le \epsilon_{\rm TS}$ and need to ensure that the errors in the eigenvalues of the unitaries are comparable. The necessary result follows from Theorem 6.3.2 of [197] and using this result and the fact that unitary matrices are unitarily diagonalizable that if $\lambda_x(\cdot)$ is the $x^{\rm th}$ eigenvalue of a matrix then for any x there exists a y such that

$$|\lambda_x(e^{-iHt}) - \lambda_y(U_{\rm TS}(t))| \le \|e^{-iHt} - U_{\rm TS}(t)\| \le \epsilon_{TS} . \tag{4.68}$$

Next, choosing the error from this step such that $\epsilon_{\rm TS} \in \Theta(\epsilon)$ we then have after optimizing over the value of p as per [44] the number of exponentials needed for the simulation is in

$$O\left(\frac{N_{\rm exp}}{\epsilon t}\right) \subseteq \left(\frac{\Lambda^{1+o(1)} n_s^{2+o(1)}}{\epsilon^{1+o(1)}}\right) . \tag{4.69}$$

Gate complexity estimates then easily follow from Eq. (4.69). The exponential that requires the most T-gates to simulate is given in Fig. 4.4. It consists of 8 Pauli operations. From Box 4.1 of Nielsen and Chuang [54], it suffices to synthesize each rotation within error $\epsilon/N_{\rm exp}$. Using an optimal synthesis method, such as [198, 199] this can be achieved using $O(\log(N_{\rm exp}/\epsilon))$ T-gates. Therefore the number of T-gates needed for the simulation is in

$$N_T \in \left(\frac{\Lambda n_s^2}{\epsilon}\right)^{1+o(1)} . \tag{4.70}$$

$\square$

A key assumption in eQED is that the mass energy of the electrons dominates the momentum contributions. This is necessary because the derivation of eQED truncates the path integral expansion of the propagator at second order. The case that most closely resembles the canonical case in the electronic structure literature is where $n_s^{1/3}/L \ll m \ll n_s^{4/3}/L$ [178, 200, 201]. In this non-relativistic case considered in the electronic structure literature, the mass energy of the electron is not included and so the Trotter error is dominated by the momentum of the terms in the Hamiltonian and the number of T gates needed for the simulation scales as $N_T \in (n_s^{10/3}/L\epsilon)^{1+o(1)}$. If we consider the thermodynamic limit where $L \in \Theta(n_s^{1/3})$, we then have that $N_T \in (n_s^3/\epsilon)^{1+o(1)}$. This result is comparable to some of the earlier results for simulations of electronic structure in local-bases [178], but does not precisely match these bounds because of the use of the SLAC kinetic operator, which is much less local than the corresponding kinetic operator used in planewave-dual simulations [178, 190].

4.3.2 Cost Estimates for Momentum Basis Simulations using Trotter

The calculation of the norm of the nested commutators for the momentum space Hamiltonian are needed to estimate the Trotterization error for the momentum space simulation. Fortunately, these nested commutators are much easier to evaluate than their position space brethren because of the lack of summation over auxiliary indices in the definition of the interaction and constraint terms in the Hamiltonian.

Theorem 2. *Let H_p be the momentum space effective QED Hamiltonian of Eq.* (4.17) *and Eq.* (4.24) *in three spatial dimensions in a cavity of volume L^3 with electrons of mass m and charge $e \in O(1)$ and external vector potential A^{ex} such that for any momentum mode within the reciprocal lattice, $|E_p - m| \in o(1)$. Then, there exists a quantum algorithm that when provided a state $|\psi\rangle$ such that $H_p |\psi\rangle = E |\psi\rangle$, the energy value E can be estimated within error ϵ for any $\epsilon > 0$ and failure probability at most $1/3$ using a number of T-gates that is in*

$$\left(\frac{n_s^3 \Lambda_p}{\epsilon}\right)^{1+o(1)},$$

where $\Lambda_p = O\left(n_s\left(\frac{m}{n_s} + \frac{e^2 n_s}{L} + e|A^{ex}|\right)\right)$.

Proof. The Hamiltonian is the sum of three terms, the kinetic energy term, the electron-electron interaction term and the external potential term. First let us consider the kinetic term, which is trivial in a momentum basis

$$H = \sum_{\sigma,\nu} C_{\sigma,\nu}(a^\dagger_{\sigma,\nu} a_{\sigma,\nu} + b^\dagger_{\sigma,\nu} b_{\sigma,\nu}) \tag{4.71}$$

where

$$C_{\sigma,\nu} := E_\nu = \sqrt{m^2 + \frac{4\pi^2}{L^2}|\vec{\nu}|^2} \in \Theta(m) \tag{4.72}$$

The two-body interactions are much more complicated in momentum representation. For example, the fermion-fermion interaction can be written as

$$\sum_{p,q,r,\sigma_1,\sigma_2,\sigma_3,\sigma_4} e^2 D_{p,q,r,\sigma_1,\sigma_2,\sigma_3,\sigma_4} a^\dagger_{(p+q-r),\sigma_4} a^\dagger_{r,\sigma_3} a_{q,\sigma_2} a_{p,\sigma_1}, \tag{4.73}$$

where

$$|D_{p,q,r,\sigma_1,\sigma_2,\sigma_3,\sigma_4}| \leq \frac{\mathcal{M}}{4L^3\sqrt{E_{p+q-r}E_r E_p E_q}} \in \Theta\left(\frac{\mathcal{M}}{L^3 m^2}\right) . \tag{4.74}$$

Here for convenience we take $\mathcal{M}$ an upper bound on the values of the coefficients in Eq. (34), (35), (36), (37) and (38). By doing so we make the result of (4.74) hold for all the two body interactions in the problem. First, we see that (in units where $e = 1$)

$$\begin{aligned}\mathcal{M} &\in O\left(\max_{p,q}\left(\frac{\max_j\{\|u_j(p)\|^4, \|v_j(p)\|^4\}}{|(E_p - E_q)^2 - \frac{4\pi^2}{L^2}|\vec{p}-\vec{q}|^2|}\right)\right)\\ &\subseteq O\left(\max_{p}\left(\frac{(E_p + m)^2}{\min_q |(E_p - E_q)^2 - |\vec{p}-\vec{q}|^2/L^2|}\right)\right)\\ &\subseteq O\left(m^2 L^2\right)\end{aligned} \tag{4.75}$$

Therefore,

$$|D_{p,q,r,\sigma_1,\sigma_2,\sigma_3,\sigma_4}| \in O\left(\frac{1}{L}\right). \tag{4.76}$$

The exact same scaling holds by inspection for every two body term in the momentum space Hamiltonian.

The external potential (in momentum space) is given by Eq. (4.24). The Hamiltonian in this case can be chosen (in units where $e = 1$) to be

$$H_{p,ext} = \sum_{\sigma_1,\sigma_2,p,q} E_{\sigma_1,\sigma_2,p,q} a_p^\dagger a_q \tag{4.77}$$

where

$$|E_{\sigma_1,\sigma_2,p,q}| \in O\left(\frac{\max_p |u_p|^2 e \max|A^{ex}|}{m}\right) \subseteq O\left(\frac{\max_p (E_p + m) e \max|A^{ex}|}{m}\right) \subseteq O(e|A^{ex}|). \tag{4.78}$$

Next let us consider a Lie-Polynomial of kinetic, mass, interaction and external potential terms consisting of $N_m, N_{\text{ext}}, N_T, N_V$ mass, external potential, kinetic and two-body interaction terms. As noted above, the indices for each mass term must match the indices of existing terms in the polynomial; whereas all other terms must match at least one term. Therefore the total number of valid commutators that can be present is in

$$O(n_s^{1+N_{\text{ext}}+2N_V}). \tag{4.79}$$

Next, let us assume that $N_{\text{ext}} + N_T + N_V = \ell$. We can then see that the sum of all nested commutators of order ℓ is in

$$
\begin{aligned}
&O\left(2^{\ell}(\max_{\sigma,\nu}|C_{\sigma,\nu}|^{N_T}\max_{\substack{p,q,r,\\ \sigma_1,\sigma_2,\sigma_3,\sigma_4}}|D_{p,q,r,\sigma_1,\sigma_2,\sigma_3,\sigma_4}|^{N_v}+\max_{p,q,\sigma_1,\sigma_2}|E_{p,q,\sigma_1,\sigma_2}|^{N_{ext}}n_s^{1+N_{ext}+2N_V})\right)\\
&\subseteq O\left((2n_s)^{\ell}\left(\frac{(\max_{\sigma,\nu}|C_{\sigma,\nu}/n_s|}{n_s}\right)^{N_T}\max_{\substack{p,q,r,\\ \sigma_1,\sigma_2,\sigma_3,\sigma_4}}(e^2|D_{p,q,r,\sigma_1,\sigma_2,\sigma_3,\sigma_4}|)^{N_v}\left(n_s\max_{p,q,\sigma_1,\sigma_2}|E_{p,q,\sigma_1,\sigma_2}|\right)^{N_{ext}}\right)
\end{aligned}
\tag{4.80}
$$

Next if we let

$$
\begin{aligned}
\Lambda_p &:= \max\left\{\frac{\max_{\sigma,\nu}|C_{\sigma,\nu}/n_s|}{n_s},\ \max_{\substack{p,q,r,\\ \sigma_1,\sigma_2,\sigma_3,\sigma_4}} e^2|D_{p,q,r,\sigma_1,\sigma_2,\sigma_3,\sigma_4}|,\ n_s\max_{p,q,\sigma_1,\sigma_2}|E_{p,q,\sigma_1,\sigma_2}|\right\}\\
&\in O\left(n_s\left(\frac{m}{n_s}+\frac{e^2 n_s}{L}+e\max|A^{ex}|\right)\right)
\end{aligned}
\tag{4.81}
$$

We then have from Theorem 6 of [190] that the error in the p^{th}-order Trotter-Suzuki formula is

$$
\Delta_{TS}(p)\in n_s(\Lambda_p t)^{p+1}e^{O(p)}.
\tag{4.82}
$$

Thus if we wish to have $\Delta_{TS}(p)\le\epsilon_{TS}$ then it suffices to choose

$$
t\in\Theta\left(\frac{1}{\Lambda_p}\left(\frac{\epsilon_{TS}}{n_s}\right)^{1/(p+1)}\right)
\tag{4.83}
$$

We can then invoke Eq. (4.68) to show that this corresponds to a systematic error of at most ϵ_{TS} in the eigenvalues of e^{-iHt} that arises from the Trotter-Suzuki approximation. Let us define the correct eigenphase that we would see from phase estimation to be Et and the approximate phase $\widetilde{E}_{TS}t$. This means we can use phase estimation on the Trotter-Suzuki approximation to learn the eigenphase $\widetilde{E}_{TS}t$ within error $\epsilon_{TS}t$ and probability of failure less than $1/3$ using $O(1/\epsilon_{TS}t)$ applications of the Trotter-Suzuki formula [202]. Thus the total number of operator exponentials that need to be invoked in the simulation in order to learn the $\widetilde{E}t$ within error $O(\epsilon_{TS}t)$ is in

$$
O\left(\frac{N_{\exp}}{\epsilon_{\mathrm{TS}}t}\right)\subseteq O\left(\frac{n_s^{3+1/(p+1)}\Lambda_p 5^{p/2}}{\epsilon_{\mathrm{TS}}^{1+1/(p+1)}}\right),
\tag{4.84}
$$

Provided that $t(\|H\| + \epsilon_{TS}) \leq \pi$, we can unambiguously infer E from this result by taking

$$E = \frac{\widetilde{E}t}{t} + O(\epsilon_{TS}), \tag{4.85}$$

which implies that this estimate also suffices to provide E within error $O(\epsilon_{TS})$ with probability at least $2/3$.

The final step involves following the reasoning laid out in [44, 190] to choose p to minimize the number of operator exponentials needed to achieve error $\epsilon \geq \epsilon_{\rm TS}$. This corresponds to taking $p \in O(\sqrt{\log(n_s t/\epsilon)})$, which when substituted into Eq. (4.84) leads to a number of operator exponentials that scales as $(\frac{n_s^3\Lambda_p}{\epsilon})^{1+o(1)}$, where $(\cdot)^{o(1)}$ is used to refer to factors that are at most sub-polynomial (but not necessarily poly-logarithmic).

We then see from our circuit constructions that each operator exponential requires a number of T gates that scales as $O(\log(n_s\Lambda t/\epsilon))$ thus the number of T-gates required by the simulation obeys

$$N_T \in \left(\frac{n_s^3\Lambda_p}{\epsilon}\right)^{1+o(1)}. \tag{4.86}$$

$\square$

The asymptotics of the simulation complexity in momentum space are interesting for a number of reasons. First, let us consider the case where the two-body interaction term dominates the Trotter-Suzuki error. This occurs when $\frac{n_s^{1/3}}{L} \ll m \ll \frac{n_s^2}{L}$. Note that we require that the lower bound hold in order to justify the assumptions in Theorem 2 as well as to ensure that we remain in the situation where effective QED, rather than full QED, is appropriate. In the thermodynamic limit, we take $L \propto n_s^{1/3}$ and therefore have that

$$N_T^{therm} \in \left(\frac{n_s^{4+2/3}}{\epsilon}\right)^{1+o(1)} \tag{4.87}$$

The continuum limit, unfortunately, is not naturally defined without making further promises on the system. This is because in the continuum limit we need to take $L \in o(n_s^{1/3})$, which leads to momentum modes where the kinetic contribution to the energy dominates the mass energy. Such modes invalidate our assumptions and so effective QED cannot be considered valid in the continuum limit for finite mass electrons without imposing restrictions on the input state. Note that these issues arise for both the position and momentum space formulations of eQED. Taking the continuum limit is also complicated by the issue of renormalization. To ensure the electron mass takes the correct value and the potential between two electrons has the correct $1/r$ dependence, the electron mass and charge in the Hamiltonian must be varied as a function of the lattice spacing. For the continuum limit of QED, this leads to the electron charge being forced to zero as the lattice spacing goes to zero. This is known as triviality and is due to QED likely not being a valid interacting field theory when defined without a cutoff [203, 204, 205, 206].

4.3.3 Cost Estimates for Qubitization

In recent years, qubitization has emerged as an alternative to Trotter-Suzuki simulations on fault tolerant hardware [207, 38, 208, 209, 210, 201]. Unlike Trotter-Suzuki methods, qubitization is known to saturate lower bounds on the query complexity for quantum simulation. Further, it is much simpler to provide tight bounds for the complexity of simulation using qubitization [191]. However, qubitization is not space optimal and further cannot directly exploit locality of the Hamiltonian to reduce the costs of simulation unlike Trotter-Suzuki methods. For these reasons, qubitization does not supplant Trotter-Suzuki methods but rather provide us with a new set of tools that can perform favorably to Trotter-Suzuki methods under certain circumstances.

The central idea of qubitization is that a walk operator, $W \in \mathbb{C}^{(N+M)\times(N+M)}$, can be constructed for any Hamiltonian such that if $H = \sum_j \lambda_j H_j \in \mathbb{C}^{N\times N}$ for unitary H_j then for every eigenvector $|\psi\rangle$ of H and any integer q, $W^q |\psi\rangle |0\rangle^M$ is a vector within a two dimensional subspace spanned by the non-orthogonal vectors $|\psi\rangle |0\rangle^M$ and $W|\psi\rangle |0\rangle^M$. Further let $\lambda = \sum_{j=1}^m |\lambda_j|$. With these assumptions in place, if we define $|\psi\rangle^\perp$ to be the orthogonal component of $W|\psi\rangle |0\rangle^M$, then within the basis $|\psi\rangle |0\rangle^M$ and $\left|\psi^\perp\right\rangle$, the walk operator restricted to this two-dimensional subspace then takes the form

$$(|\psi\rangle\langle\psi| \otimes |0\rangle\langle 0| + \left|\psi^\perp\right\rangle\left\langle\psi^\perp\right|)W(|\psi\rangle\langle\psi| \otimes |0\rangle\langle 0| + \left|\psi^\perp\right\rangle\left\langle\psi^\perp\right|) = \begin{bmatrix} \frac{\langle\psi|H|\psi\rangle}{\lambda} & -\sqrt{1-\frac{\langle\psi|H|\psi\rangle^2}{\lambda^2}} \\ \sqrt{1-\frac{\langle\psi|H|\psi\rangle^2}{\lambda^2}} & \frac{\langle\psi|H|\psi\rangle}{\lambda} \end{bmatrix} \tag{4.88}$$

which is isospectral to the rotation $e^{-iY\cos^{-1}(\langle\psi|H|\psi\rangle/\lambda)}$.

This shows that if the eigenvalues of H can be estimated, given knowledge of λ, we can then construct an estimator $\hat{E}$ for the energy, from an estimator for the phase $\hat{\phi}$ using [209, 211]

$$\hat{E} = \lambda \cos\left(\hat{\phi}\right). \tag{4.89}$$

Thus the energy can be estimated within error ϵ using $O(\lambda/\epsilon)$ applications of W [209]. The position space normalization can be found by examining the Jordan-Wigner representation of each of the terms individually. Specifically, we have that for each $\vec{x}$, $a_{\vec{x}}^\dagger$ is expressed as a sum of 2 Pauli-operators in the Jordan-Wigner representation. Since Pauli operators are unitary we can compute the asymptotic scaling of any term in the Hamiltonian by treating the fermionic operators as if they were unitary because only constant factors are introduced by expanding the Jordan-Wigner representation. We further have that $\lambda = \lambda_m + \lambda_{ext} + \lambda_{int} + \lambda_{SLAC}$, which are the contributions to the normalization terms from the mass, external vector potential and the kinetic operator. These expressions are straightforward to compute

$$
\begin{aligned}
H_m &= \sum_{\vec{x}} m a_{\vec{x}}^\dagger \gamma^0 a_{\vec{x}} \Rightarrow \lambda_m \in O(m n_s) \\
H_{L,ext} &= \sum_{\vec{x}} e a_{\vec{x}}^\dagger \gamma^0 \gamma^\mu A_\mu^{ex}(\vec{x}) a_{\vec{x}} \Rightarrow \lambda_{ext} \in O\left(n_s e \max_{\vec{x}} |A^{ex}(\vec{x})|\right) \\
H_{SLAC} &= \frac{2\pi}{n_s^{1/3} L} \sum_{\vec{x},\vec{y},\vec{p}} e^{-i2\pi n_s^{-1/3} \vec{p}\cdot(\vec{x}-\vec{y})} a_{\vec{x}}^\dagger \gamma^0 \gamma^j p_j a_{\vec{x}} \Rightarrow \lambda_{SLAC} \in O\left(\frac{n_s^{5/3}}{L}\right) \\
H_{int} &= \sum_{\vec{x}\neq\vec{y}} \sum_{\mu,\nu} g_{\mu\mu} \frac{n_s^{1/3} e^2}{8\pi L |\vec{x}-\vec{y}|} (a_{\vec{x}}^\dagger \gamma^0 \gamma^\mu a_{\vec{x}})(a_{\vec{y}}^\dagger \gamma^0 \gamma^\nu a_{\vec{y}}) \Rightarrow \lambda_{int} \in O\left(\frac{n_s^2 e^2}{L}\right),
\end{aligned}
\tag{4.90}
$$

where the last expression in Eq. (4.90) follows from the average over position of $1/|\vec{x}-\vec{y}|$ given in (4.52). We therefore have that the normalization constant in position space eQED is

$$
\lambda_{pos} \in O\left(m n_s + n_s e \max_{\vec{x}} |A^{ex}(\vec{x})| + (n_s^{-1/3} + e^2)\frac{n_s^2}{L})\right)
\tag{4.91}
$$

It is straightforward to compute the values of λ for the momentum space formalism for eQED under worst-case assumptions about the functional form of the external vector potential $A^{ex}(x)$:

$$
\lambda_{mom} \in O\left(m n_s + \frac{n_s^3}{L} + n_s^2 e \max_{\vec{x}} |A^{ex}(\vec{x})|\right)
\tag{4.92}
$$

More specifically, the walk operator is constructed from a pair of unitary operations `SELECT` and `PREPARE`. For simplicity let us assume without loss of generality that $\lambda_j \geq 0$ (any signs or phases can be absorbed into the H_j). The operator `PREPARE` is defined to prepare an initial state

$$
\texttt{PREPARE}\,|0\rangle = \frac{1}{\sqrt{m}} \sum_j \sqrt{\frac{\lambda_j}{\lambda}}\,|j\rangle\,.
\tag{4.93}
$$

Note the operation of `PREPARE` on states other than $|0\rangle$ is not specified here because any unitary matrix that satisfies Eq. (4.93) can be used to construct the walk operator W.

The action of select is similarly defined via

$$
\texttt{SELECT}\,|j\rangle\,|\psi\rangle = |j\rangle\,H_j\,|\psi\rangle\,.
\tag{4.94}
$$

The walk operator W is then defined to be

$$W := (1 - 2\texttt{PREPARE}\,|0\rangle\langle 0|\,\texttt{PREPARE}^{\dagger})\texttt{SELECT}. \tag{4.95}$$

It is then clear from this exposition that the cost of performing the quantum simulation depends directly on two quantities: the normalization constant λ and the costs of performing `SELECT` and `PREPARE`. The costs, however, depend sensitively on the construction used for these two operations and the circuit constructions for the two operations are complicated relative to those used in Trotter-Suzuki simulations.

For simplicity, we will adapt the construction of [200, 209] which was derived for simulations of non-relativistic chemistry in an arbitrary basis to the relativistic case considered here. The prepare circuit is implemented using a memory access model known as a QROM, which can be thought of as an oracle replacement that uses a lookup table to store each of the unique amplitudes in the state $\texttt{PREPARE}\,|0\rangle$. If there are K such amplitudes then the cost of preparing the state within error ϵ is in $O(K + \log(1/\epsilon))$ using the approach outlined in Section 3.D of [209].

The number of unique coefficients in the position space Hamiltonian, K_{pos}, is substantially lower than the number of terms in the Hamiltonian. While the number of terms in the postion space Hamiltonian is in $O(n_s^2)$ only $O(n_s)$ of these can take unique values. This can easily be seen from Eq. (4.90) wherein H_m only takes $O(1)$ values, $H_{L,ext}$ takes at most $O(n_s)$ values (assuming each $A^{ex}(\vec{x})$ is unique). H_{SLAC} contains $O(n_s^{2/3})$ unique exponentials of the form $e^{-i2\pi n_s^{-1/3}\vec{p}\cdot(\vec{x}-\vec{y})}$ and $O(n_s^{1/3})$ values of p_j. Thus the total number of distinct amplitudes for H_{SLAC} is at most in $O(n_s)$ as well. Finally the fermion-fermion interaction consists of only $O(n_s^{1/3})$ distinct values and hence

$$K_{pos} \in O(n_s). \tag{4.96}$$

The number of unique coefficients in the momentum space Hamiltonian is much more challenging to analyze and such simple patterns in the magnitudes of the coefficients do not naturally reveal themselves. As such, we use the trivial bound of

$$K_{mom} \in O(n_s^3). \tag{4.97}$$

It is likely, however, that by refactoring the momentum space Hamiltonian using techniques analogous to [**?**] that a substantial reduction in K_{mom} may be attainable.

The last piece that needs to be considered is the implementation of `SELECT`. The approach that we use again mirrors the presentation in Fig. 9 of [209]. The strategy we take is to decompose the fermionic operators into Majorana operators of the form $X \otimes Z \otimes \cdots \otimes Z$

and $Y \otimes Z \otimes \cdots Z$. At most four Majorana operators are needed in both position and momentum space and thus the cost of implementing the select operator is $O(1)$ times the cost of applying the selected Majorana operator. The construction in [212] allows such Majorana operators to be selected in time $O(n_s)$ and therefore the cost of the select circuit is in $O(n_s)$ in both the position and momentum bases. Therefore, with this construction the cost of state preparation dominates the cost of the select circuit.

The number of T-gates needed in the qubitized simulation is therefore the product of the number of applications of W needed by phase estimation and the sum of the number of T-gates needed by the prepare and select circuits. This means that the complexity for the position space simulation under the assumption that $e^2 \gg n_s^{-1/3}$ is

$$N_{T,pos} \in \widetilde{O}\left(\frac{\lambda_{pos}(K_{pos}+n_s)}{\epsilon}\right) \subseteq \widetilde{O}\left(\frac{n_s^2(m+e\max_{\vec{x}}|A^{ex}(\vec{x})|+e^2\frac{n_s}{L})}{\epsilon}\right). \tag{4.98}$$

Similarly, the number of gates needed to perform the momentum space simulation at most scales as

$$N_{T,mom} \in \widetilde{O}\left(\frac{\lambda_{mom}(K_{mom}+n_s)}{\epsilon}\right) \subseteq \widetilde{O}\left(\frac{n_s^4(m+\frac{n_s^2}{L}+n_s e\max_{\vec{x}}|A^{ex}(\vec{x})|)}{\epsilon}\right). \tag{4.99}$$

If we assume the thermodynamic limit, then we have that the scaling of qubitization is upper bounded by $\widetilde{O}(\frac{n_s^{2+2/3}}{\epsilon})$ in position space and $\widetilde{O}(\frac{n_s^{5+2/3}}{\epsilon})$ in momentum space. The scaling of qubitization in position basis is slightly superior to the upper bound on the scaling of Trotterization, $(\frac{n_s^3}{\epsilon})^{1+o(1)}$. In momentum basis, the use of a brute force prepare circuit switches this behavior and leads to worse scaling than the $(n_s^{4+2/3}/\epsilon)^{1+o(1)}$ scaling provided by Trotter formulas. This bound, however, is likely pessimistic and by taking advantage of symmetries in the Hamiltonian terms it is likely that the number of unique coefficients can be further compressed. A summary of the results presented in this section are given in Table 4.1.

Method	Hamiltonian Basis	T-gate Complexity
Trotter-Suzuki	Position	$O(n_s^3/\epsilon)^{1+o(1)}$
Trotter-Suzuki	Momentum	$O(n_s^{4+2/3}/\epsilon)^{1+o(1)}$
Qubitization	Position	$\widetilde{O}(n_s^{2+2/3}/\epsilon)$
Qubitization	Momentum	$\widetilde{O}(n_s^{5+2/3}/\epsilon)$

Table 4.1: The T-gate complexities for both Trotter-Suzuki and Qubitization simulations in the position and momentum based eQED Hamiltonians in the thermodynamic limit.

A final point of interest is that the performance of Trotter-Suzuki methods in the non-relativistic limit may be superior to qubitization. Specifically, if we define the non-relativistic limit to be the case where $m \gg n_s^2/L$, then the scaling of position space simulation using Trotter-Suzuki methods becomes $(n_s^2 m/\epsilon)^{1+o(1)}$. On the other hand, qubitization's cost scales as $\widetilde{O}(n_s^2 m/\epsilon)$ in this limit. Thus for cases where relativistic effects are small, but highly accurate simulations are required then the bounds for Trotterization coincide (up to sub-polynomial factors) with those of qubitization. Further, since the empirical performance of Trotter-Suzuki methods is often much better than the upper bounds [213, 191] it is natural to suspect that Trotter's performance may be even better than this bound as also noted in the following section.

4.4 Rellium Model Analysis

4.4.1 Numerical Evaluation of Momentum Space Commutators

In this section, we present a numerical study of the momentum space rellium Hamiltonian commutators. We focus on the momentum space Hamiltonian because said Hamiltonian can be simply constructed, where the spinor interaction terms are computed with planewave integrals. For the following simulations, the Hamiltonian terms and integral coefficients were constructed utilizing the SymPy software package [214], and the cell box size was kept constant at $L = 1$. Each successive model system with different numbers of planewaves n_s, were created by modifying the planewave energy cutoff, E_{cut} within this constant box size. Additionally, renormalization terms in the rellium Hamiltonian, Eq. (4.17), were ignored for simplicity.

In the following result, the expectation value over i, j, k of the nested commutator, also called the second order commutator, $\|[H_i, [H_j, H_k]]\|$ was computed by randomly sampling Hamiltonian terms using Monte Carlo. The indices i, j, k in this case represent any possible term in the Hamiltonian. A total of 8 different rellium systems were used by defining the planewave energy cutoff values at $E_{cut} = 8, 9, 11, 14, 15, 17, 20, 23, 26$ eV which correspond to the number of planewaves being $N = 24, 72, 104, 128, 224, 320, 584, 808, 1216$ respectively. Each average commutator value was computed by running a Monte Carlo simulation with increasing sample numbers in order to evaluate the limit of the average commutator, and then taking the average of the corresponding Monte Carlo runs. Specifically, 13 simulations were performed for each rellium system equally spaced on the logarithmic scale between a minimum of 10^6 and a maximum of 10^{10} samples inclusively.

The results of the Monte Carlo simulations are presented in Fig. 4.5, where each data point is the average of all runs for each system, including the standard deviation in the error bars. By using a least squares power law fit, we can compare how the number of terms

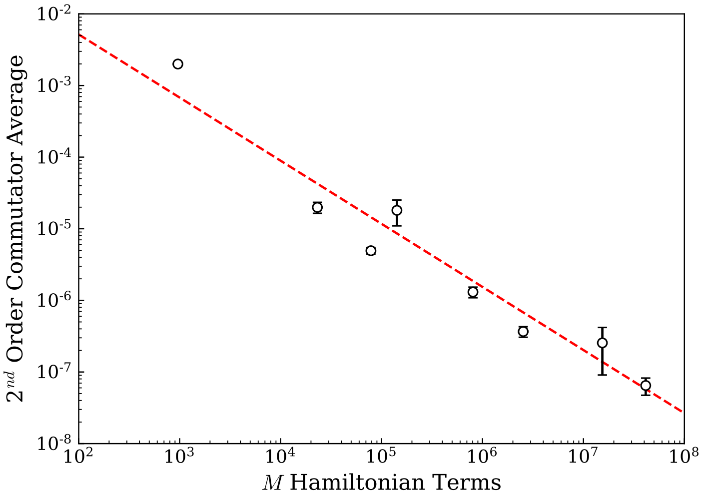

Figure 4.5: The Monte Carlo sampled 2^{nd} order commutator average for different E_{cut} values defining different rellium systems with constant box length $L = 1$. Plotted points are the average value across all Monte Carlo runs, and the error bars denote the standard deviation. The dashed red line corresponds to the least-squares power law fit where $f(M) = 0.3M^{-0.9}$

in the Hamiltonian, M, affect the average second order commutator. The power law fit function from the commutator average data in Fig. 4.5, results in $f(M) = 0.3M^{-0.9}$. Using the fact that the number of terms in the Hamiltonian M scales as $O(n_s^3)$ with the number of planewaves, we can naïvely state that the complexity of the second order commutator would scale as $O(n_s^9)$. However, since there needs to be at least one index in common between each Hamiltonian term, the upper bound is actually $O(n_s^7)$. By multiplying the upper bound for the number of second order commutator terms to evaluate, n_s^7, with the fitted function $f(M)$, where $M = n_s^3$, we see that the relationship of this complexity is observed to be $\sim O(n_s^4)$, performing better than the upper bound. The derivation of the estimated T-gate complexity is detailed in the following section.

4.4.2 Cost Estimate for QPE

The most common goal of Hamiltonian simulation in general is to find ground state energies. By using the above rellium model for analysis, we can gain an understanding of the error scaling throughout the Trotter-Suzuki decomposition, quantum phase estimation (QPE), and T-gate synthesis. First, in the standard surface code model of fault-tolerant quantum computation, all Clifford gates are trivial in cost, where non-Clifford gates such as the T-

gate end up dominating the computational cost of an arbitrary circuit. Therefore, we can simply understand the cost of our simulation with the number of R_z gates required, which are typically implemented as a circuit of multiple T-gates.

Second, it is important to note that the problem of finding ground states is generically hard. Specifically, if we could find a ground state energy in polynomial time then the complexity class BQP would contain QMA, which is the quantum analog of $P = NP$. For this reason, we strongly suspect that the generic ground state preparation problem is intractable on quantum computers unless a sufficiently good guess of the ground state can be provided to the phase estimation algorithm. Although we discuss in the following section strategies that can ameliorate this problem, it is important to note that we do not necessarily know how well these methods will work with a particular instance of a rellium simulation and hence the only thing we can say with confidence is that the estimates contained here will give the cost of sampling from the spectrum of rellium.

In order to eventually compute the ground state energy tolerance within some precision ϵ, we first need to find out the error scaling in the Trotter-Suzuki (TS) decomposition, ϵ_{TS}. Specifically we will focus on the second order decomposition of our unitary time propagator the error in which is given by [190] to be at most

$$\epsilon_{TS} \leq \frac{t^3}{12} \sum_{\gamma} \left\| \left[\sum_{\alpha} H_\alpha, \left[\sum_{\beta} H_\beta, H_\gamma \right] \right] \right\| + \frac{t^3}{24} \sum_{\gamma} \left\| \left[H_\gamma, \left[\sum_{\beta} H_\gamma, H_\beta \right] \right] \right\| \leq \frac{t^3}{8} \sum_{\gamma,\alpha,\beta} ||[H_\alpha, [H_\beta, H_\gamma]]|| \tag{4.100}$$

Using Ref. [215], the root-mean-square error in the measured phase during phase estimation can be denoted as the following

$$\Delta\phi \approx \sqrt{\left(\frac{\pi}{2^{n+1}}\right)^2 + (\epsilon_{\mathrm{TS}} + \epsilon_{\mathrm{syn}} + \pi\epsilon_{\mathrm{QFT}})^2} \tag{4.101}$$

where n is the number of ancilla qubits used. We will now neglect the cost of the quantum Fourier transform as it needs to be done only once and so ϵ_{QFT} can be taken to be an incredibly small value without altering the time-complexity of the simulation.

$$\Delta\phi \approx \sqrt{\left(\frac{\pi}{2^{n+1}}\right)^2 + (\epsilon_{\mathrm{TS}} + \epsilon_{\mathrm{syn}})^2} \tag{4.102}$$

We can now set the phase error target to be equivalent to the total RMS error in the energy multiplied by the total time propagation t

$$\epsilon = \frac{\Delta\phi}{t} \approx \frac{1}{t}\sqrt{\left(\frac{\pi}{2^{n+1}}\right)^2 + (\epsilon_{\rm TS} + \epsilon_{\rm syn})^2} \tag{4.103}$$

For simplicity, we choose $\epsilon_{TS} = \epsilon_{syn} = \pi\sqrt{3}/2^{n+2}$. With this choice we find

$$\epsilon \approx \frac{1}{t}\sqrt{\frac{1}{4}\left(\frac{\pi}{2^n}\right)^2 + \frac{3}{4}\left(\frac{\pi}{2^n}\right)^2} = \frac{\pi}{t2^n}, \tag{4.104}$$

where n is the number of qubits used in the phase estimation routine.

Next, using the fitted function from the Monte Carlo simulation given in Figure 4.5, we can take

$$\sum_{\gamma,\alpha,\beta} ||[H_\alpha, [H_\beta, H_\gamma]]|| \approx \frac{0.3n_s^7}{M^{0.9}} = 0.3n_s^{4.3} \tag{4.105}$$

which we can define as

$$\chi_H = An_s^b \tag{4.106}$$

where $A = 0.3$ and $b = 4.3$. Note that if we assumed the worst case commutator scaling that would be predicted from the commutators would be $b = 7$ for momentum basis simulations. This shows that substantial gaps likely exist between the worst case scalings and the actual scaling for eQED, similar to observations that have already been made for quantum simulations of non-relativistic chemistry.

Therefore, we can substitute the estimate in Eq. (4.105) into ϵ_{TS} to find

$$\frac{\pi\sqrt{3}}{2^{n+2}} \leq \frac{t^3\chi_H}{8}\ . \tag{4.107}$$

Now we find that the correct choice of t, relative to these bounds, will satisfy

$$\sqrt[3]{\frac{\pi\sqrt{3}}{\chi_H 2^{n-1}}} \leq t\ . \tag{4.108}$$

Picking t to saturate the lower bound (which corresponds to the worst-case scenario) we find that $t = \sqrt[3]{\frac{\pi\sqrt{3}}{\chi_H 2^{n-1}}}$, and can then solve for the number of qubits required in the QPE procedure.

$$n = \left\lceil \frac{\log\left(\frac{\pi^2\chi_H}{2\sqrt{3}\epsilon^3}\right)}{2\log(2)} \right\rceil\ . \tag{4.109}$$

For a single Trotter step, the number of rotations required is based on the total number of terms in the Hamiltonian

$$N_{terms} = 2n_s + 9n_s^3 \ . \tag{4.110}$$

Using the above formula, the max number of rotations required for a single term being equal to 8, and the fact that the number of exponentials required for the second order TS formula is $N_{exp} = 2N_{terms}$; The total number of rotations per trotter step is

$$N_{Rot} = 8 \times 2N_{terms} \leq 32n_s + 144n_s^3 \ . \tag{4.111}$$

The number of rotations needed in QPE is 2^n, therefore the overall number of rotations needed for the simulation is

$$N_{Rot}^{Sim} = 2^n \left(32n_s + 144n_s^3\right) \tag{4.112}$$

Using chemical accuracy, $\epsilon = 1.6$mHa for our error target, we can then estimate the number of qubits needed for QPE, and ultimately the number of T-gates required to obtain the ground state energy eigenvalue within the error tolerance of choice. The number of T-gates per rotation can be computed using the scaling from Ref. [216], and our chosen error for the T-gate synthesis, ϵ_{syn}, where

$$N_T = 1.15 \log_2(1/\epsilon_{syn}) \times N_{Rot}^{Sim} \ . \tag{4.113}$$

Since the error in the eigenvalue scales at most linearly with the error in the unitary matrix [197] and since the error in the unitary scales at most linearly with the number of gates comprising the unitary from Box 4.1 of Ref. [54] we have that it suffices to take $\epsilon_{syn} = \epsilon N_{Rot}$. With this assignment N_T becomes

$$N_T = 1.15 \log_2(N_{Rot}/\epsilon) \times N_{Rot}^{Sim} \quad . \tag{4.114}$$

Using the empirical values for A and b defined above, chemical accuracy ϵ, the number of qubits necessary for QPE in Eq. (4.109), the relation for T-gate count in Eq. (4.114), we can finally estimate the T-gate count for the full QPE routine given some number of planewaves for the system, n_s. The log-log plot of this relationship is given in Fig. 4.6. The full equation for this relationship is

$$N_T = \left\lceil 1.15 \times 2^n \left(32n_s + 144n_s^3\right) \log_2 \left(\frac{\left(32n_s + 144n_s^3\right)}{\pi\sqrt{3}/2^{n+2}} \right) \right\rceil \in \widetilde{O}\left(\frac{n_s^3\sqrt{\chi_H}}{\epsilon^{3/2}}\right) = \widetilde{O}\left(\frac{n_s^{5.2}}{\epsilon^{3/2}}\right) \tag{4.115}$$

for an error of $\epsilon = 1.6$mHa, and n is determined from Eq. (4.109).

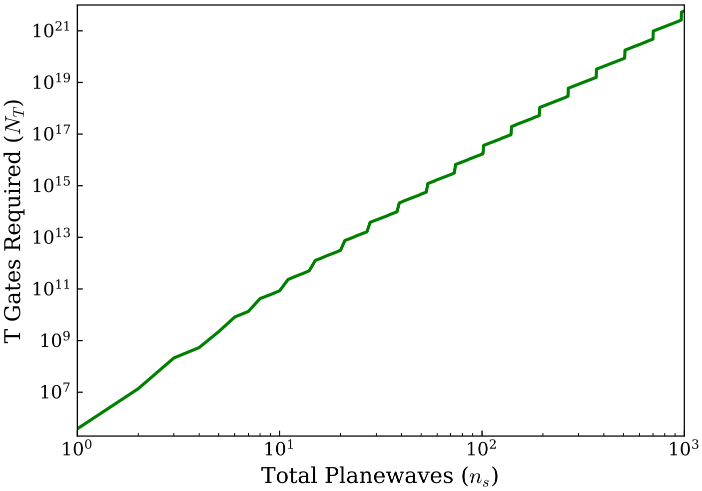

Figure 4.6: The estimated total number of T-gates required to sample from the spectrum of the rellium Hamiltonian for a box of length $L = 1$ within an error tolerance of $\epsilon = 1.6$mHa corresponding to chemical accuracy as a function of the number of planewaves in the system, n_s.

In contrast to Eq. (4.115), the costs for such a planewave simulation in the constant L and ϵ limit are given by Theorem 2 to be in $n_s^{5+o(1)}$ for adaptively chosen high-order Trotter-Suzuki formulas. We find empirically that for the second-order Trotter-Suzuki formula the number of gates needed to reach 1.6mHa is in $\widetilde{O}(n_s^{5.2})$. This suggests that, the empirical performance of this simulation is comparable to what we expect from our prior theoretical analysis; however, it is worth considering that this analysis still does rely on crude triangle-inequality based estimates that disregard cancellation between terms in the expansion of the error operator, and that further studies may be needed to determine the impact of neglecting such cancellations.

Finally, the number of non-Clifford operations needed to perform a classically challenging simulation using 20 plane waves (comprising 80 logical qubits) is projected by our results to be on the order of 10^{13} non-Clifford operations. In contrast, the best known results for simulating jellium using Trotter methods are on the order of 10^{9} non-Clifford operations for systems of 27 spin orbitals (54 qubits). The gulfs between these two estimates suggest that further optimization may be needed to allow eQED to reach the same levels of performance that we can reach for non-relativistic electronic structure calculations, however, the gulfs between the two are not so large as to suspect that such simulations will be infeasible once subjected to the same optimizations that lowered the costs of simulation for challenge problems in chemistry from 10^{14} non-Clifford gates [217] to on the order of 10^9 non-Clifford gates [201, 210]

4.5 State Preparation

In order to efficiently simulate any Hamiltonian on a quantum register, it is necessary to start with a high quality wavefunction ansätz that has a large overlap with the true wavefunction. For the jellium or rellium Hamiltonian, the degeneracy of the ground state is a non-trivial problem. Typically this is referred to as "strong correlation" where many different electronic configurations are entangled and contribute to the ground state wavefunction. This is in contrast to the familiar Hartee-Fock ground state, where a single electronic configuration *is* the wavefunction. Ground state electronic systems where the Hartree-Fock configuration is not dominant are sometimes called multi-reference (MR) ground states, where using the Hartree-Fock reference has a small overlap with the true ground state wavefunction due to other configurations being just as important. The multi-reference nature of electronic systems is also present in many chemical systems, typically large conjugated carbon systems, and multi-metal centered molecules due to the abundance of low lying spin states.

A commonly known classical method for computing multi-reference wavefunctions in quantum chemistry is called multi-reference configuration interaction (MRCI). [218, 219] In short, this method captures static correlation by first expanding the Hartree-Fock reference into a complete active space (CAS) of all configurations included within a truncated orbital and particle space, typically centered around the occupied and unoccupied valence orbitals. Next, a number of additional configurations are added for capturing correlation effects beyond the CAS space, sometimes referred to as "dynamic correlation." A common version of MRCI, is MRCI singles and doubles (MRCISD), where additional determinants are added to the CAS wavefunction, including single and double particle excitations. Additionally, the singly and doubly excited particle and hole space spans a larger space then just the initial CAS determinants, and are commonly referred as restricted active space 1 (RAS1) for the additional occupied orbitals, and subsequently RAS3 for the virtual orbitals. The single and double excitations span across all three spaces. As an aside, RAS2 sometimes refers to the original CAS space in the literature.

The number of determinants required to build an MRCI ansätz can be defined by the chosen active spaces, RAS1, CAS, and RAS3. Following the notation in Ref. [220] where we only consider singly occupied spin-orbitals that follow the Jordan-Wigner mapping.

$$N_{\text{det}}^{MRCI} = \sum_{i_h=0}^{m_h} \sum_{i_e=0}^{m_e} \binom{N_{RAS1}}{i_h} \binom{N_{CAS}}{n_e - N_{RAS1} + i_h - i_e} \binom{N_{RAS3}}{i_e} \tag{4.116}$$

where N_{RAS1}, N_{CAS}, and N_{RAS3} are the number of orbitals in each active space respectively, n_e is the total number of electrons in all of the correlated spaces, i_h is the hole index, i_e is the particle index, m_h and m_e are the number of holes in RAS1 and the particles in RAS3 respectively. For the MRCISD ansätz the number of determinants then scales exponentially with N_{CAS}, but quadratically in both N_{RAS1} and N_{RAS3}. Additionally for MRCISD, $m_h = m_e = 2$.

For the purpose of state-preparation on a quantum computer, we can pre-compute the MRCISD wave function classically, and then use the coefficients for the determinants to initialize a better wavefunction that hopefully has a much higher overlap with the true ground state. A convenient method to prepare the initial MRCISD state is to use a Givens rotation on the creation and annihilation operators, defined by a general Slater determinant generated by the classical MRCISD wavefunction. [221, 178] The general Slater determinant can be defined as

$$|\Phi\rangle = \hat{d}_1^\dagger \cdots \hat{d}_{N_f}^\dagger |0\rangle, \qquad \hat{d}_i^\dagger = \sum_j^{n_s} Q_{ij} \hat{c}_j^\dagger \tag{4.117}$$

where $\hat{c}^\dagger$ is the arbitrary particle type creation operator in the computational basis, $\hat{d}^\dagger$ is the rotated creation operator for the new basis based off of fractional particle occupation, N_f is the number of fermions, and n_s is the number of orbitals in the chosen basis. The $N_f \times n_s$ matrix Q rotates the original creation/annihilation operators into the rotated basis based off the choice of initial wavefunction. Therefore the rows of Q correspond to single particle wavefunctions that are linear combinations of the original orbital basis. In general, the rotated Slater determinant can be generated by a unitary rotation of a simple computational basis state generated by the original creation operators

$$|\Phi\rangle = U \hat{c}_1^\dagger \cdots \hat{c}_{N_f}^\dagger |0\rangle, \qquad \hat{d}_i^\dagger = U \hat{c}_i^\dagger U^\dagger \tag{4.118}$$

Following Ref. [221] we see that this unitary transformation can be represented by sequences of 2-qubit rotations, also known as Givens rotations where

$$U = G_{N_G} \cdots G_2 G_1 \tag{4.119}$$

where N_G is the total number of Givens rotations, and the Givens rotation matrix between spin-orbitals p, q is defined as

$$G(\theta, \varphi) = \begin{pmatrix} \cos\theta & -e^{i\varphi}\sin\theta \\ \sin\theta & e^{i\varphi}\cos\theta \end{pmatrix} \tag{4.120}$$

where the angles θ and φ can be solved classically by diagonalizing the Q matrix, where

$Q = V^\dagger DU$. The number of Givens rotations required to perform the basis transform is

$$N_G = (n_s - N_f)\, N_f \in O(n_s^2). \tag{4.121}$$

Each Givens rotation, $G(\theta, \varphi)$, can be implemented using a rotation of the form $e^{-i(e^{-i\varphi}a_p^\dagger a_q + e^{i\varphi}a_q^\dagger a_p)\theta}$. As discussed, each exponential can be simulated using $O(\log(1/\epsilon))$ T-gates. The complexity of performing this state preparation is therefore in $O\big(n_s^2 \log\big(n_s^2/\epsilon\big)\big)$, which is sub-dominant to the cost of simulation in momentum basis which is in $\widetilde{O}(n_s^{4+2/3}/\epsilon)$ in the thermodynamic limit. For this reason, we neglect the cost of the state preparation in all of our previous analysis.

Additionally, for typical electronic systems of interest, we only care about linear combinations of electronic single particle functions and the positronic block is trivially occupied. This means that for a system of N_{elec} number of electrons our matrix Q will already be diagonal in the positronic space, meaning simply that $N_f = N_{elec}$.

4.6 Planewave Cutoff Estimates for Heavy Atoms

In this section we will provide heuristic arguments that estimate the number of planewaves needed to solve a realistic relativistic problem in the momentum basis. This is important because the cost of both the MRCISD ansätz as well as the simulation of the dynamics can be non-trivial. As a target problem, we focus on the simulation of atomic gold. This is chosen because relativistic effects are needed in order to even qualitatively understand the spectrum of gold and thus such a simulation is arguably the first logical benchmark problem to consider after simulation of the relativistic free electron gas (rellium). In the estimates below we use the atomic unit convention where $\hbar = m_e = e = 1$.

For the momentum space planewave Hamiltonian, we estimate that a single all-electron gold atom will require at least 31 million planewaves, which is obviously beyond the reach of quantum computers in the foreseeable future. The number of planewaves N_{PW} needed for an arbitrary system is defined by the cell volume L^3 and energy cutoff.

$$N_{PW} = \frac{L^3}{2\pi^2} E_{cut}^{3/2} \tag{4.122}$$

To find the lowest possible cutoff energy, we can calculate the highest possible kinetic energy of an electron in an atomic potential with nuclear charge Z, which will be in the $1s$ orbital. The kinetic energy of the $1s$ electron can be estimated to be the following, using the hydrogenic Dirac equation

$$E = c^2 \left[\frac{1}{\sqrt{1 + \frac{Z^2\alpha^2}{\left(n-(j+1/2)+\sqrt{(j+1/2)^2-Z^2\alpha^2}\right)^2}}} - 1 \right] \tag{4.123}$$

where α is the fine structure constant, $n = 1$ is the principle quantum number and for the ground state s orbital, $j = \frac{1}{2}$. By plugging in $Z = 79$ and $L = 2r_A$ where r_A is the atomic radius, using $3.14a_0$ for gold , and finally setting $E_{cut} = E_{kin}$ we estimate that the all electron gold atom to require at least 3.08×10^7 planewaves and in turn roughly 1.23×10^8 logical qubits. This means that based on the number of sites in the reciprocal lattice and the cost of the simulation, enforcing chemical accuracy (1.6 mHa), will require roughly on the order of 10^{38} non-Clifford operations. Our analysis therefore suggests that such simulations will likely be out of reach for any quantum computer in the next few decades and beyond, since the number of planewaves for a single atom all electron system is expected to increase as $O(L^3Z^3)$. We expect similar conclusions to hold for other heavy element atomic systems as well.

This is not too surprising since planewave simulations in general need a large number of basis functions to properly describe atomic core orbitals. The most obvious remedy to this issue is to switch to a different basis set. In particular, Gaussian orbitals model the nuclear cusp condition much better than planewaves and so the number of Gaussians needed to describe the system to within chemical accuracy can be substantially lower. This makes them often a more natural choice.

The opposite approach would be to instead of investigating eQED in second quantization to look at it instead in first quantization using an appropriately anti-symmetrized wave function. Within such a framework, the number of qubits needed to store the atomic configuration can be exponentially smaller. The prefactors, however, make such applications outside of the reach of existing or near-future quantum computers.

4.7 Discussion

In this chapter, we have presented how to simulate the eQED Hamiltonian on a quantum computer. Specifically, we presented an analysis of both the position basis using a cubic lattice, and the momentum basis planewave formulations of the Hamiltonians. From this analysis we find that for the position basis, the number of T-gates required for simulating the Hamiltonian scales as $\left(\frac{\Lambda n_s^2}{\epsilon}\right)^{1+o(1)}$ where $\Lambda = \max\left(m + e\max_x \|A^{ex}(x)\|, \frac{e^2 n_s}{L}, \frac{n_s^{4/3}}{L}\right)$. For the momentum basis, the number of T-gates required scales as $\left(\frac{\Lambda_p n_s^3}{\epsilon}\right)^{1+o(1)}$ where

$\Lambda_p \in O\left(n_s\left(\frac{m}{n_s} + \frac{n_s}{L} + e|A_\mu^{ex}|\right)\right)$. This shows that the the ground state energy can be computed in polynomial time given that a copy of the ground state is provided to a quantum computer, which suggests that the problem of deciding whether there exists an eigenstate with energy less than a threshold, is contained within the complexity class QMA, for effective QED.

Further, we investigated the cost of using quantum phase estimation to estimate the ground state energy of the relativistic jellium (rellium) model as the simplest momentum based eQED Hamiltonian. Specifically we computed the number of T-gates needed empirically for quantum phase estimation using the second order Trotter-Suzuki decomposition, and using Monte Carlo sampling of different rellium Hamiltonians by increasing the cutoff energy for the system. For this routine, we find that for a constant box size, $L = 1$, the number of T-gates needed to estimate the ground state energy eigenvalue within an error of chemical accuracy $\epsilon = 1.6$mHa is on the order of 10^{16} T-gates for a classically intractable problem involving 100 planewaves (400 qubits) or 10^{13} T-gates for a classically challenging problem with 20 plane waves (80) qubits. These costs, while substantial, suggest that by further optimizing our simulation algorithm that the costs of quantum simulation may be reduced to reasonable levels.

While this chapter has explored how eQED can be simulated in general, the momentum space and lattice formulations of the Hamiltonian are not necessarily the most pertinent for all applications to physics and chemistry. Specifically, the focus of including QED corrections to relativistic effects in molecular systems is most prominent for heavy elements at the bottom of the periodic table which have large potential wells from the nuclear charge. However, QED corrections to the energies and properties of light elements can be important in certain situations as well. Future work will focus on adapting this method for simulating eQED on quantum computers to other more convenient basis sets for chemistry, such as the well known Gaussian basis sets that can more compactly model the electronic wavefunction at the nuclear cusp.

Chapter 5

ALGORITHM FOR QUANTUM COMPUTATION OF PARTICLE DECAYS

5.1 Introduction

The predictions of QCD are often tested in experiments where unstable hadrons decay and their decay products are observed. For high energy phenomenon, Feynman diagrams and other perturbative techniques provide an excellent description. In the low energy region, the QCD coupling constant becomes large and these methods fail. Nonperturbative approaches such as lattice QCD (LQCD), chirial perturbation theory and other effective field theories have enabled the calculation of some hadronic properties in this region. For example, Luscher's method [222, 223] has allowed the computation of some decay rates and scattering cross sections using LQCD by relating them to finite volume energy shifts. It has been used to compute scattering phase shifts for several low energy processes [10, 12, 11, 224], and the decay widths of ρ and σ mesons [225, 226]. The extraction of finite volume energy levels becomes difficult for excited states and for large lattices which limits the applicability of the method. In this chapter, a method of extracting particle decay rates and scattering cross sections from a Green's function calculated on a quantum computer is demonstrated. This method only requires the ability to prepare initial particle states and perform real time evolution. It has been shown for scalar and fermionic field theories that state preparation and real time evolution can be performed on quantum computers using resources that scale polynomially with the system size [16, 84, 83]. The computational costs of classically performing real time evolution usually scales exponentially with the system size [227, 228, 229, 230, 231, 232, 233, 234] so the use of quantum computers would represent an exponential speedup. A classical simulation of this quantum algorithm is explicitly demonstrated for a 1+1 dimensional QFT where a heavy scalar decays to a pair of light scalars. A $0+1$ dimensional demonstration is performed using IBM's superconducting hardware. Although this calculation is demonstrated for a specific model, the approach is based on general properties of Green's functions and it is expected that it can be applied to particle decays or scattering in other theories.

This chapter is organized as follows. The method of computing the decay rate from the Green's function is described in Section 5.2 and the mathematical details are shown in Appendix .5.1. The quantum circuit used to calculate the Green's function is described in Appendix .5.2. The time truncation and discretization errors are analyzed in Appendix .5.3. The systematic errors present in extracting a decay rate from a finite volume Green's function are analyzed in Appendices .5.3 and .5.3. The errors due to finite particle number truncations for theories containing bosons are analyzed in Appendix .5.3. A classical simulation of this quantum algorithm is performed in Section 5.3. IBM's quantum processor is used to implement this algorithm in Section 5.4. The Trotterization procedure used in this demonstration is described in Appendix .5.5.

5.2 Quantum Computation of Green's Functions

For a single particle state $|\psi\rangle$, the Green's function can be written as $\langle\psi| \frac{1}{\omega-\hat{H}+i\eta} |\psi\rangle = \frac{1}{\omega-E+i\eta-\langle\psi|\hat{T}(\omega+i\eta)|\psi\rangle}$, where E is the energy of the state $|\psi\rangle$, $\hat{H}$ is the Hamiltonian and $\hat{T}$ is the scattering T matrix as shown in Appendix .5.1. If the Hamiltonian, H, can be split into a free piece H_0 that describes the propagation of free particles and an interaction piece V that describes the interaction of particles, the state $|\psi\rangle$ can be prepared on a quantum computer as an eigenstate of H_0 using previously developed methods [16, 84, 235]. For theories like QCD, where no such division is known, an unstable particle state can be prepared by simulating two stable particles colliding on resonance. For example, a ρ meson can be prepared by simulating the collision of two pions with total energy equal to the ρ meson mass. The inclusive decay rate of a particle in d spatial dimensions is given by

$$\Gamma = \sum_{X_f} \int dP_{X_f} (2\pi)^{d+1} \delta^{d+1}(P_{X_f} - P_\psi) \Big| \langle X_f | \hat{T}(E_\psi) |\psi\rangle \Big|^2 \tag{5.1}$$

where P_ψ is the energy-momentum vector of the initial particle, P_{X_f} is the energy-momentum vector of the final state X_f, the sum is performed over all possible final states and the integral is performed over all possible energy-momenta vectors of the final state. The optical theorem relates this sum to the forward matrix element of the T matrix by $\Gamma = -2 \lim_{\eta\to 0} \mathrm{Im}(\langle\psi| \hat{T}(E+i\eta) |\psi\rangle)$ [7]. Therefore, if the Green's function can be computed in the $\eta \to 0$ limit, the inclusive decay rate can be extracted from it. For $\eta \neq 0$, the difference between $\mathrm{Im}(\langle\psi| \hat{T}(E+i\eta) |\psi\rangle$ and Γ is $O(\eta)$ as shown in Appendix .5.3. Furthermore, if $|\psi\rangle$ is a two particle state, the same kind of relationship between the Green's function and the T matrix holds, and the optical theorem can be used to find the inclusive scattering cross section for the two particles present in the state. To simplify the following discussion, the case of particle decays will be focused on. When the theory describing the particle is simulated inside a finite volume box with periodic boundary conditions, the difference between $\mathrm{Im}(\langle\psi| \hat{T}(E+i\eta) |\psi\rangle)$ in the finite volume and the infinite volume value for a $1 \to N$ decay is $O(E^{\frac{d-1}{2}N-2} e^{-\frac{\eta}{N+1}\frac{L}{2}})$ for a $d+1$ dimensional theory with a mass gap, and $O(\frac{1}{\eta^2 L})$

otherwise, where L is the length of a side of the finite volume box, as shown in Appendix .5.3. Therefore, if the Green's function can be calculated in a finite volume for a theory with a mass gap, Γ for $1 \to N$ decays can be determined with finite η errors that are $O(\eta)$ and finite volume errors that are $O(M^{\frac{d-1}{2}N-2}e^{-\frac{\eta}{N+1}\frac{L}{2}})$. It should be noted that the $L \to \infty$ and $\eta \to 0$ limits are not independent and to have finite volume errors vanish in the $L \to \infty$ limit, η must be chosen such that $\eta L \to \infty$. To evaluate this Green's function, it is helpful to express it in integral form,

$$\langle\psi| \frac{1}{\omega - \hat{H} + i\eta} |\psi\rangle = -i \int_0^\infty \langle\psi| e^{i(\omega+i\eta-\hat{H})t} |\psi\rangle \, dt \quad . \tag{5.2}$$

If this integral is truncated at finite time T, a Riemann sum approximation,

$$R = \sum_{k=0}^{T/\Delta t} e^{i(\omega+i\eta)k\Delta t} \langle\psi| e^{-i\hat{H}k\Delta t} |\psi\rangle \, \Delta t \quad , \tag{5.3}$$

to this integral can be evaluated on a quantum computer with the techniques described in Appendix .5.2 within an accuracy of ϵ using a gate count that scales as

$$\text{Gate Count} = O\left(\frac{\log\left(\frac{2}{\epsilon\eta}\right)}{\eta^2\epsilon} \, (\omega + E + \eta) \, p\left(\frac{1}{\eta}\log\left(\frac{2}{\eta\epsilon}\right), \eta\epsilon\right)\right) \tag{5.4}$$

where $p(t, \delta)$ is the gate count required to evolve to time t with accuracy δ, provided that $|\psi\rangle$ has already been prepared and E is the energy of the state $|\psi\rangle$. Once the Green's function has been computed, the particle decay rate can be extracted from the imaginary part of its pole. It should be noted that in the $\eta \to 0$ limit, the imaginary part of the Green's function becomes the spectral density function and other work has been done on using quantum computers to calculate the spectral density function [236, 237, 238]. Γ can be extracted from the peak of the Green's function which takes the value $\frac{2}{\Gamma}$. Therefore, to compute Γ to within an accuracy $\delta\Gamma$, the Green's function must be computed to within an accuracy of $\frac{\delta\Gamma}{\Gamma^2}$. Since the uncertainty in Γ scales linearly with η, Γ can be determined to an accuracy of $\delta\Gamma$ using

$$\text{Gate Count} = O\left(\frac{\log\left(\frac{2\delta\Gamma}{\Gamma}\right)}{\delta\Gamma^3} \, \Gamma^2 \, (2E + \delta\Gamma) \, p\left(\frac{2}{\delta\Gamma}\log\left(\frac{\sqrt{2}\Gamma}{\delta\Gamma}\right), \left(\frac{\delta\Gamma}{\Gamma}\right)^2\right)\right) \tag{5.5}$$

gates with a lattice whose size scales as $O(\frac{1}{\delta\Gamma}\log(\frac{1}{\delta\Gamma}))$ when the theory has a mass gap.

Another approach to computing the decay rate of an unstable particle would be to prepare the initial state, evolve for some time and measure detector operators at the border of the box, similar to the algorithm for the scattering of scalar particles in previous work [16]. This requires the simulation to run for a time $t = O(\frac{1}{\Gamma})$ before measuring the detector operators. The algorithm presented here only requires the simulation to run for a time $t = \frac{2}{\delta\Gamma}\log\left(\frac{\sqrt{2}\Gamma}{\delta\Gamma}\right)$. Therefore, this algorithm is expected to perform better for particles with a long lifetime. This algorithm also provides a method of computing decay rates that is different from direct time evolution and should have different systematic errors. Comparing decay rates computed with these two different methods will allow them to be determined with a higher degree of confidence.

As an example, one could consider applying this algorithm to study glueball resonances in lattice QCD. The resources required can be estimated from the techniques developed in Chapter 1 and Chapter 2. Previous work has shown glueballs can be reliably studied on lattices with a spatial volume of 24 × 24 × 24 [239]. Using the truncation of $p, q \leq 3$ as discussed in Chapter 1, leads to this calculation requiring $O(10^5)$ qubits. The computational cost of performing this calculation will be dominated by the implementation of the magnetic terms in the Kogut-Susskind Hamiltonian. From Chapter 1, each plaquette operator will require $O(10^7)$ rotations to be performed each of which will require roughly 30 gates. The number of Trotter steps performed to approximate the time evolution shoud be roughly the same order of magnitued as the length of the lattice so at this lattice volume, the entire calculation on a quantum computer should require $O(10^{15})$ gates. Note that this estimate ignores potential improvements that could come from using improved Hamiltonians as described in Chapter 3 or possible reductions in gate cost from careful ordering of the rotations needed to simulate the plaquette operator.

5.3 Decay of a Heavy Scalar

A demonstration of the algorithm discussed in previous sections will be provided by a classical simulation of the decay of a heavy scalar, ϕ, to a pair of light scalars, χ, in 1+1 dimensions. The Lagrangian for this process is given by

$$\mathcal{L} = \frac{1}{2}(\partial\phi)^2 + \frac{1}{2}(\partial\chi)^2 - \frac{1}{2}M_0^2\phi^2 - \frac{1}{2}m_0^2\chi^2 - \frac{1}{2}g\phi\chi^2 - \frac{1}{4!}\lambda\chi^4 \tag{5.6}$$

where M_0 and m_0 have been chosen such that the heavy particle's mass is 2.01 times the light particle's mass (so the $\phi \to 2\chi$ channel is the only allowed decay channel) and $\lambda > \frac{3g}{M_0^2}$ (to ensure a stable vacuum without spontaneous symmetry breaking in the infinite volume continuum theory). This theory was placed on a lattice with periodic boundary conditions and with lattice spacing $a = 0.2m^{-1}$ where m is the light particle's mass. This was done for lattices with three, five and seven sites. With these boundary conditions, the allowed momentum modes are in the set $\{-\frac{\pi(n_s-1)}{L}, -\frac{\pi(n_s-1)}{L} + \frac{2\pi}{L}, ..., \frac{\pi(n_s-1)}{L}\}$, where n_s is the number of sites and $L = n_s a$ is the length of the finite volume box. To simulate this on a classical computer, the ϕ occupation numbers were truncated at one for each momentum mode and the χ occupation numbers were truncated at two for each momentum mode. Since the mass of the heavy particle is only slightly larger than two times the light particle's mass, the arguments of Appendix .5.3 indicate that the error in the decay rate calculation due to this particle number truncation should be negligible.

A classical computer was used to determine the renormalization parameters, and to simulate the quantum algorithm from the previous section. The renormalization conditions were that the vacuum has zero energy and the mass of the heavy scalar is 2.01 times the mass of the light scalar. For each lattice volume, η was chosen to minimize the sum of the finite volume and finite η error calculated using the methods in Appendices .5.3 and .5.3.

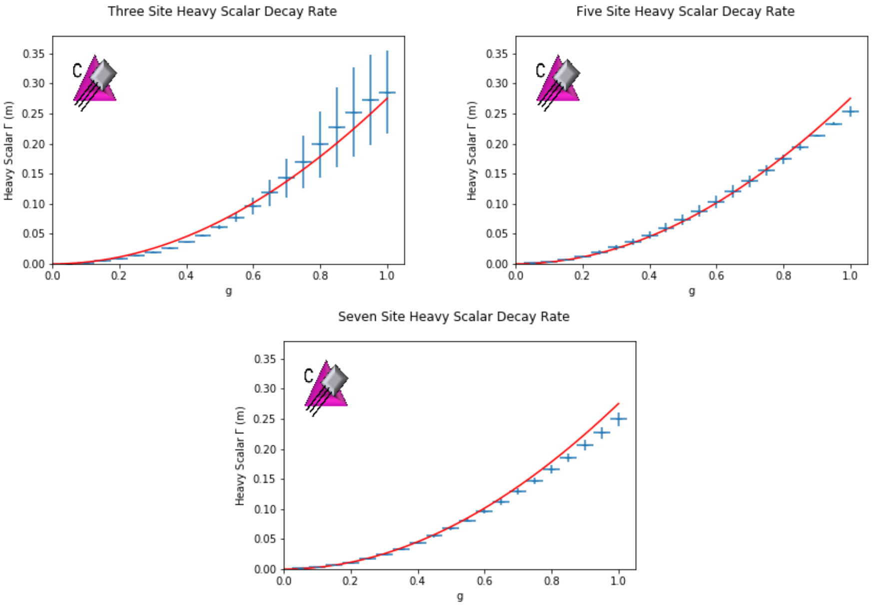

Figure 5.1: Heavy particle decay rates calculated on different lattice volumes plotted as a function of the coupling constant. The blue points are the decay rates calculated in the classical simulations of the quantum algorithm and the red curves are the one loop infinite volume continuum calculation. The error bars on the finite lattice decay rates represent finite volume and finite η errors calculated using the methods in Appendix .5.3. The icons appearing are defined in Ref. [240].

The heavy particle decay rates calculated classically in this example are displayed in Fig. 5.1. The finite volume and finite η uncertainties were calculated using the methods described in Appendix .5.3. To improve the precision of this calculation, a larger lattice must eventually be used. No matter what truncation is used, the dimension of the Hilbert space will grow exponentially with the number of lattice sites. The Green's function can be computed on a classical computer using matrix inversion techniques, the fastest of which scale as the dimension of the Hilbert space which grows exponentially with the number of sites [241, 242]. Due to this exponential scaling, it is infeasible to use a classical computer to compute Green's functions on a large lattice. However, using previously developed techniques for simulating scalar field theories, the method described in the previous section can be used to compute the Green's function on a quantum computer using resources that scale polynomially [16, 243].

5.4 Demonstration of 0+1 Theory on IBM's Quantum Processor

The calculations in the previous section were performed using classical computers, but it is possible to use existing quantum computers to do these calculations for a single lattice site with the truncations from the previous section. The Ourense quantum processor made available by IBM was used to implement this method for a one site calculation of the heavy particle decay rate.

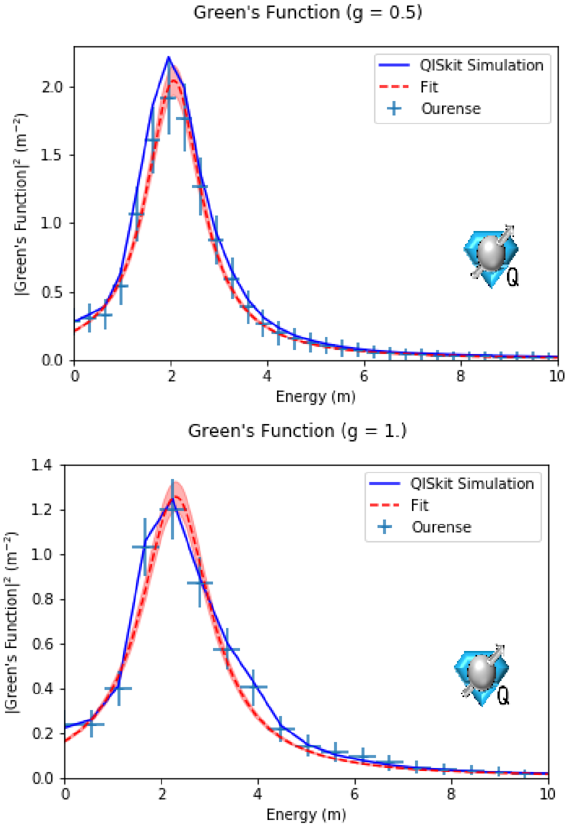

Figure 5.2: Green's functions computed with the Ourense quantum processor. The solid blue curve is a zero noise classical simulation of this calculation with Qiskit. The light blue points were computed using the error mitigated amplitudes from the Ourense quantum processor. The error bars represent uncertainties from the error mitigation extrapolation. The red curve is the Lorentzian fit to the error mitigated Green's functions.

The details of how the theory was discretized and how time evolution was implemented on the quantum computer are described in Appendix .5.5. The Hadamard test method [244] was used to obtain $\langle\phi| e^{-i\hat{H}\Delta tk} |\phi\rangle$ for $\Delta t = 0.2m^{-1}$ and $k = 1, 2, ..., 96$, where $|\phi\rangle$ is a state describing a single heavy scalar at rest. Two Trotter steps were used to calculate each time slice so the circuits used to calculate the real component of $\langle\phi| e^{-i\hat{H}\Delta tk} |\phi\rangle$ used 36 single qubit gates and 28 CNOT gates. The circuit used to estimate the imaginary component had one additional single qubit gate. Due to the length of the circuit used, the effect of imperfect gate implementation on the Ourense quantum processor is non-negligible. The contribution of imperfect gate implementation to the error in the computed amplitudes was estimated using the technique described in Appendix .5.6. Each circuit used in the Hadamard test was sampled 8000 times so the resulting statistical error was negligible relative to the systematic gate errors. To mitigate the effects of gate errors, an error mitigation technique described in Appendix .5.4 was used to extrapolate to the zero CNOT gate error limit. The Green's function,

$$G = \left| \sum_k e^{i(\omega + i\eta)k\Delta t} \langle \phi | e^{-i\hat{H}\Delta t k} | \phi \rangle \Delta t \right|^2 \quad , \tag{5.7}$$

was calculated classically using the error mitigated amplitudes and the results for two different couplings are displayed in Fig. 5.4. The heavy particle decay rate was extracted from the Green's function by performing a least squares fit to a Lorentzian distribution. The extracted decay rate is compared to the ideal decay rate,

$$\Gamma = -\operatorname{Im}\left(\langle \phi | \hat{T}(M + i\eta) | \phi \rangle \right) = \sum_n \frac{2\eta}{(M - E_n)^2 + \eta^2} \left| \langle E_n | \hat{V} | \phi \rangle \right|^2 \tag{5.8}$$

where the states $|E_n\rangle$ are eigenstates of the Hamiltonian with energy E_n, that would be computed in the absence of any finite T or Δt errors in Table 5.1.

g	Ideal Γ	Extracted Γ
0.5	$0.070m$	$(0.099 \pm 0.037)m$
1.	$0.287m$	$(0.286 \pm 0.047)m$

Table 5.1: Heavy particle decay rates calculated with the Ourense quantum processor. The first column is the coupling constant. The second column is the value of Γ that would be computed in the absence of any finite T or Δt errors. The third column is the decay rate calculated with the Ourense quantum processor. The error represents uncertainties in the fit to the Green's function.

The heavy particle decay rates calculated on the Ourense quantum processor are in agreement with the ideal calculation. However, even after using these error mitigation techniques, the error due to imperfect gates remained large.

5.5 Discussion

In this chapter, a quantum algorithm to calculate the decay rate of unstable particles and scattering cross sections has been introduced. The resources required to implement this method scale polynomially with the system size provided that state preparation and time evolution can be performed using resources that scale polynomially in the system size and field value truncations. It has been shown that this is possible for scalar and fermionic field theories [16, 84, 235]. This technique can be applied to LQCD using the techniques developed in the previous chapter. IBM's Ourense quantum processor was used to apply this algorithm to a scalar field theory defined on a single lattice site with truncated occupation numbers. Bounds on the finite volume error of 1 → N decay rates and 2 → N scattering cross sections computed with this method have been determined. More work will need to be done to understand how different truncations effect the error in the computed decay rate. The method presented here only requires preparation of the initial state and the ability to simulate the Hamiltonian. Classical methods of computing decay rates and cross sections from lattice calculations such as Luscher's method rely on relating these observables to finite volume energy shifts. In general this is a difficult process, and only allows the calculation of decay rates and cross sections for limited processes. Due to the greater generality of this method, it is expected that quantum computers will be able to calculate decay rates and cross sections beyond the reach of classical computers.

Part III

ANALOG QUANTUM SIMULATION

Chapter 6

SIMULATING HEISENBERG INTERACTIONS IN THE ISING MODEL WITH STRONG DRIVE FIELDS

6.1 Introduction

In this chapter, the potential for using Ising systems for analog simulations of physical systems that can be mapped to the Heisenberg model is investigated. The Ising model is considered because a number of platforms available for quantum simulation, such as Rydberg atoms, trapped ions and superconducting qubits, can be natively described by this Hamiltonian [245, 246, 247, 248, 249, 250, 251, 252]. Unlike previous approaches, this method of analog simulation of the Heisenberg model can be implemented with a time-independent Hamiltonian which could be beneficial for some platforms. There is an extensive literature regarding the time evolution of Ising models in background fields [253, 254, 255, 256, 257, 258, 259, 260, 261, 261, 262, 263, 264, 265, 266, 267, 268], including recent work related to transitions to chaotic phases induced by finite-time steps in Trotterized time evolution in digital quantum simulations [267, 268], identified through studying the system at periodic times. Previous work has shown that Ising interactions with a transverse field generate time evolution according to the XY model [255, 256, 257, 258, 269]. Studying the time evolution of the Ising model has also shown that the Ising model undergoes confinement analogous to QCD near its critical point with a field in the $\hat{x}$ and $\hat{z}$ directions [254, 253, 270]. Known to be universal in a computational sense [271], developing analog simulations of the Heisenberg model is expected to also advance simulations of other physical systems. We show how constant driving fields in the Ising model generate an effective Heisenberg model Hamiltonian to leading order in the inverse field strength at periodic times. The systematic errors associated with the periodic dynamics are quantified, revealing that the convergence of the expansion in the inverse field strength is limited by the location of dynamical quantum phase transitions (DQPTs) in the Ising model with an external field.

6.2 Heisenberg from Ising with Strong Fields

The Ising Hamiltonian with constant global driving fields is given by

$$\hat{H}^{\text{Ising}} = \sum_{i>j} J_{ij} \hat{Z}_i \hat{Z}_j + \frac{1}{2} \sum_i \Omega_x \hat{X}_i + \Omega_y \hat{Y}_i + \Omega_z \hat{Z}_i \quad . \tag{6.1}$$

To analyze the evolution of this Hamiltonian, it is helpful to transform into the interaction picture, where the driving fields are taken to be the "free" term in the Hamiltonian. The interaction-picture Hamiltonian is

$$\hat{H}_I^{\text{Ising}}(t) = \sum_{i>j} J_{ij} \hat{Z}_{I,i}(t) \hat{Z}_{I,j}(t) \quad , \tag{6.2}$$

where $\hat{Z}_{I,i}(t) = \hat{U}_0^\dagger(t)\hat{Z}_i\hat{U}_0(t) = \vec{e}(t)\cdot\vec{S}$, $\hat{U}_0(t) = \prod_j e^{-it\left(\Omega_x\hat{X}_j+\Omega_y\hat{Y}_j+\Omega_z\hat{Z}_j\right)}$, $\vec{S}$ is a vector of Pauli matrices and $\vec{e}(t)$ is a unit vector. From this perspective, the driving fields can be viewed as rotating $\vec{e}(t)$ from the north pole to other points on the unit sphere. By choosing periodic driving fields that generate closed paths on the sphere, it is possible to engineer evolution according to different Hamiltonians. The use of periodic dynamics to generate different Hamiltonians, known as Floquet engineering, has been used to simulate a range of interactions [272, 273, 274, 275, 276, 277, 278, 279, 280, 281, 282, 283, 284], including the Ising Hamiltonian from the Heisenberg interaction in quantum-dot systems [285, 286]. Floquet engineering has also been previously applied to static Hamiltonians in the interaction picture to understand how some systems prethermalize to a Hamiltonian that is not the generator of their evolution [287, 288, 289, 290]. In particular, it has been used to show that the dynamics of the XYZ-Heisenberg model with a strong external field are approximated by the XXZ-Heisenberg model for times that are exponential in the driving field [287]. We will show that in the Ising model, evolution according to the XXZ-Heisenberg Hamiltonian can be approximated by taking $\Omega_x = \Omega\sin\theta$, $\Omega_y = 0$, and $\Omega_z = \Omega\cos\theta$. With these driving fields, the interaction Hamiltonian becomes periodic over time intervals $\frac{2\pi}{\Omega}$, and the Schrodinger picture becomes equivalent to the interaction picture at these periods. A representative path generated by such fields on the unit sphere is shown in Fig. 7.1. The time-evolution of the system after discrete time intervals, and the associated Magnus expansion is given by

$$\begin{aligned}\hat{U}_F &= \mathcal{T}\exp\left\{-i\int_0^{\frac{2\pi}{\Omega}} dt'\ \hat{H}_I^{\text{Ising}}(t')\right\} \\ &= \hat{U}_B^\dagger \exp\left\{-i\frac{2\pi}{\Omega}\left(\hat{H}_1\ +\ O\left(\frac{1}{\Omega}\right)\ \right)\right\}\hat{U}_B\ ,\end{aligned} \tag{6.3}$$

where

$$\hat{H}_1 = \sum_{i>j} J_{ij}\left[\cos^2\!\theta\ \hat{Z}_i\hat{Z}_j + \frac{\sin^2\!\theta}{2}\left(\hat{X}_i\hat{X}_j + \hat{Y}_i\hat{Y}_j\right)\right], \tag{6.4}$$

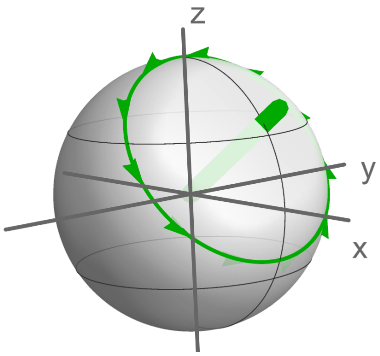

Figure 6.1: A representative path on the unit sphere taken by $\vec{e}(t)$ that generates time evolution according to the XXX-Heisenberg model. The green line corresponds to the direction of the driving field.

where $\hat{U}_B$ is a local change of basis given by $\hat{U}_B = \prod_j e^{+i\theta\hat{Y}_j/2}$ (that aligns the driving field with the z axis). Therefore, time evolution of the Ising model with this choice of driving fields approximates that of the XXZ-Heisenberg model between discrete intervals of $\Delta t = \frac{2\pi}{\Omega}$. Note that while the formalism of Floquet engineering was used to derive this result, the Hamiltonian is time independent and the periodicity is only manifest in the interaction picture. Also, the Ising model with a fast oscillating drive field could be used to simulate an XXZ-Heisenberg model because the dynamics of a transversely driven Ising model are equivalent to that of a time-independent Ising model with external fields in the $\hat{z}$ and $\hat{x}$ directions [259]. The $O\left(\frac{1}{\Omega^2}\right)$ higher-order terms in the Magnus expansion of the Floquet operator in Eq. (6.3) have one-body and three-body operators. The one-body operators can be eliminated by renormalization of the "free" Hamiltonian employed to transform to the interaction picture, but the three-body terms are a genuine deviation from the Heisenberg Hamiltonian. Such higher-order terms in the Magnus expansion can be removed through the use of time-dependent driving fields [291].

This approach to simulating the XXZ-Heisenberg model is similar in spirit to recent proposals for simulating gauge theories by adding terms to the Hamiltonian that generate gauge symmetries [292, 293, 294, 295, 296]. In these proposals, an energy penalty for breaking gauge invariance decouples the gauge invariant sector from the rest of Hilbert space analogously to how dynamical decoupling can be used to decouple systems from their enviroment [295]. In this chapter, the addition of driving fields to the Ising model can be interpreted as adding an energy penalty for violating the global $U(1)$ symmetry generated by the driving fields. This causes the different symmetry sectors to decouple, leading to time evolution that can be described by the XXZ-Heisenberg model.

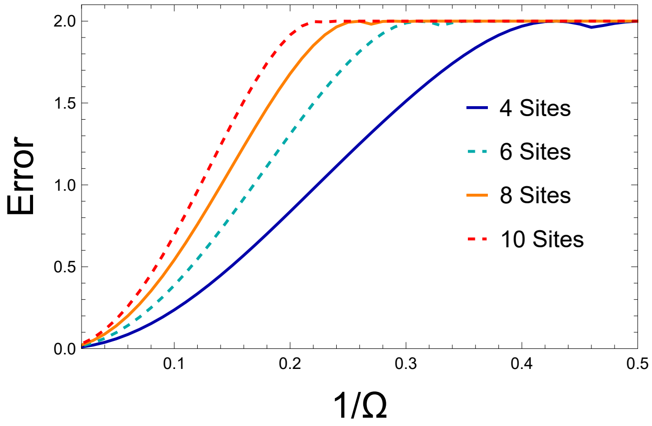

Figure 6.2: The spectral norm (magnitude of the largest eigenvalue) $||e^{-i\frac{2\pi}{\Omega}\hat{H}^{\text{Heis.}}_{\text{XXX}}} - \hat{U}_F||$ of the difference between the XXX-Heisenberg chain time-evolution operator derived from Eq. (6.5) and the Floquet engineered approximation in Eqs. (6.3) and (6.4) as a function of the driving field strength Ω, for a selection of chain lengths.

6.3 Beyond Leading Order in the Magnus Expansion and Dynamical Phase Transitions

The derivation of the approximate Heisenberg time evolution indicates that systematic errors from the Magnus expansion are suppressed by Ω^{-1} compared to leading order. However, the Magnus expansion is known to have a finite radius of convergence, and a priori it is not obvious what the minimum value of Ω is for the leading order term to accurately describe dynamics. As mentioned previously, numerical studies of digital quantum simulations have been used to show that Trotterized time evolution transitions into chaotic dynamics for sufficiently large time steps [267, 268]. In this context, the Floquet-period $\Delta t = \frac{2\pi}{\Omega}$ is analogous to a Trotter time step, and we show that at small Ω the breakdown of the Magnus expansion is associated with a dynamical quantum phase transition in the Ising model.

As an example, we focus on the special point $\theta = \tan^{-1}\sqrt{2}$, where the leading order Eq. (6.4) becomes an XXX-Heisenberg Hamiltonian with enhanced non-abelian $O(3)$-symmetry

$$\hat{H}^{\text{Heis.}}_{\text{XXX}} = \frac{1}{3}\sum_i \hat{X}_i\hat{X}_{i+1} + \hat{Y}_i\hat{Y}_{i+1} + \hat{Z}_i\hat{Z}_{i+1}. \tag{6.5}$$

The systematic errors in the time evolution (of any state) are bounded by the spectral norm (magnitude of the largest eigenvalue) of the difference between the exact Heisenberg time-evolution operator and the Floquet engineered approximation given in Eqs. (6.3) and

(6.4), $||e^{-i\frac{2\pi}{\Omega}\hat{H}^{\text{Heis.}}_{\text{XXX}}} - \hat{U}_F||$. This is shown for the one-dimensional XXX-Heisenberg model with $J = 1/3$ in Fig. 6.2 as a function of Ω for varying chain lengths. At large values of Ω, systematic deviations in the spectral norm decrease with increasing Ω as predicted by the Magnus expansion. At small values of Ω, the spectral norm saturates below a critical value Ω_c. Unfortunately, the lattice sizes for which the spectral norm can be efficiently computed are not large enough to determine the scaling of Ω_c with chain length. For longer chain lengths, Loschmidt echoes of the ground state of the XXX-Heisenberg model in Eq. (6.5), $|\psi_G\rangle$, time evolved over $t = \frac{2\pi}{\Omega}$ with the driven Ising model,

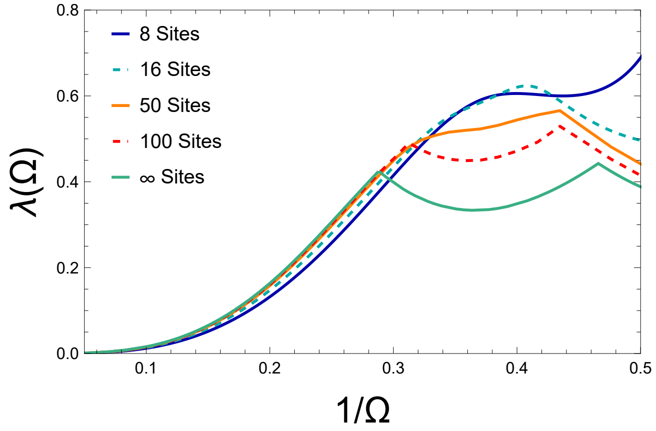

Figure 6.3: The rate function, defined in Eq. 6.8, for the ground state of XXX-Heisenberg chains of different lengths.

$$\hat{H}^{\text{Ising}} = \sum_i \hat{Z}_i \hat{Z}_{i+1} + \frac{\Omega}{2\sqrt{3}} \left(\hat{Z}_i + \sqrt{2}\hat{X}_i \right) \ , \tag{6.6}$$

are computed. If the time evolution of the XXX-Heisenberg model were perfectly reproduced by the driven Ising model, the Loschmidt echo, defined as the probability to return to the initial state, i.e.,

$$\mathcal{L}(\Omega) = \left| \langle \psi_G | \, e^{-i\frac{2\pi}{\Omega}\hat{H}^{\text{Ising}}} \, |\psi_G\rangle \right|^2 , \tag{6.7}$$

would equal unity, and deviation from unity provide an estimate of contributions beyond leading order in the Magnus expansion. As $\log \mathcal{L}(\Omega)$ is an extensive quantity, the rate function

$$\lambda(\Omega) = -\log\left(\mathcal{L}(\Omega)\right)/L \quad , \tag{6.8}$$

is computed to compare chains of different lengths L, as shown in Fig. 6.3. For chains of $L \leq 16$, time evolution was computed using exact diagonalization. The ground states of the $L =$

50 and $L = 100$ chains were computed using DMRG and time evolution was performed using TDVP [148, 115, 149, 297, 298, 299]. The ground state and time evolution of the infinite Heisenberg chain was computed using iTEBD [300, 301, 150]. At large Ω, $\lambda(\Omega)$ decreases with increasing Ω, indicating that the leading order Magnus expansion is correctly describing the dynamics of the model. This asymptotic behavior only occurs beyond a "kink" in $\lambda(\Omega)$, indicating that at small values of Ω the Magnus expansion is failing to converge. The presence of a kink (non-analytic behavior) in $\lambda(\Omega)$ is the defining characteristic of a dynamical quantum phase transition [260]. Note that other inequivalent definitions of dynamical phase transitions have been introduced in the literature [302]. DQPTs have previously been studied in spin systems and have been shown to be associated with unstable renormalization group fixed points [260, 261, 261, 262, 263, 264, 303]. Our results show that the Ising model with a constant driving field $\vec{\Omega} = \Omega\left(\frac{1}{\sqrt{3}}\hat{z} + \sqrt{\frac{2}{3}}\hat{x}\right)$ undergoes a DQPT into a regime with an approximate $O(3)$ symmetry at discrete time intervals, as seen in Fig. 6.3.

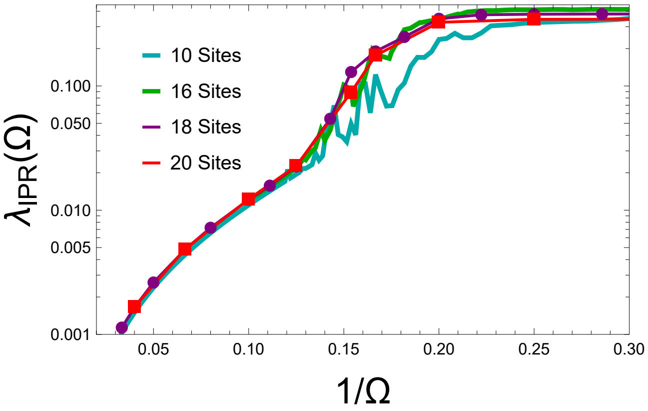

Figure 6.4: The log IPR for the ground state of XXX-Heisenberg chains of different lengths. The IPR for the chain of length 10 was computed with exact diagonalization and the IPR for larger chains was computed by averaging the Loschmidt echo over 1000 periods.

These calculations demonstrate that for short time scales Heisenberg evolution is being successfully simulated, provided a sufficiently large driving field strength is used. However, this does not guarantee that the dynamics are reproduced at long times. Generically, periodically driven systems are expected to heat at late times [304, 305, 306], however in the context of digital quantum simulation it has been shown that quantum localization prevents this in Trotterized time evolution [267, 268]. The Floquet engineering technique used in this chapter uses a static Ising Hamiltonian so one would expect that at large field strengths the eigenstates of the Ising model are perturbatively close to those of the Heisenberg Hamil-

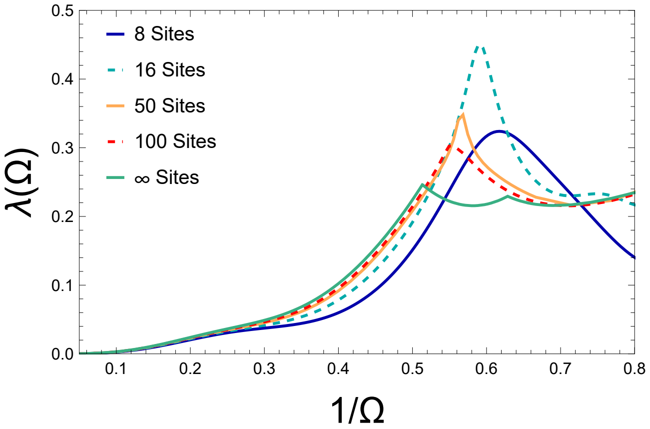

Figure 6.5: The rate function for the ground state of XY-Heisenberg chains of different lengths.

tonian. This would guarantee that long time dynamics are correctly reproduced as in the case of Trotterized time evolution. This perturbative argument can be verified through the calculation of the inverse participation ratio (IPR). For a given state, $|\psi\rangle$, and eigenstates, $|n\rangle$ of some Hamiltonian, the IPR is defined by

$$\mathrm{IPR} = \sum_n |\langle n|\psi\rangle|^4 \quad . \tag{6.9}$$

The IPR measures how localized $|\psi\rangle$ is relative to the eigenbasis $|n\rangle$. In practice, it can be evaluated by averaging the Loschmidt echo over long periods of time. To compare systems of different sizes, a normalized IPR, defined by $\lambda_{\mathrm{IPR}}(L) = -\frac{1}{L}\log(\mathrm{IPR})$ for a chain of length L, was computed for the ground state of the XXX-Heisenberg model in Fig. 6.4. For the chain of length 10, the IPR was computed by explicitly evaluating Eq. 6.9, while for the larger chains the IPR was computed by averaging Loschmidt echos. As this figure shows, for large Ω the log IPR is small which indicates the perturbative argument holds and the XXX-Heisenberg ground state is localized with respect to the Ising Hamiltonian. This indicates that the long time dynamics of the XXX-Heisenberg model is being successfully simulated with this technique.

When the constant driving field is taken to be in another direction, an approximate $O(2)$ symmetry emerges. The arguments above suggest that there should be a DQPT that occurs in this case as well. As an example, the traditional one-dimensional transverse field Ising model with the driving field purely in the $\hat{x}$ direction will generate evolution according to the XY-Heisenberg model (up to a change of basis),

$$\hat{H}_{XY}^{\text{Heis.}} = \frac{1}{2}\sum_{i} \hat{Y}_i\hat{Y}_{i+1} + \hat{Z}_i\hat{Z}_{i+1} \ . \tag{6.10}$$

The rate function $\lambda(\Omega)$ for the ground state of $\hat{H}_{XY}$ evolved under the transverse field Ising Hamiltonian for one period is shown in Fig. 6.5. As is the case for the XXX-Heisenberg model, there is a series of kinks indicating a DQPT before the rate function begins to decrease. It is interesting to note that the final kink is at $\Omega^* \approx 1.948$ which is close to, but not quite at the critical point of the transverse field Ising model at $\Omega = 2$. While this chapter shows that the Ising model can be used to simulate $\hat{H}_{XY}$ in the strong field limit, it has been shown in previous work that in $2+1$ dimensions, the weak field limit of the Ising model also reproduces the dynamics of the XY-Heisenberg model [265, 266].

These results explicitly show that in 1D, this technique can be used to simulate Heisenberg model physics for long times with a driving field that is not extensive with the system size. While there are classical computational tools that enable the study of large 1D systems such as tensor networks, simulating real time evolution in 1D systems still has computational costs that grow exponentially with time and analog quantum simulation may be of practical use. While these calculation were only performed for 1D, this technique can also be applied to simulate higher dimensional Heisenberg models and it is likely that the required driving field strength for simulating dynamics accurately is not extensive with the system size as well. Even if the required driving field strength is extensive with system size in higher dimensions, this technique may still be of practical importance as real time evolution for even modest sized 2D systems is difficult for classical computers. In addition to enabling analog quantum simulation of the Heisenberg model on platforms with Ising interactions such as Rydberg atoms and superconducting qubits, this technique could be combined with the results of Ref. [271] to potentially perform analog quantum simulation of an arbitrary Hamiltonian. This could potentially enable analog simulations of any quantum field theory of physical interest on these platforms.

6.4 Discussion

In this chapter, a method for analog simulation of the Heisenberg model has been proposed that can be implemented on platforms whose natural evolution is described by the Ising model with constant external fields. For a specific driving field, the time-evolution operator of the Ising model is approximately that of the Heisenberg model over periodic time intervals. Interestingly, the leading-order effective Heisenberg operator has enhanced symmetry over the intrinsic Hamiltonian.

The systematic errors associated with this method at small external-field strength are limited by non-analytic behavior in the Ising model, associated with dynamical quantum phase transitions, which indicates the Magnus expansion is failing to converge. Beyond a critical value of the driving field, the effective Hamiltonian describing the time-evolution can be determined from a Magnus expansion, with each increasing order in $1/\Omega$ introducing operators involving an increasing number of spins.

The technique presented in this chapter could be implementable on a range of quantum devices, including systems of Rydberg atoms or even superconducting qubits, in any dimension. While Rydberg systems are very promising as analog quantum simulators, one of the main challenges is that natively they offer a very narrow class of interactions, which severely limits their applicability. Therefore, being able to engineer new interactions makes an important step forward in expanding the systems that can be studied on these platforms. Furthermore, unlike previous proposals for quantum simulations of Heisenberg models, this method can be implemented using time-independent fields, which is extremely important for experimental platforms with a limited slew rate for the external fields. In the near term, analog quantum simulations will be the only method of probing the long time dynamics of large systems. The dynamics of the Heisenberg model are of particular interest, not only for condensed matter applications, but also for high-energy physics, such as in coherent neutrino oscillations and as a lattice regularization of the O(3) nonlinear σ model which will be important for developing quantum simulations of QCD. Importantly, this technique easily scales to higher dimensions. By enabling analog simulation of the Heisenberg model on Rydberg atoms and superconducting qubits, systems beyond the reach of classical computers may potentially be simulated.

Chapter 7

STATE PREPARATION IN THE HEISENBERG MODEL THROUGH ADIABATIC SPIRALING

7.1 Introduction

The Heisenberg model with arbitrary couplings is computationally universal in the sense that all other lattice models can be simulated in arbitrary dimensions, particle content and interactions by simulations of Heisenberg models [271]. Therefore, detailed understandings of quantum simulations of the Heisenberg model inform the simulations of quantum field theories describing the forces of nature. Translating results obtained from lattice field theories to predictions that can be compared with experiment requires that all relevant physical length scales are much larger than the scale of discretization of spacetime, and universality guarantees that low-energy continuum physics can be reproduced from simulations that are tuned near a 2nd order critical point [307, 308, 309]. As an example, it has been proposed that universality assures that the continuum physics of the $1+1$d O(3) NLσM, which has been studied as a toy model of quantum chromodynamics (QCD) due to sharing a number of qualitative features such as asymptotic freedom, dynamical transmutation, the generation of a non-perturbative mass gap and non-trivial θ vacua, can be recovered from simulations of an anti-ferromagnetic Heisenberg model [310, 22, 311, 24, 25, 312, 313, 314]. Thus, quantum simulations of the low-energy dynamics of the anti-ferromagnetic Heisenberg model, which requires preparing a low-energy state and evolving it forward in time, are expected to provide key insights into strategies for simulating QCD, including state preparation.

To enable practical quantum simulations of physical systems, preparation of states that have energies much less than the inverse lattice spacing is required. One proposal for preparing low energy states in both digital and analog quantum simulation is adiabatic switching. This works by beginning in the ground state of a known Hamiltonian and slowly varying the Hamiltonian through a path in parameter space where the energy gap does not close. Implementation of adiabatic switching in a quantum simulation requires the ability to prepare the eigenstate of the initial Hamiltonian and simulate time evolution. Schemes for simulating the Heisenberg model's time evolution have been proposed using digital quantum simulation [191, 190], hybrid digital-analog simulation [315], periodically driven trapped ions [283], global microwave pulses on Rydberg atoms [282], nuclear spins [316, 317], and adding strong single qubit terms to systems described by Ising interactions [318].

In this chapter, we present an argument that the eigenstates of the Heisenberg model are approximate eigenstates of the Ising model with a strong external field pointed in an appropriate direction. This is used to develop an analogue quantum simulation technique, called the adiabatic spiral, to adiabatically prepare the ground state of the Heisenberg model by adiabatically varying the direction of the external field in the Ising model. The feasibility of implementing the adiabatic spiral on Rydberg atoms and D-Wave's quantum annealer is investigated. It is found that current Rydberg atom experiments have sufficient coherence time and drive field strengths to implement the adiabatic spiral, while the D-Wave quantum annealer suffers from some limitations.

7.2 Adiabatic Spirals: Spiraling Toward Ground States

We recently showed that the Ising model with large external fields in the transverse and longitudinal directions can approximate the time evolution of the Heisenberg model at discrete time intervals [318]. This generalizes previous work showing the Ising model with a large transverse field approximates the dynamics of the XY model [255, 256, 257, 258, 269], and is related to techniques used to study pre-thermalization [287, 288, 289, 290]. Explicitly, if a quantum simulator evolves under the Hamiltonian

$$\hat{H}^{\text{Ising}} = \sum_{i,j} J_{i,j} \hat{Z}_i \hat{Z}_j + \sum_i \frac{\Omega}{2} \left(\cos\theta \hat{Z}_i + \sin\theta \hat{X}_i \right) \quad , \tag{7.1}$$

then the time evolution of

$$\hat{H}^{\text{Heis.}} = \sum_{i,j} J_{i,j} \left[\cos^2\theta \hat{Z}_i \hat{Z}_j + \frac{\sin^2\theta}{2} \left(\hat{X}_i \hat{X}_j + \hat{Y}_i \hat{Y}_j \right) \right] \tag{7.2}$$

will be approximated at times that are integer multiples of $t = \frac{2\pi}{\Omega}$, up to a change of basis and corrections that are $O\left(\frac{1}{\Omega}\right)$. In this work, $\hat{X}$, $\hat{Y}$ and $\hat{Z}$ refer to the respective Pauli operators.

We now observe that if the time evolution was reproduced exactly at these time intervals, it would guarantee that $\hat{H}^{\text{Heis.}}$ and $\hat{H}^{\text{Ising}}$ share the same eigenstates and that their energy levels agree up to integer multiples of Ω. This would suggest that by beginning with $\theta = 0$ and adiabatically increasing θ, it should be possible to prepare an eigenstate of the Heisenberg model from an eigenstate of the Pauli $\hat{Z}$ operators. When viewed in the interaction picture where the free part of the Hamiltonian is taken to be the single spin driving terms

$$H_0(t) = \frac{\Omega}{2} \sum_i \vec{h}(t) \cdot \vec{\sigma}_i \quad , \tag{7.3}$$

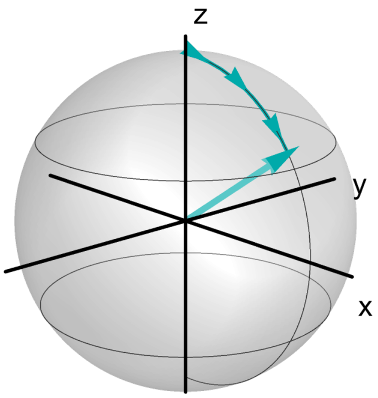

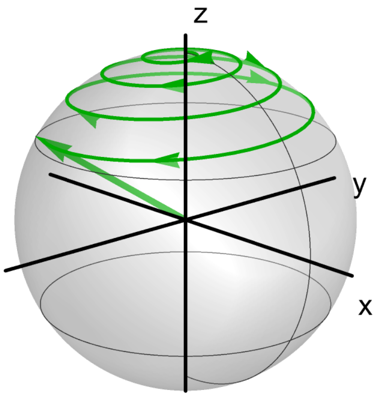

Figure 7.1: The top graphic shows the path on the unit sphere taken by $\vec{h}(t)$ (the time-dependent drive field defined in Eq. (7.3)) and the bottom graphic shows $\vec{e}(t)$ (defining the time dependence of the $\hat{Z}$ operator in the interaction picture) during the course of the adiabatic spiral. $\theta(t)$ is taken to be $\theta(t) = \arccos\left(\frac{1}{\sqrt{3}}\right)\frac{t}{T}$ and t varies from $t = 0$ to $t = T$. During the evolution, $\vec{e}(t)$ is precessing around $\vec{h}(t)$ while the opening angle θ changes adiabatically, resulting in a spiral path on the unit sphere in the interaction picture. Vectors from the origin indicate the direction at the end of the spiral evolution.

the local $\hat{Z}$ operator becomes

$$\hat{Z}_j^I(t) = U_0^\dagger(t)\hat{Z}_j U_0(t) = \vec{e}(t) \cdot \vec{\sigma}_j \quad , \tag{7.4}$$

where $\vec{\sigma}_j$ is a vector of Pauli matrices and $\vec{e}(t)$ is a unit vector. For the Hamiltonian in Eq. (7.1), $\vec{e}(t)$ rotates in a circle about a vector pointing in the $\cos\theta\hat{z} + \sin\theta\hat{x}$ direction. As θ is adiabatically varied to prepare the ground state of a Heisenberg model, $\vec{e}(t)$ will move in a spiral motion along the surface of the sphere as shown in Fig. 7.1. For this reason we call this method of state preparation adiabatic spiraling. It is important to note that the implementation of the adiabatic spiral does not require the switching time to be an integer multiple of $\frac{2\pi}{\Omega}$. Studying the evolution of the Ising model at periodic times was only necessary to argue that the eigenstates of the Heisenberg model are also eigenstates of the Ising model up to $O\left(\frac{1}{\Omega}\right)$ corrections. Typically in quantum simulation, adiabatic switching is done between ground states of gapped Hamiltonians. In contrast, the adiabatic spiral can be understood as performing adiabatic switching in the middle of the spectrum of the Ising model to prepare eigenstates of the Heisenberg model.

In practice, the initial eigenstate of the Ising model will often be degenerate, and this degeneracy will need to be split for the adiabatic approximation to be valid. This can be done by modifying the single-spin terms in the Hamiltonian. Explicitly, at times that are integer multiples of $t = \frac{2\pi}{\Omega}$, the time evolution generated by

$$\hat{H}^{\text{Ising}} = \sum_{i,j} J_{i,j}\hat{Z}_i\hat{Z}_j + \sum_j \frac{\Omega}{2}\left(\cos\theta\hat{Z}_j + \sin\theta\hat{X}_j\right) + \frac{h_P(j)}{2}\hat{Z}_j \quad , \tag{7.5}$$

can be approximated by the Floquet operator,

$$\begin{aligned}\hat{U}_F = \hat{U}_B^\dagger \exp\Bigg\{ &- i\frac{2\pi}{\Omega}\sum_{ij} J_{ij}\left(\cos^2\theta\hat{Z}_i\hat{Z}_j + \frac{\sin^2\theta}{2}\left(\hat{X}_i\hat{X}_j + \hat{Y}_i\hat{Y}_j\right)\right) \\ &- i\frac{2\pi}{\Omega}\sum_j \frac{1}{2}\cos\theta\; h_P(j)\; \hat{Z}_j + O\left(\frac{1}{\Omega^2}\right)\Bigg\}\hat{U}_B \quad ,\end{aligned} \tag{7.6}$$

where $\hat{U}_B$ is a local change of basis given by $\hat{U}_B = \prod_j e^{i\frac{\theta}{2}\hat{Y}_j}$. The additional single-qubit term can be tuned to create an energy penalty that breaks the degeneracy of the initial Hamiltonian which enables the application of the adiabatic approximation. With these additional single-qubit terms present, the same arguments at large Ω can be used to justify the applicability of the adiabatic spiral.

As an explicit demonstration, we consider the preparation of the ground state of the anti-ferromagnetic Heisenberg model on a 1D chain, with a Hamiltonian of the form

$$\hat{H}^{\text{Heis.}} = J\sum_j \left[\hat{X}_j\hat{X}_{j+1} + \hat{Y}_j\hat{Y}_{j+1} + \hat{Z}_j\hat{Z}_{j+1}\right] \quad . \tag{7.7}$$

Preparing the ground state of this system with the adiabatic spiral will require beginning in an eigenstate of the Ising model that is adiabatically connected to the ground state of the Heisenberg model. Equation 7.2 reproduces Eq. 7.7 when $\theta = \arccos\frac{1}{\sqrt{3}}$ and would suggest that the ground state of Eq. 7.7 is connected to the ground state of Eq. 7.2 at other values of θ. The ground state of the Heisenberg Hamiltonian with $\theta = 0$ is a state with spins alternating up and down in the $\hat{z}$ direction (a Néel state), e.g., $|\uparrow\downarrow\uparrow\downarrow\uparrow\downarrow ...\rangle$. This ground state is degenerate and the degeneracy can be split by adding a single qubit term to the Hamiltonian with alternating signs. Therefore, the ground state of the full Heisenberg model can be prepared by beginning in a Néel state and applying a time-dependent Hamiltonian of the form

$$\hat{H}(t) = \sum_j \left[J\hat{Z}_j\hat{Z}_{j+1} + \frac{\Omega}{2}\left(\frac{1}{\sqrt{3}}\hat{Z}_j + f(t)\hat{X}_j\right) + \frac{h_P(t)}{2}(-1)^j\hat{Z}_j\right] \quad , \tag{7.8}$$

for a time T, where $h_P(0) > 0$, $h_P(T) = 0$, $f(0) = 0$, and $f(T) = \sqrt{\frac{2}{3}}$. Explicitly, if $|Vac\rangle$ is the ground state of the anti-ferromagnetic Heisenberg model given in Eq. (7.7) and $|N\acute{e}el\rangle$ is a Néel state, then

$$|Vac\rangle = \mathcal{T}e^{-i\int_0^T dt\hat{H}(t)}\,|N\acute{e}el\rangle \quad , \tag{7.9}$$

up to $O\left(\frac{1}{\Omega}\right)$ and finite time corrections where $\hat{H}(t)$ is the time-dependent Hamiltonian defined in Eq. (7.8).

Typically, analog quantum simulators are initialized with all qubits in their ground state, e.g., $|\downarrow\rangle^{\otimes n}$. However, to apply the adiabatic spiral to the anti-ferromagnetic Heisenberg model, relevant for simulations of the O(3) NLσM, the initial state should be a Néel state, which can be accomplished by applying a rotation on every other qubit. Alternately, computations could be performed in a different basis. If $\mathbf{X}$ is defined to be a product of Pauli X's on every other site such that $|N\acute{e}el\rangle = \mathbf{X}\,|\downarrow\rangle^{\otimes n}$ where $|\downarrow\rangle^{\otimes n}$ is the state with all spins down, then Eq. (7.9) can be written as

$$|Vac\rangle = \mathcal{T}e^{-i\int_0^T dt\hat{H}(t)}\mathbf{X}\,|\downarrow\rangle^{\otimes n} \quad . \tag{7.10}$$

Multiplying both sides of this equation by $\mathbf{X}$ yields

$$\mathbf{X}\,|Vac\rangle = \mathbf{X}\mathcal{T}e^{-i\int_0^T dt\hat{H}(t)}\mathbf{X}\,|\downarrow\rangle^{\otimes n} = \mathcal{T}e^{-i\int_0^T dt\tilde{H}(t)}\,|\downarrow\rangle^{\otimes n} \quad , \tag{7.11}$$

where

$$\tilde{H}(t) = \sum_j \left[-J\hat{Z}_j\hat{Z}_{j+1} + \frac{\Omega}{2}\left(\frac{(-1)^j}{\sqrt{3}}\hat{Z}_j + f(t)\hat{X}_j\right) + \frac{h_P(t)}{2}\hat{Z}_j \right] \quad . \tag{7.12}$$

If the quantum simulator can directly implement $\tilde{H}(t)$, then an adiabatic spiral can be used to adiabatically prepare the Heisenberg ground state from the $|{\downarrow}\rangle^{\otimes n}$ state up to a basis transformation. However, on some analog quantum simulators such as Rydberg atom systems, the sign of the two-spin interaction is fixed to be positive. This does not present an issue in using an adiabatic spiral, as it can be implemented with $-\tilde{H}(t)$. This is because a change of overall sign does not change the eigenstates or presence of an energy gap between eigenstates, indicating that the adiabatic approximation remains valid.

7.3 A Numerical Example

To implement the adiabatic spiral in Eqs. (7.8) and (7.12), specific choices have to be made for $h_P(t)$ and $f(t)$. As an example, we consider the Heisenberg comb that has recently been shown to reproduce the O(3) NLσM in the continuum and infinite-volume limits. It has modest qubit requirements, making it a good candidate for near term quantum simulations [24, 25]. The Hamiltonian is given by

$$\hat{H} = \sum_x \left[J\vec{S}_{x,1}\cdot\vec{S}_{x+1,1} + J_p\vec{S}_{x,1}\cdot\vec{S}_{x,2} \right] \quad , \tag{7.13}$$

where $\vec{S}_{x,y} = \frac{1}{2}\vec{\sigma}_{x,y}$ is the vector of Pauli matrices divided by 2 at position (x, y) on the lattice. An adiabatic spiral can be used to prepare the ground state of this model from a Néel state with the Hamiltonian

$$\hat{H}(t) = \frac{1}{4}\sum_x \left[J\hat{Z}_{x,1}\hat{Z}_{x+1,1} + J_p\hat{Z}_{x,1}\hat{Z}_{x,2} \right] + \sum_{x,y}\left[\frac{\Omega}{2}\left(\frac{1}{\sqrt{3}}\hat{Z}_{x,y} + f(t)\hat{X}_{x,y}\right) + \frac{h_P(t)}{2}(-1)^{x+y}\hat{Z}_{x,y} \right] \quad . \tag{7.14}$$

The simplest choices for $f(t)$ and $h_P(t)$ are linear functions of t. Once the functional forms of $f(t)$ and $h_P(t)$ have been chosen, implementing the adiabatic spiral further requires choices of Ω, T, and $h_P(0)$. To ensure the eigenstates of the Ising model are as close to eigenstates of the Heisenberg model as possible, and the conditions of the adiabatic theorem are satisfied, Ω and T should be taken to be as large as possible. As an example, Fig. 7.2 shows the energy of a state obtained using the adiabatic spiral as a function of Ω for a Heisenberg comb of length 4 with $J = J_P = 1$ and a switching time of $T = 25$. In this calculation, $h_P(t) = 0$ for all times and $f(t)$ was taken to be a linear function. Evolution under $\hat{H}(t)$ was evaluated numerically by computing $\prod_{n=1}^{N} e^{-i\frac{T}{N}\hat{H}(\frac{n}{N}T)}$ and increasing N until convergence. At small values of Ω, the eigenstates of the Ising model and Heisenberg model are not close and the adiabatic spiral fails. At large Ω, the adiabatic spiral is able to prepare a state with an energy below the energy of the first excited state. The reason the energy of the state in Fig. 7.2 saturates above the ground-state energy is due to a combination of the amount of time used in the switching and the initial degeneracy in the ground state.

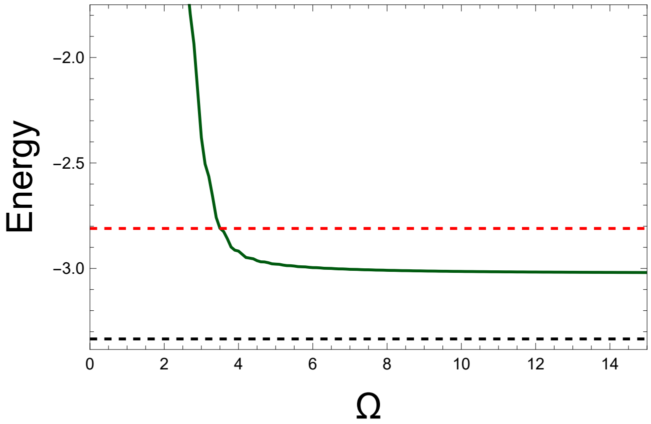

Figure 7.2: The energy of the final-state obtained after implementing an adiabatic spiral as a function Ω for a comb of length 4 with $J = J_P = 1$ and a switching time of $T = 25$, starting from a Néel state. The spiral utilized the Hamiltonian given in Eq. (7.14), with $h_P(t) = 0$ and $f(t)$ a linear function. The black dashed line is the energy of the ground state and the red dashed line is the energy of the first excited state.

The energy of the state prepared by the adiabatic spiral can be lowered by taking a non-zero value of $h_P(0)$. Unlike with Ω and T, the energy of the state prepared by an adiabatic spiral is not monotonic in $h_P(0)$. If $h_P(0)$ is taken to be too large, the process of switching off the initial energy penalty in a finite amount of time can break adiabaticity, leading to a state with larger energy being prepared. An optimal value of $h_P(0)$ can be found variationally. Fig. 7.3 shows the energy obtained from the adiabatic spiral with $\Omega = 8$ and $h_P(0) = 0.18$. This value for $h_P(0) = 0.18$ was selected by minimizing the energy obtained by performing the adiabatic spiral with $\Omega = 8$ and $T = 25$.

The adiabatic spiral's performance can be improved further by optimizing the path taken through parameter space. If $h_p(t)$ is taken to be a linear function of time, and $f(t)$ taken to be

$$f(t) = \sqrt{\frac{2}{3}} \left(\frac{t}{T} + \sum_{n<N} \beta_n \sin\left(n\pi \frac{t}{T} \right) \right) \quad , \tag{7.15}$$

an optimal path through parameter space can be found by minimizing the energy obtained as a function of the β_ns. Note that if the maximum driving field strength is limited on the analog simulator, this will constrain the values that the β_ns can take. For long switching times, assuming that the maximum value of the driving field is obtained at the end of the spiral and truncating at β_1, it was found that the energy obtained by the adiabatic spiral was monotonic as a function of β_1. This means that in practice, the largest value of β_1 allowed by the constraint should be used so that the maximum value of the driving field is obtained at the end of the spiral, which is $\beta_1 = \frac{1}{\pi}$. The energy of the state obtained by performing the adiabatic spiral with this path is also shown in Fig. 7.3. At long switching times, this path can offer an improved performance over linear switching. It was also found that including more terms in the expansion in Eq. (7.15) offered minimal improvements in the performance of the adiabatic spiral.

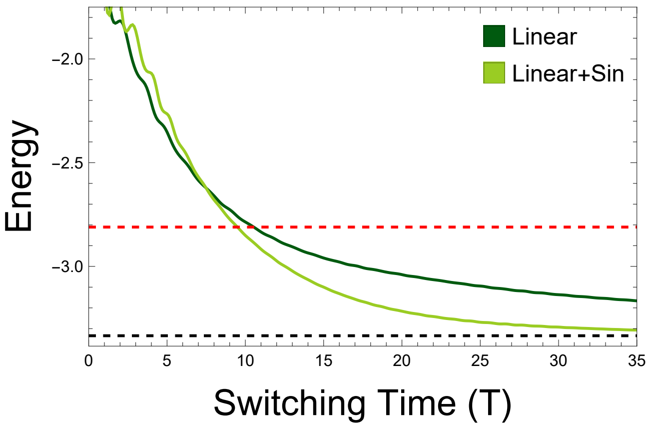

Figure 7.3: The dependence of the final state energy, after implementing an adiabatic spiral, on the total switching time used for a comb of length 4 with $J = J_P = 1$. The dark green curve shows the energy obtained when $f(t)$ and $h_P(t)$ are taken to be linear functions. The light green curve shows the energy obtained when $f(t) = \sqrt{\frac{2}{3}}\left(\frac{t}{T} + \frac{1}{\pi}\sin\left(\pi\frac{t}{T}\right)\right)$. The black dashed line is the energy of the ground state and the red dashed line is the energy of the first excited state.

7.4 Potential Hardware Implementations

7.4.1 Rydberg Atoms

Arrays of Rydberg atoms are an experimental platform that could be used to implement the adiabatic spiral. If the atoms in the Rydberg state interact through the Van der Waals

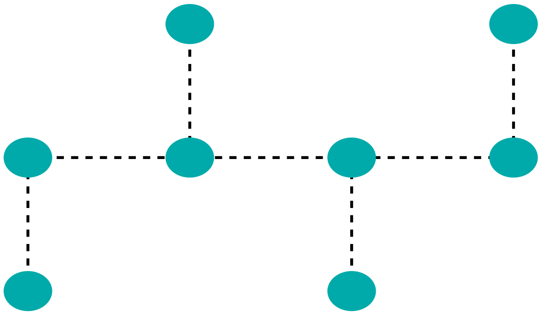

Figure 7.4: An arrangement of Rydberg atoms that can be used to perform an analog quantum simulation of the Heisenberg comb.

interaction, the Hamiltonian describing their dynamics is

$$\hat{H}^{\mathrm{Ryd.}}(t) = \frac{\Omega(t)}{2}\sum_i \hat{X}_i - \Delta(t)\sum_i \hat{n}_i + \sum_{i<j}\frac{V_0}{|\vec{x}_i - \vec{x}_j|^6}\hat{n}_i\hat{n}_j \quad , \tag{7.16}$$

where $\hat{n}_i$ is the Rydberg state occupation at site i, $\vec{x}_i$ is the position of site i and $\hat{X}_i$ couples the ground state of the atom at site i to its Rydberg state. This native implementation of Ising interactions has enabled the use of Rydberg atoms to perform analog simulations of the Ising model in 1D and 2D [319, 320, 321, 322, 323, 324, 325, 326, 246, 245]. Their native Ising interactions allows for the implementation of adiabatic spirals.

This is not the only technique that can be used to simulate the Heisenberg interaction on Rydberg atoms. In recent work, a method of simulating Heisenberg interactions on Rydberg atoms making use of dipole-dipole interactions and an external microwave field was proposed [282]. This approach uses global microwave pulses to rotate the dipole-dipole interaction to generate time evolution approximating an XXZ Heisenberg Hamiltonian, analogous to how one could Trotterize the Heisenberg interaction on a digital quantum computer. While this proposal makes use of dipole-dipole interactions, the same approach could be used for Rydberg atom simulations that use the Van der Waals interaction to couple atoms. In that experimental setup, an effective $\hat{Z}_i\hat{Z}_j$ is available. In principle, the ground state of a Heisenberg model could be prepared on this hardware using the adiabatic spiral or by using global pulses to perform a Trotterized adiabatic switching. The choice of which method to use will depend on the specific analog simulator being used. As a case study, we can consider hardware parameters used in a recent experiment to study phases of the 2D

Ising model [245]. This experimental setup used a driving field with a max amplitude of $\Omega_{max} = 2\pi \times 4.3$MHz and had a max coherence time of 3μs. With these hardware parameters, the preparation of the ground state of a Heisenberg comb with the adiabatic spiral parameters from the previous section can be performed by placing atoms in an array as shown in Fig. 7.4 with a lattice spacing of $a \approx 10.5\mu$m. Note that the Hamiltonian simulated will not quite be the same as the Hamiltonian from the previous section due to the $\frac{1}{r^6}$ coupling between the atoms, but the alternating vertical positions of atoms will ensure the next-to-nearest neighbor interactions will be suppressed. This same arrangement of atoms could be used to implemented Trotterized adiabatics. In this approach, $\frac{\pi}{2}$ pulses are alternated with periods of the external field turned off to construct a first order Trotterized approximation of time evolution according to

$$\hat{H}(t) = \sum_{i,j} J_{i,j}\left(\hat{Z}_i\hat{Z}_j + \frac{t}{T}\left(\hat{X}_i\hat{X}_j + \hat{Y}_i\hat{Y}_j\right)\right) + h_P\left(1 - \frac{t}{T}\right)\sum_i (-1)^i\hat{Z}_i \quad , \tag{7.17}$$

where $(-1)^i$ represents an alternating pattern of signs that breaks the initial degeneracy of the Hamiltonian. The errors in this state preparation method come from a finite switching time, standard Trotterization errors and the amount of time required to implement the $\frac{\pi}{2}$ pulses. This is similar in spirit to previous proposals to simulate time evolution using global controls [327]. The explicit pulse sequences for first order Trotterization can be found in Appendix .6.1.

Figure 7.5 shows the energy that can be obtained using the path optimized adiabatic spiral and Trotterized adiabatics with different numbers of Trotter steps as a function of total runtime on the analog simulator. At short times, a small number of Trotter steps are able to outperform the spiral. However, if the number of Trotter steps is fixed and the switching time is increased, the Trotterization error will grow and the energy of the state obtained eventually will increase. This can be mitigated by performing more Trotter steps, but as the number of Trotter steps increases the contribution to the error from the finite pulse time will accumulate. As shown in Fig. 7.5, this effectively puts a limit on the total number of Trotter steps that can be performed before adiabatics is no longer being effectively simulated. As shown in Appendix .6.2, some of these errors can be cancelled at leading order with a modified pulse sequence. The dashed curves in Fig. 7.5 show the energy of the state that can be obtained by mitigating these errors at leading order in Trotterized adiabatics. The adiabatic spiral does not suffer from either of these issues. Increasing the amount of time used in the adiabatic spiral only increases the overlap with the ground state. It should also be noted that in the Trotterization simulations it was assumed that the drive field can be instantly ramped to its maximum value. In practice, this is not possible and

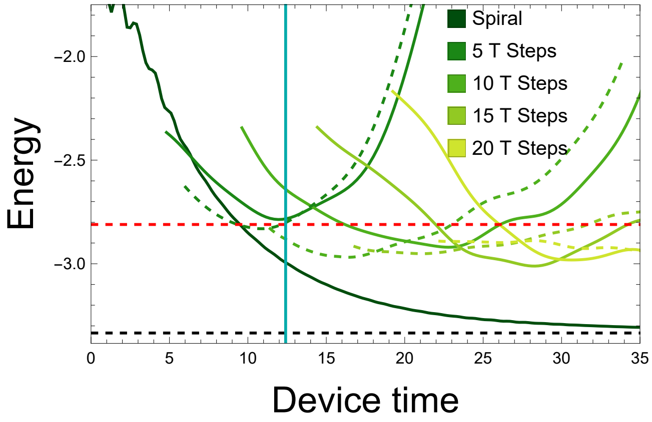

Figure 7.5: The dependence of the final-state energy from an adiabatic spiral and Trotterized adiabatics on the total switching time used for a comb of length 4 with $J = J_P = 1$. The solid lines used the Trotter sequence from Appendix .6.1 and the dashed curves used the improved Trotter sequence from Appendix .6.2. The horizontal black dashed line is the energy of the ground state and the horizontal red dashed line is the energy of the first excited state. The vertical blue line indicates the coherence time of 3μs in units of J^{-1}.

the shape of the pulse while ramping on the drive field will contribute to errors in the time evolution. Given these limitations, it appears that the adiabatic spiral is a better choice for preparing the ground state of a Heisenberg model than Trotterized adiabatics on a Rydberg system. It should also be noted that the pulse sequences required to implement the adiabatic spiral are quite similar to other pulse sequences that have been implemented on Rydberg atoms [320, 325, 246, 245]. As such, it is expected that the adiabatic spiral will be robust against experimental errors when implemented on Rydberg atoms.

7.4.2 D-Wave

Another experimental platform that could potentially implement the adiabatic spiral is D-Wave's quantum annealer. The D-Wave quantum annealer implements time evolution according to the Hamiltonian,

$$\hat{H}^{\mathrm{DW}}(t) = -\frac{\mathrm{A}(s(t))}{2}\sum_i \hat{X}_i + \frac{\mathrm{B}(s(t))}{2}\left(\sum_i h_i \hat{Z}_i + \sum_{i<j} J_{ij}\hat{Z}_i\hat{Z}_j\right) \quad , \tag{7.18}$$

where $\mathrm{A}(s)$ and $\mathrm{B}(s)$ are fixed functions, but $s(t)$, h_i and J_{ij} can be programmed by the user, up to some constraints. Although it is designed to solve optimization problems, D-Wave's hardware has been used to perform analog simulations of the Ising model [328, 329, 330, 331, 332, 333, 334, 335, 336, 337, 338]. In previous work, D-Wave's quantum annealer has also been used to simulate time evolution and perform state preparation for lattice gauge theories, however these mappings to quantum simulation have more in common with digital quantum simulation than the analog protocol we are proposing [154, 339, 132]. To implement the adiabatic spiral on the D-Wave annealer, a set of qubits with a comb pattern coupling must be selected. Given the connectivity of the hardware, this is straightforward to do. J_{ij} and h_i should be chosen so that the implemented Hamiltonian is

$$\hat{H}^{\mathrm{DW}}(t) = -\frac{\mathrm{A}(s(t))}{2}\sum_{x,y}\hat{X}_{x,y} + \frac{\mathrm{B}(s(t))}{2}\left(\sum_{x,y} h\hat{Z}_{x,y} + \sum_{x} J\hat{Z}_{x,1}\hat{Z}_{x+1,1} + J_p\hat{Z}_{x,1}\hat{Z}_{x,2}\right) \quad . \tag{7.19}$$

The spiral can be implemented by using D-Wave's reverse annealing function to begin in a Néel state with $\mathrm{A}(s(0)) = 0$, and adiabatically evolve to s^* such that $\mathrm{A}(s^*) = \sqrt{2}\mathrm{B}(s^*)h$. As long as $J, J_p \ll h$, the adiabatic spiral will be able to prepare an equal superposition of the ground state and the first excited state of the Heisenberg comb. The pure ground state will not be prepared because an energy penalty cannot be implemented to break the degeneracy within the initial state. Note that to perform a measurement on the D-Wave QPU, the pulse schedule must end with $\mathrm{A}(s = 1) = 0$. The process of turning off $\mathrm{A}(s)$ will create errors in the state preparation whose size are controlled by the slew rate of $\mathrm{A}(s)$ and the choice of s^*. One choice of time dependence of $\mathrm{A}(t)$ and $\mathrm{B}(t)$ to implement the adiabatic spiral is shown in Fig. 7.6. As an explicit example, we once again consider the Heisenberg comb of length 4 with $J = J_p$. The energy of states prepared with classical simulations

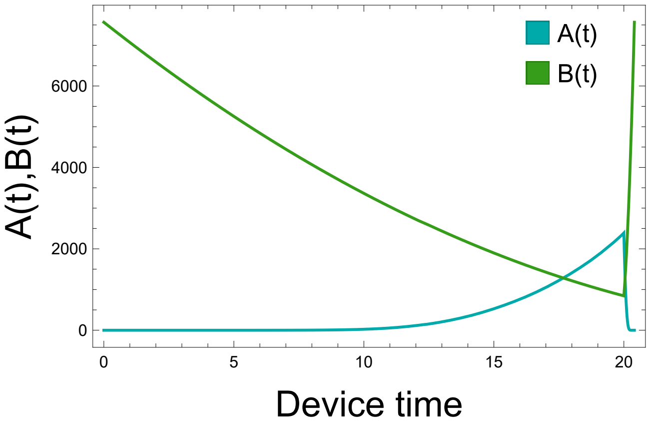

Figure 7.6: Annealing schedule on the D-Wave's `Advantage` 6.1 to implement the adiabatic spiral with $h = 2$. $\mathrm{A}(t)$ and $\mathrm{B}(t)$ are given in units of MHz and time is in units of μs.

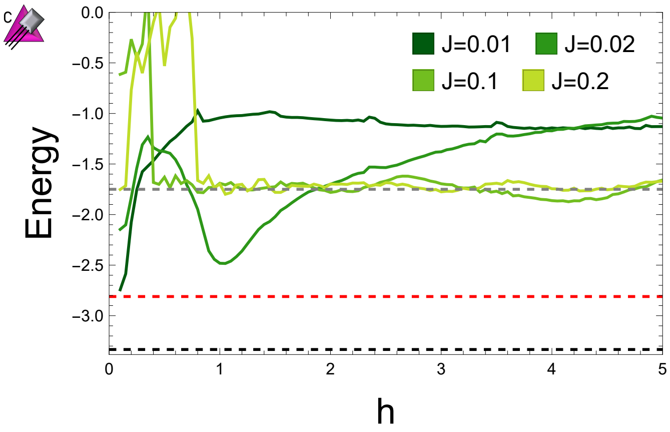

Figure 7.7: Energy of the state produced on a simulation of D-Wave's `Advantage` 6.1 hardware for different values of J and h. The gray line is the energy of the initial state. The black line is the vacuum energy, and the red line is the energy of the first excited state. Note that the energy shown here is measured in units of J.

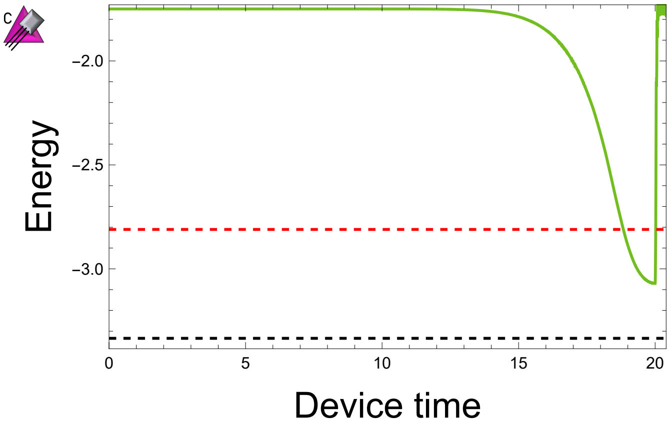

Figure 7.8: Energy of the state produced on a simulation of D-Wave's `Advantage` 6.1 as a function of time for a comb of length 4 with $J = J_P = 0.1$ and $h = 2$. The black dashed line is the energy of the ground state and the red dashed line is the energy of the first excited state. Note that the energy is given in units of J.

(`Mathematica` and `python`) of the D-Wave `Advantage` 6.1 hardware for different choices of J and h are shown in Fig. 7.7. For small values of J and h, simulations of the D-Wave hardware are able to produce states with a lower energy than the initial state. However, the quantum device has calibration errors on the order of $\delta J \approx 4 * 10^{-3}$, making it unlikely that these parameters can be used in practice. For larger values of J, the simulations cannot reach states with energy lower than the initial state. As an example, the energy of states as a function of time for $J = 0.1$ and $h = 2$ found in simulations of `Advantage` are shown in Fig. 7.8. As seen, `Advantage` is expected to be able to prepare a low energy state with respect to the Heisenberg Hamiltonian part-way through a simulation. However, in the process of turning off $\mathrm{A}(s)$ as required to perform a measurement, the time evolution is still approximately adiabatic, and the system ends up in a final state with large overlap with the initial state. If the slew rate of `Advantage` could be increased, or if measurements could be performed without fully turning off $\mathrm{A}(t)$, it would be possible to perform measurements of the low-energy state prepared by the adiabatic spiral and potentially use `Advantage` in a scalable manner for quantum simulation of the Heisenberg model. Implementing the adiabatic spiral on `Advantage` also suffers from the complication that the single qubit terms must be tuned to a specific value to successfully implement the spiral. While a pulse schedule is provided by D-wave for this hardware, the pulses actually implemented can vary from this schedule by up to 30%. This is not an issue for the classical optimization problems the `Advantage` quantum annealer is designed to solve, but represents a significant issue for reliable implementation of the adiabatic spiral on this hardware.

7.5 Discussion

In this chapter, a method of simulating the Heisenberg model on quantum hardware with native Ising interactions was extended to perform adiabatic state preparation of the Heisenberg ground state. Due to the number of quantum simulation platforms able to natively implement the Ising model, this technique is likely to have experimental applicability. It was shown that it should be feasible to implement this technique on Rydberg atoms, and that it can out-perform a Trotterized approach to adiabatic state preparation. The feasibility of implementing the adiabatic spiral on D-Wave quantum annealers was also investigated, and it was found that the requirement of turning off the $\hat{X}$ driving field at the end of the calculation limits its efficacy. The ability of the adiabatic spiral to prepare low-energy states of the Heisenberg model on these hardware platforms suggests that near-term quantum simulators can be used to perform analog quantum simulations of the $O(3)$ NLσM, and other such theories of importance to nuclear and particle physics. While the case of the fully symmetric XXX Heisenberg model was focused on in this work, the adiabatic spiral can also be applied to the XXZ Heisenberg model as well. As the approximation of the dynamics of the Heisenberg model by an Ising model with strong drive fields is a special case of the more generic phenomena of prethermalization [287, 288, 289, 290], similar ideas may find applicability for other Hamiltonians on analog quantum simulators with different native couplings.

Chapter 8

QUANTUM SIMULATION OF THE 1+ 1D O (3) NON-LINEAR σ-MODEL USING COLD ATOMS

8.1 Introduction

The O(3) NLSM in $1 + 1$ dimensions is a theory of interacting scalar particles that is asymptotically free, and can support a topologically non-trivial ground state (vacuum). Because of these qualitative similarities with QCD, it serves as a useful test-bed for the development of computational methods for QCD. A number of mappings of the O(3) NLSM suitable for quantum simulation have been introduced, including the Heisenberg comb, fuzzy sphere, angular momentum truncations and D-theory [312, 340, 25, 310, 22, 314]. Previous work has shown that at lowest truncation, the fuzzy sphere regularization reproduces the O(3) NLSM [341], while the angular momentum truncation requires a larger local Hilbert space to do so [311]. The D-theory mapping with PBC has been shown in a number of works to reproduce the O(3) NLSM, both with and without a θ-term [310, 22, 314]. However, present-day analog simulators, including arrays of cold atoms, only support OBC.

A central ingredient in lattice simulations of asymptotically-free QFT is the perturbative matching between the continuum and the lattice at short-distances (compared to the scale at the theory becomes non-perturbative). In this work, it is shown that it should be possible to perform this matching for the O(3) NLSM on existing analog quantum simulators. A definition of the renormalized coupling in the O(3) NLSM that is suitable to be used with OBC is introduced, and implemented using tensor network simulations to compute the step-scaling function in the D-theory mapping. The step-scaling function is then matched to perturbative results at short distances (ultraviolet), and the results of Monte Carlo calculations at long-distances (infrared), allowing for the minimum number of qubits required to reproduce continuum physics of the O(3) NLSM (to a given level of precision) to be determined. Tensor-network simulations indicate that asymptotic freedom and non-perturbative dynamics beyond the capabilities of classical computers in the O(3) NLSM can be potentially simulated with current cold-atom experimental configurations.

8.2 Mapping D-Theory to Qubit Registers

The $1+1$D O(3) NLSM is defined by the action

$$S = \frac{1}{2g}\int dt\ dx\ \partial_\mu \vec{\phi}(x,t)\cdot\partial^\mu\vec{\phi}(x,t) \quad , \tag{8.1}$$

where $\vec{\phi}(x,t)$ is a vector of three scalar fields subject to the constraint $\vec{\phi}(x,t)\cdot\vec{\phi}(x,t)=1$. This constraint is responsible for transforming the free-boson action in Eq. (8.1) into an interacting asymptotically-free QFT.

This theory has been extensively studied using classical MC methods using a straightforward discretization of the above continuum action,

$$S_{\text{lat}} = -\frac{1}{g}\sum_{\langle ij\rangle}\vec{\phi}_i\cdot\vec{\phi}_j \quad . \tag{8.2}$$

where the sum is over all nearest-neighbor sites i,j on a square Euclidean spacetime lattice.

Simulating this theory on a quantum computer requires a truncation of the field, and the D-theory formulation provides a natural mapping onto qubit degrees of freedom, and an intrinsic truncation, utilizing dimensional reduction. In this mapping, spin-$\frac{1}{2}$ degrees of freedom are placed on a 2D rectangular lattice of length L_x sites in the x direction and L_y sites in the y direction and coupled through an antiferromagnetic Heisenberg interaction, i.e.,

$$\hat{H}^D = J_x\sum_{x,y}\vec{S}_{x,y}\cdot\vec{S}_{x+1,y} + J_y\sum_{x,y}\vec{S}_{x,y}\cdot\vec{S}_{x,y+1} \quad . \tag{8.3}$$

To obtain the 1+1D O(3) NLSM, we choose J_x, J_y such that the 2D model is in a massless (symmetry broken) phase when $L_x, L_y\to\infty$. With these choice of parameters, the continuum limit of the NLSM is obtained in the limit $L_x\gg L_y\gg 1$, as has been demonstrated in several previous works for $J_x=J_y$ [342, 22, 343, 310, 314]. This has enabled classical Monte Carlo studies of the O(3) NLSM at finite density [342] and with a θ term [314] without a sign problem. In the isotropic ($J_x=J_y$) D-theory approach, each even L_y corresponds to a fixed coupling, and as the correlation length grows exponentially in L_y, this corresponds to a coarse set of lattice spacings. A more refined set of lattice spacings can be explored by varying J_x/J_y. In the regime $J_x/J_y\lesssim 1$, dimensional reduction should still occur, while the correlation length is reduced.

Determining the lattice spacing (in physical units) in any simulation of a QFT requires matching one or more dimensionful quantities calculated in lattice units to the corresponding experimentally or theoretically determined quantity. Such determinations have associated systematic errors due to the finite volume, imprecise input parameters, and other effects, see for example Ref. [344]. For the O(3) NLSM, the renormalized coupling can be used to set the length scale. Typically, Monte Carlo studies of the O(3) NLSM have been performed in a Euclidean spacetime with PBC, and the renormalized coupling, $\bar{g}(L)$, is defined in terms of two-point spacetime correlation functions projected onto momentum modes [345]. This definition is somewhat problematic for our present purposes because quantum simulation platforms do not have direct access to Euclidean spacetime correlation functions, and, further, it is more natural to implement OBC (for which momentum modes are no longer non-interacting eigenstates) on current platforms. Previous work has explored renormalized couplings defined in terms of energy gaps with OBC [341]. However, this is resource intensive to extract in practice on hardware, as it requires accurate preparation of both the ground state and first excited state and measurements of their energies. In this work, we introduce a new definition of $\bar{g}(L)$, given in terms of spatial correlations, that recovers the traditional definition in the perturbative regime, and which can be practically implemented in quantum simulations. Explicitly, $\bar{g}(L)$ is defined by

$$\bar{g}(L) = \frac{1}{2}\sqrt{\frac{1}{L\sin\left(\frac{\pi}{2L}\right)}\left(\frac{G_0}{G_1} - 1\right)} \quad , \tag{8.4}$$

where G_0 and G_1 are the largest and second largest eigenvalues of the vacuum correlation matrix, G_{x_1,x_2}, defined by

$$G_{x_1,x_2} = \sum_{y_1,y_2} (-1)^{x_1+y_1+x_2+y_2} \langle\psi|\, \hat{S}^z_{x_1,y_1}\hat{S}^z_{x_2,y_2}\,|\psi\rangle \ , \tag{8.5}$$

where $|\psi\rangle$ is the vacuum state of the Hamiltonian in Eq. (8.3), and $\hat{S}^z_{x,y}$ is the z-component of the spin operator at site (x, y). Recently, another method to extract the running coupling on quantum platforms for 2+1D quantum electrodynamics was proposed in Ref. [**?**], albeit with PBC.

To show that the continuum physics of the O(3) NLSM can be recovered on a quantum device, we compute a universal step-scaling function, $F_s(z)$, defined as

$$F_s(z) = s\frac{\bar{g}(sL, g_{\text{bare}})}{\bar{g}(L, g_{\text{bare}})} \quad , \tag{8.6}$$

where $z = \bar{g}(L, g_{\text{bare}})$. Here, we emphasize that the bare coupling g_{bare} is kept fixed on the right hand side. In the limit $z \to 0$, $F_s(z)$ probes IR physics and in the $z \to \infty$ limit, $F_s(z)$ probes UV physics. Therefore, if a lattice regularization reproduces the entire step scaling function it can be said to reproduce the continuum physics of the O(3) NLSM. Any lattice regularization should be able to bridge the gap between perturbative UV physics and the

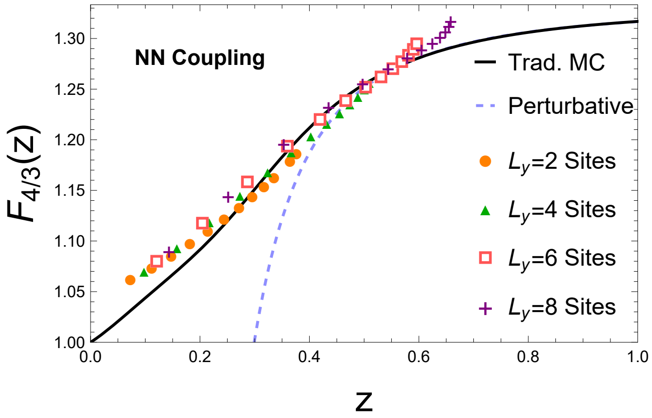

Figure 8.1: The step scaling function $F_{\frac{4}{3}}(z)$ for the coupling in Eq. (8.4) computed by varying $\frac{J_x}{J_y}$ for the nearest neighbor (NN) D-theory Hamiltonian for going from a lattice of size $6 \times L_y$ sites to $8 \times L_y$ sites. The black line is a fit to results of Monte Carlo calculations using the traditional lattice regularization. The dashed blue line is the perturbative result [345].

non-perturbative IR physics. For simulations of asymptotically-free theories, it is essential to match the lattice theory to the continuum theory (UV) with as few computational resources as possible, as the resulting non-perturbative IR physics emerges at parametrically larger length scales.

To determine the size of lattices required to reproduce the O(3) NLSM, DMRG calculations were performed using the C++ `ITensor` library [147, 148] to obtain the vacuum state of the Hamiltonian in Eq. (8.3) for lattices of size $6 \times L_y$ and $8 \times L_y$ with OBC [148, 115, 149, 150]. The renormalized couplings defined by Eq. (8.4) were used to compute $F_s(z)$ with $s = \frac{4}{3}$. Note that while traditionally $F_s(z)$ is computed for $s = 2$, any value of s may be used in principle, and we have used $s = \frac{4}{3}$ to reduce the classical computing overhead. Different points on the $F_{\frac{4}{3}}(z)$ curve, shown in Fig. 8.1, were computed by varying $\frac{J_x}{J_y}$ in the range $0.1 \leq \frac{J_x}{J_y} \leq 1.3$. At the lower end of the perturbative regime, $z \lesssim 0.55$, $F_s(z)$ is reproduced sufficiently well with $L_x = 6, 8$ lattice sites, provided a large transverse direction $L_y = 8$ is used. This indicates that perturbative matching between the continuum and lattice O(3) NLSM theories can be accomplished with as few as 64 qubits on a quantum device.

While the D-theory Hamiltonian with nearest-neighbor couplings is natural to consider, some quantum simulation platforms, such as cold atoms, have long range couplings. For example, arrays of Rydberg atoms with an s-wave coupling are described by a Hamiltonian

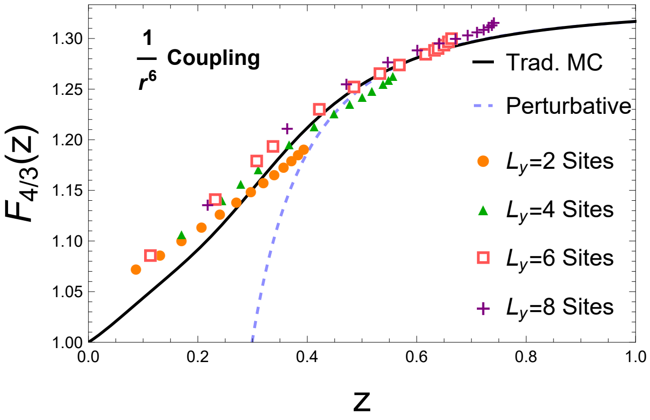

Figure 8.2: The step-scaling function computed by varying $\frac{a_x}{a_y}$ for the $\frac{1}{r^6}$ D-theory Hamiltonian for going from a lattice of size $6 \times L_y$ sites to $8 \times L_y$ sites.

with the form,

$$\hat{H}^{\text{Ryd.}} = \sum_i \frac{\Omega_i(t)}{2} \hat{X}_i + \sum_i \Delta_i(t) \hat{n}_i + \sum_{i<j} \frac{C_6 \ \hat{n}_i \hat{n}_j}{|\vec{x}_i - \vec{x}_j|^6} \quad , \tag{8.7}$$

where $\hat{n}_i$ is the Rydberg-state occupation of atom i, $\vec{x}_i$ is the position of atom i, and $\hat{X}_i$ couples the ground state of atom i to its excited Rydberg state [346, 347]. $\Omega_i(t)$ specifies the strength of the driving field at atom i, and $\Delta_i(t)$ specifies a local detuning. By identifying the excited-state occupation number with the z-component of a spin, it can be seen that this system is described by an Ising Hamiltonian with long-range interactions and time-dependent external fields. Due to this native encoding of the Ising model, Rydberg atoms have been used in a number of studies to perform analog quantum simulations of the Ising model [245, 246, 320, 348]. As we have shown in previous works, the Ising model with a strong transverse and longitudinal field can reproduce the dynamics of the Heisenberg model, and time dependent external fields can be used to adiabatically prepare ground states of the Heisenberg model with long range interactions [318, 349]. In particular, by arranging atoms in a rectangular lattice and identifying the number operator of the atom at site (x, y), $\hat{n}_{x,y}$ with a staggered z-component of a spin operator, i.e., $\hat{n}_{x,y} = \frac{1}{2} + (-1)^{x+y} \hat{S}^z_{x,y}$, it is possible to engineer a Heisenberg Hamiltonian,

$$\hat{H}^{\text{D6}} = \sum_{x_1,y_1,x_2,y_2} \frac{(-1)^{1+x_1+y_1+x_2+y_2}}{\left(a_x^2(x_1-x_2)^2 + a_y^2(y_1-y_2)^2\right)^3} \vec{S}_{x_1,y_1} \cdot \vec{S}_{x_2,y_2} \quad , \tag{8.8}$$

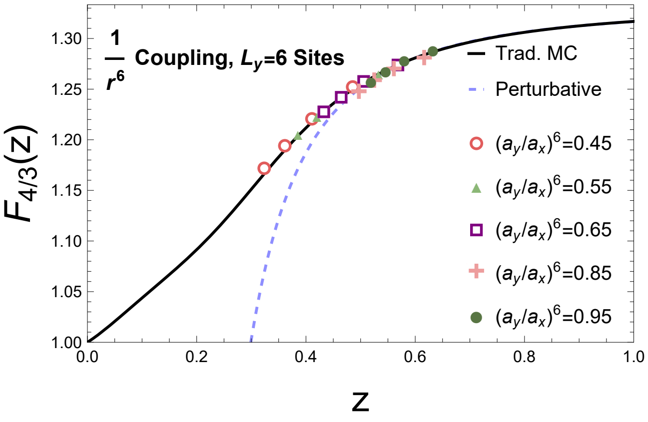

Figure 8.3: The step-scaling function computed for $L_x = 6, 12, 18$ and 24 sites with the $\frac{1}{r^6}$ D-theory Hamiltonian with $L_y = 6$ sites.

where $a_{x,y}$ are the lattice spacings in the x, y directions. The staggered identification of the number operator with the spin operator is necessary to ensure that the state with all atoms in their ground state, in which the system will begin in a quantum simulation, corresponds to a state with staggered spins that is adiabatically connected to the ground state of Eq. 8.8. The staggering identification also makes the long range interactions frustration-free. Note that the Hamiltonian implemented on hardware will differ from that of Eq. 8.8 by a sign, but due to time reversal symmetry this does not present an issue. This Hamiltonian is equivalent to the Hamiltonian in Eq. (8.3) with the addition of long-range frustration-free Heisenberg interactions. Therefore, it is expected that $a_{x,y}$ can be tuned so that dimensional reduction occurs and the low energy degrees of freedom are described by the $1+1$D O(3) NLSM. To verify this, the step-scaling function for the vacuum state of this Hamiltonian was computed using DMRG, with the results shown in Fig. 8.2, where $\frac{a_y}{a_x}$ was varied in the range $0.1 \leq \left(\frac{a_y}{a_x}\right)^6 \leq 1.3$. The step-scaling function computed with $L_y = 6$ reproduces the perturbative function over a range of parameters well into the perturbative regime, demonstrating that, for this range of couplings, the UV physics of the O(3) NLSM is correctly reproduced. It is interesting to note that $L_y = 6$ with nearest neighbor couplings only is not able to reproduce the step-scaling function as precisely in this region, and in this sense, the $\frac{1}{r^6}$ coupling effectively implements an “improved” Hamiltonian that enables more precise matching with fewer qubits. However, $L_y = 6$ appears to be an optimum in this case, since $L_y = 8$ has again larger systematic errors for this L_x.

With controlled matching to the continuum theory, non-perturbative IR physics of the O(3) NLSM is expected to be able to be simulated by keeping the Hamiltonian parameters

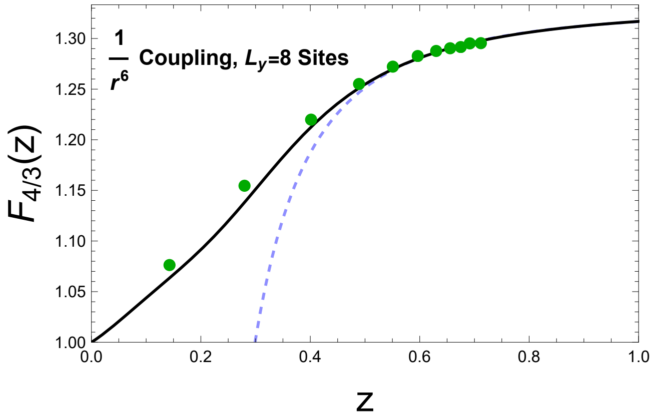

Figure 8.4: $F_{4/3}(z)$ computed by varying $\frac{a_x}{a_y}$ for the $\frac{1}{r^6}$ D-theory Hamiltonian for going from a lattice of size 12 × 8 sites to 16 × 8 sites.

J_x, J_y, L_y fixed while increasing the lattice size L_x. To demonstrate that this procedure reproduces the IR correctly, $F_s(z)$ was computed with DMRG for lattices with larger L_x and $L_y = 6$, as shown in Fig. 8.3. $F_{\frac{4}{3}}(z)$ is correctly recovered in the nonperturbative regime as the lattice size is increased (when compared with the results of classical Monte Carlo calculations), over a wide range of anisotropy $0.45 \leq (a_y/a_x)^6 \leq 0.95$.

To match at scales further into the UV, lattices with larger L_y must be used. However, when $L_y > L_x$ it is possible for dimensional reduction to fail and the 1 + 1D O(3) NLSM may not be reproduced, as is found for $L_y = 8$ where the results overshoot the Monte Carlo and perturbative step-scaling functions, as shown in Fig. 8.2. This can be remedied by using lattices with larger L_x. In Fig. 8.4, $F_{4/3}(z)$ from 12 × 8 to 16 × 8 lattices with the $\frac{1}{r^6}$ D-theory Hamiltonian is shown, which correctly reproduces the known result over a larger range than with the $L_y = 6$, $\frac{1}{r^6}$ D-theory Hamiltonian. This demonstrates how larger correlation lengths may be accessed, and hence the approach to the continuum limit.

8.3 Quantum Simulations of O(3) NLSM using Rydberg Atoms

Arrays of cold atoms are a promising platform for quantum simulation and as shown above, modest lattice sizes of 6 × 6 and 8 × 6 are sufficient to reproduce the UV physics of the O(3) NLSM, and demonstrate asymptotic freedom. This provides an opportunity for a first attempt at performing quantum simulations of non-perturbative (IR) dynamics of the O(3) NLSM. To do so will require the preparation of a low energy state with respect to the Hamiltonian in eq. (8.8). The adiabatic spiral [349] can be used to adiabatically prepare the ground state of this Hamiltonian on an array of cold atoms. To understand the quantum

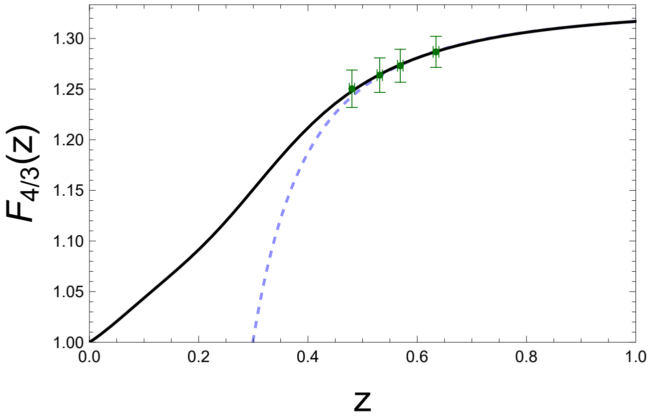

Figure 8.5: Results for $F_{4/3}(z)$ computed in a TDVP simulation of a rectangular array of ^{87}Rb atoms assuming 5000 shots are used.

resources required to adiabatically prepare states with energy that is sufficiently low to reproduce low-lying physics of the O(3) NLSM, we performed TDVP simulations of the adiabatic spiral using the C++ `ITensor` library [148, 147, 297, 298, 299]. Details of these calculations can be found in Appendix .7. The classical simulations we performed assumed a rectangular array of ^{87}Rb atoms, with $C_6 = 5.42 \times 10^6$ MHz μm^6, with a vertical lattice spacing of 11 μm, and a selection of horizontal lattice spacings to probe different couplings. We assumed a maximum Rabi frequency of $\Omega = 25$ MHz, and a maximum coherence time of $4\mu s$. The initial state of the system with all atoms in their ground state corresponds to a Nèel state that is degenerate due to a symmetry under reflection of the spins. This degeneracy can be split by evolving with a global detuning term that is turned off during the course of the adiabatic evolution to apply an energy penalty. The initial size of the energy penalty was variationally optimized so that the renormalized coupling of the prepared state matched the vacuum state. The specific energy penalties and horizontal lattice spacings that we used are shown in Tables 8.1 and 8.2. Results for the step scaling obtained from these simulations are shown in Fig. 8.5, where the uncertainties are derived from a sample of 5000 shots in computing the renormalized coupling for each lattice configuration.

These simulations show that an ideal cold-atom quantum simulator with only 48 atoms can correctly recover the UV physics of the O(3) NLSM with sufficient precision. To perform this quantum simulation in reality would require a rectangular array of ^{87}Rb atoms with a global driving field and a staggered detuning term. The parameters used in these simulations are close to those that have been implemented in previous cold-atom experiments [245, 246, 320, 348, 350]. Therefore, it is anticipated that analog quantum simulations of the O(3)

a_X (μm)	Energy Penalty (MHz)	Final Energy (Δ)
12.5	0.44	2.81
12.1	0.52	2.90
11.8	0.56	3.43
11.1	0.49	4.64

Table 8.1: Energy of the ground states prepared using the adiabatic spiral. The left column shows the lattice spacing used for the tensor network simulations of a 6 × 6 lattice. The center column shows the energy penalty used to match the vacuum renormalized coupling. The right column shows the energy of the state prepared by the adiabatic spiral in units of the Hamiltonian's energy gap.

a_X (μm)	Energy Penalty (MHz)	Final Energy (Δ)
12.5	0.3	4.52
12.1	0.4	4.56
11.8	0.46	5.43
11.1	0.45	7.52

Table 8.2: Energy of the ground states prepared using the adiabatic spiral. The left column shows the lattice spacing used for the tensor network simulations of a 8 × 6 lattice. The center column shows the energy penalty used to match the vacuum renormalized coupling. The right column shows the energy of the state prepared by the adiabatic spiral in units of the Hamiltonian's energy gap.

NLSM should soon be within reach. Due to the similarity to previous cold atom experiments, it is expected that these simulations can be performed with a high degree of fidelity. Scaling to larger systems will require the same pulse sequences applied to larger arrays of atoms. This is not expected to present an issue as larger arrays of Rydberg atoms have been utilized in experiment [245, 246, 348] and the techniques used to simulate Heisenberg evolution have been shown to scale to large systems [318]. Note that while the simulations performed here are for arrays of ^{87}Rb atoms, similar calculations could be performed using different atomic species, such as Cs [351, 352].

Reproducing the step scaling curve shows that O(3) NLSM physics is actually being reproduced on the quantum simulator and is the first step towards achieving a quantum advantage in the simulation of the O(3) NLSM. Once an approximate vacuum state has been prepared on quantum hardware, particle wavepackets can be excited by varying a local detuning or driving term. By exciting multiple particles in this manner, scattering in the O(3) NLSM can be directly simulated. Alternatively, all of this can be also be done at a nonzero θ, by moving the atoms from a rectangular array into a staggered array [314].

Using dynamical reconfiguration of atoms, this could even be done dynamically, simulating a quench of the θ term. Rapidly turning on θ would correspond to a rapidly changing axion field [353, 354] and has been shown to generate a dynamical quantum phase transition in the context of lattice gauge theories [355, 356]. Both of these calculations involve real-time dynamics that have exponentially scaling computational costs on classical computers, and their successful simulation on a quantum computer could represent a true quantum advantage of scientific relevance to high energy physics.

Note that these problems on the lattice sizes simulated in this section are within the reach of classical computers. Also, a true quantum advantage in simulations of the 1+1D O(3) NLSM will need to be performed with a choice of parameters that are outside the reach of perturbation theory. Based on Fig. 8.3, performing these simulations on a lattice of size 18×6 with $(a_y/a_x)^6 = 0.45$ is a potential candidate for quantum advantage. A lattice of this size is outside the reach of statevector simulation and lies in the non-perturbative region of the step scaling curve. The DMRG calculations to produce Fig. 8.3 required a bond dimension of 2000 to converge and simulating scattering dynamics or a θ quench will involve an exponentially growing bond dimension beyond this. Note however, that some tensor networks more suited to 2D such as PEPS may be able to perform this calculation with a lower bond dimension. Regardless, a simulation on this lattice size will be in a regime that is difficult for classical computers and would represent a first chance at seeing a quantum advantage.

8.4 Discussion

For strong interactions, asymptotic freedom has been key in enabling non-perturbative classical calculations with lattice QCD of near-static quantities, and much of the associated technology will translate across to quantum simulations. In this chapter, we have studied a different asymptotically-free field theory. By developing new methods and performing classical simulations, we have shown that present-day analog quantum simulators have the potential to perform quantum simulations of non-perturbative dynamics within this QFT with fully-quantifiable uncertainties. A definition of the renormalized coupling for the 1+1D O(3) NLSM with OBC was developed to enable the first perturbative matching of lattice calculations on quantum simulators to the continuum. It is expected that this will enable the use of quantum simulators to compute quantities of interest in the continuum limit of the 1+1D O(3) NLSM. Additionally, this definition was used to determine the minimal number of qubits required for a quantum computer to reproduce continuum physics. Remarkably, a cold atom quantum simulator only needs a rectangular array of 48 atoms to begin to quantitatively reproduce non-perturbative dynamics within the O(3) NLSM. Cold atoms have been previously used to simulate larger systems and tensor network simulations suggest that existing cold-atom experiments should be capable of demonstrating the asymptotic freedom of the O(3) NLSM. We have also shown that the long-range coupling present in cold-atom quantum simulators enables them to make contact with the continuum physics of the O(3) NLSM with fewer qubits than mappings that are restricted to nearest neighbor couplings. This is the first concrete example of an "improved" Hamiltonian that reduces the qubit count required for a quantum simulation of a lattice field theory to rigorously simulate continuum physics with controlled uncertainties.

While the 1+1D O(3) NLSM does not describe any of the fundamental forces in nature, it does share a number of qualitative aspects with QCD so these simulations will provide valuable insights into how to perform quantum simulations of Standard Model physics. Our calculations correctly recover the classically-computed step-scaling function, and demonstrate that the continuum O(3) NLSM is being matched, within tolerances, to lattices, and provides new and valuable further steps toward rigorously extracting information about a continuum QFT from quantum computers. Once matching has been performed, a quantum computer can be used to simulate non-perturbative quantities in the theory that are beyond the reach of classical computers, including scattering and fragmentation, and θ-quenches. Further, the D-theory mapping studied in this work has the potential to be used to simulate the O(3) NLSM in $2+1$ dimensions by making use of 3D cold-atom arrays which have recently been experimentally demonstrated [357].

Part IV

SUMMARY

The research in this dissertation has focused on the development of quantum simulation techniques for lattice QCD. An encoding of SU(3) gauge fields onto a quantum computer was investigated. This encoding was used to simulate time evolution on a quantum computer for small lattices. The potential for scaling up this encoding to larger lattices was investigated. Techniques for preparing the vacuum state with this encoding were also developed and applied on quantum processors. The scalability of these techniques were investigated using tensor network simulations. Improved Hamiltonians have been derived to correct for truncating the gauge fields encoded on a quantum processor, enabling the first quantum simulation of lattice QCD with quarks in three spatial dimensions. Time evolution algorithms for a fermionic Hamiltonian were developed and their worst case performance was bounded. An algorithm was introduced to compute particle decay rates. This algorithm was implemented to study a scalar field theory and the theoretical scaling of the algorithm was determined. These investigations in the first part of this dissertation are expected to be directly relevant for performing quantum simulations of lattice QCD at scale in the future.

The second part of this dissertation investigated analog quantum simulation of the O(3) non-linear σ model. Due to the simplicity of this model, it was possible to construct observables and determine the resources required to probe the continuum limit on a quantum simulator. It is expected that the insights from this investigation will be relevant for taking the continuum limit of a lattice QCD calculation performed on a quantum computer. These investigations also led to new insights into approximate symmetries of the Ising model with strong external fields which describes a number of quantum simulation platforms.

The techniques discussed in this dissertation have enabled quantum simulations of lattice QCD on small lattices. In the time in which the work in this dissertation was performed, quantum computers have grown in size and error rates have fallen. Error mitigation techniques have also improved and enabled more sophisticated calculations to be performed on quantum processors. With these advances, it is now possible to begin probing non-trivial dynamics of lattice QCD on quantum computers. This will enable the use of near term quantum computers to begin computing dynamical quantities such as the QCD viscosity and real time simulations of hadronization. These first calculations will be limited to small lattices with coarse spacings but will be useful for developing techniques for more accurate calculations in the future. As quantum computers grow in capability and theoretical techniques improve, these calculations will be refined and provide new insights into the dynamics of QCD.

Part V

APPENDIX

.1 *SU(3) Plaquette Operators*

.1.1 *Plaquette Matrix Elements*

A derivation of plaquette operator matrix elements is presented after classical incorporation of the local vector indices. Due to the single-link delocalization of the plaquette operator in a generically structured Hilbert space, as discussed in Section 1.2.1, calculating matrix elements on a three plaquette lattice will be sufficient for evaluations of plaquette strings of arbitrary length.

Employing the labels of Fig. 1.1, the wavefunction for the three-plaquette system with open boundary conditions is

$$\left| \begin{pmatrix} \mathbf{C}_1, \mathbf{R}_t, \mathbf{C}_3 \\ \mathbf{Q}_\ell, \mathbf{Q}_r \\ \mathbf{C}_2, \mathbf{R}_b, \mathbf{C}_4 \end{pmatrix} \right\rangle = \frac{1}{\dim(\mathbf{Q}_\ell)\dim(\mathbf{Q}_r)}$$

$$\sum_{all} |\mathbf{C}_1, a, b\rangle |\mathbf{Q}_\ell, c, d\rangle |\mathbf{C}_2, e, f\rangle |\mathbf{R}_t, g, h\rangle |\mathbf{Q}_r, i, j\rangle |\mathbf{R}_b, k, \ell\rangle |\mathbf{C}_3, m, n\rangle |\mathbf{C}_4, p, q\rangle$$

$$\langle \mathbf{C}_1, b, \overline{\mathbf{R}}_t, g | \overline{\mathbf{Q}}_\ell, d\rangle_{\Gamma_1} \langle \mathbf{R}_t, h, \overline{\mathbf{C}}_3, m | \overline{\mathbf{Q}}_r, j\rangle_{\Gamma_2} \langle \mathbf{C}_2, f, \overline{\mathbf{R}}_b, k | \mathbf{Q}_\ell, c\rangle_{\Gamma_3} \langle \mathbf{R}_b, \ell, \overline{\mathbf{C}}_4, p | \mathbf{Q}_r, i\rangle_{\Gamma_4} \quad , \tag{9}$$

where the sum is over all component indices, characterized by color isospin and color hypercharge quantum numbers. The normalization of this state has been determined through the application of the CG sum relation,

$$\sum_{a,\alpha,a'} |\langle \mathbf{R}_1, a, \mathbf{R}_2, \alpha | \mathbf{R}', a'\rangle_\Gamma|^2 = \dim(\mathbf{R}') \qquad , \qquad \mathbf{R}' \in \mathbf{R}_1 \otimes \mathbf{R}_2 \quad . \tag{10}$$

Application of the plaquette operator can be expressed in terms of four local link operators,

$$\hat{U}^{(\mathbf{3})}_{\alpha,\beta}\hat{U}^{(\mathbf{3})}_{\beta,\gamma}\left(\hat{U}^{(\mathbf{3})}_{\gamma,\delta}\right)^{\dagger}\left(\hat{U}^{(\mathbf{3})}_{\delta,\alpha}\right)^{\dagger}\left|\begin{pmatrix}\mathbf{C}_1,\mathbf{R}_t,\mathbf{C}_3\\ \mathbf{Q}_\ell,\mathbf{Q}_r\\ \mathbf{C}_2,\mathbf{R}_b,\mathbf{C}_4\end{pmatrix}\right\rangle \;=\; \frac{1}{\dim(\mathbf{Q}_\ell)\dim(\mathbf{Q}_r)}\sum_{all}$$
$$\langle\mathbf{C}_1,b,\overline{\mathbf{R}}_t,g|\overline{\mathbf{Q}}_\ell,d\rangle_{\Gamma_1}\langle\mathbf{R}_t,h,\overline{\mathbf{C}}_3,m|\overline{\mathbf{Q}}_r,j\rangle_{\Gamma_2}\langle\mathbf{C}_2,f,\overline{\mathbf{R}}_b,k|\mathbf{Q}_\ell,c\rangle_{\Gamma_3}\langle\mathbf{R}_b,\ell,\overline{\mathbf{C}}_4,p|\mathbf{Q}_r,i\rangle_{\Gamma_4}$$
$$|\mathbf{C}_1,a,b\rangle\hat{U}^{(\bar{\mathbf{3}})}_{\alpha,\delta}|\mathbf{Q}_\ell,c,d\rangle|\mathbf{C}_2,e,f\rangle\hat{U}^{(\bar{\mathbf{3}})}_{\delta,\gamma}|\mathbf{R}_t,g,h\rangle\hat{U}^{(\mathbf{3})}_{\beta,\gamma}|\mathbf{Q}_r,i,j\rangle\hat{U}^{(\mathbf{3})}_{\alpha,\beta}|\mathbf{R}_b,k,\ell\rangle|\mathbf{C}_3,m,n\rangle|\mathbf{C}_4,p,q\rangle \quad . \tag{11}$$

Explicitly acting in the left and right spaces, the link operator functions as,

$$\begin{aligned}\hat{U}^{(\mathbf{3})}_{\ell r}|\mathbf{R},a,b\rangle &= \hat{U}^{(\mathbf{3})}_{\ell r}|\overline{\mathbf{R}},a\rangle\otimes|\mathbf{R},b\rangle \quad ,\\ &= \sum_{\oplus\mathbf{R}',\vec{\Gamma}}\sqrt{\frac{\dim\mathbf{R}}{\dim\mathbf{R}'}}\;|\bar{\mathbf{R}}',a'\rangle\langle\overline{\mathbf{R}}',a'|\overline{\mathbf{R}},a,\overline{\mathbf{3}},\ell\rangle_{\Gamma_1}\otimes|\mathbf{R},b\rangle\langle\mathbf{R}',b'|\mathbf{R},b,\mathbf{3},r\rangle_{\Gamma_2} \quad ,\\ &= \sum_{\oplus\mathbf{R}',\vec{\Gamma}}\sqrt{\frac{\dim\mathbf{R}}{\dim\mathbf{R}'}}\;|\mathbf{R}',a',b'\rangle\;\langle\mathbf{R},a,\mathbf{3},\ell|\mathbf{R}',a'\rangle_{\Gamma_1}\langle\mathbf{R}',b'|\mathbf{R},b,\mathbf{3},r\rangle_{\Gamma_2} \quad ,\end{aligned} \tag{12}$$

leading to a final state of,

$$\hat{\Box}\left|\begin{pmatrix}\mathbf{C}_1,\mathbf{R}_t,\mathbf{C}_3\\ \mathbf{Q}_\ell,\mathbf{Q}_r\\ \mathbf{C}_2,\mathbf{R}_b,\mathbf{C}_4\end{pmatrix}\right\rangle = \frac{1}{\dim(\mathbf{Q}_\ell)\dim(\mathbf{Q}_r)}\sum_{all}\;\sum_{\oplus\vec{\mathbf{R}}',\vec{\mathbf{Q}}',\vec{\Gamma}}\sqrt{\frac{\dim(\mathbf{R}_t)\dim(\mathbf{R}_b)\dim(\mathbf{Q}_\ell)\dim(\mathbf{Q}_r)}{\dim(\mathbf{R}'_t)\dim(\mathbf{R}'_b)\dim(\mathbf{Q}'_\ell)\dim(\mathbf{Q}'_r)}}$$
$$\langle\mathbf{C}_1,b,\overline{\mathbf{R}}_t,g|\overline{\mathbf{Q}}_\ell,d\rangle_{\Gamma_1}\langle\mathbf{R}_t,h,\overline{\mathbf{C}}_3,m|\overline{\mathbf{Q}}_r,j\rangle_{\Gamma_2}\langle\mathbf{C}_2,f,\overline{\mathbf{R}}_b,k|\mathbf{Q}_\ell,c\rangle_{\Gamma_3}\langle\mathbf{R}_b,\ell,\overline{\mathbf{C}}_4,p|\mathbf{Q}_r,i\rangle_{\Gamma_4}$$
$$\langle\mathbf{R}_b,k,\mathbf{3},\alpha|\mathbf{R}'_b,k'\rangle_{\Gamma_5}\langle\mathbf{R}'_b,\ell'|\mathbf{R}_b,\ell,\mathbf{3},\beta\rangle_{\Gamma_6}$$
$$\langle\mathbf{Q}_r,i,\mathbf{3},\beta|\mathbf{Q}'_r,i'\rangle_{\Gamma_7}\langle\mathbf{Q}'_r,j'|\mathbf{Q}_r,j,\mathbf{3},\gamma\rangle_{\Gamma_8}$$
$$\langle\mathbf{R}_t,g,\overline{\mathbf{3}},\delta|\mathbf{R}'_t,g'\rangle_{\Gamma_9}\langle\mathbf{R}'_t,h'|\mathbf{R}_t,h,\overline{\mathbf{3}},\gamma\rangle_{\Gamma_{10}}$$
$$\langle\mathbf{Q}_\ell,c,\overline{\mathbf{3}},\alpha|\mathbf{Q}'_\ell,c'\rangle_{\Gamma_{11}}\langle\mathbf{Q}'_\ell,d'|\mathbf{Q}_\ell,d,\overline{\mathbf{3}},\delta\rangle_{\Gamma_{12}}$$
$$|\mathbf{C}_1,a,b\rangle|\mathbf{Q}'_\ell,c',d'\rangle|\mathbf{C}_2,e,f\rangle|\mathbf{R}'_t,g',h'\rangle|\mathbf{Q}'_r,i',j'\rangle|\mathbf{R}'_b,k',\ell'\rangle|\mathbf{C}_3,m,n\rangle|\mathbf{C}_4,p,q\rangle \quad . \tag{13}$$

Contraction with a final state produces the following matrix elements,

$$
\begin{aligned}
&\left\langle \begin{pmatrix} \mathbf{C}_1, \mathbf{R}'_t, \mathbf{C}_3 \\ \mathbf{Q}'_\ell, \mathbf{Q}'_r \\ \mathbf{C}_2, \mathbf{R}'_b, \mathbf{C}_4 \end{pmatrix} \middle| \hat{\square} \middle| \begin{pmatrix} \mathbf{C}_1, \mathbf{R}_t, \mathbf{C}_3 \\ \mathbf{Q}_\ell, \mathbf{Q}_r \\ \mathbf{C}_2, \mathbf{R}_b, \mathbf{C}_4 \end{pmatrix} \right\rangle = \\
&\frac{1}{\dim(\mathbf{Q}_\ell)\dim(\mathbf{Q}_r)\dim(\mathbf{Q}'_\ell)\dim(\mathbf{Q}'_r)} \sum_{all,\vec{\Gamma}} \sqrt{\frac{\dim(\mathbf{R}_t)\dim(\mathbf{R}_b)\dim(\mathbf{Q}_\ell)\dim(\mathbf{Q}_r)}{\dim(\mathbf{R}'_t)\dim(\mathbf{R}'_b)\dim(\mathbf{Q}'_\ell)\dim(\mathbf{Q}'_r)}} \\
&\langle \mathbf{C}_1, b, \overline{\mathbf{R}}_t, g | \overline{\mathbf{Q}}_\ell, d\rangle_{\Gamma_1} \langle \mathbf{R}_t, h, \overline{\mathbf{C}}_3, m | \overline{\mathbf{Q}}_r, j\rangle_{\Gamma_2} \langle \mathbf{C}_2, f, \overline{\mathbf{R}}_b, k | \mathbf{Q}_\ell, c\rangle_{\Gamma_3} \langle \mathbf{R}_b, \ell, \overline{\mathbf{C}}_4, p | \mathbf{Q}_r, i\rangle_{\Gamma_4} \\
&\langle \mathbf{R}_b, k, \mathbf{3}, \alpha | \mathbf{R}'_b, k'\rangle_{\Gamma_5} \langle \mathbf{R}'_b, \ell' | \mathbf{R}_b, \ell, \mathbf{3}, \beta\rangle_{\Gamma_6} \\
&\langle \mathbf{Q}_r, i, \mathbf{3}, \beta | \mathbf{Q}'_r, i'\rangle_{\Gamma_7} \langle \mathbf{Q}'_r, j' | \mathbf{Q}_r, j, \mathbf{3}, \gamma\rangle_{\Gamma_8} \\
&\langle \mathbf{R}_t, g, \overline{\mathbf{3}}, \delta | \mathbf{R}'_t, g'\rangle_{\Gamma_9} \langle \mathbf{R}'_t, h' | \mathbf{R}_t, h, \overline{\mathbf{3}}, \gamma\rangle_{\Gamma_{10}} \\
&\langle \mathbf{Q}_\ell, c, \overline{\mathbf{3}}, \alpha | \mathbf{Q}'_\ell, c'\rangle_{\Gamma_{11}} \langle \mathbf{Q}'_\ell, d' | \mathbf{Q}_\ell, d, \overline{\mathbf{3}}, \delta\rangle_{\Gamma_{12}} \\
&\langle \overline{\mathbf{Q}}'_\ell, d' | \mathbf{C}_1, b, \overline{\mathbf{R}}'_t, g'\rangle_{\Gamma_{13}} \langle \overline{\mathbf{Q}}'_r, j' | \mathbf{R}'_t, h', \overline{\mathbf{C}}_3, m\rangle_{\Gamma_{14}} \langle \mathbf{Q}'_\ell, c' | \mathbf{C}_2, f, \overline{\mathbf{R}}'_b, k'\rangle_{\Gamma_{15}} \langle \mathbf{Q}'_r, i' | \mathbf{R}'_b, \ell', \overline{\mathbf{C}}_4, p\rangle_{\Gamma_{16}} \quad .
\end{aligned} \tag{14}
$$

This expression can be collected into four vertex factors

$$
\begin{aligned}
&\left\langle \begin{pmatrix} \mathbf{C}_1, \mathbf{R}'_t, \mathbf{C}_3 \\ \mathbf{Q}'_\ell, \mathbf{Q}'_r \\ \mathbf{C}_2, \mathbf{R}'_b, \mathbf{C}_4 \end{pmatrix} \middle| \hat{\square} \middle| \begin{pmatrix} \mathbf{C}_1, \mathbf{R}_t, \mathbf{C}_3 \\ \mathbf{Q}_\ell, \mathbf{Q}_r \\ \mathbf{C}_2, \mathbf{R}_b, \mathbf{C}_4 \end{pmatrix} \right\rangle = \\
&\sqrt{\frac{\dim(\mathbf{R}_t)\dim(\mathbf{R}_b)}{\dim(\mathbf{R}'_t)\dim(\mathbf{R}'_b)\dim(\mathbf{Q}_\ell)\dim(\mathbf{Q}_r)\dim(\mathbf{Q}'_\ell)^3\dim(\mathbf{Q}'_r)^3}} \\
&\sum \langle \mathbf{C}_1, b, \overline{\mathbf{R}}_t, g | \overline{\mathbf{Q}}_\ell, d\rangle_{\Gamma_1} \langle \mathbf{R}_t, g, \overline{\mathbf{3}}, \delta | \mathbf{R}'_t, g'\rangle_{\Gamma_2} \langle \mathbf{Q}'_\ell, d' | \mathbf{Q}_\ell, d, \overline{\mathbf{3}}, \delta\rangle_{\Gamma_3} \langle \overline{\mathbf{Q}}'_\ell, d' | \mathbf{C}_1, b, \overline{\mathbf{R}}'_t, g'\rangle_{\Gamma_4} \\
&\sum \langle \mathbf{R}_t, h, \overline{\mathbf{C}}_3, m | \overline{\mathbf{Q}}_r, j\rangle_{\Gamma_5} \langle \mathbf{Q}'_r, j' | \mathbf{Q}_r, j, \mathbf{3}, \gamma\rangle_{\Gamma_6} \langle \mathbf{R}'_t, h' | \mathbf{R}_t, h, \overline{\mathbf{3}}, \gamma\rangle_{\Gamma_7} \langle \overline{\mathbf{Q}}'_r, j' | \mathbf{R}'_t, h', \overline{\mathbf{C}}_3, m\rangle_{\Gamma_8} \\
&\sum \langle \mathbf{C}_2, f, \overline{\mathbf{R}}_b, k | \mathbf{Q}_\ell, c\rangle_{\Gamma_9} \langle \mathbf{R}_b, k, \mathbf{3}, \alpha | \mathbf{R}'_b, k'\rangle_{\Gamma_{10}} \langle \mathbf{Q}_\ell, c, \overline{\mathbf{3}}, \alpha | \mathbf{Q}'_\ell, c'\rangle_{\Gamma_{11}} \langle \mathbf{Q}'_\ell, c' | \mathbf{C}_2, f, \overline{\mathbf{R}}'_b, k'\rangle_{\Gamma_{12}} \\
&\sum \langle \mathbf{R}_b, \ell, \overline{\mathbf{C}}_4, p | \mathbf{Q}_r, i\rangle_{\Gamma_{13}} \langle \mathbf{R}'_b, \ell' | \mathbf{R}_b, \ell, \mathbf{3}, \beta\rangle_{\Gamma_{14}} \langle \mathbf{Q}_r, i, \mathbf{3}, \beta | \mathbf{Q}'_r, i'\rangle_{\Gamma_{15}} \langle \mathbf{Q}'_r, i' | \mathbf{R}'_b, \ell', \overline{\mathbf{C}}_4, p\rangle_{\Gamma_{16}} \quad .
\end{aligned} \tag{15}
$$

Using a phase convention of real CGs, thus equivalent in the left and right spaces, and a full-conjugation of the irreps in 4 of the 16 above CGs to standardize indices, yields the identification of plaquette matrix elements as written in Eq. (1.6).

Below is presented the collection of physical plaquette matrix elements of Eq. (1.6) for the 8 unique control sectors of the local plaquette operator in the truncated qutrit space $\{\mathbf{1}, \mathbf{3}, \overline{\mathbf{3}}\}$.

$\begin{pmatrix}\mathbf{1} & & \mathbf{1}\\ & (\hat{\Box},\hat{\Box}^{\dagger}) & \\ \mathbf{1} & & \mathbf{1}\end{pmatrix}$	$\left\vert\begin{pmatrix}\bullet,\mathbf{1},\bullet\\ \mathbf{1},\mathbf{1}\\ \bullet,\mathbf{1},\bullet\end{pmatrix}\right\rangle$	$\left\vert\begin{pmatrix}\bullet,\mathbf{3},\bullet\\ \mathbf{3},\overline{\mathbf{3}}\\ \bullet,\overline{\mathbf{3}},\bullet\end{pmatrix}\right\rangle$	$\left\vert\begin{pmatrix}\bullet,\overline{\mathbf{3}},\bullet\\ \overline{\mathbf{3}},\mathbf{3}\\ \bullet,\mathbf{3},\bullet\end{pmatrix}\right\rangle$
$\left\langle\begin{pmatrix}\bullet,\mathbf{1},\bullet\\ \mathbf{1},\mathbf{1}\\ \bullet,\mathbf{1},\bullet\end{pmatrix}\right\vert$	$(0,0)$	$(1,0)$	$(0,1)$
$\left\langle\begin{pmatrix}\bullet,\mathbf{3},\bullet\\ \mathbf{3},\overline{\mathbf{3}}\\ \bullet,\overline{\mathbf{3}},\bullet\end{pmatrix}\right\vert$	$(0,1)$	$(0,0)$	$(1,0)$
$\left\langle\begin{pmatrix}\bullet,\overline{\mathbf{3}},\bullet\\ \overline{\mathbf{3}},\mathbf{3}\\ \bullet,\mathbf{3},\bullet\end{pmatrix}\right\vert$	$(1,0)$	$(0,1)$	$(0,0)$

$\begin{pmatrix}\mathbf{1} & & \mathbf{3}\\ & (\hat{\Box},\hat{\Box}^{\dagger}) & \\ \mathbf{1} & & \overline{\mathbf{3}}\end{pmatrix}$	$\left\vert\begin{pmatrix}\bullet,\mathbf{1},\bullet\\ \mathbf{1},\mathbf{3}\\ \bullet,\mathbf{1},\bullet\end{pmatrix}\right\rangle$	$\left\vert\begin{pmatrix}\bullet,\mathbf{3},\bullet\\ \mathbf{3},\mathbf{1}\\ \bullet,\overline{\mathbf{3}},\bullet\end{pmatrix}\right\rangle$	$\left\vert\begin{pmatrix}\bullet,\overline{\mathbf{3}},\bullet\\ \overline{\mathbf{3}},\overline{\mathbf{3}}\\ \bullet,\mathbf{3},\bullet\end{pmatrix}\right\rangle$
$\left\langle\begin{pmatrix}\bullet,\mathbf{1},\bullet\\ \mathbf{1},\mathbf{3}\\ \bullet,\mathbf{1},\bullet\end{pmatrix}\right\vert$	$(0,0)$	$(\frac{1}{3},0)$	$(0,\frac{1}{\sqrt{3}})$
$\left\langle\begin{pmatrix}\bullet,\mathbf{3},\bullet\\ \mathbf{3},\mathbf{1}\\ \bullet,\overline{\mathbf{3}},\bullet\end{pmatrix}\right\vert$	$(0,\frac{1}{3})$	$(0,0)$	$(\frac{1}{\sqrt{3}},0)$
$\left\langle\begin{pmatrix}\bullet,\overline{\mathbf{3}},\bullet\\ \overline{\mathbf{3}},\overline{\mathbf{3}}\\ \bullet,\mathbf{3},\bullet\end{pmatrix}\right\vert$	$(\frac{1}{\sqrt{3}},0)$	$(0,\frac{1}{\sqrt{3}})$	$(0,0)$

$\begin{pmatrix}\mathbf{1} & & \mathbf{1}\\ & (\hat{\Box},\hat{\Box}^\dagger) & \\ \mathbf{3} & & \mathbf{3}\end{pmatrix}$	$\left\lvert\begin{pmatrix}\bullet,\mathbf{3},\bullet\\ \mathbf{3},\overline{\mathbf{3}}\\ \bullet,\mathbf{1},\bullet\end{pmatrix}\right\rangle$	$\left\lvert\begin{pmatrix}\bullet,\overline{\mathbf{3}},\bullet\\ \overline{\mathbf{3}},\mathbf{3}\\ \bullet,\overline{\mathbf{3}},\bullet\end{pmatrix}\right\rangle$	$\left\lvert\begin{pmatrix}\bullet,\mathbf{1},\bullet\\ \mathbf{1},\mathbf{1}\\ \bullet,\mathbf{3},\bullet\end{pmatrix}\right\rangle$
$\left\langle\begin{pmatrix}\bullet,\mathbf{3},\bullet\\ \mathbf{3},\overline{\mathbf{3}}\\ \bullet,\mathbf{1},\bullet\end{pmatrix}\right\rvert$	$(0,0)$	$(\frac{1}{\sqrt{3}},0)$	$(0,\frac{1}{3})$
$\left\langle\begin{pmatrix}\bullet,\overline{\mathbf{3}},\bullet\\ \overline{\mathbf{3}},\mathbf{3}\\ \bullet,\overline{\mathbf{3}},\bullet\end{pmatrix}\right\rvert$	$(0,\frac{1}{\sqrt{3}})$	$(0,0)$	$(\frac{1}{\sqrt{3}},0)$
$\left\langle\begin{pmatrix}\bullet,\mathbf{1},\bullet\\ \mathbf{1},\mathbf{1}\\ \bullet,\mathbf{3},\bullet\end{pmatrix}\right\rvert$	$(\frac{1}{3},0)$	$(0,\frac{1}{\sqrt{3}})$	$(0,0)$

$\begin{pmatrix}\mathbf{1} & & \mathbf{3}\\ & (\hat{\Box},\hat{\Box}^\dagger) & \\ \mathbf{3} & & \mathbf{1}\end{pmatrix}$	$\left\lvert\begin{pmatrix}\bullet,\mathbf{3},\bullet\\ \mathbf{3},\mathbf{1}\\ \bullet,\mathbf{1},\bullet\end{pmatrix}\right\rangle$	$\left\lvert\begin{pmatrix}\bullet,\overline{\mathbf{3}},\bullet\\ \overline{\mathbf{3}},\overline{\mathbf{3}}\\ \bullet,\overline{\mathbf{3}},\bullet\end{pmatrix}\right\rangle$	$\left\lvert\begin{pmatrix}\bullet,\mathbf{1},\bullet\\ \mathbf{1},\mathbf{3}\\ \bullet,\mathbf{3},\bullet\end{pmatrix}\right\rangle$
$\left\langle\begin{pmatrix}\bullet,\mathbf{3},\bullet\\ \mathbf{3},\mathbf{1}\\ \bullet,\mathbf{1},\bullet\end{pmatrix}\right\rvert$	$(0,0)$	$(-\frac{1}{\sqrt{3}},0)$	$(0,\frac{1}{3})$
$\left\langle\begin{pmatrix}\bullet,\overline{\mathbf{3}},\bullet\\ \overline{\mathbf{3}},\overline{\mathbf{3}}\\ \bullet,\overline{\mathbf{3}},\bullet\end{pmatrix}\right\rvert$	$(0,-\frac{1}{\sqrt{3}})$	$(0,0)$	$(-\frac{1}{\sqrt{3}},0)$
$\left\langle\begin{pmatrix}\bullet,\mathbf{1},\bullet\\ \mathbf{1},\mathbf{3}\\ \bullet,\mathbf{3},\bullet\end{pmatrix}\right\rvert$	$(\frac{1}{3},0)$	$(0,-\frac{1}{\sqrt{3}})$	$(0,0)$

$\begin{pmatrix}\mathbf{1} & & \overline{\mathbf{3}} \\ & (\hat{\Box},\hat{\Box}^{\dagger}) & \\ \mathbf{3} & & \overline{\mathbf{3}}\end{pmatrix}$	$\left\vert \begin{pmatrix}\bullet,\mathbf{3},\bullet \\ \mathbf{3},\mathbf{3} \\ \bullet,\mathbf{1},\bullet\end{pmatrix} \right\rangle$	$\left\vert \begin{pmatrix}\bullet,\overline{\mathbf{3}},\bullet \\ \overline{\mathbf{3}},\mathbf{1} \\ \bullet,\overline{\mathbf{3}},\bullet\end{pmatrix} \right\rangle$	$\left\vert \begin{pmatrix}\bullet,\mathbf{1},\bullet \\ \mathbf{1},\overline{\mathbf{3}} \\ \bullet,\mathbf{3},\bullet\end{pmatrix} \right\rangle$
$\left\langle \begin{pmatrix}\bullet,\mathbf{3},\bullet \\ \mathbf{3},\mathbf{3} \\ \bullet,\mathbf{1},\bullet\end{pmatrix} \right\vert$	$(0,0)$	$(\frac{1}{3},0)$	$(0,-\frac{1}{3})$
$\left\langle \begin{pmatrix}\bullet,\overline{\mathbf{3}},\bullet \\ \overline{\mathbf{3}},\mathbf{1} \\ \bullet,\overline{\mathbf{3}},\bullet\end{pmatrix} \right\vert$	$(0,\frac{1}{3})$	$(0,0)$	$(-\frac{1}{3},0)$
$\left\langle \begin{pmatrix}\bullet,\mathbf{1},\bullet \\ \mathbf{1},\overline{\mathbf{3}} \\ \bullet,\mathbf{3},\bullet\end{pmatrix} \right\vert$	$(-\frac{1}{3},0)$	$(0,-\frac{1}{3})$	$(0,0)$

$\begin{pmatrix}\mathbf{3} & & \mathbf{3} \\ & (\hat{\Box},\hat{\Box}^{\dagger}) & \\ \mathbf{3} & & \mathbf{3}\end{pmatrix}$	$\left\vert \begin{pmatrix}\bullet,\overline{\mathbf{3}},\bullet \\ \mathbf{3},\overline{\mathbf{3}} \\ \bullet,\mathbf{1},\bullet\end{pmatrix} \right\rangle$	$\left\vert \begin{pmatrix}\bullet,\mathbf{1},\bullet \\ \overline{\mathbf{3}},\mathbf{3} \\ \bullet,\overline{\mathbf{3}},\bullet\end{pmatrix} \right\rangle$	$\left\vert \begin{pmatrix}\bullet,\mathbf{3},\bullet \\ \mathbf{1},\mathbf{1} \\ \bullet,\mathbf{3},\bullet\end{pmatrix} \right\rangle$
$\left\langle \begin{pmatrix}\bullet,\overline{\mathbf{3}},\bullet \\ \mathbf{3},\overline{\mathbf{3}} \\ \bullet,\mathbf{1},\bullet\end{pmatrix} \right\vert$	$(0,0)$	$(\frac{1}{3},0)$	$(0,\frac{1}{3\sqrt{3}})$
$\left\langle \begin{pmatrix}\bullet,\mathbf{1},\bullet \\ \overline{\mathbf{3}},\mathbf{3} \\ \bullet,\overline{\mathbf{3}},\bullet\end{pmatrix} \right\vert$	$(0,\frac{1}{3})$	$(0,0)$	$(\frac{1}{3\sqrt{3}},0)$
$\left\langle \begin{pmatrix}\bullet,\mathbf{3},\bullet \\ \mathbf{1},\mathbf{1} \\ \bullet,\mathbf{3},\bullet\end{pmatrix} \right\vert$	$(\frac{1}{3\sqrt{3}},0)$	$(0,\frac{1}{3\sqrt{3}})$	$(0,0)$

$\begin{pmatrix}\mathbf{3} & & \mathbf{3}\\ & (\hat{\Box},\hat{\Box}^{\dagger}) & \\ \overline{\mathbf{3}} & & \overline{\mathbf{3}}\end{pmatrix}$	$\left\lvert\begin{pmatrix}\bullet,\mathbf{1},\bullet\\ \overline{\mathbf{3}},\mathbf{3}\\ \bullet,\mathbf{1},\bullet\end{pmatrix}\right\rangle$	$\left\lvert\begin{pmatrix}\bullet,\mathbf{3},\bullet\\ \mathbf{1},\mathbf{1}\\ \bullet,\overline{\mathbf{3}},\bullet\end{pmatrix}\right\rangle$	$\left\lvert\begin{pmatrix}\bullet,\overline{\mathbf{3}},\bullet\\ \mathbf{3},\overline{\mathbf{3}}\\ \bullet,\mathbf{3},\bullet\end{pmatrix}\right\rangle$
$\left\langle\begin{pmatrix}\bullet,\mathbf{1},\bullet\\ \overline{\mathbf{3}},\mathbf{3}\\ \bullet,\mathbf{1},\bullet\end{pmatrix}\right\rvert$	$(0,0)$	$(\frac{1}{9},0)$	$(0,\frac{1}{3})$
$\left\langle\begin{pmatrix}\bullet,\mathbf{3},\bullet\\ \mathbf{1},\mathbf{1}\\ \bullet,\overline{\mathbf{3}},\bullet\end{pmatrix}\right\rvert$	$(0,\frac{1}{9})$	$(0,0)$	$(\frac{1}{3},0)$
$\left\langle\begin{pmatrix}\bullet,\overline{\mathbf{3}},\bullet\\ \mathbf{3},\overline{\mathbf{3}}\\ \bullet,\mathbf{3},\bullet\end{pmatrix}\right\rvert$	$(\frac{1}{3},0)$	$(0,\frac{1}{3})$	$(0,0)$

$\begin{pmatrix}\mathbf{3} & & \overline{\mathbf{3}}\\ & (\hat{\Box},\hat{\Box}^{\dagger}) & \\ \overline{\mathbf{3}} & & \mathbf{3}\end{pmatrix}$	$\left\lvert\begin{pmatrix}\bullet,\mathbf{1},\bullet\\ \overline{\mathbf{3}},\overline{\mathbf{3}}\\ \bullet,\mathbf{1},\bullet\end{pmatrix}\right\rangle$	$\left\lvert\begin{pmatrix}\bullet,\mathbf{3},\bullet\\ \mathbf{1},\mathbf{3}\\ \bullet,\overline{\mathbf{3}},\bullet\end{pmatrix}\right\rangle$	$\left\lvert\begin{pmatrix}\bullet,\overline{\mathbf{3}},\bullet\\ \mathbf{3},\mathbf{1}\\ \bullet,\mathbf{3},\bullet\end{pmatrix}\right\rangle$
$\left\langle\begin{pmatrix}\bullet,\mathbf{1},\bullet\\ \overline{\mathbf{3}},\overline{\mathbf{3}}\\ \bullet,\mathbf{1},\bullet\end{pmatrix}\right\rvert$	$(0,0)$	$(\frac{1}{3\sqrt{3}},0)$	$(0,\frac{1}{3\sqrt{3}})$
$\left\langle\begin{pmatrix}\bullet,\mathbf{3},\bullet\\ \mathbf{1},\mathbf{3}\\ \bullet,\overline{\mathbf{3}},\bullet\end{pmatrix}\right\rvert$	$(0,\frac{1}{3\sqrt{3}})$	$(0,0)$	$(\frac{1}{3},0)$
$\left\langle\begin{pmatrix}\bullet,\overline{\mathbf{3}},\bullet\\ \mathbf{3},\mathbf{1}\\ \bullet,\mathbf{3},\bullet\end{pmatrix}\right\rvert$	$(\frac{1}{3\sqrt{3}},0)$	$(0,\frac{1}{3})$	$(0,0)$

.1.2 One SU(2) Plaquette

The SU(2) gauge theory of a single plaquette is interesting to study in the context of SU(3) as it allows a first glimpse of what may be expected for the behavior of color fields associated with low-energy states in larger systems. Of course, SU(2) Hamiltonian gauge theory has been extensively studied in the past, for example, Refs. [358, 359]. The Hamiltonian for SU(2) Yang-Mills theory for one plaquette is similar to that for SU(3) in form,

$$\hat{H} \ = \ \frac{g^2}{2} \sum_{\mathrm{a,links}} |\mathbf{E}^a|^2 \ + \ \frac{1}{2g^2} \left(4 \ - \ \hat{\Box} - \hat{\Box}^\dagger \ \right) \quad . \tag{16}$$

Working with normalized states that satisfy Gauss's law at each of the four vertices, and in the basis eigenstates of the Casimir operator, $|\chi_j\rangle$, the Hamiltonian matrix in this basis is,

$$H_{j,j'} \ = \ \frac{1}{2} g^2 j(j+1)\delta_{j,j'} \ + \ \frac{1}{g^2}\left(2\delta_{j,j'} - \delta_{j+1,j'} - \delta_{j-1,j'}\right) \quad , \tag{17}$$

where $j, j' \geq 0$. Recognizing the form of the magnetic operator as the single-separation finite-difference approximation to ∇^2, and neglecting boundary and positivity issues, and taking the continuum limit in j-space, the Hamiltonian can then be written as,

$$\hat{H} \ \rightarrow \ \frac{1}{2} g^2 \hat{J}^2 - \frac{1}{g^2} \nabla_j^2 \quad , \tag{18}$$

acting in j-space, where $\hat{J}^2$ is the SU(2) Casimir operator. The eigenstates of the low-lying wavefunctions satisfy,

$$\nabla_j^2 \psi(j) \ + \ \left(g^2 E - \frac{1}{2} g^4 j(j+1) \right) \psi(j) = 0 \quad , \tag{19}$$

a Weber type-A differential equation, with Parabolic Cylinder functions as solutions. Asymptotically for large j, these functions scale as

$$\psi \ \rightarrow \ e^{-\frac{g^2}{2\sqrt{2}}(j+\frac{1}{2})^2} \quad , \tag{20}$$

demonstrating Gaussian convergence in field space. Considerations have to be given to the discrete nature of the field, to the boundary conditions at $j = 0$, and so forth, but for wavefunctions with support over many j-values, the approximate dependence on large j is expected to be given by Eq. (20). This result is encouraging as it suggests a rapid convergence in j-space for $j \gtrsim 4/g$, which provides a guide for the extent of field values in a finite dimensional Hilbert space defining the plaquette. To obtain comparable fidelity for somewhat higher lying states, only modest increases in maximum field values are expected to be required. This distribution resembles that of the low-lying field configurations in scalar field theory.

Extending this discussion to multi-plaquette systems, it is anticipated that the support of the field on any given link in the low-lying states will have a localized distribution that is similar to Eq. (20) up to polynomial corrections. This remains to be verified by direct simulation. Further, the comparison between SU(2) and SU(3) is complicated by the non-linear behavior in color space of SU(3). However, the expectation is that SU(3) color fields are also localized in irrep space, in a way that resembles the behavior found in SU(2).

.1.3 Benchmarks for Single Plaquette Time Evolution

It is important to establish robust benchmarks to guide future quantum simulations of gauge field theories. Section 1.3 of the main text explores bases within the multiplet digitization of an SU(3) plaquette and their consequences for digital quantum simulation. To complement, subsection 1.3.4 focuses on the effectiveness of simulations in capturing local maxima and minima in time evolution. Tables 3 and 4 provided in this appendix show the numerical values in Fig. 1.9 of the main text.

First Maximum of $\langle H_E \rangle$ for $g = 1$						
Basis Truncation	Exact	Trotter Steps	Order	CNOTs	Trotterized	`Athens`
Global Basis $p, q \to \infty$	0.9389	-	-	-	-	-
Color Parity truncated at **3**	0.7967	-	-	0	-	$0.829\left(^{+0.039}_{-0.045}\right)$
Global Basis $p, q \leq 1$	0.8699	1	2	3	1.1602	1.06 ± 0.08
Global Basis $p, q \leq 1$	0.8699	2	2	6	0.9019	0.91 ± 0.18
Global Basis $p, q \leq 1$	0.8699	3	2	9	0.8837	0.9 ± 0.4
Global Basis $p, q \leq 1$	0.8699	4	2	12	0.8776	1.0 ± 0.5
Color Parity truncated at **6**	0.9296	1	1	5	4.2582	4.3 ± 0.4
Color Parity truncated at **6**	0.9296	2	1	10	1.8280	1.9 ± 0.5
Color Parity truncated at **6**	0.9296	1	2	7	0.8820	0.94 ± 0.24

Table 3: The first maximum of $\langle H_E \rangle$ for $g = 1$ in the time evolution of the trivial vacuum for a single plaquette. The columns of entries correspond to: (first) the basis truncation, (second) results of exact time evolution performed on a classical computer, (third) the number of Trotter steps, (fourth) the order of the Trotterization, (fifth) the number of CNOT's used on the `Athens` quantum processor, (sixth) the results of Trotterized time evolution using a classical computer, (seventh) the results of Trotterized time evolution obtained from IBM's `Athens` quantum processor.

First Minimum of $\langle H_E \rangle$ for $g = 1$						
Basis Truncation	Exact	Trotter Steps	Order	CNOTs	Trotterized	`Athens`
Global Basis $p, q \to \infty$	0.0234	-	-	-	-	-
Color Parity truncated at **3**	0.0000	-	-	0	-	$0.0037\left(^{+0.012}_{-0.0033}\right)$
Global Basis $p, q \leq 1$	0.0096	1	2	3	0.0000	0.04 ± 0.08
Global Basis $p, q \leq 1$	0.0096	2	2	6	0.0803	0.11 ± 0.1
Global Basis $p, q \leq 1$	0.0096	3	2	9	0.0452	0.18 ± 0.29
Global Basis $p, q \leq 1$	0.0096	4	2	12	0.0140	0.09 ± 0.24
Color Parity truncated at **6**	0.0206	1	1	5	2.782	-
Color Parity truncated at **6**	0.0206	2	1	10	1.1840	1.1 ± 0.7
Color Parity truncated at **6**	0.0206	1	2	7	0.1555	0.25 ± 0.2

Table 4: The first minimum of $\langle H_E \rangle$ for $g = 1$ in the time evolution of the trivial vacuum for a singe plaquette. The columns of entries correspond to: (first) the basis truncation, (second) results of exact time evolution performed on a classical computer, (third) the number of Trotter steps, (fourth) the order of the Trotterization, (fifth) the number of CNOT's used on the `Athens` quantum processor, (sixth) the results of Trotterized time evolution using a classical computer, (seventh) the results of Trotterized time evolution obtained from IBM's `Athens` quantum processor. In the simulations, if a minimum was not obtained in the time evolution, the seventh column contains a dash.

.1.4 SU(3) Clebsch Gordan Coefficients

The methods proposed in the main text for the implementation of real time dynamics of SU(3) lattice gauge theory through the use of quantum devices currently require the classical calculation of CG tensorial projections in the contraction of SU(3) irreducible representations. While the calculation of generic CG coefficients has been classified as #P-complete and thus a daunting dependency, the restriction to fixed rank (2 for SU(3)) has been identified as a sufficient condition for the existence of a polynomial time algorithm [360]. As shown in Eq. (1.6), matrix elements of the local plaquette operator can be formulated through 9-R composite CG vertex factors. These vertex factors and plaquette matrix elements are independent of the basis chosen to enumerate the states within each irrep. Due to discrepancies we have observed in the CG coefficients calculated with publicly accessible codes when multiplicities occur in tensor decomposition (e.g., Ref [361]), an explicit set of 9-R symbols for irreps appearing at index truncation $\Lambda_p = \Lambda_q = 1$ is provided in Eq. (21).

$$\begin{aligned}
&\begin{Bmatrix} \mathbf{1} & \mathbf{3} & \mathbf{3} \\ \overline{\mathbf{3}} & \mathbf{1} & \overline{\mathbf{3}} \\ \overline{\mathbf{3}} & \mathbf{3} & \mathbf{1} \end{Bmatrix} = 1
&&\begin{Bmatrix} \mathbf{1} & \mathbf{3} & \mathbf{3} \\ \overline{\mathbf{3}} & \mathbf{1} & \overline{\mathbf{3}} \\ \overline{\mathbf{3}} & \mathbf{3} & \mathbf{8} \end{Bmatrix} = 8
&&\begin{Bmatrix} \mathbf{3} & \overline{\mathbf{3}} & \mathbf{1} \\ \overline{\mathbf{3}} & \mathbf{1} & \overline{\mathbf{3}} \\ 8 & \overline{\mathbf{3}} & \overline{\mathbf{3}} \end{Bmatrix} = 2\sqrt{2} \\
&\begin{Bmatrix} \mathbf{3} & \overline{\mathbf{3}} & \mathbf{1} \\ \mathbf{3} & \mathbf{1} & \mathbf{3} \\ \overline{\mathbf{3}} & \overline{\mathbf{3}} & \mathbf{3} \end{Bmatrix} = \sqrt{3}
&&\begin{Bmatrix} \mathbf{3} & \mathbf{3} & \overline{\mathbf{3}} \\ \mathbf{3} & \mathbf{1} & \mathbf{3} \\ \overline{\mathbf{3}} & \mathbf{3} & \mathbf{1} \end{Bmatrix} = -1
&&\begin{Bmatrix} \mathbf{3} & \mathbf{3} & \overline{\mathbf{3}} \\ \mathbf{3} & \mathbf{1} & \mathbf{3} \\ \overline{\mathbf{3}} & \mathbf{3} & \mathbf{8} \end{Bmatrix} = 4 \qquad (21) \\
&\begin{Bmatrix} \mathbf{3} & \mathbf{3} & \overline{\mathbf{3}} \\ \overline{\mathbf{3}} & \mathbf{1} & \overline{\mathbf{3}} \\ 8 & \mathbf{3} & \mathbf{3} \end{Bmatrix} = -\sqrt{6}
&&\begin{Bmatrix} 8 & 8 & 8 \\ \mathbf{3} & \mathbf{1} & \mathbf{3} \\ \mathbf{3} & 8 & \mathbf{3} \end{Bmatrix} = \frac{3}{4}\left(\sqrt{5}+3\right)
&&\begin{Bmatrix} 8 & 8 & 8 \\ \overline{\mathbf{3}} & \mathbf{1} & \overline{\mathbf{3}} \\ \overline{\mathbf{3}} & 8 & \overline{\mathbf{3}} \end{Bmatrix} = \frac{3}{4}\left(\sqrt{5}-3\right)
\end{aligned}$$

Importantly, note that the antisymmetric contribution within the $\mathbf{8} \otimes \mathbf{8} \to \mathbf{8}$ CG produces a factor of (-1) upon conjugation of the last 9-R symbol in this set.

.1.5 *Local Operators for* $\{\mathbf{1}, \mathbf{3}, \overline{\mathbf{3}}\}$ *Magnetic Time Evolution*

In this appendix, we provide an explicit enumeration of the 81 operators in the $\{\mathbf{1}, \mathbf{3}, \overline{\mathbf{3}}\}$ local basis contributing to Trotterized magnetic time evolution, see Eqns. (1.51)-(1.58).

Control Sector			Givens Rotation	
$\{\mathbf{C}_1, \mathbf{C}_2, \mathbf{C}_3, \mathbf{C}_4\}$	$\{\mathbf{C}_1, \mathbf{C}_2, \mathbf{C}_3, \mathbf{C}_4\}_{(p,q)}$	coefficient	$\{\mathbf{R}_b, \mathbf{Q}_r, \mathbf{R}_t, \mathbf{Q}_\ell\}$	$\{\mathbf{R}_b, \mathbf{Q}_r, \mathbf{R}_t, \mathbf{Q}_\ell\}_{(p,q)}$
$\{\mathbf{1}, \mathbf{1}, \mathbf{1}, \mathbf{1}\}$	$\{00000000\}$	1	$\mathcal{X}_{01}\mathcal{X}_{01}\mathcal{X}_{02}\mathcal{X}_{02}$	$\mathcal{X}_{01}\mathbb{I}\mathcal{X}_{01}\mathbb{I}\mathbb{I}\mathcal{X}_{01}\mathbb{I}\mathcal{X}_{01}$
		1	$\mathcal{X}_{02}\mathcal{X}_{02}\mathcal{X}_{01}\mathcal{X}_{01}$	$\mathbb{I}\mathcal{X}_{01}\mathbb{I}\mathcal{X}_{01}\mathcal{X}_{01}\mathbb{I}\mathcal{X}_{01}\mathbb{I}$
		1	$\mathcal{X}_{12}\mathcal{X}_{12}\mathcal{X}_{12}\mathcal{X}_{12}$	$\mathcal{X}_{01}\mathcal{X}_{01}\mathcal{X}_{01}\mathcal{X}_{01}\mathcal{X}_{01}\mathcal{X}_{01}\mathcal{X}_{01}\mathcal{X}_{01}$
$\{\mathbf{1}, \mathbf{1}, \mathbf{3}, \overline{\mathbf{3}}\}$	$\{00001001\}$	$\frac{1}{\sqrt{3}}$	$\mathcal{X}_{01}\mathcal{X}_{12}\mathcal{X}_{02}\mathcal{X}_{02}$	$\mathcal{X}_{01}\mathbb{I}\mathcal{X}_{01}\mathcal{X}_{01}\mathbb{I}\mathcal{X}_{01}\mathbb{I}\mathcal{X}_{01}$
		$\frac{1}{3}$	$\mathcal{X}_{02}\mathcal{X}_{01}\mathcal{X}_{01}\mathcal{X}_{01}$	$\mathbb{I}\mathcal{X}_{01}\mathcal{X}_{01}\mathbb{I}\mathcal{X}_{01}\mathbb{I}\mathcal{X}_{01}\mathbb{I}$
		$\frac{1}{\sqrt{3}}$	$\mathcal{X}_{12}\mathcal{X}_{02}\mathcal{X}_{12}\mathcal{X}_{12}$	$\mathcal{X}_{01}\mathcal{X}_{01}\mathbb{I}\mathcal{X}_{01}\mathcal{X}_{01}\mathcal{X}_{01}\mathcal{X}_{01}\mathcal{X}_{01}$
$\{\mathbf{1}, \mathbf{3}, \mathbf{1}, \mathbf{3}\}$	$\{00100010\}$	$\frac{1}{3}$	$\mathcal{X}_{01}\mathcal{X}_{02}\mathcal{X}_{01}\mathcal{X}_{01}$	$\mathcal{X}_{01}\mathbb{I}\mathbb{I}\mathcal{X}_{01}\mathcal{X}_{01}\mathbb{I}\mathcal{X}_{01}\mathbb{I}$
		$\frac{1}{\sqrt{3}}$	$\mathcal{X}_{02}\mathcal{X}_{12}\mathcal{X}_{12}\mathcal{X}_{12}$	$\mathbb{I}\mathcal{X}_{01}\mathcal{X}_{01}\mathcal{X}_{01}\mathcal{X}_{01}\mathcal{X}_{01}\mathcal{X}_{01}\mathcal{X}_{01}$
		$\frac{1}{\sqrt{3}}$	$\mathcal{X}_{12}\mathcal{X}_{01}\mathcal{X}_{02}\mathcal{X}_{02}$	$\mathcal{X}_{01}\mathcal{X}_{01}\mathcal{X}_{01}\mathbb{I}\mathbb{I}\mathcal{X}_{01}\mathbb{I}\mathcal{X}_{01}$
$\{\mathbf{1}, \mathbf{3}, \mathbf{3}, \mathbf{1}\}$	$\{00101000\}$	$\frac{1}{3}$	$\mathcal{X}_{01}\mathcal{X}_{01}\mathcal{X}_{01}\mathcal{X}_{01}$	$\mathcal{X}_{01}\mathbb{I}\mathcal{X}_{01}\mathbb{I}\mathcal{X}_{01}\mathbb{I}\mathcal{X}_{01}\mathbb{I}$
		$-\frac{1}{\sqrt{3}}$	$\mathcal{X}_{02}\mathcal{X}_{02}\mathcal{X}_{12}\mathcal{X}_{12}$	$\mathbb{I}\mathcal{X}_{01}\mathbb{I}\mathcal{X}_{01}\mathcal{X}_{01}\mathcal{X}_{01}\mathcal{X}_{01}\mathcal{X}_{01}$

		$-\frac{1}{\sqrt{3}}$	$\mathcal{X}_{12}\mathcal{X}_{12}\mathcal{X}_{02}\mathcal{X}_{02}$	$\mathcal{X}_{01}\mathcal{X}_{01}\mathcal{X}_{01}\mathcal{X}_{01}\mathbb{I}\mathcal{X}_{01}\mathbb{I}\mathcal{X}_{01}$
$\{\mathbf{1},\mathbf{3},\overline{\mathbf{3}},\overline{\mathbf{3}}\}$	$\{00100101\}$	$-\frac{1}{3}$	$\mathcal{X}_{01}\mathcal{X}_{12}\mathcal{X}_{01}\mathcal{X}_{01}$	$\mathcal{X}_{01}\mathbb{I}\mathcal{X}_{01}\mathcal{X}_{01}\mathcal{X}_{01}\mathbb{I}\mathcal{X}_{01}\mathbb{I}$
		$\frac{1}{3}$	$\mathcal{X}_{02}\mathcal{X}_{01}\mathcal{X}_{12}\mathcal{X}_{12}$	$\mathbb{I}\mathcal{X}_{01}\mathcal{X}_{01}\mathbb{I}\mathcal{X}_{01}\mathcal{X}_{01}\mathcal{X}_{01}\mathcal{X}_{01}$
		$-\frac{1}{3}$	$\mathcal{X}_{12}\mathcal{X}_{02}\mathcal{X}_{02}\mathcal{X}_{02}$	$\mathcal{X}_{01}\mathcal{X}_{01}\mathbb{I}\mathcal{X}_{01}\mathbb{I}\mathcal{X}_{01}\mathbb{I}\mathcal{X}_{01}$
$\{\mathbf{3},\mathbf{3},\mathbf{3},\mathbf{3}\}$	$\{10101010\}$	$\frac{1}{3\sqrt{3}}$	$\mathcal{X}_{01}\mathcal{X}_{02}\mathcal{X}_{12}\mathcal{X}_{01}$	$\mathcal{X}_{01}\mathbb{I}\mathbb{I}\mathcal{X}_{01}\mathcal{X}_{01}\mathcal{X}_{01}\mathcal{X}_{01}\mathbb{I}$
		$\frac{1}{3}$	$\mathcal{X}_{02}\mathcal{X}_{12}\mathcal{X}_{02}\mathcal{X}_{12}$	$\mathbb{I}\mathcal{X}_{01}\mathcal{X}_{01}\mathcal{X}_{01}\mathbb{I}\mathcal{X}_{01}\mathcal{X}_{01}\mathcal{X}_{01}$
		$\frac{1}{3\sqrt{3}}$	$\mathcal{X}_{12}\mathcal{X}_{01}\mathcal{X}_{01}\mathcal{X}_{02}$	$\mathcal{X}_{01}\mathcal{X}_{01}\mathcal{X}_{01}\mathbb{I}\mathcal{X}_{01}\mathbb{I}\mathbb{I}\mathcal{X}_{01}$
$\{\mathbf{3},\overline{\mathbf{3}},\mathbf{3},\overline{\mathbf{3}}\}$	$\{10011001\}$	$\frac{1}{3}$	$\mathcal{X}_{01}\mathcal{X}_{12}\mathcal{X}_{02}\mathcal{X}_{12}$	$\mathcal{X}_{01}\mathbb{I}\mathcal{X}_{01}\mathcal{X}_{01}\mathbb{I}\mathcal{X}_{01}\mathcal{X}_{01}\mathcal{X}_{01}$
		$\frac{1}{9}$	$\mathcal{X}_{02}\mathcal{X}_{01}\mathcal{X}_{01}\mathcal{X}_{02}$	$\mathbb{I}\mathcal{X}_{01}\mathcal{X}_{01}\mathbb{I}\mathcal{X}_{01}\mathbb{I}\mathbb{I}\mathcal{X}_{01}$
		$\frac{1}{3}$	$\mathcal{X}_{12}\mathcal{X}_{02}\mathcal{X}_{12}\mathcal{X}_{01}$	$\mathcal{X}_{01}\mathcal{X}_{01}\mathbb{I}\mathcal{X}_{01}\mathcal{X}_{01}\mathcal{X}_{01}\mathcal{X}_{01}\mathbb{I}$
$\{\mathbf{3},\overline{\mathbf{3}},\overline{\mathbf{3}},\mathbf{3}\}$	$\{10010110\}$	$\frac{1}{3\sqrt{3}}$	$\mathcal{X}_{01}\mathcal{X}_{02}\mathcal{X}_{02}\mathcal{X}_{12}$	$\mathcal{X}_{01}\mathbb{I}\mathbb{I}\mathcal{X}_{01}\mathbb{I}\mathcal{X}_{01}\mathcal{X}_{01}\mathcal{X}_{01}$
		$\frac{1}{3\sqrt{3}}$	$\mathcal{X}_{02}\mathcal{X}_{12}\mathcal{X}_{01}\mathcal{X}_{02}$	$\mathbb{I}\mathcal{X}_{01}\mathcal{X}_{01}\mathcal{X}_{01}\mathcal{X}_{01}\mathbb{I}\mathbb{I}\mathcal{X}_{01}$
		$\frac{1}{3}$	$\mathcal{X}_{12}\mathcal{X}_{01}\mathcal{X}_{12}\mathcal{X}_{01}$	$\mathcal{X}_{01}\mathcal{X}_{01}\mathcal{X}_{01}\mathbb{I}\mathcal{X}_{01}\mathcal{X}_{01}\mathcal{X}_{01}\mathbb{I}$
$\{\mathbf{1},\mathbf{1},\overline{\mathbf{3}},\mathbf{3}\}$	$\{00000110\}$	$\frac{1}{3}$	$\mathcal{X}_{01}\mathcal{X}_{02}\mathcal{X}_{02}\mathcal{X}_{02}$	$\mathcal{X}_{01}\mathbb{I}\mathbb{I}\mathcal{X}_{01}\mathbb{I}\mathcal{X}_{01}\mathbb{I}\mathcal{X}_{01}$
		$\frac{1}{\sqrt{3}}$	$\mathcal{X}_{02}\mathcal{X}_{12}\mathcal{X}_{01}\mathcal{X}_{01}$	$\mathbb{I}\mathcal{X}_{01}\mathcal{X}_{01}\mathcal{X}_{01}\mathcal{X}_{01}\mathbb{I}\mathcal{X}_{01}\mathbb{I}$
		$\frac{1}{\sqrt{3}}$	$\mathcal{X}_{12}\mathcal{X}_{01}\mathcal{X}_{12}\mathcal{X}_{12}$	$\mathcal{X}_{01}\mathcal{X}_{01}\mathcal{X}_{01}\mathbb{I}\mathcal{X}_{01}\mathcal{X}_{01}\mathcal{X}_{01}\mathcal{X}_{01}$
$\{\mathbf{3},\mathbf{1},\mathbf{3},\mathbf{1}\}$	$\{10001000\}$	$\frac{1}{3}$	$\mathcal{X}_{01}\mathcal{X}_{01}\mathcal{X}_{01}\mathcal{X}_{02}$	$\mathcal{X}_{01}\mathbb{I}\mathcal{X}_{01}\mathbb{I}\mathcal{X}_{01}\mathbb{I}\mathbb{I}\mathcal{X}_{01}$
		$\frac{1}{\sqrt{3}}$	$\mathcal{X}_{02}\mathcal{X}_{02}\mathcal{X}_{12}\mathcal{X}_{01}$	$\mathbb{I}\mathcal{X}_{01}\mathbb{I}\mathcal{X}_{01}\mathcal{X}_{01}\mathcal{X}_{01}\mathcal{X}_{01}\mathbb{I}$
		$\frac{1}{\sqrt{3}}$	$\mathcal{X}_{12}\mathcal{X}_{12}\mathcal{X}_{02}\mathcal{X}_{12}$	$\mathcal{X}_{01}\mathcal{X}_{01}\mathcal{X}_{01}\mathcal{X}_{01}\mathbb{I}\mathcal{X}_{01}\mathcal{X}_{01}\mathcal{X}_{01}$
$\{\mathbf{3},\mathbf{1},\mathbf{1},\mathbf{3}\}$	$\{10000010\}$	$\frac{1}{3}$	$\mathcal{X}_{01}\mathcal{X}_{02}\mathcal{X}_{01}\mathcal{X}_{02}$	$\mathcal{X}_{01}\mathbb{I}\mathbb{I}\mathcal{X}_{01}\mathcal{X}_{01}\mathbb{I}\mathbb{I}\mathcal{X}_{01}$
		$-\frac{1}{\sqrt{3}}$	$\mathcal{X}_{02}\mathcal{X}_{12}\mathcal{X}_{12}\mathcal{X}_{01}$	$\mathbb{I}\mathcal{X}_{01}\mathcal{X}_{01}\mathcal{X}_{01}\mathcal{X}_{01}\mathcal{X}_{01}\mathcal{X}_{01}\mathbb{I}$
		$-\frac{1}{\sqrt{3}}$	$\mathcal{X}_{12}\mathcal{X}_{01}\mathcal{X}_{02}\mathcal{X}_{12}$	$\mathcal{X}_{01}\mathcal{X}_{01}\mathcal{X}_{01}\mathbb{I}\mathbb{I}\mathcal{X}_{01}\mathcal{X}_{01}\mathcal{X}_{01}$
$\{\mathbf{3},\mathbf{1},\overline{\mathbf{3}},\overline{\mathbf{3}}\}$	$\{10000101\}$	$-\frac{1}{3}$	$\mathcal{X}_{01}\mathcal{X}_{12}\mathcal{X}_{01}\mathcal{X}_{02}$	$\mathcal{X}_{01}\mathbb{I}\mathcal{X}_{01}\mathcal{X}_{01}\mathcal{X}_{01}\mathbb{I}\mathbb{I}\mathcal{X}_{01}$
		$-\frac{1}{3}$	$\mathcal{X}_{02}\mathcal{X}_{01}\mathcal{X}_{12}\mathcal{X}_{01}$	$\mathbb{I}\mathcal{X}_{01}\mathcal{X}_{01}\mathbb{I}\mathcal{X}_{01}\mathcal{X}_{01}\mathcal{X}_{01}\mathbb{I}$
		$\frac{1}{3}$	$\mathcal{X}_{12}\mathcal{X}_{02}\mathcal{X}_{02}\mathcal{X}_{12}$	$\mathcal{X}_{01}\mathcal{X}_{01}\mathbb{I}\mathcal{X}_{01}\mathbb{I}\mathcal{X}_{01}\mathcal{X}_{01}\mathcal{X}_{01}$
$\{\overline{\mathbf{3}},\mathbf{3},\overline{\mathbf{3}},\mathbf{3}\}$	$\{01100110\}$	$\frac{1}{9}$	$\mathcal{X}_{01}\mathcal{X}_{02}\mathcal{X}_{02}\mathcal{X}_{01}$	$\mathcal{X}_{01}\mathbb{I}\mathbb{I}\mathcal{X}_{01}\mathbb{I}\mathcal{X}_{01}\mathcal{X}_{01}\mathbb{I}$
		$\frac{1}{3}$	$\mathcal{X}_{02}\mathcal{X}_{12}\mathcal{X}_{01}\mathcal{X}_{12}$	$\mathbb{I}\mathcal{X}_{01}\mathcal{X}_{01}\mathcal{X}_{01}\mathcal{X}_{01}\mathbb{I}\mathcal{X}_{01}\mathcal{X}_{01}$

		$\frac{1}{3}$	$\mathcal{X}_{12}\mathcal{X}_{01}\mathcal{X}_{12}\mathcal{X}_{02}$	$\mathcal{X}_{01}\mathcal{X}_{01}\mathcal{X}_{01}\mathbb{I}\mathcal{X}_{01}\mathcal{X}_{01}\mathbb{I}\mathcal{X}_{01}$
$\{\overline{\mathbf{3}},\mathbf{3},\mathbf{3},\overline{\mathbf{3}}\}$	$\{01101001\}$	$\frac{1}{3\sqrt{3}}$	$\mathcal{X}_{01}\mathcal{X}_{12}\mathcal{X}_{02}\mathcal{X}_{01}$	$\mathcal{X}_{01}\mathbb{I}\mathcal{X}_{01}\mathcal{X}_{01}\mathbb{I}\mathcal{X}_{01}\mathcal{X}_{01}\mathbb{I}$
		$\frac{1}{3\sqrt{3}}$	$\mathcal{X}_{02}\mathcal{X}_{01}\mathcal{X}_{01}\mathcal{X}_{12}$	$\mathbb{I}\mathcal{X}_{01}\mathcal{X}_{01}\mathbb{I}\mathcal{X}_{01}\mathbb{I}\mathcal{X}_{01}\mathcal{X}_{01}$
		$\frac{1}{3}$	$\mathcal{X}_{12}\mathcal{X}_{02}\mathcal{X}_{12}\mathcal{X}_{02}$	$\mathcal{X}_{01}\mathcal{X}_{01}\mathbb{I}\mathcal{X}_{01}\mathcal{X}_{01}\mathcal{X}_{01}\mathbb{I}\mathcal{X}_{01}$
$\{\mathbf{1},\overline{\mathbf{3}},\mathbf{1},\overline{\mathbf{3}}\}$	$\{00010001\}$	$\frac{1}{\sqrt{3}}$	$\mathcal{X}_{01}\mathcal{X}_{12}\mathcal{X}_{12}\mathcal{X}_{12}$	$\mathcal{X}_{01}\mathbb{I}\mathcal{X}_{01}\mathcal{X}_{01}\mathcal{X}_{01}\mathcal{X}_{01}\mathcal{X}_{01}\mathcal{X}_{01}$
		$\frac{1}{3}$	$\mathcal{X}_{02}\mathcal{X}_{01}\mathcal{X}_{02}\mathcal{X}_{02}$	$\mathbb{I}\mathcal{X}_{01}\mathcal{X}_{01}\mathbb{I}\mathbb{I}\mathcal{X}_{01}\mathbb{I}\mathcal{X}_{01}$
		$\frac{1}{\sqrt{3}}$	$\mathcal{X}_{12}\mathcal{X}_{02}\mathcal{X}_{01}\mathcal{X}_{01}$	$\mathcal{X}_{01}\mathcal{X}_{01}\mathbb{I}\mathcal{X}_{01}\mathcal{X}_{01}\mathbb{I}\mathcal{X}_{01}\mathbb{I}$
$\{\mathbf{1},\overline{\mathbf{3}},\overline{\mathbf{3}},\mathbf{1}\}$	$\{00010100\}$	$-\frac{1}{\sqrt{3}}$	$\mathcal{X}_{01}\mathcal{X}_{01}\mathcal{X}_{12}\mathcal{X}_{12}$	$\mathcal{X}_{01}\mathbb{I}\mathcal{X}_{01}\mathbb{I}\mathcal{X}_{01}\mathcal{X}_{01}\mathcal{X}_{01}\mathcal{X}_{01}$
		$\frac{1}{3}$	$\mathcal{X}_{02}\mathcal{X}_{02}\mathcal{X}_{02}\mathcal{X}_{02}$	$\mathbb{I}\mathcal{X}_{01}\mathbb{I}\mathcal{X}_{01}\mathbb{I}\mathcal{X}_{01}\mathbb{I}\mathcal{X}_{01}$
		$-\frac{1}{\sqrt{3}}$	$\mathcal{X}_{12}\mathcal{X}_{12}\mathcal{X}_{01}\mathcal{X}_{01}$	$\mathcal{X}_{01}\mathcal{X}_{01}\mathcal{X}_{01}\mathcal{X}_{01}\mathcal{X}_{01}\mathbb{I}\mathcal{X}_{01}\mathbb{I}$
$\{\mathbf{1},\overline{\mathbf{3}},\mathbf{3},\mathbf{3}\}$	$\{00011010\}$	$\frac{1}{3}$	$\mathcal{X}_{01}\mathcal{X}_{02}\mathcal{X}_{12}\mathcal{X}_{12}$	$\mathcal{X}_{01}\mathbb{I}\mathbb{I}\mathcal{X}_{01}\mathcal{X}_{01}\mathcal{X}_{01}\mathcal{X}_{01}\mathcal{X}_{01}$
		$-\frac{1}{3}$	$\mathcal{X}_{02}\mathcal{X}_{12}\mathcal{X}_{02}\mathcal{X}_{02}$	$\mathbb{I}\mathcal{X}_{01}\mathcal{X}_{01}\mathcal{X}_{01}\mathbb{I}\mathcal{X}_{01}\mathbb{I}\mathcal{X}_{01}$
		$-\frac{1}{3}$	$\mathcal{X}_{12}\mathcal{X}_{01}\mathcal{X}_{01}\mathcal{X}_{01}$	$\mathcal{X}_{01}\mathcal{X}_{01}\mathcal{X}_{01}\mathbb{I}\mathcal{X}_{01}\mathbb{I}\mathcal{X}_{01}\mathbb{I}$
$\{\overline{\mathbf{3}},\overline{\mathbf{3}},\overline{\mathbf{3}},\overline{\mathbf{3}}\}$	$\{01010101\}$	$\frac{1}{3}$	$\mathcal{X}_{01}\mathcal{X}_{12}\mathcal{X}_{01}\mathcal{X}_{12}$	$\mathcal{X}_{01}\mathbb{I}\mathcal{X}_{01}\mathcal{X}_{01}\mathcal{X}_{01}\mathbb{I}\mathcal{X}_{01}\mathcal{X}_{01}$
		$\frac{1}{3\sqrt{3}}$	$\mathcal{X}_{02}\mathcal{X}_{01}\mathcal{X}_{12}\mathcal{X}_{02}$	$\mathbb{I}\mathcal{X}_{01}\mathcal{X}_{01}\mathbb{I}\mathcal{X}_{01}\mathcal{X}_{01}\mathbb{I}\mathcal{X}_{01}$
		$\frac{1}{3\sqrt{3}}$	$\mathcal{X}_{12}\mathcal{X}_{02}\mathcal{X}_{02}\mathcal{X}_{01}$	$\mathcal{X}_{01}\mathcal{X}_{01}\mathbb{I}\mathcal{X}_{01}\mathbb{I}\mathcal{X}_{01}\mathcal{X}_{01}\mathbb{I}$
$\{\overline{\mathbf{3}},\mathbf{1},\overline{\mathbf{3}},\mathbf{1}\}$	$\{01000100\}$	$\frac{1}{\sqrt{3}}$	$\mathcal{X}_{01}\mathcal{X}_{01}\mathcal{X}_{12}\mathcal{X}_{02}$	$\mathcal{X}_{01}\mathbb{I}\mathcal{X}_{01}\mathbb{I}\mathcal{X}_{01}\mathcal{X}_{01}\mathbb{I}\mathcal{X}_{01}$
		$\frac{1}{3}$	$\mathcal{X}_{02}\mathcal{X}_{02}\mathcal{X}_{02}\mathcal{X}_{01}$	$\mathbb{I}\mathcal{X}_{01}\mathbb{I}\mathcal{X}_{01}\mathbb{I}\mathcal{X}_{01}\mathcal{X}_{01}\mathbb{I}$
		$\frac{1}{\sqrt{3}}$	$\mathcal{X}_{12}\mathcal{X}_{12}\mathcal{X}_{01}\mathcal{X}_{12}$	$\mathcal{X}_{01}\mathcal{X}_{01}\mathcal{X}_{01}\mathcal{X}_{01}\mathcal{X}_{01}\mathbb{I}\mathcal{X}_{01}\mathcal{X}_{01}$
$\{\overline{\mathbf{3}},\mathbf{1},\mathbf{1},\overline{\mathbf{3}}\}$	$\{01000001\}$	$-\frac{1}{\sqrt{3}}$	$\mathcal{X}_{01}\mathcal{X}_{12}\mathcal{X}_{12}\mathcal{X}_{02}$	$\mathcal{X}_{01}\mathbb{I}\mathcal{X}_{01}\mathcal{X}_{01}\mathcal{X}_{01}\mathcal{X}_{01}\mathbb{I}\mathcal{X}_{01}$
		$\frac{1}{3}$	$\mathcal{X}_{02}\mathcal{X}_{01}\mathcal{X}_{02}\mathcal{X}_{01}$	$\mathbb{I}\mathcal{X}_{01}\mathcal{X}_{01}\mathbb{I}\mathbb{I}\mathcal{X}_{01}\mathcal{X}_{01}\mathbb{I}$
		$-\frac{1}{\sqrt{3}}$	$\mathcal{X}_{12}\mathcal{X}_{02}\mathcal{X}_{01}\mathcal{X}_{12}$	$\mathcal{X}_{01}\mathcal{X}_{01}\mathbb{I}\mathcal{X}_{01}\mathcal{X}_{01}\mathbb{I}\mathcal{X}_{01}\mathcal{X}_{01}$
$\{\overline{\mathbf{3}},\mathbf{1},\mathbf{3},\mathbf{3}\}$	$\{01001010\}$	$-\frac{1}{3}$	$\mathcal{X}_{01}\mathcal{X}_{02}\mathcal{X}_{12}\mathcal{X}_{02}$	$\mathcal{X}_{01}\mathbb{I}\mathbb{I}\mathcal{X}_{01}\mathcal{X}_{01}\mathcal{X}_{01}\mathbb{I}\mathcal{X}_{01}$
		$-\frac{1}{3}$	$\mathcal{X}_{02}\mathcal{X}_{12}\mathcal{X}_{02}\mathcal{X}_{01}$	$\mathbb{I}\mathcal{X}_{01}\mathcal{X}_{01}\mathcal{X}_{01}\mathbb{I}\mathcal{X}_{01}\mathcal{X}_{01}\mathbb{I}$
		$\frac{1}{3}$	$\mathcal{X}_{12}\mathcal{X}_{01}\mathcal{X}_{01}\mathcal{X}_{12}$	$\mathcal{X}_{01}\mathcal{X}_{01}\mathcal{X}_{01}\mathbb{I}\mathcal{X}_{01}\mathbb{I}\mathcal{X}_{01}\mathcal{X}_{01}$
$\{\overline{\mathbf{3}},\mathbf{3},\mathbf{1},\mathbf{1}\}$	$\{01100000\}$	$\frac{1}{3}$	$\mathcal{X}_{01}\mathcal{X}_{01}\mathcal{X}_{02}\mathcal{X}_{01}$	$\mathcal{X}_{01}\mathbb{I}\mathcal{X}_{01}\mathbb{I}\mathbb{I}\mathcal{X}_{01}\mathcal{X}_{01}\mathbb{I}$

		$\frac{1}{\sqrt{3}}$	$\mathcal{X}_{02}\mathcal{X}_{02}\mathcal{X}_{01}\mathcal{X}_{12}$	$\mathbb{I}\mathcal{X}_{01}\mathbb{I}\mathcal{X}_{01}\mathcal{X}_{01}\mathbb{I}\mathcal{X}_{01}\mathcal{X}_{01}$
		$\frac{1}{\sqrt{3}}$	$\mathcal{X}_{12}\mathcal{X}_{12}\mathcal{X}_{12}\mathcal{X}_{02}$	$\mathcal{X}_{01}\mathcal{X}_{01}\mathcal{X}_{01}\mathcal{X}_{01}\mathcal{X}_{01}\mathcal{X}_{01}\mathbb{I}\mathcal{X}_{01}$
$\{\mathbf{3},\mathbf{3},\mathbf{1},\overline{\mathbf{3}}\}$	$\{10100001\}$	$\frac{1}{3}$	$\mathcal{X}_{01}\mathcal{X}_{12}\mathcal{X}_{12}\mathcal{X}_{01}$	$\mathcal{X}_{01}\mathbb{I}\mathcal{X}_{01}\mathcal{X}_{01}\mathcal{X}_{01}\mathcal{X}_{01}\mathcal{X}_{01}\mathbb{I}$
		$-\frac{1}{3}$	$\mathcal{X}_{02}\mathcal{X}_{01}\mathcal{X}_{02}\mathcal{X}_{12}$	$\mathbb{I}\mathcal{X}_{01}\mathcal{X}_{01}\mathbb{I}\mathbb{I}\mathcal{X}_{01}\mathcal{X}_{01}\mathcal{X}_{01}$
		$-\frac{1}{3}$	$\mathcal{X}_{12}\mathcal{X}_{02}\mathcal{X}_{01}\mathcal{X}_{02}$	$\mathcal{X}_{01}\mathcal{X}_{01}\mathbb{I}\mathcal{X}_{01}\mathcal{X}_{01}\mathbb{I}\mathbb{I}\mathcal{X}_{01}$
$\{\mathbf{3},\overline{\mathbf{3}},\mathbf{1},\mathbf{1}\}$	$\{10010000\}$	$\frac{1}{\sqrt{3}}$	$\mathcal{X}_{01}\mathcal{X}_{01}\mathcal{X}_{02}\mathcal{X}_{12}$	$\mathcal{X}_{01}\mathbb{I}\mathcal{X}_{01}\mathbb{I}\mathbb{I}\mathcal{X}_{01}\mathcal{X}_{01}\mathcal{X}_{01}$
		$\frac{1}{3}$	$\mathcal{X}_{02}\mathcal{X}_{02}\mathcal{X}_{01}\mathcal{X}_{02}$	$\mathbb{I}\mathcal{X}_{01}\mathbb{I}\mathcal{X}_{01}\mathcal{X}_{01}\mathbb{I}\mathbb{I}\mathcal{X}_{01}$
		$\frac{1}{\sqrt{3}}$	$\mathcal{X}_{12}\mathcal{X}_{12}\mathcal{X}_{12}\mathcal{X}_{01}$	$\mathcal{X}_{01}\mathcal{X}_{01}\mathcal{X}_{01}\mathcal{X}_{01}\mathcal{X}_{01}\mathcal{X}_{01}\mathcal{X}_{01}\mathbb{I}$
$\{\mathbf{3},\mathbf{3},\overline{\mathbf{3}},\mathbf{1}\}$	$\{10100100\}$	$-\frac{1}{3}$	$\mathcal{X}_{01}\mathcal{X}_{01}\mathcal{X}_{12}\mathcal{X}_{01}$	$\mathcal{X}_{01}\mathbb{I}\mathcal{X}_{01}\mathbb{I}\mathcal{X}_{01}\mathcal{X}_{01}\mathcal{X}_{01}\mathbb{I}$
		$-\frac{1}{3}$	$\mathcal{X}_{02}\mathcal{X}_{02}\mathcal{X}_{02}\mathcal{X}_{12}$	$\mathbb{I}\mathcal{X}_{01}\mathbb{I}\mathcal{X}_{01}\mathbb{I}\mathcal{X}_{01}\mathcal{X}_{01}\mathcal{X}_{01}$
		$\frac{1}{3}$	$\mathcal{X}_{12}\mathcal{X}_{12}\mathcal{X}_{01}\mathcal{X}_{02}$	$\mathcal{X}_{01}\mathcal{X}_{01}\mathcal{X}_{01}\mathcal{X}_{01}\mathcal{X}_{01}\mathbb{I}\mathbb{I}\mathcal{X}_{01}$
$\{\overline{\mathbf{3}},\overline{\mathbf{3}},\mathbf{1},\mathbf{3}\}$	$\{01010010\}$	$-\frac{1}{3}$	$\mathcal{X}_{01}\mathcal{X}_{02}\mathcal{X}_{01}\mathcal{X}_{12}$	$\mathcal{X}_{01}\mathbb{I}\mathbb{I}\mathcal{X}_{01}\mathcal{X}_{01}\mathbb{I}\mathcal{X}_{01}\mathcal{X}_{01}$
		$\frac{1}{3}$	$\mathcal{X}_{02}\mathcal{X}_{12}\mathcal{X}_{12}\mathcal{X}_{02}$	$\mathbb{I}\mathcal{X}_{01}\mathcal{X}_{01}\mathcal{X}_{01}\mathcal{X}_{01}\mathcal{X}_{01}\mathbb{I}\mathcal{X}_{01}$
		$-\frac{1}{3}$	$\mathcal{X}_{12}\mathcal{X}_{01}\mathcal{X}_{02}\mathcal{X}_{01}$	$\mathcal{X}_{01}\mathcal{X}_{01}\mathcal{X}_{01}\mathbb{I}\mathbb{I}\mathcal{X}_{01}\mathcal{X}_{01}\mathbb{I}$
$\{\overline{\mathbf{3}},\overline{\mathbf{3}},\mathbf{3},\mathbf{1}\}$	$\{01011000\}$	$-\frac{1}{3}$	$\mathcal{X}_{01}\mathcal{X}_{01}\mathcal{X}_{01}\mathcal{X}_{12}$	$\mathcal{X}_{01}\mathbb{I}\mathcal{X}_{01}\mathbb{I}\mathcal{X}_{01}\mathbb{I}\mathcal{X}_{01}\mathcal{X}_{01}$
		$-\frac{1}{3}$	$\mathcal{X}_{02}\mathcal{X}_{02}\mathcal{X}_{12}\mathcal{X}_{02}$	$\mathbb{I}\mathcal{X}_{01}\mathbb{I}\mathcal{X}_{01}\mathcal{X}_{01}\mathcal{X}_{01}\mathbb{I}\mathcal{X}_{01}$
		$\frac{1}{3}$	$\mathcal{X}_{12}\mathcal{X}_{12}\mathcal{X}_{02}\mathcal{X}_{01}$	$\mathcal{X}_{01}\mathcal{X}_{01}\mathcal{X}_{01}\mathcal{X}_{01}\mathbb{I}\mathcal{X}_{01}\mathcal{X}_{01}\mathbb{I}$

Table 5: Local operators in the 27 control sectors of the generic plaquette operator with irrep truncation on each link of $\{\mathbf{1},\mathbf{3},\overline{\mathbf{3}}\}$ mapped to qutrit levels $\{0,1,2\}$ or (p,q)-qutrit pair levels of $\{(0,0),(1,0),(0,1)\}$.

$\{\mathbf{C}_1, \mathbf{C}_2\}$	coefficient	Givens Operator
$\{\mathbf{1}, \mathbf{1}\}$	1	$\mathcal{X}_{01}\mathcal{X}_{01}\mathcal{X}_{02}\mathcal{X}_{02}$
	1	$\mathcal{X}_{02}\mathcal{X}_{02}\mathcal{X}_{01}\mathcal{X}_{01}$
	1	$\mathcal{X}_{12}\mathcal{X}_{12}\mathcal{X}_{12}\mathcal{X}_{12}$
$\{\mathbf{1}, \mathbf{3}\}$	$\frac{1}{3}$	$\mathcal{X}_{01}\mathcal{X}_{02}\mathcal{X}_{01}\mathcal{X}_{01}$
	$\frac{1}{\sqrt{3}}$	$\mathcal{X}_{02}\mathcal{X}_{12}\mathcal{X}_{12}\mathcal{X}_{12}$
	$\frac{1}{\sqrt{3}}$	$\mathcal{X}_{12}\mathcal{X}_{01}\mathcal{X}_{02}\mathcal{X}_{02}$
$\{\mathbf{3}, \mathbf{3}\}$	$\frac{1}{3\sqrt{3}}$	$\mathcal{X}_{01}\mathcal{X}_{02}\mathcal{X}_{12}\mathcal{X}_{01}$
	$\frac{1}{3}$	$\mathcal{X}_{02}\mathcal{X}_{12}\mathcal{X}_{02}\mathcal{X}_{12}$
	$\frac{1}{3\sqrt{3}}$	$\mathcal{X}_{12}\mathcal{X}_{01}\mathcal{X}_{01}\mathcal{X}_{02}$
$\{\mathbf{3}, \overline{\mathbf{3}}\}$	$\frac{1}{3}$	$\mathcal{X}_{01}\mathcal{X}_{12}\mathcal{X}_{02}\mathcal{X}_{12}$
	$\frac{1}{9}$	$\mathcal{X}_{02}\mathcal{X}_{01}\mathcal{X}_{01}\mathcal{X}_{02}$
	$\frac{1}{3}$	$\mathcal{X}_{12}\mathcal{X}_{02}\mathcal{X}_{12}\mathcal{X}_{01}$
$\{\mathbf{3}, \mathbf{1}\}$	$\frac{1}{3}$	$\mathcal{X}_{01}\mathcal{X}_{01}\mathcal{X}_{01}\mathcal{X}_{02}$
	$\frac{1}{\sqrt{3}}$	$\mathcal{X}_{02}\mathcal{X}_{02}\mathcal{X}_{12}\mathcal{X}_{01}$
	$\frac{1}{\sqrt{3}}$	$\mathcal{X}_{12}\mathcal{X}_{12}\mathcal{X}_{02}\mathcal{X}_{12}$
$\{\overline{\mathbf{3}}, \mathbf{3}\}$	$\frac{1}{9}$	$\mathcal{X}_{01}\mathcal{X}_{02}\mathcal{X}_{02}\mathcal{X}_{01}$
	$\frac{1}{3}$	$\mathcal{X}_{02}\mathcal{X}_{12}\mathcal{X}_{01}\mathcal{X}_{12}$
	$\frac{1}{3}$	$\mathcal{X}_{12}\mathcal{X}_{01}\mathcal{X}_{12}\mathcal{X}_{02}$
$\{\mathbf{1}, \overline{\mathbf{3}}\}$	$\frac{1}{\sqrt{3}}$	$\mathcal{X}_{01}\mathcal{X}_{12}\mathcal{X}_{12}\mathcal{X}_{12}$
	$\frac{1}{3}$	$\mathcal{X}_{02}\mathcal{X}_{01}\mathcal{X}_{02}\mathcal{X}_{02}$
	$\frac{1}{\sqrt{3}}$	$\mathcal{X}_{12}\mathcal{X}_{02}\mathcal{X}_{01}\mathcal{X}_{01}$
$\{\overline{\mathbf{3}}, \overline{\mathbf{3}}\}$	$\frac{1}{3}$	$\mathcal{X}_{01}\mathcal{X}_{12}\mathcal{X}_{01}\mathcal{X}_{12}$
	$\frac{1}{3\sqrt{3}}$	$\mathcal{X}_{02}\mathcal{X}_{01}\mathcal{X}_{12}\mathcal{X}_{02}$
	$\frac{1}{3\sqrt{3}}$	$\mathcal{X}_{12}\mathcal{X}_{02}\mathcal{X}_{02}\mathcal{X}_{01}$
$\{\overline{\mathbf{3}}, \mathbf{1}\}$	$\frac{1}{\sqrt{3}}$	$\mathcal{X}_{01}\mathcal{X}_{01}\mathcal{X}_{12}\mathcal{X}_{02}$
	$\frac{1}{3}$	$\mathcal{X}_{02}\mathcal{X}_{02}\mathcal{X}_{02}\mathcal{X}_{01}$
	$\frac{1}{\sqrt{3}}$	$\mathcal{X}_{12}\mathcal{X}_{12}\mathcal{X}_{01}\mathcal{X}_{12}$

Table 6: Local operators (isolated from Table 5 for convenience) in the nine control sectors of the plaquette operator on the two-plaquette lattice with PBCs and irrep truncation on each link of $\{\mathbf{1}, \mathbf{3}, \overline{\mathbf{3}}\}$ mapped to qutrit levels $\{0, 1, 2\}$.

.2 VQE

.2.1 Hardware Calculations

To perform VQE on a quantum computer, a circuit must be designed to prepare the ansatz state. For the calculations demonstrated here, only two qubits were used, so the circuit used to construct the state was capable of preparing an arbitrary 2 qubit state whose wavefunction has only real coefficients. Once the ansatz state has been prepared on the quantum computer, the energy of the state must also be computed. This can efficiently be done by breaking the Hamiltonian up into a sum over tractable terms, applying gates that diagonalize each term of the Hamiltonian, and performing measurements in the computational basis. This approach to computing the energy will require one circuit per term in the Hamiltonian.

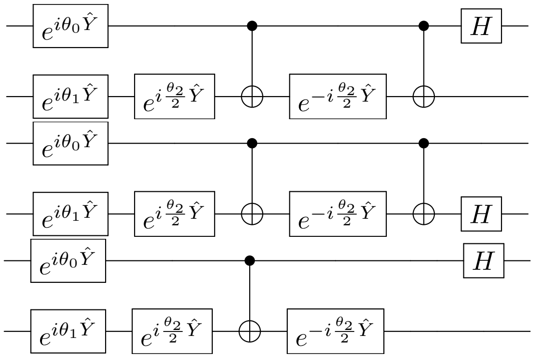

Figure 6: The top circuit is used to compute the expectation of H_1, the second circuit is used to compute the expectation of H_2, and the bottom circuit is used to compute the expectation of H_3.

Each of the Hamiltonians studied in this work can be written in the form

$$\begin{aligned}\hat{H} &= \hat{H}_1 + \hat{H}_2 + \hat{H}_3 \\ \hat{H}_1 &= h_{11}\hat{1}\otimes\hat{Z} + h_{12}\hat{X}\otimes\hat{1} + h_{13}\hat{X}\otimes\hat{Z} \\ \hat{H}_2 &= h_{21}\hat{Z}\otimes\hat{1} + h_{22}\hat{1}\otimes\hat{X} \\ \hat{H}_3 &= h_{31}\hat{X}\otimes\hat{X} + h_{32}\hat{Y}\otimes\hat{Y} + h_{33}\hat{Z}\otimes\hat{Z} \quad . \end{aligned} \tag{22}$$

These Hamiltonians can be diagonalized using the circuits shown in Fig. 6. To use gradient descent based methods in the classical optimization step of VQE, the gradient for the energy of the state as a function of the rotation angles in the ansatz circuit must be computed on the quantum computer. Due to the periodicity of sin and cos, the gradient can be computed exactly using a symmetric finite difference formula with a shift of $\frac{\pi}{4}$. Explicitly, components of the gradient are computed using

$$\partial_i E\left(\vec{\theta}\right) = E\left(\vec{\theta} + \frac{\pi}{4}\hat{i}\right) - E\left(\vec{\theta} - \frac{\pi}{4}\hat{i}\right) \quad , \tag{23}$$

where $E\left(\vec{\theta}\right)$ is the energy as a function of the angles in the ansatz circuit and $\hat{i}$ is a unit vector pointing in the i-th direction. Therefore the gradient can be computed on the quantum computer using a number of circuits equal to two times the number of parameters in the ansatz circuit. The calculation of the energy on a real quantum computer suffers from systematic errors due to errors in the implementation of the gates on the computer and errors in the measurement process. The measurement errors can be mitigated by using Qiskit's `measurement filter` subroutine, which removes the leading order measurement errors by optimizing an approximate inverse of the calculated all-to-all measurement matrix [53]. The dominant gate errors come from the implementation of CNOT gates. The errors associated with CNOT gates are mitigated using an extrapolation procedure [51, 52]. Each CNOT in the circuit is replaced with an odd number r of CNOT gates ($r = 3, 5, 7$) and a linear extrapolation is performed to $r = 0$.

.2.2 Bayesian Optimization

Bayesian optimization is a classical optimizer that can be used in the VQE algorithm. Bayesian optimization uses the data already collected to create a Gaussian process-based surrogate function that approximates the function, f, being optimized. This surrogate function is then used to create an acquisition function, which is then optimized to find a new trial point for the location of f's minimum. f is then evaluated at that new point and the result is incorporated into the data for the next iteration. The Gaussian process used requires both a mean and covariance matrix for the function f. The covariance matrix used in this work is constructed from the Gaussian kernel, which defines the covariance between $f(\mathbf{x}_1)$ and $f(\mathbf{x}_2)$ to be

$$K(\mathbf{x}_1, \mathbf{x}_2) = e^{-\Sigma_{i=1}^{d} \frac{({x_1}_i - {x_2}_i)^2}{l_i^2}} , \tag{24}$$

where d is the number of dimensions of the inputted point and l_i are hyperparameters specifying the width of the Gaussian for each component of $\mathbf{x}$. The mean of f is generically unknown, but given the covariance matrix the mean can be approximated by the best linear unbiased predictor,

$$\mu = (\mathbf{1}^{\mathbf{T}}\mathbf{C}^{-1}\mathbf{1})^{-1}\mathbf{1}^{\mathbf{T}}\mathbf{C}^{-1}\mathbf{Z} \tag{25}$$

where $\mathbf{1}$ is a vector with all entries equal to 1, $\mathbf{C}$ is the covariance matrix with matrix elements given by $\mathbf{C}_{ij} = K(\mathbf{x}_i, \mathbf{x}_j)$, and $\mathbf{Z}$ is a vector with entries given by the value of the function at the evaluated points, $\mathbf{Z}_i = f(\mathbf{x}_i)$.

Given the mean and variance of the Gaussian process, the value of f at a point $\mathbf{x_{posterior}}$ that has not already been evaluated follows a Gaussian distribution with a mean and variance given by

$$\begin{aligned} \mu_{posterior} &= \mathbf{c}^{\mathbf{T}}\mathbf{C}^{-1}\mathbf{Z} - (1 - \mathbf{c}^{\mathbf{T}}\mathbf{C}^{-1}\mathbf{1})(\mathbf{1}^{\mathbf{T}}\mathbf{C}^{-1}\mathbf{1})^{-1}\mathbf{1}^{\mathbf{T}}\mathbf{C}^{-1}\mathbf{Z} \\ \sigma^2_{posterior} &= K(\mathbf{x_{posterior}}, \mathbf{x_{posterior}}) - \mathbf{c}^{\mathbf{T}}\mathbf{C}^{-1}\mathbf{c} + (1 - \mathbf{c}^{\mathbf{T}}\mathbf{C}^{-1}\mathbf{1})^2(\mathbf{1}^{\mathbf{T}}\mathbf{C}^{-1}\mathbf{1})^{-1} \quad , \end{aligned} \tag{26}$$

where $\mathbf{c}$ is a vector with entries $\mathbf{c}_i = K(\mathbf{x_{posterior}}, \mathbf{x}_i)$. Eq. (26) expresses the posterior mean and variance under the assumption that f can be evaluated without error. In order to incorporate errors, the variance of the data must be added to the diagonal elements of the covariance matrix $\mathbf{C}$ and to $\sigma^2_{posterior}$.

To use a Gaussian process in practice, the hyperparameters of the kernel must be selected. In this work, this was done by maximizing the likelihood of the data under a multivariate Gaussian model with a mean equal to the best linear unbiased predictor's mean and with a covariance equal to $\mathbf{C}$ (with the variance of the data added to its diagonal elements) from Eq. (25). Another issue with practical implementation that arises is that $\mathbf{C}$ often ends up singular as the Gaussian process is iterated. This issue is known as multicollinearity and it occurs when one of the points used to construct $\mathbf{C}$ can be exactly predicted from the other points leading to zero being an eigenvalue of $\mathbf{C}$. This can be remedied by using Tikohonov regularization where a fake "data variance" distinct from the real data variance is added to $\mathbf{C}$ but not to $\sigma^2_{posterior}$.

The probability distribution of f at unevaluated points is used to construct an acquisition function, whose job it is to balance exploration and exploitation. The acquisition function is optimized to find the minimum of f. In this work, probability of improvement was used as the acquisition function, ie. the probability that the minimum of f is smaller than the previously found minimum is maximized. This is equivalent to minimizing

$$acq(\mathbf{x})_{PI} = \frac{\mu_{posterior}(\mathbf{x}) - f_{min}}{\sigma_{posterior}(\mathbf{x})} \tag{27}$$

where f_{min} is the previously found minimum of f.

.2.3 *Plaquette Chain Tensor Network*

The time evolving block decimation (TEBD) algorithm can be used to simulate the time evolution of an infinite translationally invariant quantum system by Trotterizing the time evolution operator [300, 301, 150]. The vacuum state of a system can be prepared by performing imaginary time evolution. This algorithm was developed for the simulation of systems whose Hamiltonian only consists of 2-site nearest-neighbor couplings, so its application to the simulation of a plaquette chain requires nonstandard modifications. Fig. 7 shows how the links in the plaquette chain can be blocked together to form a 1D quantum system whose state can be described with MPS.

In this blocking, the electric field operator on a single link becomes a single site operator, the plaquette operator becomes a three site operator, and the Gauss's law constraint become a constraint on neighboring sites. The Gauss's law constraint can be enforced by adding an energy penalty for violating Gauss's law.

The TEBD algorithm finds the vacuum by applying a Trotterized version of the imaginary time evolution operator to a translationally invariant state. For a 2-site Hamiltonian, this is accomplished by storing a unit cell of 2 sites and performing an SVD after applying

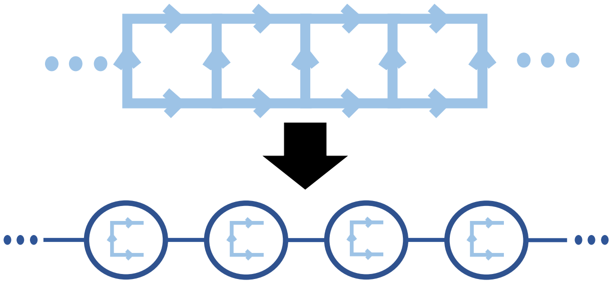

Figure 7: An infinite chain of SU(3) plaquettes can be mapped onto a 1D quantum system whose state can be represented with MPS by blocking sets of 3 links together as shown.

each gate to keep the most relevant states. For a 3-site Hamiltonian, such as the Hamiltonian obtained for the plaquette chain, a unit cell of 3 sites must be stored and two SVD's must be performed to obtain the most relevant local states as shown in Fig. 8. The approach used to perform time evolution in TEBD can also be used to apply arbitrary gates. To represent the ansatz states obtained using domains of l plaquettes, a unit cell of length $l+1$ had to be stored and the state was prepared by applying gates and performing a SVD to return to MPS form as in the case of time evolution.

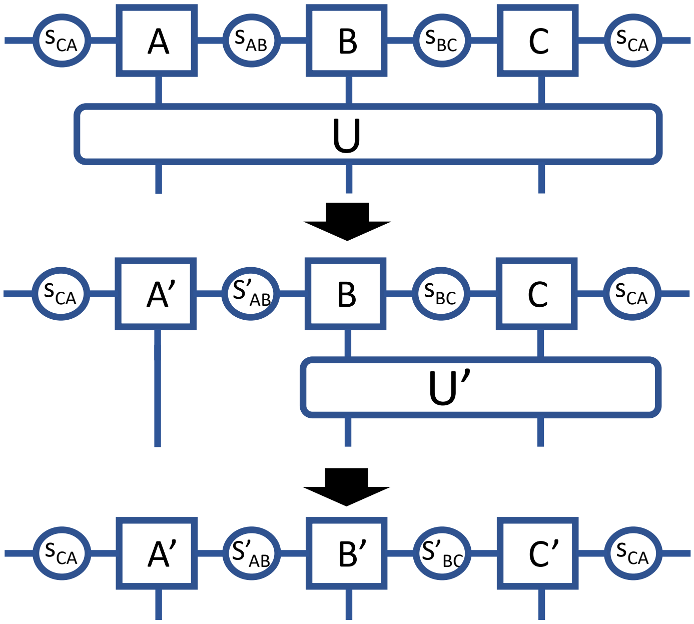

Figure 8: This figure shows the required sequence of SVDs that must be performed to return an MPS tensor network to MPS form after applying a 3 site gate.

.3 *Schrieffer-Wolff Perturbation Theory*

The improved Hamiltonians derived in this chapter are based on performing a unitary transformation before truncating the electric field to reduce the coupling to the states being removed by the truncation. This can be done perturbatively through the use of Schrieffer-Wolf perturbation theory (SWPT). In this section, the application of SWPT to the Hamiltonian in Eq. (3.2) with $m = 0$ will be demonstrated. The Hamiltonian for lattice gauge theories in 1D we wish to simulate takes the form

$$\hat{H} = \hat{H}_E + \hat{H}_D + \hat{V} \quad , \tag{28}$$

where $\hat{H}_E$ is the electric Hamiltonian, $\hat{V}$ couples the low energy subspace to the high energy subspace and $\hat{H}_D$ describes dynamics in the high energy Hilbert space. Note that the kinetic term of Eq. (3.2) is equal to $\hat{H}_D + \hat{V}$. For the zero electric field truncation, $\hat{V}$ is the piece of the kinetic term that corresponds to a baryon on a site ejecting a quark to a neighboring site and $\hat{H}_D$ is the piece of the kinetic term that describes a quark propagating freely between sites. SWPT systematically generates a unitary, $e^{\hat{S}}$ that decouples the selected low energy subspace. For lattice gauge theories, we will be decoupling the electric vacuum and states with low energy relative to the electric Hamiltonian. To leading order we have

$$\begin{aligned} e^{\hat{S}_1} \hat{H} e^{-\hat{S}_1} &= \hat{H}_E + [\hat{S}_1, \hat{H}_E + \hat{H}_D] + \hat{H}_D + \hat{V} + [\hat{S}_1, \hat{V}] \\ &+ \frac{1}{2}[\hat{S}_1, [\hat{S}_1, \hat{H}_E + \hat{H}_D] + \mathcal{O}(\hat{V}^3) \quad . \end{aligned} \tag{29}$$

The leading order coupling between the low and high energy subspace comes from $\hat{V}$ and be cancelled at leading order by choosing $\hat{S}_1$ such that $[\hat{S}_1, \hat{H}_E + \hat{H}_D] = -\hat{V}$. Explicitly, the matrix elements of $\hat{S}_1$ are

$$(S_1)_{ab} = \frac{1}{E_a - E_b} V_{ab} \quad , \tag{30}$$

where the indices label eigenstates of $\hat{H}_E + \hat{H}_D$ with eigenvalues E_a. To leading order, the effective Hamiltonian is

$$\hat{H}^1_{eff} = \hat{H}_E + \frac{1}{2}[\hat{S}_1, \hat{V}] \quad , \tag{31}$$

and provided that the low energy subspace has an electric energy of 0, the commutator is equal to

$$\frac{1}{2}[\hat{S}_1, \hat{V}] = -\hat{V} \frac{1}{\hat{H}_E + \hat{H}_D} \hat{V} = -\sum_n \left(-\hat{H}_E^{-1} \hat{H}_D\right)^n \frac{1}{\hat{H}_E} \hat{V} \quad . \tag{32}$$

Therefore to $\mathcal{O}(H_E^{-2})$, the effective Hamiltonian is given by

$$\hat{H}^1_{eff} = \hat{H}_E - \hat{V}\frac{1}{\hat{H}_E}\hat{V} + \hat{V}\frac{1}{\hat{H}_E}\hat{H}_D\frac{1}{\hat{H}_E}\hat{V} + \mathcal{O}(\hat{H}_E^{-3}) \quad . \tag{33}$$

Plugging in the corresponding pieces of Eq. (3.2) yields the improved Hamiltonian in Eq. (3.4). Techniques for performing this expansion to higher orders can be found in Ref. [138].

.4 *eQED Circuits*

.4.1 Momentum Space Hamiltonian

The interactions in an effective field theory should be chosen to correctly reproduce some physics of the full model. To correctly reproduce the physics of QED, the effective interaction will be chosen to correctly reproduce the QED scattering amplitudes at lowest order in perturbation theory. This means the potential will consist of 4 fermion terms which describe the scattering processes $e^\pm e^\pm \to e^\pm e^\pm$, $e^+e^- \to e^+e^-$, $e^\pm \rightleftharpoons e^\pm e^+ e^-$ and $0 \rightleftharpoons e^+e^-e^+e^-$. Note that the $1 \to 3$ and $0 \to 4$ scattering amplitudes will always be off-shell, so these scattering processes will not be directly observed, but including them in the Hamiltonian is necessary for scattering amplitudes at higher orders to be correctly reproduced. The necessary scattering amplitudes in the following subsections are computed using Feynman diagrams at leading order. Further details of these derivations can be found in [7].

$e^\pm e^\pm \to e^\pm e^\pm$ *Amplitudes*

The electron scattering amplitude is given by

$$\mathcal{M}^{e^-_{r,\sigma_3} e^-_{p+q-r,\sigma_4}}_{e^-_{p,\sigma_1} e^-_{p,\sigma_2}} = e^2 \left(\frac{\bar{u}_{\sigma_3}(p_3)\gamma^\mu u_{\sigma_1}(p_1)\bar{u}_{\sigma_4}(p_4)\gamma_\mu u_{\sigma_2}(p_2)}{(E_{p_3} - E_{p_1})^2 - (\vec{p_3} - \vec{p_1})^2} - \frac{\bar{u}_{\sigma_4}(p_4)\gamma^\mu u_{\sigma_1}(p_1)\bar{u}_{\sigma_3}(p_3)\gamma_\mu u_{\sigma_2}(p_2)}{(E_{p_4} - E_{p_1})^2 - (\vec{p_4} - \vec{p_1})^2} \right) . \tag{34}$$

The positron scattering amplitude takes a similar form and it is given by

$$\mathcal{M}^{e^+_{r,\sigma_3} e^+_{p+q-r,\sigma_4}}_{e^+_{p,\sigma_1} e^+_{q,\sigma_2}} = e^2 \left(\frac{\bar{v}_{\sigma_1}(p_1)\gamma^\mu v_{\sigma_3}(p_3)\bar{v}_{\sigma_2}(p_2)\gamma_\mu v_{\sigma_4}(p_4)}{(E_{p_3} - E_{p_1})^2 - (\vec{p_3} - \vec{p_1})^2} - \frac{\bar{v}_{\sigma_1}(p_1)\gamma^\mu v_{\sigma_4}(p_4)\bar{v}_{\sigma_2}(p_2)\gamma_\mu v_{\sigma_3}(p_3)}{(E_{p_4} - E_{p_1})^2 - (\vec{p_4} - \vec{p_1})^2} \right) . \tag{35}$$

$e^+e^- \to e^+e^-$ Amplitude

The electron positron scattering amplitude is given by

$$\mathcal{M}_{e^-_{p,\sigma_1} e^+_{q,\sigma_2}}^{e^-_{r,\sigma_3} e^+_{p+q-r,\sigma_4}} = e^2 \left(\frac{\bar{v}_{\sigma_2}(q_1)\gamma^\mu u_{\sigma_1}(p_1)\bar{u}_{\sigma_3}(p_2)\gamma_\mu v_{\sigma_4}(q_2)}{(E_{p_1}+E_{p_2})^2 - (\vec{p_1}+\vec{p_2})^2} + \frac{\bar{u}_{\sigma_3}(p_2)\gamma^\mu u_{\sigma_1}(p_1)\bar{v}_{\sigma_3}(q_1)\gamma_\mu v_{\sigma_4}(q_2)}{(E_{p_1}-E_{p_2})^2 - (\vec{p_1}-\vec{p_2})^2} \right) . \tag{36}$$

$e^\pm \to e^+e^-e^\pm$ Amplitude

The $e^- \to e^-e^+e^-$ scattering amplitude is given by

$$\mathcal{M}_{e^-_{p,\sigma_1}}^{e^+_{q,\sigma_2} e^-_{p_1,\sigma_3} e^-_{p-q-p_1,\sigma_4}} = e^2 \left(\frac{\bar{u}_{\sigma_3}(p_1)\gamma^\mu u_{\sigma_1}(p)\bar{u}_{\sigma_4}(p_2)\gamma_\mu v_{\sigma_2}(q)}{(E_p-E_{p_1})^2 - (\vec{p}-\vec{p_1})^2} - \frac{\bar{u}_{\sigma_4}(p_2)\gamma^\mu u_{\sigma_1}(p)\bar{u}_{\sigma_3}(p_1)\gamma_\mu v_{\sigma_2}(q)}{(E_p-E_{p_2})^2 - (\vec{p}-\vec{p_2})^2} \right) . \tag{37}$$

The $e^+ \to e^+e^+e^-$ scattering amplitude is given by

$$\mathcal{M}_{e^+_{p,\sigma_1}}^{e^-_{q,\sigma_2} e^+_{p_1,\sigma_3} e^+_{p-q-p_1,\sigma_4}} = e^2 \left(\frac{\bar{u}_{\sigma_2}(q)\gamma^\mu v_{\sigma_4}(p_2)\bar{v}_{\sigma_1}(p)\gamma_\mu v_{\sigma_3}(p_1)}{(E_p-E_{p_1})^2 - (\vec{p}-\vec{p_1})^2} - \frac{\bar{u}_{\sigma_2}(q)\gamma^\mu v_{\sigma_3}(p_3)\bar{v}_{\sigma_1}(p)\gamma_\mu v_{\sigma_4}(p_2)}{(E_p-E_{p_2})^2 - (\vec{p}-\vec{p_2})^2} \right). \tag{38}$$

Naïve Vacuum Coupling

The amplitude describing the coupling of the naïve vacuum to states with nonzero electron and positron number is given by

$$\mathcal{M}_0^{e^-_{p,\sigma_1} e^+_{q,\sigma_2} e^-_{r,\sigma_3} e^+_{-p-q-r,\sigma_4}} = \frac{\bar{u}_{\sigma_1}(p)\gamma^\mu v_{\sigma_2}(q)\bar{u}_{\sigma_3}(r)\gamma_\mu v_{\sigma_4}(-p-q-r)}{(E_p+E_q)^2 - (\vec{p}+\vec{q})^2} . \tag{39}$$

.4.2 Diagonalization of Interaction Terms

In order to derive our simulation circuits for the imaginary terms in the eQED Hamiltonian we need to show explicit simulation circuits for the mutually commuting Pauli operators of the form $YXXX, XYXX, \ldots, XYYY$. There are eight possible combinations of which four cases need to be considered. To see why this is, let us consider the cases $XYYY, YXYY, YYXY, YYYX$. The GHZ preparation circuit, G, has a symmetry in that the circuit is invariant under swaps of qubits $2, 3$ and 4. Thus if we utilize this permutational symmetry, the only cases that need to be considered are $XYYY$ and $YXYY$ as the other two are equivalent to $YXYY$ under exchange of the last three qubits. The exact same argument holds true for $XXXY, \ldots, YXXX$ and so only four cases need to be considered to understand how the modified GHZ preparation circuit G diagonalizes such terms.

The proof that the circuit G introduced in section 4.2.2 diagonalizes all the relevant Pauli operators will make use of the X and Z error propagation identity shown in Fig. 9.

Original	Equivalent	Original	Equivalent
$G^\dagger(XYYY)G$	$-ZZZZ$	$G^\dagger(YXXX)G$	$Z111$
$G^\dagger(YYYX)G$	$-ZZZ1$	$G^\dagger(XXXY)G$	$Z11Z$
$G^\dagger(YYXY)G$	$-ZZ1Z$	$G^\dagger(XXYX)G$	$Z1Z1$
$G^\dagger(YXYY)G$	$-Z1ZZ$	$G^\dagger(XYXX)G$	$ZZ11$

Table 7: Summary of diagonalization of Hamiltonian terms using the GHZ preparation circuit G

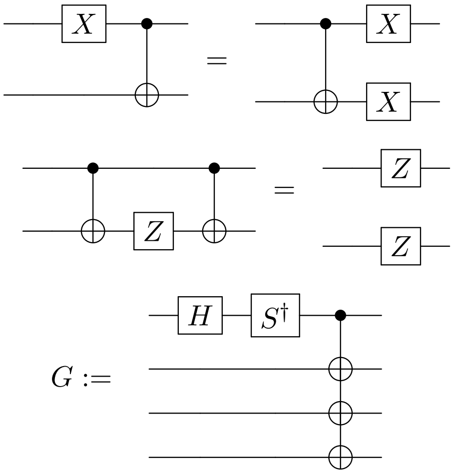

Figure 9: X and Z Error Propagation Identities and definition of the GHZ transformation circuit G

In the first line of Fig. 10, the identity $Y = iXZ$ has been used to replace the Y gate acting on the first qubit. The X error identity was then used to move the X gate acting on the first qubit past the CNOT gate. Since a Z gate acting on the control of a CNOT commutes with the CNOT and an X gate acting on the target of a CNOT commutes with the CNOT, the Z gate acting on the first qubit can be moved past the CNOTs and the X gates acting on the lower qubits can be moved past the CNOTs. This results in a cancellation of all of the CNOTs and X's acting on the three lower qubits. Calculating $G^\dagger(YXXX)G$ is reduced to computing the product of the single qubit gates in the second to last diagram of Fig. 10 which concludes the proof that $G^\dagger(YXXX)G = Z111$. The same techniques are applied in the following diagrams to diagonalize the remaining relevant Pauli operators.

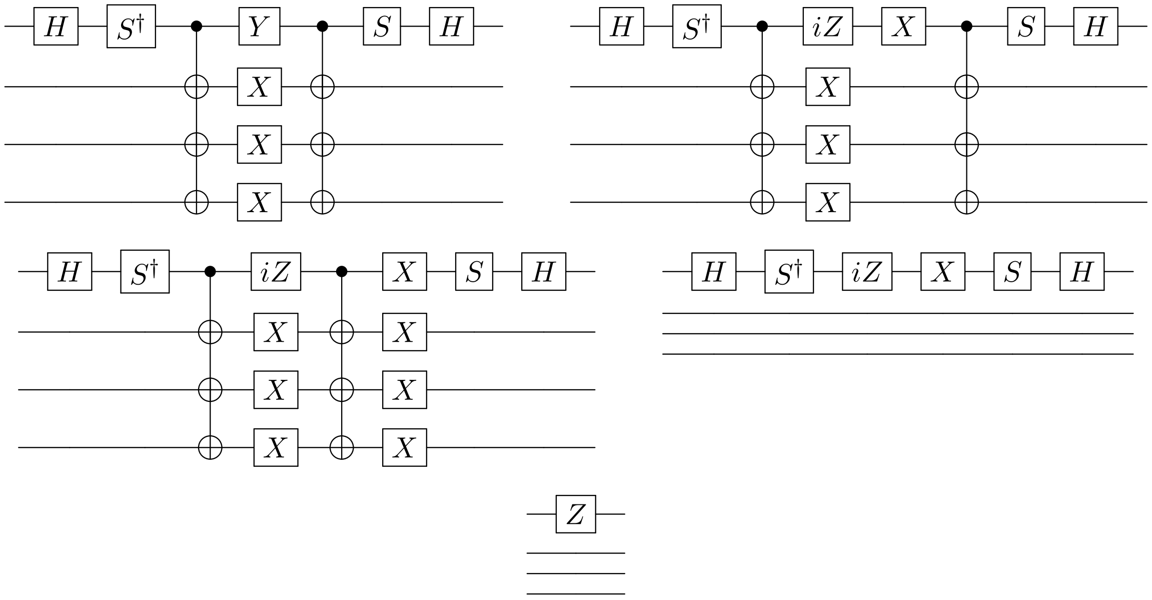

Figure 10: Diagonalization of $YXXX$

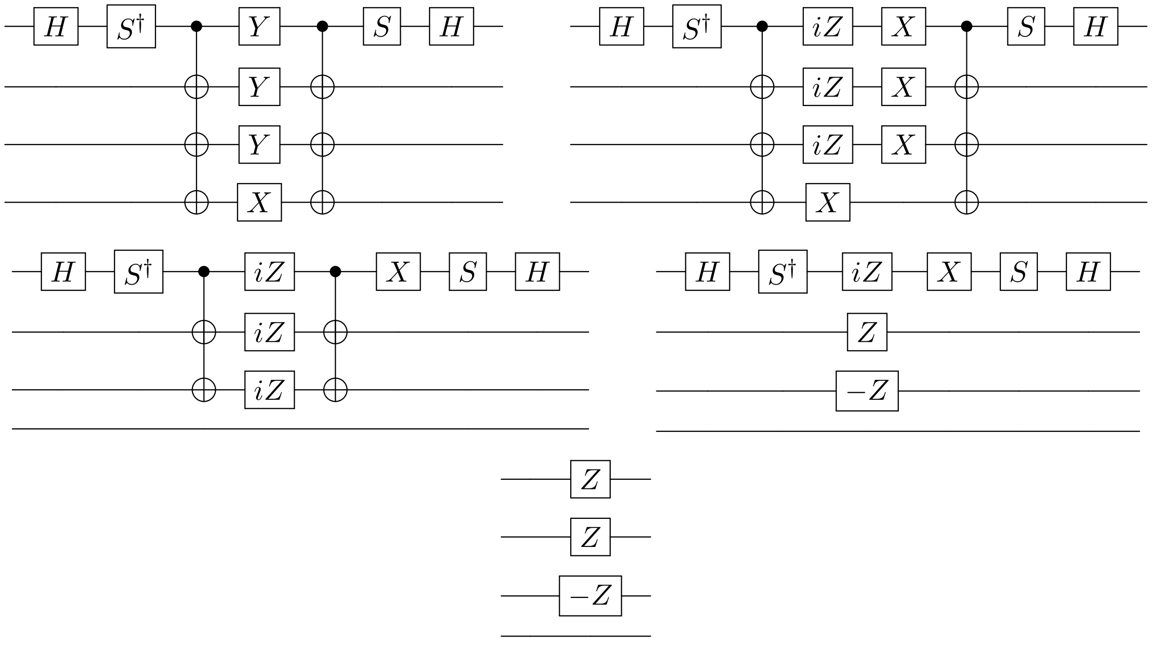

Figure 11: Steps involved in showing the diagonalization of $YYYX$ using GHZ transformations.

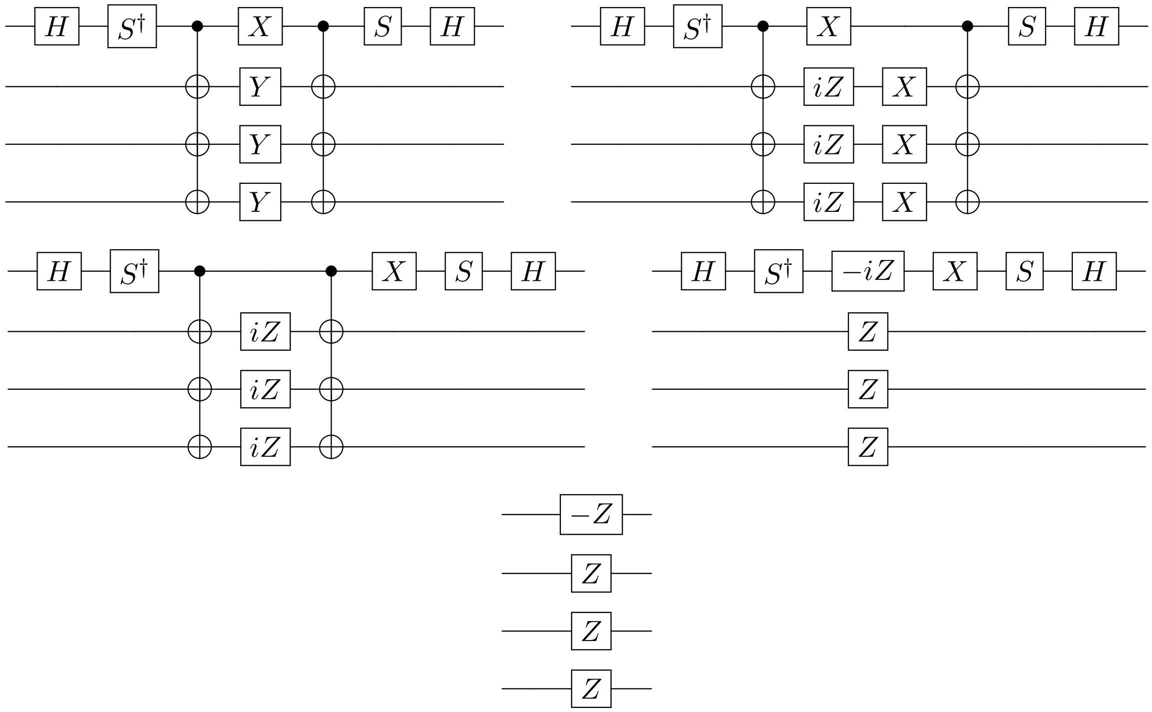

Figure 12: Diagonalization of $XYYY$

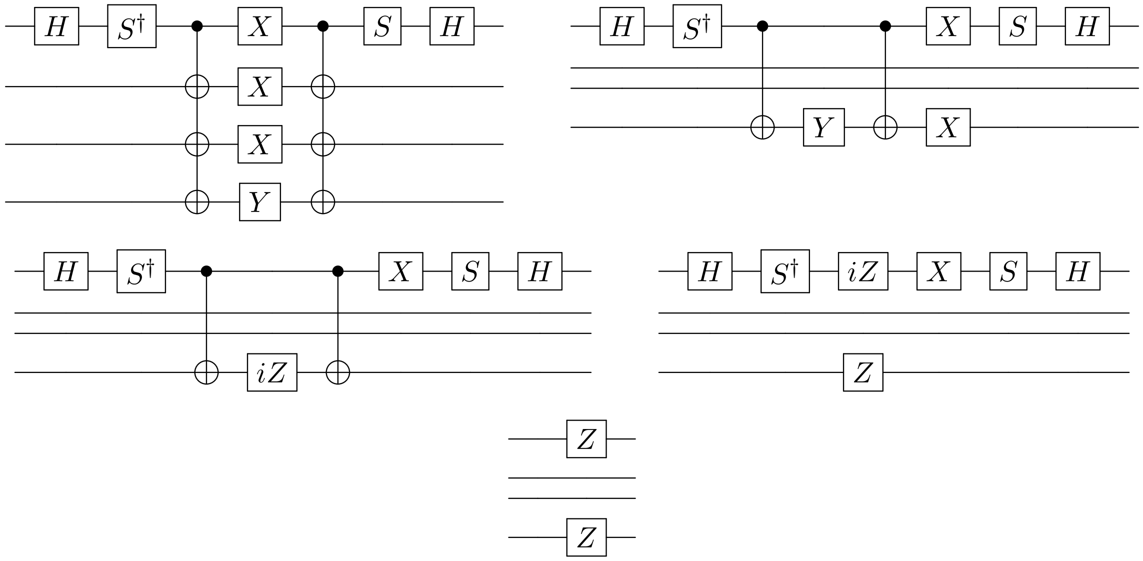

Figure 13: Diagonalization of $XXXY$

.5 Error Analysis of Particle Decay Calculations

.5.1 Green's Function Poles

The Green's function used in this method is

$$G = \langle\psi| \frac{1}{\omega - \hat{H} + i\eta} |\psi\rangle \quad , \tag{40}$$

where $|\psi\rangle$ is a state describing the particle that will be decaying and $\hat{H}$ is the Hamiltonian of the system. This Green's function has poles whose real part is the energy of the state $|\psi\rangle$ and whose imaginary part is given by the imaginary part of the forward scattering amplitude. The manipulations to show this are standard [223], but have been reproduced here for the reader's convenience. The Hamiltonian can be split into a free term and an interaction term so that $\hat{H} = \hat{H}_0 + \hat{V}$, $\hat{H}_0 |\psi\rangle = E_0 |\psi\rangle$. Let $\hat{P} = |\psi\rangle \langle\psi|$, $\hat{Q} = 1 - |\psi\rangle \langle\psi|$. The Green's function can be written as

$$G = \frac{1}{\omega - E_0 + i\eta} + \frac{1}{(\omega - E_0 + i\eta)^2} \langle\psi| \hat{V} \sum_{n=0}^{\infty} \left(\frac{1}{\omega - \hat{H}_0 + i\eta} \hat{V} \right)^n |\psi\rangle \quad . \tag{41}$$

Using the matrix identity

$$\hat{A} \sum_{n=0}^{\infty} ((\hat{B} + \hat{C})\hat{A})^n = \hat{A}' \sum_{n=0}^{\infty} (\hat{B}\hat{A}')^n \tag{42}$$

where $\hat{A}' = \hat{A} \sum\limits_{n=0}^{\infty} (\hat{C}\hat{A})^n$ with $\hat{A} = \hat{V}$, $\hat{B} = \frac{\hat{P}}{\omega - \hat{H}_0 + i\eta}$ and $\hat{C} = \frac{\hat{Q}}{\omega - \hat{H}_0 + i\eta}$, the Green's function is

$$G = \frac{1}{\omega - E_0 + i\eta} + \frac{1}{(\omega - E_0 + i\eta)^2} \langle\psi| \tilde{T} \sum_{n=0}^{\infty} \left(\frac{\hat{P}}{\omega - \hat{H}_0 + i\eta} \tilde{T} \right)^n |\psi\rangle \tag{43}$$

where

$$\tilde{T} = \hat{V} \sum_{n=0}^{\infty} \left(\frac{\hat{Q}}{\omega - \hat{H}_0 + i\eta} \hat{V} \right)^n \quad . \tag{44}$$

$$\frac{\hat{P}}{\omega - \hat{H}_0 + i\eta} = \frac{|\psi\rangle \langle\psi|}{\omega - E_0 + i\eta} \quad , \tag{45}$$

so

$$\sum_{n=0}^{\infty} \left(\frac{\hat{P}}{\omega - \hat{H}_0 + i\eta} \tilde{T} \right)^n |\psi\rangle = \sum_{n=0}^{\infty} \left(\frac{1}{\omega - E_0 + i\eta} \langle\psi| \tilde{T} |\psi\rangle \right)^n |\psi\rangle \quad . \tag{46}$$

Using this fact, Eq. (43) becomes

$$G = \frac{1}{\omega - E_0 + i\eta} + \frac{1}{(\omega - E_0 + i\eta)^2} \langle\psi| \tilde{T} |\psi\rangle + \frac{1}{(\omega - E_0 + i\eta)^3} \langle\psi| \tilde{T} |\psi\rangle^2 + \cdots$$

$$= \frac{1}{\omega - E_0 + i\eta} \left(\frac{1}{1 - \frac{1}{\omega - E_0 + i\eta} \langle\psi| \tilde{T} |\psi\rangle} \right) = \frac{1}{\omega - E_0 + i\eta - \langle\psi| \tilde{T} |\psi\rangle} \quad . \tag{47}$$

In the limit that η goes to zero, $\tilde{T}$ becomes the scattering T matrix, $\hat{T}$, and according to the optical theorem $\frac{\Gamma}{2} = -\operatorname{Im}(\langle\psi| \hat{T} |\psi\rangle)$ for a single particle state, $|\psi\rangle$. So

$$\left| \langle\psi| \frac{1}{\omega - \hat{H} + i\eta} |\psi\rangle \right|^2 = \frac{1}{(\omega - E)^2 + (\frac{\Gamma}{2} + \eta)^2} \quad , \tag{48}$$

and from Eq. (48) the decay rate can be extracted since it is proportional to the width of a Lorentzian distribution centered at the particle's energy.

.5.2 Quantum Computation of the Green's Function

Fully Quantum Approach

In the previous section, it was shown that the imaginary part of the poles of the Green's function $\langle\psi| \frac{1}{\omega - \hat{H} + i\eta} |\psi\rangle$ is $\frac{\Gamma}{2} + \eta$. Therefore, if this Green's function can be computed efficiently, then the decay rate can be computed efficiently as well. This Green's function can be expressed as an integral

$$\langle\psi| \frac{1}{\omega - \hat{H} + i\eta} |\psi\rangle = -i \int_0^\infty e^{i(\omega + i\eta)t} \langle\psi| e^{-i\hat{H}t} |\psi\rangle \, dt \quad . \tag{49}$$

If this integral is cut off at some finite large time T, it can be approximated with a Riemann sum

$$\lim_{T\to\infty, \Delta t \to 0} \sum_{k=0}^{T/\Delta t} e^{i(\omega + i\eta)k\Delta t} \langle\psi| e^{-i\hat{H}k\Delta t} |\psi\rangle \, \Delta t = i \langle\psi| \frac{1}{E - \hat{H} + i\eta} |\psi\rangle \quad . \tag{50}$$

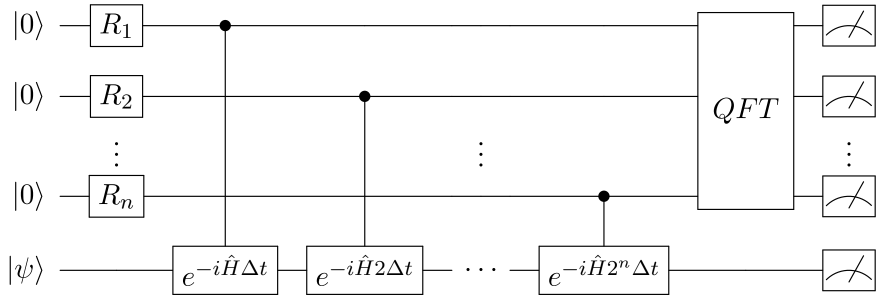

Figure 14: The quantum circuit used to calculate the Riemann sum approximation to the Green's function.

If $T = (2^{n+1} - 1)\Delta t$, this sum can be evaluated on quantum computer using a register of n ancilla qubits in addition to a register used to store the state of the system and a number of gates that scale polynomially with n and the size of the system. The circuit used to calculate the Green's function is displayed in Fig. 14. The calculation begins with the quantum computer in the state $|0\rangle^{\otimes n}|\psi\rangle$ where all qubits in the ancilla are in the state $|0\rangle$ and the system register is in the state $|\psi\rangle$ which describes the unstable particle that will be decaying. R_k is applied to the kth ancilla qubit, where $R_k = \begin{pmatrix} \cos(\theta_k) & -\sin(\theta_k) \\ \sin(\theta_k) & \cos(\theta_k) \end{pmatrix}$ and $\theta_k = \arctan\left(e^{-2^k\eta\Delta t}\right)$. Up to normalization factors, the quantum computer is in the state $\sum_{k=0}^{2^n-1} e^{-\eta k\Delta t}|k\rangle|\psi\rangle$. From the kth ancilla qubit, a controlled time evolution evolution operator is applied to the system register for time $2^k\Delta t$. Finally, the quantum Fourier transform is applied to the ancilla qubits which will put the quantum computer in the state $\sum_{m=0}^{2^n-1}\sum_{k=0}^{2^n-1} e^{i(\frac{2\pi}{(2^n-1)\Delta t}m+i\eta)k\Delta t}|m\rangle e^{-i\hat{H}k\Delta t}|\psi\rangle$. Performing a measurement on both registers, the probability that the ancilla register is in the state m and the system register is in the state ψ is

$$P(m,\psi) \propto \left|\sum_{k=0}^{2^n-1} e^{i(\omega_m+i\eta)k\Delta t}\langle\psi| e^{-i\hat{H}k\Delta t}|\psi\rangle\right|^2 \tag{51}$$

where $\omega_m = \frac{2\pi m}{(2^{n+1}-1)\Delta t}$. This is directly proportional to the Riemann sum that approximates the Green's function, and by repeatedly running this circuit, estimates for $P(m,\psi)$ can be obtained.

Hybrid Approach

The circuit described in the previous section allows the Green's function to be computed using only quantum resources. However, that circuit requires many CNOT gates and ancilla qubits which makes implementation on a near term quantum computer difficult. Previous work has introduced variational methods to compute the Green's function on near term quantum computers [362]. In this section, a method of computing Green's functions using the Hadamard test will be introduced. This method only requires a single ancilla qubit, which makes it more suitable for near term quantum computers than the method in the previous section. The Hadamard test method [244] can be used to compute $\langle\psi| e^{-i\hat{H}t} |\psi\rangle$ with a quantum computer for several time slices. For the circuit in Fig. 15a, $P(0) - P(1) = \mathrm{Re}\left(\langle\psi| e^{-i\hat{H}t} |\psi\rangle\right)$, where $P(0)$ is the probability that the ancilla qubit is measured to be in that state 0 and $P(1)$ is the probability it is measured to be 1. For the circuit in Fig. 15b, $P(0) - P(1) = \mathrm{Im}\left(\langle\psi| e^{-i\hat{H}t} |\psi\rangle\right)$. By running these two circuits n times, $\langle\psi| e^{-i\hat{H}t} |\psi\rangle$ can be computed with statistical error given by $\frac{1}{\sqrt{n}}$.

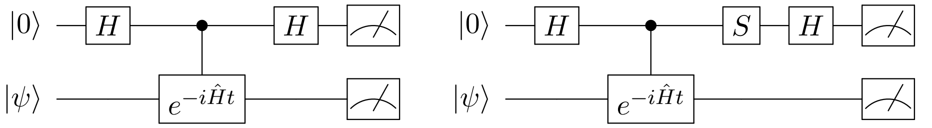

(a) Circuit used to determine $\mathrm{Re}(\langle\psi| e^{-iHt} |\psi\rangle)$

(b) Circuit used to determine $\mathrm{Im}(\langle\psi| e^{-iHt} |\psi\rangle)$

Figure 15: Circuits used in the Hadamard Test

Once $\langle\psi| e^{-i\hat{H}t} |\psi\rangle$ has been computed for several time slices, the Green's function can be computed by classically performing a discrete Fourier transform. This requires a separate quantum circuit for each time slice, but the circuits used are shorter than the circuit in the previous section which makes them better suited for implementation on near term quantum computers. Implementing the Hadamard test requires at most a polynomial overhead over the cost of implementing e^{-iHt}. Therefore, the quantum and classical resources needed to compute the Green's function scale polynomially with this method as long as $|\psi\rangle$ can be prepared using polynomially many resources and time evolution can be performed using polynomially many resources on the quantum computer.

.5.3 Error Scaling

Finite T and Δt

This calculation is based on performing a Riemann sum approximation to an integral, so errors due to a finite T cutoff and a finite step size Δt will need to be estimated. The

Riemann sum being evaluated is

$$R = \sum_{k=0}^{T/\Delta t} e^{i(\omega+i\eta)k\Delta t} \langle\psi| e^{-i\hat{H}k\Delta t} |\psi\rangle \Delta t \tag{52}$$

which approximates

$$I = \int_0^T e^{i(\omega+i\eta)t} \langle\psi| e^{-i\hat{H}t} |\psi\rangle \, dt \quad . \tag{53}$$

Eq. (53) differs from the $T \to \infty$ limit by

$$\delta I = \langle\psi| \frac{1}{\omega - \hat{H} + i\eta} e^{i(\omega-\hat{H})T} |\psi\rangle e^{-\eta T} \quad . \tag{54}$$

Therefore, to determine the Green's function to within an accuracy of ϵ, T must be taken to be $O\left(\frac{1}{\eta}\log\left(\frac{1}{\eta\epsilon}\right)\right)$. Using integration by parts, it can be shown that

$$\int_{t_1}^{t_2} dt e^{at} = (t_2 - t_1)e^{at_2} - \int_{t_1}^{t_2} dt \ (t - t_1) \ a \ e^{at} \tag{55}$$

and using Eq. 55, it can be shown that

$$I - R = -\sum_{n=1}^{n_t} \int_{\Delta t \ (n-1)}^{\Delta t \ n} dt \ (t - \Delta t \ (n-1)) \ \langle\psi| (\omega - \hat{H} + i\eta) e^{i(\omega-\hat{H}+i\eta)t} |\psi\rangle \tag{56}$$

where n_t is the number of time slices used in the Riemann sum. $|\psi\rangle$ can be expanded in the eigenbasis of $\hat{H}$ as $|\psi\rangle = \sum_n c_n |E_n\rangle$. The Hamiltonians for which this method of computing the Green's function is to be applied to have been renormalized such that the lowest energy state has zero energy. Therefore, it may be assumed that $E_n \geq 0$ for all n. If $\langle\psi| \hat{H} |\psi\rangle = E$, then

$$\left|\langle\psi| \hat{H} e^{-i\hat{H}t} |\psi\rangle\right| = \left|\sum_n |c_n|^2 E_n e^{-iE_n t}\right| \leq \sum_n |c_n|^2 E_n = E \quad . \tag{57}$$

Using this bound, it can be shown that

$$|I - R| \leq \int_0^T \Delta t \ (\omega + E + \eta) e^{-\eta t} \leq \frac{T}{\eta n_t} (\omega + \eta + E) \quad . \tag{58}$$

Therefore the number of time slices needed to determine the Green's function evaluated at $\omega + i\eta$ with an accuracy of ϵ must be

$$\text{Number of Time Slices} = O\left(\frac{\log\left(\frac{2}{\epsilon\eta}\right)}{\eta^2\epsilon}\left(\omega + E + \eta\right)\right) \quad . \tag{59}$$

Many implementations of Hamiltonian simulation on quantum computers do not implement the time evolution operator exactly [35, 38, 191, 190]. To calculate the Green's function with accuracy ϵ, the error in the implementation of the time evolution operator must be $O(\eta\epsilon)$. If the gate cost required to evolve to a time T with accuracy δ is given by $p(T, \delta)$, then the gate cost required to calculate the Green's function is

$$\text{Gate Count} = O\left(\frac{\log\left(\frac{2}{\epsilon\eta}\right)}{\eta^2\epsilon}\left(\omega + E + \eta\right) p\left(\frac{1}{\eta}\log\left(\frac{2}{\eta\epsilon}\right), \eta\epsilon\right)\right) \quad . \tag{60}$$

Finite Volume Errors

$d + 1$ Dimensions With a Mass Gap

When scattering calculations are done inside of a finite volume, first the $L \to \infty$ limit should be taken, followed by the $\eta \to 0$ limit. The order in which this limit is taken matters, as can be seen from a rearrangement of $\Gamma = -2\,\mathrm{Im}(\langle\phi|\,\hat{T}\,|\phi\rangle)$,

$$\Gamma = \sum_n \frac{2\eta}{(M - E_n)^2 + \eta^2}\left|\langle E_n|\,\hat{V}\,|\phi\rangle\right|^2 \tag{61}$$

where $|E_n\rangle$ are eigenstates of the full Hamiltonian, $|\phi\rangle$ is the state describing the unstable particle, $\hat{V}$ is the interaction piece of the Hamiltonian, and M is the mass of the particle decaying. If the $\eta \to 0$ limit is taken first then this discrete sum goes to zero. Alternatively, if $L \to \infty$ first, the energy levels become continuous and

$$\Gamma_\eta = \int \frac{2\eta}{(M - E)^2 + \eta^2}\left|\langle E|\,\hat{V}\,|\phi\rangle\right|^2 \rho(E)dE \quad . \tag{62}$$

If then $\eta \to 0$, the Lorentzian term becomes a delta function and the usual expression for the decay rate is recovered.

$$\Gamma = 2\pi\left|\langle M|\,\hat{V}\,|\phi\rangle\right|^2 \rho(M) \quad . \tag{63}$$

Finite volume errors in a $1 \to N$ particle decay rate will be calculated in the case where all of the decay products are massive. If the interaction energy between the decay products can be ignored (as in the $L \to \infty$ limit), then for a $1 \to N$ decay, the calculated decay rate is

$$\Gamma_{FV,\eta} = \sum_{\vec{n}_1,\vec{n}_2,\cdots\vec{n}_N \in \mathbb{Z}^d} \frac{2\eta}{\left(M - \sum\limits_{k=1}^{N} \sqrt{m_k^2 + \left(\frac{2\pi\vec{n}_k}{L}\right)^2}\right)^2 + \eta^2} \left| \langle \vec{n}_1, \vec{n}_2, \cdots \vec{n}_N | \, \hat{V} \, | \phi \rangle \right|^2 \tag{64}$$

in the $a \to 0$ limit, where M is the mass of the heavy particle decaying and m_k is the mass of the k-th decay product. In this case,

$$\left| \langle \vec{n}_1, \vec{n}_2, \cdots \vec{n}_N | \, \hat{V} \, | \phi \rangle \right|^2 = \int \frac{d^d\vec{x}}{L^d} e^{i\frac{2\pi}{L}\vec{x}\cdot\left(\sum\limits_{k=1}^{N}\vec{n}_k\right)} \frac{|\mathcal{M}|^2}{2M} \prod_{k=1}^{N} \frac{1}{L^d 2\sqrt{m_k^2 + \left(\frac{2\pi\vec{n}_k}{L}\right)^2}} \tag{65}$$

where $\mathcal{M}$ is the scattering amplitude which is generically an analytic function of all the decay products momentum, and $\vec{x}$ is integrated over the region $[\frac{-L}{2}, \frac{L}{2}]^d$. Therefore, the decay rate computed inside a finite volume at finite η is

$$\Gamma_{FV,\eta} = \sum_{\vec{n}_1,\vec{n}_2,\cdots\vec{n}_N \in \mathbb{Z}^d} \int \frac{d^d\vec{x}}{L^d} e^{i\frac{2\pi}{L}\vec{x}\cdot\left(\sum\limits_{k=1}^{N}\vec{n}_k\right)} \frac{2\eta}{\left(M - \sum\limits_{k=1}^{N} \sqrt{m_k^2 + \left(\frac{2\pi\vec{n}_k}{L}\right)^2}\right)^2 + \eta^2} \frac{|\mathcal{M}|^2}{2M} \prod_{k=1}^{N} \frac{1}{L^d 2\sqrt{m_k^2 + \left(\frac{2\pi\vec{n}_k}{L}\right)^2}} \tag{66}$$

If instead, the goal is to calculate a cross section for $2 \to N$ scattering in the center of mass frame, an initial state with two particles each with energy K_i must be prepared. In this case,

$$|\langle \vec{n}_1, \vec{n}_2, \cdots \vec{n}_N | \, V \, | \phi \rangle|^2 = \int \frac{d^d\vec{x}}{L^d} e^{i\frac{2\pi}{L}\vec{x}\cdot\left(\sum\limits_{k=1}^{N}\vec{n}_k\right)} \frac{|\mathcal{M}|^2}{4K_i^2 L^d} \prod_{k=1}^{N} \frac{1}{L^d 2\sqrt{m_k^2 + \left(\frac{2\pi\vec{n}_k}{L}\right)^2}} \quad . \tag{67}$$

The scattering cross section, σ, is given by the decay rate divided by the incident flux which is equal to $\frac{|\vec{v_1} - \vec{v_2}|}{L^d}$, where $\vec{v_1}$ and $\vec{v_2}$ are the velocities of the particles present in the initial state. The extracted value for the cross section at finite volume and η is given by

$$\sigma_{FV,\eta} = \sum_{\vec{n}_1,\vec{n}_2,\cdots\vec{n}_N\in\mathbb{Z}^d} \int \frac{d^d\vec{x}}{L^d} e^{i\frac{2\pi}{L}\vec{x}\cdot\left(\sum\limits_{k=1}^{N}\vec{n}_k\right)} \frac{2\eta}{\left(2K_i - \sum\limits_{k=1}^{N}\sqrt{m_k^2+\left(\frac{2\pi\vec{n}_k}{L}\right)^2}\right)^2+\eta^2}$$

$$\frac{1}{|\vec{v_1}-\vec{v_2}|}\frac{|\mathcal{M}|^2}{4K_i^2}\prod_{k=1}^{N}\frac{1}{L^d 2\sqrt{m_k^2+\left(\frac{2\pi\vec{n}_k}{L}\right)^2}} \quad . \tag{68}$$

This expression takes the same form as Eq. 66 just with M replaced by $2K_i$ and with some slightly different prefactors, so the finite volume error analysis for cross sections can proceed in the same way as the decay rate analysis. To simplify the following discussion, the finite volume errors will be computed only for decay rates.

As $L \to \infty$, the computed decay rate becomes

$$\Gamma_\eta = \prod_{k=1}^{N}\int\frac{d^d\vec{p}_k}{(2\pi)^d 2\sqrt{m_k^2+\vec{p}_k^2}}\int d^d\vec{x} e^{i\vec{x}\cdot\left(\sum\limits_{k=1}^{N}\vec{p}_k\right)} \frac{2\eta}{\left(M-\sum\limits_{k=1}^{N}\sqrt{m_k^2+\vec{p}_k^2}\right)^2+\eta^2}\frac{|\mathcal{M}|^2}{2M} \tag{69}$$

The Poisson resummation formula states that

$$\sum_{\vec{n}\in\mathbb{Z}^d} f(\vec{n}) = \int d^d\vec{x}\ f(\vec{x}) + \sum_{\vec{p}\neq\vec{0}}\int d^d\vec{x}\ e^{2\pi i\vec{p}\cdot\vec{x}} f(\vec{x}) \tag{70}$$

and using Eq. (70), the finite volume error in the calculation of Γ_η is given by

$$\delta\Gamma_{FV} = \Gamma_{FV,\eta} - \Gamma_\eta = -2\,\mathrm{Im}\left(\sum_{n\in\{\{\vec{n_1},,\vec{n_2},\cdots,\vec{n_N}\in\mathbb{Z}^d\}\}\backslash\{\vec{0},\cdots,\vec{0}\}} I_n\right) \tag{71}$$

where

$$I_n = \int\frac{d^d\vec{x}}{L^d}\prod_{k=1}^{N}\int\frac{d^d\vec{p}_k}{(2\pi)^d 2\sqrt{m_k^2+\vec{p}_k^2}} e^{i\vec{p}_k\cdot(\vec{n}_k L+\vec{x})}\frac{1}{M-\sum\limits_{k=1}^{N}\sqrt{m_k^2+\vec{p}_k^2}+i\eta}\frac{|\mathcal{M}|^2}{2M} \quad . \tag{72}$$

Using the fact that

$$\frac{1}{2\sqrt{m^2+\vec{p}^2}} = \int_\gamma \frac{dE}{2\pi i}\frac{1}{(E+i\delta)^2-\vec{p}^2-m^2} \tag{73}$$

where γ is a contour enclosing the lower right quadrant of the complex plane, Eq. 72 can be rewritten as

$$I_n = \int \frac{d^d\vec{x}}{L^d} \prod_{k=1}^{N} \int_\gamma \frac{dE_k}{2\pi i} \int \frac{d^d\vec{p}_k}{(2\pi)^d} \frac{e^{i\vec{p}_k\cdot(\vec{n}_k L+\vec{x})}}{\left(E_k + i\frac{\eta}{N+1}\right)^2 - \vec{p}_k^2 - m_k^2} \frac{1}{M - \sum\limits_{k=1}^{N} E_k + i\frac{\eta}{N+1}} \frac{|\mathcal{M}|^2}{2M} \quad . \tag{74}$$

The component of $\vec{p}_k$ parallel to $\vec{n}_k$ can be integrated over with contour integration yielding

$$I_n = \int \frac{d^d\vec{x}}{L^d} \prod_{k=1}^{N} \int_\gamma \frac{dE_k}{2\pi} \int \frac{d^{d-1}\vec{p}_k^T}{(2\pi)^{d-1}} \frac{e^{i\sqrt{(E_k+i\frac{\eta}{N+1})^2-m_k^2-(\vec{p}_k^T)^2}|n_k L+\hat{n}_k\cdot\vec{x}|+i\vec{p}_k^T\cdot\vec{x}}}{2\sqrt{(E_k + i\frac{\eta}{N+1})^2 - m_k^2 - (\vec{p}_k^T)^2}} \frac{1}{M - \sum\limits_{k=1}^{N} E_k + i\frac{\eta}{N+1}} \frac{|\mathcal{M}|^2}{2M} \tag{75}$$

where p_k^T is a d-dimensional vector integrated over vectors perpendicular to $\vec{n}_k$. The integral over p_k^T can be performed in the large L limit using the saddle point approximation method which states that

$$\int d^d\vec{x} h(\vec{x}) e^{-\lambda f(\vec{x})} = \left(\frac{2\pi}{\lambda}\right)^{\frac{d}{2}} h(\vec{x}_0) e^{-\lambda f(\vec{x}_0)} \frac{1}{\det(\text{Hessian}(f(\vec{x}_0)))^{\frac{1}{2}}} \tag{76}$$

in the $\lambda \to \infty$ limit, where $\vec{x}_0$ is a stationary point of $f(\vec{x})$ in the integration domain. Therefore, in the large L limit Eq. 75 becomes

$$I_n = \int \frac{d^d\vec{x}}{L^d} \prod_{k=1}^{N} \int_\gamma \frac{dE_k}{4\pi} \frac{1}{(2\pi)^{\frac{d-1}{2}}} \frac{\left(\sqrt{(E_k + i\frac{\eta}{N+1})^2 - m_k^2}\right)^{\frac{d-3}{2}}}{|n_k L + \hat{n}_k \cdot \vec{x}|^{\frac{d-1}{2}}} e^{i\sqrt{(E_k+i\frac{\eta}{N+1})^2-m_k^2}|n_k L+\hat{n}_k\cdot\vec{x}|}$$
$$\frac{1}{M - \sum\limits_{k=1}^{N} E_k + i\frac{\eta}{N+1}} \frac{|\mathcal{M}|^2}{2M} \quad . \tag{77}$$

The E_k integrals over γ can be written as a sum over an integral over the positive real axis and the negative imaginary axis. Explicitly writing out these integrals,

$$\begin{aligned} I_n = \sum_{\sigma\subseteq\{1,2,\cdots,N\}} \int \frac{d^d\vec{x}}{L^d} \prod_{k\notin\sigma} \int_0^\infty \frac{dE_k}{4\pi} \frac{1}{(2\pi)^{\frac{d-1}{2}}} \frac{\left(\sqrt{(E_k + i\frac{\eta}{N+1})^2 - m_k^2}\right)^{\frac{d-3}{2}}}{|n_k L + \hat{n}_k \cdot \vec{x}|^{\frac{d-1}{2}}} e^{i\sqrt{(E_k+i\frac{\eta}{N+1})^2-m_k^2}|n_kL+\hat{n}_k\cdot\vec{x}|} \\ \prod_{k\in\sigma} \int_0^\infty \frac{-idE_k}{4\pi} \frac{1}{(2\pi)^{\frac{d-1}{2}}} \frac{\left(\sqrt{(E_k - \frac{\eta}{N+1})^2 + m_k^2}\right)^{\frac{d-3}{2}}}{|n_k L + \hat{n}_k \cdot \vec{x}|^{\frac{d-1}{2}}} e^{-\sqrt{(E_k-\frac{\eta}{N+1})^2+m_k^2}|n_kL+\hat{n}_k\cdot\vec{x}|} \\ \frac{1}{M - \sum\limits_{k\notin\sigma} E_k + i\left(\frac{\eta}{N+1} + \sum\limits_{k\in\sigma} E_k\right)} \frac{|\mathcal{M}|^2}{2M} \end{aligned} \tag{78}$$

For $k \in \sigma$, the E_k integrals can be evaluated using the saddle point approximation again,

$$\begin{aligned} I_n = \sum_{\sigma\subseteq\{1,2,\cdots,N\}} \int \frac{d^d\vec{x}}{L^d} \prod_{k\notin\sigma} \int_0^\infty \frac{dE_k}{4\pi} \frac{1}{(2\pi)^{\frac{d-1}{2}}} \frac{\left(\sqrt{(E_k + i\frac{\eta}{N+1})^2 - m_k^2}\right)^{\frac{d-3}{2}}}{|n_k L + \hat{n}_k \cdot \vec{x}|^{\frac{d-1}{2}}} e^{i\sqrt{(E_k+i\frac{\eta}{N+1})^2-m_k^2}|n_kL+\hat{n}_k\cdot\vec{x}|} \\ \prod_{k\in\sigma} \frac{-i}{4\pi} \frac{1}{(2\pi)^{\frac{d}{2}}} \frac{m_k^{\frac{d-2}{2}}}{|n_k L + \hat{n}_k \cdot \vec{x}|^{\frac{d}{2}}} e^{-m_k|n_kL+\hat{n}_k\cdot\vec{x}|} \\ \frac{1}{M - \sum\limits_{k\notin\sigma} E_k + i\eta\frac{|\sigma|+1}{N+1}} \frac{|\mathcal{M}|^2}{2M} \quad . \end{aligned} \tag{79}$$

The final set of E_k integrals will be performed by making the substitution $E_k = Ef_k$,

$$\begin{aligned} I_n = \sum_{\sigma\subseteq\{1,2,\cdots,N\}} \int \frac{d^d\vec{x}}{L^d} \int_0^\infty dE E^{N-|\sigma|-1} \\ \prod_{k\notin\sigma} \int \frac{df_k}{4\pi} \frac{1}{(2\pi)^{\frac{d-1}{2}}} \frac{\left(\sqrt{(Ef_k + i\frac{\eta}{N+1})^2 - m_k^2}\right)^{\frac{d-3}{2}}}{|n_k L + \hat{n}_k \cdot \vec{x}|^{\frac{d-1}{2}}} e^{i\sqrt{(Ef_k+i\frac{\eta}{N+1})^2-m_k^2}|n_kL+\hat{n}_k\cdot\vec{x}|} \\ \prod_{k\in\sigma} \frac{-i}{4\pi} \frac{1}{(2\pi)^{\frac{d}{2}}} \frac{m_k^{\frac{d-2}{2}}}{|n_k L + \hat{n}_k \cdot \vec{x}|^{\frac{d}{2}}} e^{-m_k|n_kL+\hat{n}_k\cdot\vec{x}|} \frac{1}{M - E + i\eta\frac{|\sigma|+1}{N+1}} \frac{|\mathcal{M}|^2}{2M} \end{aligned} \tag{80}$$

where the f_k are integrated over the region $0 \leq f_k \leq 1$ and $\sum f_k = 1$. The integral over E can be performed by performing a contour integration over a contour enclosing the upper quadrant of the complex plane. Performing this contour integral yields

$$I_n = \sum_{\sigma\subseteq\{1,2,\cdots,N\}} A_n(\sigma) + B_n(\sigma) \tag{81}$$

where

$$A_n(\sigma) = i \int \frac{d^d\vec{x}}{L^d} \prod_{k\notin\sigma} \int \frac{dE_k}{4\pi} \frac{1}{(2\pi)^{\frac{d-1}{2}}} \frac{\left(\sqrt{(E_k + \frac{\eta}{N+1})^2 + m_k^2}\right)^{\frac{d-3}{2}}}{|n_k L + \hat{n}_k \cdot \vec{x}|^{\frac{d-1}{2}}} e^{-\sqrt{(E_k+\frac{\eta}{N+1})^2+m_k^2}|n_k L+\hat{n}_k\cdot\vec{x}|}$$
$$\prod_{k\in\sigma} \frac{-i}{4\pi} \frac{1}{(2\pi)^{\frac{d}{2}}} \frac{m_k^{\frac{d-2}{2}}}{|n_k L + \hat{n}_k \cdot \vec{x}|^{\frac{d}{2}}} e^{-m_k|n_k L+\hat{n}_k\cdot\vec{x}|} \frac{1}{M - \sum_{k\notin\sigma} iE_k + i\eta\frac{|\sigma|+1}{N+1}} \frac{|\mathcal{M}|^2}{2M} \quad (82)$$

comes from integrating along the positive imaginary axis and

$$B_n(\sigma) = -2\pi i \left(M + i\eta\frac{|\sigma|+1}{N+1}\right)^{N-|\sigma|-1} \prod_{k\notin\sigma} \int \frac{df_k}{4\pi} \frac{1}{(2\pi)^{\frac{d-1}{2}}} \frac{\left(\sqrt{\left(\left(M + i\eta\frac{|\sigma|+1}{N+1}\right) f_k + i\frac{\eta}{N+1}\right)^2 - m_k^2}\right)^{\frac{d-3}{2}}}{|n_k L + \hat{n}_k \cdot \vec{x}|^{\frac{d-1}{2}}}$$
$$e^{i\sqrt{\left(\left(M+i\eta\frac{|\sigma|+1}{N+1}\right)f_k+i\frac{\eta}{N+1}\right)^2-m_k^2}|n_k L+\hat{n}_k\cdot\vec{x}|}$$
$$\prod_{k\in\sigma} \frac{-i}{4\pi} \frac{1}{(2\pi)^{\frac{d}{2}}} \frac{m_k^{\frac{d-2}{2}}}{|n_k L + \hat{n}_k \cdot \vec{x}|^{\frac{d}{2}}} e^{-m_k|n_k L+\hat{n}_k\cdot\vec{x}|} \frac{|\mathcal{M}|^2}{2M} \quad (83)$$

comes from the pole located at $E = M + i\eta\frac{|\sigma|+1}{N+1}$ The integrals in Eq. 82 can be evaluated using the saddle point approximation and using the fact that $|n_k L + \hat{n}_k \cdot \vec{x}| \geq (n_k - \frac{1}{2})L$, it follows that $A_n(\sigma) = O(\frac{1}{M^2} \prod_k e^{-m_k(n_k-\frac{1}{2})L})$. Using the bound

$$\mathrm{Im}\left(\sqrt{\left(\left(M + i\eta\frac{|\sigma|+1}{N+1}\right) f_k + i\frac{\eta}{N+1}\right)^2 - m_k^2}\right) \geq \frac{\eta}{N+1} \quad , \quad (84)$$

it can be seen that

$$B_n(\sigma) = O\left(M^{\frac{d-1}{2}N-2} \prod_{k\in\sigma} e^{-m_k(n_k-\frac{1}{2})L} \prod_{k\notin\sigma} e^{-\frac{\eta}{N+1}(n_k-\frac{1}{2})L}\right) \quad . \quad (85)$$

Therefore, in the limit of small η,

$$I_n = O\left(M^{\frac{d-1}{2}N-2} \prod_{k=1}^{N} e^{-\frac{\eta}{N+1}(n_k-\frac{1}{2})L}\right) \quad , \quad (86)$$

and

$$\delta\Gamma_{FV} = O\left(M^{\frac{d-1}{2}N-2} e^{-\frac{\eta}{N+1}\frac{L}{2}}\right) \quad . \quad (87)$$

$d+1$ Dimensions Without a Mass Gap

The bound in the previous section was calculated under the assumption that all decay products are massive, however this is not always the case. In the case where there are massless particles, the decay rate calculated in finite volume is again given by Eq. 64, and the infinite volume limit is given by Eq. 69. $\Gamma_{FV,\eta}$ is a Riemann sum approximation to Γ_η and using the multidimensional bound on the Riemann sum error for integrating over a k dimensional hypercube with side length R

$$\left| \int d^k x \; f(\vec{x}) - \sum_{\vec{n}\in\mathbb{Z}^n\setminus\{|n_i|\Delta x\geq\frac{R}{2}\}} \Delta x^n \; f(\Delta x\vec{n}) \right| \leq \frac{\sum_{i=1}^k \max\left|\frac{\partial f}{\partial x_i}\right|}{2} R^k \; \Delta x \quad , \tag{88}$$

it can be seen that $\delta\Gamma_{FV}$ is $O(\frac{1}{\eta^2 L})$ for small η.

Finite η Errors

The value of Γ calculated for a $1 \to N$ particle decay at finite η in an infinite volume is given by $\Gamma_\eta = -2\,\mathrm{Im}(T(M+i\eta))$ where

$$T(z) = \prod_{k=1}^N \int \frac{d^d\vec{p}_k}{(2\pi)^d 2\sqrt{m_k^2+\vec{p}_k^2}} \frac{(2\pi)^d\delta^d\left(\sum\limits_{k=1}^N \vec{p}_k\right)}{z-\sum\limits_{k=1}^N \sqrt{m_k^2+\vec{p}_k^2}} \frac{|\mathcal{M}|^2}{2M} \tag{89}$$

is the forward scattering amplitude, M is the mass of the particle decaying, m_k is the mass of the k-th decay product and $\mathcal{M}$ is the scattering amplitude for the given decay channel. The decay rate Γ is given by $\lim\limits_{\eta\to 0}\Gamma_\eta$. It will be shown in this section that $\delta\Gamma_\eta = \Gamma_\eta - \Gamma$ is $O(\eta)$ for small η. Changing to spherical coordinates and making the substitution $E_k = \sqrt{p_k^2+m_k^2} - m_k$, Eq. 89 becomes

$$T(z) = \prod_{k=1}^N \int_0^\infty dE_k \int d\Omega_k \frac{(E_k^2+2m_kE_k)^{\frac{d-2}{2}}}{2(2\pi)^d} \frac{(2\pi)^d\delta^d\left(\sum\limits_{k=1}^N \vec{p}_k\right)}{z-\sum\limits_{k=1}^N (E_k+m_k)} \frac{|\mathcal{M}|^2}{2M} \quad . \tag{90}$$

Now making the substitution $E_k = f_k E$, $T(z)$ can be expressed in the form

$$T(z) = \int_0^\infty dE f(E) \frac{1}{z-E-\sum_{k=1}^N m_k} \tag{91}$$

where

$$f(E) = E^{N-1}\prod_{k=1}^{N}\int df_k\int d\Omega_k\frac{(E^2f_k^2+2m_kEf_k)^{\frac{d-2}{2}}}{2(2\pi)^d}(2\pi)^d\delta^d\left(\sum_{k=1}^{N}\vec{p}_k\right)\frac{|\mathcal{M}|^2}{2M} \quad . \tag{92}$$

where the f_k are integrated over the region $0 \leq f_k \leq 1$ and $\sum_{k=1}^{N} f_k = 1$. Note that $f(E)$ has the following properties, $2\pi f(\Delta M) = \Gamma$ where $\Delta M = M - \sum_{k=1}^{N} m_k$, $f(0) = 0$, and $f(E) \geq 0$. $T(z)$ is known to be analytic in the upper half of the complex plane [7] which implies $\lim\limits_{E\to\infty} f(E) = 0$, since otherwise $\mathrm{Re}(T(z))$ would diverge. The decay rate calculated at finite η is

$$\Gamma_\eta = \int_0^\infty dE f(E)\frac{2\eta}{(\Delta M - E)^2+\eta^2} \quad . \tag{93}$$

Integrating Eq. 93 by parts gives

$$\begin{aligned}\Gamma_\eta &= -2\int_0^\infty dE f'(E)\tan^{-1}\left(\frac{E-\Delta M}{\eta}\right)\\ &= 2\int_\infty^{\Delta M} dE f'(E)\cot^{-1}\left(\frac{\eta}{E-\Delta M}\right) - 2\int_0^{\Delta M} dE f'(E)\cot^{-1}\left(\frac{\eta}{E-\Delta M}\right)\end{aligned} \tag{94}$$

To show that $\delta\Gamma_\eta = \Gamma_\eta - \Gamma$ is $O(\eta)$ for small η, it suffices to show that

$$\lim_{\eta\to 0^+}\left(\frac{\delta\Gamma_\eta}{\eta}\right) = \frac{d\Gamma_\eta}{d\eta}\bigg|_{\eta=0^+} \tag{95}$$

is finite. Differentiating under the integral shows that for $\eta > 0$,

$$\frac{d\Gamma_\eta}{d\eta} = 2\int_0^\infty dE f'(E)\frac{E-\Delta M}{\eta^2+(E-\Delta M)^2} = 2\mathcal{P}\int_0^\infty dE f'(E)\frac{E-\Delta M}{\eta^2+(E-\Delta M)^2} \quad . \tag{96}$$

Therefore,

$$\frac{d\Gamma_\eta}{d\eta}\bigg|_{\eta=0^+} = 2\mathcal{P}\int_0^\infty dE f'(E)\frac{1}{E-\Delta M} \quad . \tag{97}$$

The integral in Eq. 97 is finite due to the properties of $f(E)$ discussed above and so $\delta\Gamma_\eta$ is $O(\eta)$ for small η.

Particle Number Truncation

When a quantum field theory describing bosons is simulated on a quantum computer, the degrees of freedom must be truncated. For the bosonic theories considered in this paper, this was done by simulating the theory on a finite lattice with particle numbers truncated. The calculations in the previous section bounded the error in the computed decay rate due to the finite lattice and in this section, the error due to the particle number truncation will be calculated. The scattering T matrix can be computed from the recurrence relation

$$\hat{T} = \hat{V} + \hat{V}\frac{1}{E - \hat{H}_0 + i\eta}\hat{T} \tag{98}$$

where V_0 is the free part of the Hamiltonian describing the motion of free particles and $\hat{V}$ is the interaction part of the Hamiltonian. If $\hat{P}$ projects out the finite particle subspace under consideration, then the T matrix computed with this truncation satisfies the recurrence relation

$$\hat{T}_f = \hat{V} + \hat{V}\frac{\hat{P}}{E - \hat{H}_0 + i\eta}\hat{T}_f \tag{99}$$

Then the difference between the actual T matrix and the T matrix computed with a particle number truncation, $\hat{\delta} = \hat{T} - \hat{T}_f$ satisfies

$$\hat{\delta} = \hat{V}\frac{1}{E - \hat{H}_0 + i\eta}\hat{\delta} + \hat{V}\frac{1 - \hat{P}}{E - \hat{H}_0 + i\eta}\hat{T}_f \quad . \tag{100}$$

This can be rewritten as

$$\hat{\delta} = \hat{T}\frac{1 - \hat{P}}{E - \hat{H}_0 + i\eta}\hat{T}_f \quad . \tag{101}$$

Therefore, if the lightest particle in the theory has mass m and particle number is truncated at n, then the error in $T(E)$ due to the particle number truncation is $O\left(\frac{1}{E-m(n+1)}\right)$.

.5.4 *Error Mitigation*

While the Hadamard test enables the computation of matrix elements, it does not address errors due to imperfect gates on the device itself. To mitigate this error, an extrapolation technique was used [51, 52]. In each circuit, every CNOT was replaced with an odd number, r (for $r = 3, 5, 7$), of CNOT's, and each amplitude was linearly extrapolated to $r = 0$. If there was no noise, these additional CNOT gates would make no change to the outcome of the circuit.

This procedure reduces the error from imperfect implementation of CNOT gates on the quantum computer, but does not mitigate readout errors. To address readout errors, the default calibration matrix method included in the Qiskit Ignis package was used [50].

.5.5 *Hamiltonian Simulation*

The one site calculation done on IBM's quantum computer was done in the momentum basis. While the gate cost of performing time evolution in the momentum basis does not scale to large lattices as well as in the position basis, it is suitable for small calculations

[243]. With a single site,

$$\hat{\phi} = \frac{1}{\sqrt{2M}}(\hat{a}_\phi + \hat{a}_\phi^\dagger)$$

$$\hat{\chi} = \frac{1}{\sqrt{2m}}(\hat{a}_\chi + \hat{a}_\chi^\dagger)$$

$$\hat{\pi}_\phi = -i\sqrt{\frac{M}{2}}(\hat{a}_\phi - \hat{a}_\phi^\dagger)$$

$$\hat{\pi}_\chi = -i\sqrt{\frac{m}{2}}(\hat{a}_\chi - \hat{a}_\chi^\dagger)$$

$$\hat{H} = \frac{1}{2}\hat{\pi}_\phi^2 + \frac{1}{2}\hat{\pi}_\chi^2 + \frac{1}{2}M^2\hat{\phi}^2 + \frac{1}{2}m^2\hat{\chi}^2 + \frac{1}{2}g\ \hat{\phi}\ \hat{\chi}^2 + \frac{1}{4!}\lambda\ \hat{\chi}^4 + \frac{1}{2}\delta M^2\hat{\phi}^2 + \frac{1}{2}\delta m^2\hat{\chi}^2 + \Lambda \quad . \quad (102)$$

where H is the Hamiltonian, M is the mass of the heavy particle, m is the mass of the light particle, Λ is chosen to make the vacuum energy equal to zero, and δM and δm are the differences between the physical and bare masses. This Hamiltonian only couples states with the same parity in the number of χ particles so states with an even number of χ particles are the only ones needed. The mapping of basis states to qubit states is listed in Table 8. Two qubits were used to store the state of the system and one ancilla qubit was used to implement the amplitude estimation algorithm described in Appendix .5.2.

Qubit State	Basis State
00	Vacuum
01	1 ϕ
10	2 χ
11	1 ϕ and 2 χ

Table 8: Basis States

In this truncated basis, the Hamiltonian is

$$
\begin{aligned}
\bar{H} = &\left(\frac{M}{2} + m + \frac{7\lambda}{32m^2} + \frac{\delta M^2}{2M} + \frac{3\delta m^2}{4m} + \Lambda\right) \hat{1} \otimes \hat{1} \\
+ &\left(\left(\frac{\lambda}{8\sqrt{2}m^2} + \frac{\sqrt{2}\delta m^2}{4m}\right)\hat{X} - \left(m + \frac{3\lambda}{16m^2} + \frac{\delta m^2}{2m}\right)\hat{Z}\right) \otimes \hat{1} \\
&+ \hat{1} \otimes \left(\frac{3g}{4m\sqrt{2M}}\hat{X} - \left(\frac{M}{2} + \frac{\delta M^2}{4M}\right)\hat{Z}\right) \\
&+ \left(\frac{g}{4m\sqrt{M}}\hat{X} - \frac{g}{2m\sqrt{2M}}\hat{Z}\right) \otimes \hat{X} \quad .
\end{aligned}
\tag{103}
$$

The amplitude estimation procedure described in the previous section requires implementation of a controlled time evolution operator which was implemented using a Trotter-Suzuki decomposition $e^{-i\sum H_k \delta t} \approx \prod_k e^{-iH_k\delta t}$ where

$$
\begin{aligned}
\hat{H}_0 &= \left(\frac{M}{2} + m + \frac{7\lambda}{32m^2} + \frac{\delta M^2}{2M} + \frac{3\delta m^2}{4m} + \Lambda\right) \hat{1} \otimes \hat{1} \\
\hat{H}_1 &= \left(\left(\frac{\lambda}{8\sqrt{2}m^2} + \frac{\sqrt{2}\delta m^2}{4m}\right)\hat{X} - (m + \frac{3\lambda}{16m^2} + \frac{\delta m^2}{2m})\hat{Z}\right) \otimes \hat{1} \\
\hat{H}_2 &= \hat{1} \otimes \left(\frac{3g}{4m\sqrt{2M}}\hat{X} - \left(\frac{M}{2} + \frac{\delta M^2}{4M}\right)\hat{Z}\right) \\
\hat{H}_3 &= \left(\frac{g}{4m\sqrt{M}}\hat{X} - \frac{g}{2m\sqrt{2M}}\hat{Z}\right) \otimes \hat{X} \quad .
\end{aligned}
\tag{104}
$$

Implementing a controlled version of this time evolution operator requires the ability to perform controlled unitary transformations of the form $e^{ic\hat{1}\otimes\hat{1}}$, $e^{i(c_1\hat{X}+c_2\hat{Z})\otimes\hat{1}}$ and $e^{i(c_1\hat{X}+c_2\hat{Z})\otimes\hat{X}}$. A controlled $e^{ic\hat{1}\otimes\hat{1}}$ can be performed by applying $\begin{pmatrix} 1 & 0 \\ 0 & e^{ic} \end{pmatrix}$ to the control qubit. $c_1\hat{X} + c_2\hat{Z}$ is a 2x2 Hermitian matrix, and the matrix U that maps the computational basis to the eigenbasis of this matrix can be found classically. Using this matrix U, it is trivial to modify the textbook implementation of a controlled $\hat{Z}$ rotation [**?**] to a controlled rotation about $c_1\hat{X}+c_2\hat{Z}$ as shown in Fig. 16. A similar trick can be used to implement the $(c_1\hat{X}+c_2\hat{Z})\otimes\hat{X}$ term as shown in Fig. 17.

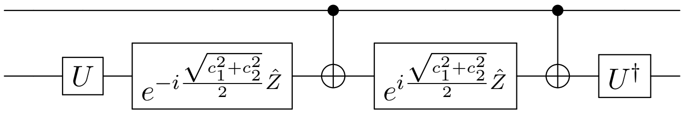

Figure 16: Circuit for $e^{-i(c_1\hat{X}+c_2\hat{Z})}$ controlled on the first qubit

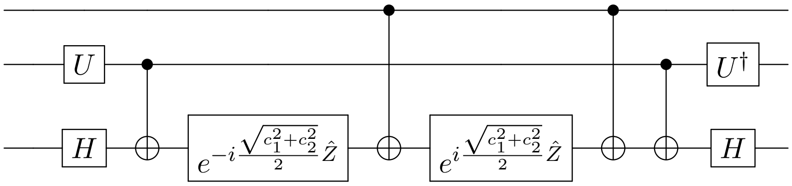

Figure 17: Circuit for $e^{-i(c_1\hat{X}+c_2\hat{Z})\otimes\hat{X}}$ controlled on the first qubit

.5.6 Estimation of Imperfect Gate Implementation Errors

On NISQ era quantum computers, the statistical error and error due to imperfect implementation of logic gates on the quantum processor must both be addressed. In general, the density matrix describing the state of the quantum computer is given by

$$\rho_{exp} = (1-p)\rho_{ideal} + \sum_i E_i \rho_{ideal} E_i^\dagger \tag{105}$$

where ρ_{ideal} is the density matrix describing the state of the quantum computer if every gate was implemented perfectly, p is the probability there is an error anywhere in the circuit, E_i are the Krauss operators describing the errors and $\sum\limits_i E_i E_i^\dagger = p$. The difference between the probability observed on a real quantum computer and an ideal quantum computer is given by

$$Tr\left(-p\ O\ \rho_{ideal} + \sum_i O\ E_i\ \rho_{ideal}\ E_i^\dagger\right) = p\ Tr\left(\frac{O}{p}\ \sum_i E_i\ \rho_{ideal}\ E_i^\dagger - O\ \rho_{ideal}\right) \tag{106}$$

where O is the projection operator corresponding to the measurement result. $\frac{1}{p}\sum\limits_i E_i \rho_{ideal} E_i^\dagger$ is a density matrix because $\sum\limits_i E_i E_i^\dagger = p$. So $Tr\left(\frac{O}{p}\sum\limits_i E_i\ \rho_{ideal}\ E_i^\dagger - O\rho_{ideal}\right)$ is a difference of probabilities which must be bounded above by one. As a result, the difference between the probability of a given measurement observed on a real quantum computer and an ideal quantum computer is bounded above by p. For the calculation on IBM's Ourense quantum processor, p was calculated using the calibration data provided by IBM, and was used as an estimate of the error due to imperfect gate implementation.

.6 Engineering Time Evolution on Rydberg Atoms

.6.1 First Order Trotterization with Rydberg Atoms

In this section, it will be shown how to engineer a Trotterized approximation to an adiabatic turning on of the Heisenberg interaction on an array of Rydberg atoms. Assuming access to a global and staggered driving field, the Hamiltonian describing the time evolution of an array of Rydberg atoms is given by

$$\hat{H}^{\text{Ryd.}}(t) = \sum_{i,j} J_{i,j} \hat{Z}_i \hat{Z}_j + \sum_i \vec{\omega}(t) \cdot \vec{S}_i + \sum_i \frac{h(t)}{2} (-1)^i \hat{Z}_i \quad . \tag{107}$$

It will also be assumed that the strength of the global drive field is limited, $|\vec{\omega}(t)| \leq \Omega$, as is the case in actual Rydberg atom experiments. The approximation to Heisenberg time evolution will be assembled from the following set of global analog gates,

$$\begin{aligned} R_X^{\pm}(\epsilon) &= \exp\left\{ -i\epsilon \sum_{i,j} J_{i,j} \hat{Z}_i \hat{Z}_j \mp \frac{i\pi}{4} \sum_j \hat{X}_j \right\} \quad , \\ R_Y^{\pm}(\epsilon) &= \exp\left\{ -i\epsilon \sum_{i,j} J_{i,j} \hat{Z}_i \hat{Z}_j \mp \frac{i\pi}{4} \sum_j \hat{Y}_j \right\} \quad , \\ R_Z(t,\kappa) &= \exp\left\{ -it \sum_{i,j} J_{i,j} \hat{Z}_i \hat{Z}_j - i\frac{\kappa}{2} \sum_j (-1)^j \hat{Z}_j \right\} \quad . \end{aligned} \tag{108}$$

$R_X^{\pm}(\epsilon)$ and $R_Y^{\pm}(\epsilon)$ correspond to global $\frac{\pi}{2}$-pulses about the x and y axes respectively and can be generated using the global drive field. $R_Z(t,\kappa)$ can be generated by only turning on the staggered driving field. Due to the maximum driving field strength, Ω, the $\frac{\pi}{2}$-pulses, $R_{X,Y}^{\pm}$, need a minimum device time $\epsilon = \frac{\pi}{2\Omega}$ during which the $\hat{Z}_i \hat{Z}_j$ interaction cannot be "turned off." This leads to $\mathcal{O}(\epsilon)$ cross-talk errors that will be studied in further detail in Appendix .6.2. With this analog gate set, a first order Trotter approximation to a generic

XXZ Heisenberg evolution with a staggered single qubit term is given by

$$\begin{aligned} U_{XXZ}(x,z,h) &= \exp\left\{ -i\sum_{i,j} J_{i,j}\left(x\hat{X}_i\hat{X}_j + x\hat{Y}_i\hat{Y}_j + z\hat{Z}_i\hat{Z}_j\right) - ih\sum_i (-1)^i \hat{Z}_i \right\} \\ &\approx \left(\prod_j \hat{Z}_j\right) R_Z(z,h) R_X^+(\epsilon) R_Z(x,0) R_X^+(\epsilon) R_Y^+(\epsilon) R_Z(x,0) R_Y^+(\epsilon) \quad . \end{aligned} \tag{109}$$

Note that since $\sum \hat{Z}_j$ commutes with the XXZ Heisenberg Hamiltonian, the product over $\hat{Z}_j$'s can be neglected when performing adiabatic state preparation as its only contribution is to change the overall phase of the prepared eigenstate. With this pulse sequence, the time evolution generated by the Hamiltonian in Eq. 7.17 can be approximated by

$$\mathcal{T}e^{-i\int_0^T dt\ \hat{H}(t)} \approx \prod_{n=1}^{N} R_Z\left(\frac{T}{N}, \frac{T}{N}h_P\left(1-\frac{n}{N}\right)\right) R_X^+(\epsilon) R_Z\left(\frac{Tn}{N^2}, 0\right) R_X^+(\epsilon) R_Y^+(\epsilon) R_Z\left(\frac{Tn}{N^2}, 0\right) R_Y^+(\epsilon) \quad . \tag{110}$$

.6.2 *Cross-talk Mitigated Trotter Sequence*

The accuracy of the Trotterized approximation to the time-evolution operator can be improved by using shorter Trotter steps or higher order formulas. However, for Trotter step sizes comparable to the $\frac{\pi}{2}$ pulse length, it becomes important to compensate for the $\mathcal{O}(\epsilon)$ contributions to the error. In this section, it will be shown how a modification of the pulse sequence in Appendix .6.1 can be performed to cancel this error at leading order. To leading order in ϵ, the $\frac{\pi}{2}$ rotations are given by

$$\begin{aligned} R_X^{\pm}(\epsilon) &= \exp\left\{\mp\frac{i\pi}{4}\sum_j \hat{X}_j\right\}\exp\left\{-\frac{i}{2\Omega}\sum_{i,j} J_{i,j}\left(\frac{\pi}{2}\left(\hat{Z}_i\hat{Z}_j + \hat{Y}_i\hat{Y}_j\right) \pm \left(\hat{Z}_i\hat{Y}_j + \hat{Y}_i\hat{Z}_j\right)\right)\right\} + \mathcal{O}(\epsilon^2) \quad , \\ R_Y^{\pm}(\epsilon) &= \exp\left\{\mp\frac{i\pi}{4}\sum_j \hat{Y}_j\right\}\exp\left\{-\frac{i}{2\Omega}\sum_{i,j} J_{i,j}\left(\frac{\pi}{2}\left(\hat{Z}_i\hat{Z}_j + \hat{X}_i\hat{X}_j\right) \mp \left(\hat{Z}_i\hat{X}_j + \hat{X}_i\hat{Z}_j\right)\right)\right\} + \mathcal{O}(\epsilon^2) \quad . \end{aligned} \tag{111}$$

Using these expressions, it can be shown that at leading order in ϵ the pulse sequence from Appendix .6.1 is

$$R_Z(z,h)R_X^+(\epsilon)R_Z(x,0)R_X^+(\epsilon)R_Y^+(\epsilon)R_Z(x,0)R_Y^+(\epsilon) \approx \left(\prod_j \hat{Z}_j\right)$$
$$\exp\left\{-i\sum_{i,j} J_{i,j}\left((x+\epsilon)\hat{X}_i\hat{X}_j + (x+\epsilon)\hat{Y}_i\hat{Y}_j + (z+2\epsilon)\hat{Z}_i\hat{Z}_j\right) - ih\sum_i (-1)^i \hat{Z}_i\right\} \quad . \tag{112}$$

By shifting the length of pulses in the sequence from Appendix .6.1, the $\mathcal{O}(\epsilon)$ terms can be absorbed into the time evolution. This motivates the improved adiabatic Trotter sequence given by

$$\begin{aligned}\mathcal{T}e^{-i\int_0^T dt\ \hat{H}(t)} \approx \prod_{n=1}^{N} & R_Z\left(\frac{T}{N} - 2\epsilon, \frac{T}{N}h_P\left(1 - \frac{n}{N}\right)\right) \\ & R_X^+(\epsilon)R_Z\left(\left(\frac{Tn}{N^2} - \epsilon\right)\theta\left(\frac{Tn}{N^2} - \epsilon\right), 0\right)R_X^+(\epsilon) \\ & R_Y^+(\epsilon)R_Z\left(\left(\frac{Tn}{N^2} - \epsilon\right)\theta\left(\frac{Tn}{N^2} - \epsilon\right), 0\right)R_Y^+(\epsilon) \quad ,\end{aligned} \tag{113}$$

where $\theta(x)$ is the Heaviside theta function. When $\frac{T}{N^2}$ is larger than ϵ, this pulse sequence cancels the cross-talk errors at $\mathcal{O}(\epsilon)$. When the Trotter step size is taken to be smaller, this pulse sequence will only cancel the cross-talk errors for the later steps in the sequence.

.7 *Classical Simulation of Rydberg Atoms*

The Hamiltonian describing the evolution of a rectangular array of Rydberg atoms is

$$\begin{aligned}\hat{H}^{\text{Ryd.}}(t) = & \\ & \sum_{x_1,y_1,x_2,y_2} \frac{C_6\ \hat{n}_{x_1,y_1}\hat{n}_{x_2,y_2}}{\left(a_x^2(x_1-x_2)^2 + a_y^2(y_1-y_2)^2\right)^3} \\ & + \sum_{x,y}\Delta_{x,y}(t)\hat{n}_{x,y} + \sum_{x,y}\frac{\Omega_{x,y}(t)}{2}\hat{X}_{x,y} \quad ,\end{aligned} \tag{114}$$

where $\hat{n}_{x,y}$ is the Rydberg occupation number, $\Delta_{x,y}(t)$ is a position dependent detuning term, $\Omega_{x,y}(t)$ is a position dependent driving term, a_x is the horizontal lattice spacing and a_y is the vertical lattice spacing. As presented in the main text, the Rydberg number operator can be identified with a staggered spin operator, i.e., $\hat{n}_{x,y} = \frac{1}{2} + (-1)^{x+y}\hat{S}^z_{x,y}$, such that the state with all atoms in their ground state corresponds to a Néel state. With this identification, the adiabatic spiral introduced in Ref. [349] can be used to prepare a low energy state of the Hamiltonian in Eq. (8.8), by using

$$\begin{aligned}
\Delta_{x,y}(t) &= (-1)^{x+y}\Omega_D + h_P\left(1-\frac{t}{T}\right) \\
&\quad + \frac{1}{2}\sum_{(x_2,y_2)\neq(x,y)} \frac{C_6}{\left(a_x^2(x-x_2)^2 + a_y^2(y-y_2)^2\right)^3} \ , \\
\Omega_{x,y}(t) &= \sqrt{2}\ \Omega_D\left(\frac{t}{T} + \frac{1}{\pi}\sin\left(\pi\frac{t}{T}\right)\right) \quad , \qquad (115)
\end{aligned}$$

where h_P is an initial energy penalty, Ω_D specifies the final strength of the driving field, and T is the total time used for the adiabatic state preparation. For our calculations, we have used $\Omega_D = \frac{1}{\sqrt{2}}25$ MHz, $T = 3.83\mu s$, and h_P is presented in Tables 8.1 and 8.2. Performing a measurement on a Rydberg atom simulator requires the drive field to be turned off, which we simulated by quenching $\Omega_{x,y}(t)$ to zero over a time interval of 0.1 μs. We assumed that a combined time of 0.07 μs was required to turn the detuning on and off.

The adiabatic spiral described here was simulated with tensor networks. This was done with the C++ `iTensor` library with `OpenBLAS` as the backend to parallelize the linear algebra operations [148]. The state of the system was represented with a matrix product state (MPS) tensor network that wound through the 2D lattice. Time evolution was performed by discretizing $\hat{H}^{\text{Ryd.}}(t)$ into 200 time independent steps and evolving with 1-site TDVP [297, 298]. Before each step, the bond dimension was increased using the global Krylov method [299], with a maximum allowed bond dimension of 550.

BIBLIOGRAPHY

[1] Kenneth G. Wilson. Confinement of quarks. *Phys. Rev. D*, 10:2445–2459, Oct 1974.

[2] Richard P Feynman. Simulating physics with computers, 1981. *International Journal of Theoretical Physics*, 21(6/7), 1981.

[3] H David Politzer. Asymptotic freedom: An approach to strong interactions. *Physics Reports*, 14(4):129–180, 1974.

[4] David J. Gross and Frank Wilczek. Ultraviolet behavior of non-abelian gauge theories. *Phys. Rev. Lett.*, 30:1343–1346, Jun 1973.

[5] H. David Politzer. Reliable perturbative results for strong interactions? *Phys. Rev. Lett.*, 30:1346–1349, Jun 1973.

[6] Franz Gross, Eberhard Klempt, Stanley J. Brodsky, Andrzej J. Buras, Volker D. Burkert, Gudrun Heinrich, Karl Jakobs, Curtis A. Meyer, Kostas Orginos, Michael Strickland, Johanna Stachel, Giulia Zanderighi, Nora Brambilla, Peter Braun-Munzinger, Daniel Britzger, Simon Capstick, Tom Cohen, Volker Crede, Martha Constantinou, Christine Davies, Luigi Del Debbio, Achim Denig, Carleton DeTar, Alexandre Deur, Yuri Dokshitzer, Hans Günter Dosch, Jozef Dudek, Monica Dunford, Evgeny Epelbaum, Miguel A. Escobedo, Harald Fritzsch, Kenji Fukushima, Paolo Gambino, Dag Gillberg, Steven Gottlieb, Per Grafstrom, Massimiliano Grazzini, Boris Grube, Alexey Guskov, Toru Iijima, Xiangdong Ji, Frithjof Karsch, Stefan Kluth, John B. Kogut, Frank Krauss, Shunzo Kumano, Derek Leinweber, Heinrich Leutwyler, Hai-Bo Li, Yang Li, Bogdan Malaescu, Chiara Mariotti, Pieter Maris, Simone Marzani, Wally Melnitchouk, Johan Messchendorp, Harvey Meyer, Ryan Edward Mitchell, Chandan Mondal, Frank Nerling, Sebastian Neubert, Marco Pappagallo, Saori Pastore, José R. Peláez, Andrew Puckett, Jianwei Qiu, Klaus Rabbertz, Alberto Ramos, Patrizia Rossi, Anar Rustamov, Andreas Schäfer, Stefan Scherer, Matthias Schindler, Steven Schramm, Mikhail Shifman, Edward Shuryak, Torbjörn Sjöstrand, George Sterman, Iain W. Stewart, Joachim Stroth, Eric Swanson, Guy F. de Téramond, Ulrike Thoma, Antonio Vairo, Danny van Dyk, James Vary, Javier Virto, Marcel Vos, Christian Weiss, Markus Wobisch, Sau Lan Wu, Christopher Young, Feng Yuan, Xingbo Zhao, and Xiaorong Zhou. 50 years of quantum chromodynamics, 2022.

[7] Matthew D Schwartz. *Quantum field theory and the standard model*. Cambridge university press, 2014.

[8] Sz. Borsanyi, S. Durr, Z. Fodor, C. Hoelbling, S. D. Katz, S. Krieg, L. Lellouch, T. Lippert, A. Portelli, K. K. Szabo, and B. C. Toth. Ab initio calculation of the neutron-proton mass difference. *Science*, 347(6229):1452–1455, 2015.

[9] F. Karsch, K. Redlich, and A. Tawfik. Hadron resonance mass spectrum and lattice QCD thermodynamics. *The European Physical Journal C*, 29(4):549–556, aug 2003.

[10] Brian C. Tiburzi, Michael L. Wagman, Frank Winter, Emmanuel Chang, Zohreh Davoudi, William Detmold, Kostas Orginos, Martin J. Savage, and Phiala E. Shanahan. Double-β decay matrix elements from lattice quantum chromodynamics. *Phys. Rev. D*, 96:054505, Sep 2017.

[11] Silas R. Beane, Emmanuel Chang, William Detmold, Kostas Orginos, Assumpta Parreño, Martin J. Savage, and Brian C. Tiburzi. Ab initio calculation of the $np \to d\gamma$ radiative capture process. *Phys. Rev. Lett.*, 115:132001, Sep 2015.

[12] Martin J. Savage, Phiala E. Shanahan, Brian C. Tiburzi, Michael L. Wagman, Frank Winter, Silas R. Beane, Emmanuel Chang, Zohreh Davoudi, William Detmold, and Kostas Orginos. Proton-proton fusion and tritium β decay from lattice quantum chromodynamics. *Phys. Rev. Lett.*, 119:062002, Aug 2017.

[13] John Kogut and Leonard Susskind. Hamiltonian formulation of wilson's lattice gauge theories. *Phys. Rev. D*, 11:395–408, Jan 1975.

[14] Tim Byrnes and Yoshihisa Yamamoto. Simulating lattice gauge theories on a quantum computer. *Phys. Rev. A*, 73:022328, Feb 2006.

[15] Stephen P. Jordan, Keith S. M. Lee, and John Preskill. Quantum algorithms for quantum field theories. *Science*, 336(6085):1130–1133, 2012.

[16] Stephen P. Jordan, Keith S. M. Lee, and John Preskill. Quantum computation of scattering in scalar quantum field theories. *Quantum Info. Comput.*, 14(11–12):1014–1080, sep 2014.

[17] Mari Carmen Bañuls, Krzysztof Cichy, J. Ignacio Cirac, Karl Jansen, and Stefan Kühn. Efficient basis formulation for $(1+1)$-dimensional su(2) lattice gauge theory: Spectral calculations with matrix product states. *Phys. Rev. X*, 7:041046, Nov 2017.

[18] Natalie Klco, Martin J. Savage, and Jesse R. Stryker. Su(2) non-abelian gauge field theory in one dimension on digital quantum computers. *Phys. Rev. D*, 101:074512, Apr 2020.

[19] D. Horn. Finite matrix models with continuous local gauge invariance. *Physics Letters B*, 100(2):149 – 151, 1981.

[20] Peter Orland and Daniel Rohrlich. Lattice gauge magnets: Local isospin from spin. *Nuclear Physics B*, 338(3):647 – 672, 1990.

[21] S Chandrasekharan and U.-J Wiese. Quantum link models: A discrete approach to gauge theories. *Nuclear Physics B*, 492(1):455–471, 1997.

[22] R. Brower, S. Chandrasekharan, S. Riederer, and U.-J. Wiese. D-theory: field quantization by dimensional reduction of discrete variables. *Nuclear Physics B*, 693(1):149–175, 2004.

[23] U.-J. Wiese. D-theory: A quest for nature's regularization. *Nuclear Physics B - Proceedings Supplements*, 153(1):336–347, 2006. Proceedings of the Workshop on Computational Hadron Physics.

[24] Hersh Singh and Shailesh Chandrasekharan. Qubit regularization of the $o(3)$ sigma model. *Phys. Rev. D*, 100:054505, Sep 2019.

[25] Tanmoy Bhattacharya, Alexander J. Buser, Shailesh Chandrasekharan, Rajan Gupta, and Hersh Singh. Qubit regularization of asymptotic freedom. *Phys. Rev. Lett.*, 126:172001, Apr 2021.

[26] Alexandru Macridin, Panagiotis Spentzouris, James Amundson, and Roni Harnik. Digital quantum computation of fermion-boson interacting systems. *Phys. Rev. A*, 98:042312, Oct 2018.

[27] Natalie Klco and Martin J. Savage. Digitization of scalar fields for quantum computing. *Phys. Rev. A*, 99:052335, May 2019.

[28] K. Symanzik. Continuum Limit and Improved Action in Lattice Theories. 1. Principles and phi**4 Theory. *Nucl. Phys. B*, 226:187–204, 1983.

[29] N. Klco, E. F. Dumitrescu, A. J. McCaskey, T. D. Morris, R. C. Pooser, M. Sanz, E. Solano, P. Lougovski, and M. J. Savage. Quantum-classical computation of schwinger model dynamics using quantum computers. *Phys. Rev. A*, 98:032331, Sep 2018.

[30] Hsuan-Hao Lu, Natalie Klco, Joseph M. Lukens, Titus D. Morris, Aaina Bansal, Andreas Ekström, Gaute Hagen, Thomas Papenbrock, Andrew M. Weiner, Martin J. Savage, and Pavel Lougovski. Simulations of subatomic many-body physics on a quantum frequency processor. *Phys. Rev. A*, 100:012320, Jul 2019.

[31] Alexandru Macridin, Panagiotis Spentzouris, James Amundson, and Roni Harnik. Electron-Phonon Systems on a Universal Quantum Computer. *Phys. Rev. Lett.*, 121(11):110504, 2018.

[32] Zohreh Davoudi, Indrakshi Raychowdhury, and Andrew Shaw. Search for efficient formulations for hamiltonian simulation of non-abelian lattice gauge theories. *Phys. Rev. D*, 104:074505, Oct 2021.

[33] Jan F. Haase, Luca Dellantonio, Alessio Celi, Danny Paulson, Angus Kan, Karl Jansen, and Christine A. Muschik. A resource efficient approach for quantum and classical simulations of gauge theories in particle physics. *Quantum*, 5:393, feb 2021.

[34] N.E. Ligterink, N.R. Walet, and R.F. Bishop. A many body treatment of Hamiltonian lattice gauge theory. *Nucl. Phys. A*, 663:983–986, 2000.

[35] Dominic W. Berry, Andrew M. Childs, Richard Cleve, Robin Kothari, and Rolando D. Somma. Simulating hamiltonian dynamics with a truncated taylor series. *Phys. Rev. Lett.*, 114:090502, Mar 2015.

[36] Guang Hao Low and Isaac L. Chuang. Optimal hamiltonian simulation by quantum signal processing. *Phys. Rev. Lett.*, 118:010501, Jan 2017.

[37] Guang Hao Low and Nathan Wiebe. Hamiltonian simulation in the interaction picture. *arXiv preprint arXiv:1805.00675*, 2018.

[38] Guang Hao Low and Isaac L. Chuang. Hamiltonian simulation by qubitization. *Quantum*, 3:163, jul 2019.

[39] Andrew M. Childs and Yuan Su. Nearly optimal lattice simulation by product formulas. *Phys. Rev. Lett.*, 123:050503, Aug 2019.

[40] H. Trotter. On the product of semi-groups of operators. 1959.

[41] Masuo Suzuki. General theory of fractal path integrals with applications to many-body theories and statistical physics. *Journal of Mathematical Physics*, 32(2):400–407, 1991.

[42] Seth Lloyd. Universal quantum simulators. *Science*, 273(5278):1073–1078, 1996.

[43] Christof Zalka. Simulating quantum systems on a quantum computer. *Proceedings of the Royal Society of London. Series A: Mathematical, Physical and Engineering Sciences*, 454(1969):313–322, jan 1998.

[44] Dominic W. Berry, Graeme Ahokas, Richard Cleve, and Barry C. Sanders. Efficient quantum algorithms for simulating sparse hamiltonians. *Communications in Mathematical Physics*, 270(2):359–371, dec 2006.

[45] Yuan Su, Hsin-Yuan Huang, and Earl T. Campbell. Nearly tight trotterization of interacting electrons. *Quantum*, 5:495, jul 2021.

[46] Nathan Wiebe, Dominic W Berry, Peter Høyer, and Barry C Sanders. Simulating quantum dynamics on a quantum computer. *Journal of Physics A: Mathematical and Theoretical*, 44(44):445308, oct 2011.

[47] G. Vidal and C. M. Dawson. Universal quantum circuit for two-qubit transformations with three controlled-not gates. *Phys. Rev. A*, 69:010301, Jan 2004.

[48] Mark W. Coffey, Ron Deiotte, and Torey Semi. Comment on "universal quantum circuit for two-qubit transformations with three controlled-not gates" and "recognizing small-circuit structure in two-qubit operators". *Phys. Rev. A*, 77:066301, Jun 2008.

[49] IBM Quantum Experience. ibmq_athens v1.3.4. `https://quantum-computing.ibm.com`, 2020.

[50] Gadi Aleksandrowicz, Thomas Alexander, Panagiotis Barkoutsos, Luciano Bello, Yael Ben-Haim, David Bucher, F Jose Cabrera-Hernández, Jorge Carballo-Franquis, Adrian Chen, Chun-Fu Chen, et al. Qiskit: An open-source framework for quantum computing. *Accessed on: Mar*, 16, 2019.

[51] Ying Li and Simon C. Benjamin. Efficient variational quantum simulator incorporating active error minimization. *Phys. Rev. X*, 7:021050, Jun 2017.

[52] Kristan Temme, Sergey Bravyi, and Jay M. Gambetta. Error mitigation for short-depth quantum circuits. *Phys. Rev. Lett.*, 119:180509, Nov 2017.

[53] IBM Quantum Experience. ibmq_measurement error. `https://qiskit.org/documentation/tutorials/noise/3_measurement_error_mitigation.html`, 2020.

[54] Michael A. Nielsen and Isaac L. Chuang. *Quantum Computation and Quantum Information: 10th Anniversary Edition.* Cambridge University Press, New York, NY, USA, 10th edition, 2011.

[55] Frank Gray. Pulse code communication, Mar 1953.

[56] Craig Gidney. Using quantum gates instead of ancilla bits.

[57] Adriano Barenco, Charles H. Bennett, Richard Cleve, David P. DiVincenzo, Norman Margolus, Peter Shor, Tycho Sleator, John Smolin, and Harald Weinfurter. Elementary gates for quantum computation. *Phys. Rev. A*, 52:3457, 1995.

[58] E.F. Dumitrescu, A.J. McCaskey, G. Hagen, G.R. Jansen, T.D. Morris, T. Papenbrock, R.C. Pooser, D.J. Dean, and P. Lougovski. Cloud Quantum Computing of an Atomic Nucleus. *Phys. Rev. Lett.*, 120(21):210501, 2018.

[59] Gerard 't Hooft. A Planar Diagram Theory for Strong Interactions. *Nucl. Phys. B*, 72:461, 1974.

[60] Edward Witten. Baryons in the 1/n Expansion. *Nucl. Phys. B*, 160:57–115, 1979.

[61] Sidney Coleman. The clebschâgordan series for su(3). *Journal of Mathematical Physics*, 5(9):1343–1344, 1964.

[62] D. J. Rowe, B. C. Sanders, and H. de Guise. Representations of the weyl group and wigner functions for su(3). *Journal of Mathematical Physics*, 40(7):3604–3615, Jul 1999.

[63] Alex Clesio Nunes Martins, Mark W. Suffak, and Hubert de Guise. $SU(3)$ Clebsch–Gordan coefficients and some of their symmetries. *J. Phys. A*, 53(2):025201, 2020. https://github.com/marksuffak/SU-3-CG-Code.

[64] M. Luscher and P. Weisz. On-Shell Improved Lattice Gauge Theories. *Commun. Math. Phys.*, 97:59, 1985. [Erratum: Commun.Math.Phys. 98, 433 (1985)].

[65] G.Peter Lepage and Paul B. Mackenzie. On the viability of lattice perturbation theory. *Phys. Rev. D*, 48:2250–2264, 1993.

[66] Mark G. Alford, W. Dimm, G.P. Lepage, G. Hockney, and P.B. Mackenzie. Lattice QCD on small computers. *Phys. Lett. B*, 361:87–94, 1995.

[67] David B. Kaplan and Jesse R. Stryker. Gauss's law, duality, and the hamiltonian formulation of u(1) lattice gauge theory. *Phys. Rev. D*, 102:094515, Nov 2020.

[68] D. Horn and D. Schreiber. t expansion of lowest hadron masses. *Phys. Rev. D*, 47:2081–2088, Mar 1993.

[69] D. Schreiber. t-expansion calculation of $\langle\overline{\psi}\psi\rangle$ in the chiral limit. *Phys. Rev. D*, 49:4751–4754, May 1994.

[70] Torsten V. Zache, Daniel González-Cuadra, and Peter Zoller. Quantum and classical spin network algorithms for q-deformed kogut-susskind gauge theories, 2023.

[71] Tomoya Hayata and Yoshimasa Hidaka. Breaking new ground for quantum and classical simulations of SU(3) yang-mills theory, 2023.

[72] Rolando D. Somma. Quantum simulations of one dimensional quantum systems, 2016.

[73] Daniel C. Hackett, Kiel Howe, Ciaran Hughes, William Jay, Ethan T. Neil, and James N. Simone. Digitizing Gauge Fields: Lattice Monte Carlo Results for Future Quantum Computers. *Phys. Rev.*, A99(6):062341, 2019.

[74] Natalie Klco and Martin J. Savage. Systematically Localizable Operators for Quantum Simulations of Quantum Field Theories. *Phys. Rev. A*, 102(1):012619, 2020.

[75] Natalie Klco and Martin J. Savage. Fixed-point quantum circuits for quantum field theories. *Phys. Rev. A*, 102:052422, Nov 2020.

[76] Eric T. Holland, Kyle A. Wendt, Konstantinos Kravvaris, Xian Wu, W. Erich Ormand, Jonathan L DuBois, Sofia Quaglioni, and Francesco Pederiva. Optimal Control for the Quantum Simulation of Nuclear Dynamics. *Phys. Rev. A*, 101(6):062307, 2020.

[77] A. Romanenko, R. Pilipenko, S. Zorzetti, D. Frolov, M. Awida, S. Belomestnykh, S. Posen, and A. Grassellino. Three-dimensional superconducting resonators at $T < 20$ mK with the photon lifetime up to $\tau = 2$ seconds. *Phys. Rev. Applied*, 13:034032, 2020.

[78] Pei Jiang Low, Brendan M. White, Andrew A. Cox, Matthew L. Day, and Crystal Senko. Practical trapped-ion protocols for universal qudit-based quantum computing. *Phys. Rev. Research*, 2:033128, Jul 2020.

[79] Ramesh Anishetty and T. P. Sreeraj. Mass gap in the weak coupling limit of $(2+1)$-dimensional su(2) lattice gauge theory. *Phys. Rev. D*, 97:074511, Apr 2018.

[80] Indrakshi Raychowdhury. Low energy spectrum of su (2) lattice gauge theory: An alternate proposal via loop formulation. *arXiv preprint arXiv:1804.01304*, 2018.

[81] Indrakshi Raychowdhury and Jesse R. Stryker. Loop, string, and hadron dynamics in su(2) hamiltonian lattice gauge theories. *Phys. Rev. D*, 101:114502, Jun 2020.

[82] Mario Motta, Chong Sun, Adrian T. K. Tan, Matthew J. O'Rourke, Erika Ye, Austin J. Minnich, Fernando G. S. L. Brandão, and Garnet Kin-Lic Chan. Determining eigenstates and thermal states on a quantum computer using quantum imaginary time evolution. *Nature Physics*, 16(2):205–210, nov 2019.

[83] John Preskill. Simulating quantum field theory with a quantum computer, 2018.

[84] Stephen Jordan, Keith Lee, and John Preskill. Quantum algorithms for fermionic quantum field theories. 2014-04-28 2014.

[85] Alberto Peruzzo, Jarrod McClean, Peter Shadbolt, Man-Hong Yung, Xiao-Qi Zhou, Peter J. Love, Alán Aspuru-Guzik, and Jeremy L. O'Brien. A variational eigenvalue solver on a photonic quantum processor. *Nature Communications*, 5(1), jul 2014.

[86] Jarrod R McClean, Jonathan Romero, Ryan Babbush, and Alán Aspuru-Guzik. The theory of variational hybrid quantum-classical algorithms. *New Journal of Physics*, 18(2):023023, feb 2016.

[87] P. J. J. O'Malley, R. Babbush, I. D. Kivlichan, J. Romero, J. R. McClean, R. Barends, J. Kelly, P. Roushan, A. Tranter, N. Ding, B. Campbell, Y. Chen, Z. Chen, B. Chiaro, A. Dunsworth, A. G. Fowler, E. Jeffrey, E. Lucero, A. Megrant, J. Y. Mutus, M. Neeley, C. Neill, C. Quintana, D. Sank, A. Vainsencher, J. Wenner, T. C. White, P. V. Coveney, P. J. Love, H. Neven, A. Aspuru-Guzik, and J. M. Martinis. Scalable quantum simulation of molecular energies. *Phys. Rev. X*, 6:031007, Jul 2016.

[88] Abhinav Kandala, Antonio Mezzacapo, Kristan Temme, Maika Takita, Markus Brink, Jerry M. Chow, and Jay M. Gambetta. Hardware-efficient variational quantum eigensolver for small molecules and quantum magnets. *Nature*, 549(7671):242–246, sep 2017.

[89] Cornelius Hempel, Christine Maier, Jonathan Romero, Jarrod McClean, Thomas Monz, Heng Shen, Petar Jurcevic, Ben P. Lanyon, Peter Love, Ryan Babbush, Alán Aspuru-Guzik, Rainer Blatt, and Christian F. Roos. Quantum chemistry calculations on a trapped-ion quantum simulator. *Phys. Rev. X*, 8:031022, Jul 2018.

[90] J. I. Colless, V. V. Ramasesh, D. Dahlen, M. S. Blok, M. E. Kimchi-Schwartz, J. R. McClean, J. Carter, W. A. de Jong, and I. Siddiqi. Computation of molecular spectra on a quantum processor with an error-resilient algorithm. *Phys. Rev. X*, 8:011021, Feb 2018.

[91] Scott E. Smart and David A. Mazziotti. Quantum-classical hybrid algorithm using an error-mitigating n-representability condition to compute the mott metal-insulator transition. *Phys. Rev. A*, 100:022517, Aug 2019.

[92] R. Sagastizabal, X. Bonet-Monroig, M. Singh, M. A. Rol, C. C. Bultink, X. Fu, C. H. Price, V. P. Ostroukh, N. Muthusubramanian, A. Bruno, M. Beekman, N. Haider, T. E. O'Brien, and L. DiCarlo. Experimental error mitigation via symmetry verification in a variational quantum eigensolver. *Phys. Rev. A*, 100:010302, Jul 2019.

[93] Harper R. Grimsley, Sophia E. Economou, Edwin Barnes, and Nicholas J. Mayhall. An adaptive variational algorithm for exact molecular simulations on a quantum computer. *Nature Communications*, 10(1), jul 2019.

[94] Abhinav Kandala, Kristan Temme, Antonio D Córcoles, Antonio Mezzacapo, Jerry M Chow, and Jay M Gambetta. Error mitigation extends the computational reach of a noisy quantum processor. *Nature*, 567(7749):491–495, 2019.

[95] Google AI Quantum, Collaborators*†, Frank Arute, Kunal Arya, Ryan Babbush, Dave Bacon, Joseph C. Bardin, Rami Barends, Sergio Boixo, Michael Broughton, Bob B. Buckley, David A. Buell, Brian Burkett, Nicholas Bushnell, Yu Chen, Zijun Chen, Benjamin Chiaro, Roberto Collins, William Courtney, Sean Demura, Andrew Dunsworth, Edward Farhi, Austin Fowler, Brooks Foxen, Craig Gidney, Marissa Giustina, Rob Graff, Steve Habegger, Matthew P. Harrigan, Alan Ho, Sabrina Hong, Trent Huang, William J. Huggins, Lev Ioffe, Sergei V. Isakov, Evan Jeffrey, Zhang Jiang, Cody Jones, Dvir Kafri, Kostyantyn Kechedzhi, Julian Kelly, Seon Kim, Paul V. Klimov, Alexander Korotkov, Fedor Kostritsa, David Landhuis, Pavel Laptev, Mike Lindmark, Erik Lucero, Orion Martin, John M. Martinis, Jarrod R. McClean, Matt McEwen, Anthony Megrant, Xiao Mi, Masoud Mohseni, Wojciech Mruczkiewicz, Josh Mutus, Ofer Naaman, Matthew Neeley, Charles Neill, Hartmut Neven, Murphy Yuezhen Niu, Thomas E. O'Brien, Eric Ostby, Andre Petukhov, Harald Putterman, Chris Quintana, Pedram Roushan, Nicholas C. Rubin, Daniel Sank, Kevin J. Satzinger, Vadim Smelyanskiy, Doug Strain, Kevin J. Sung, Marco Szalay, Tyler Y. Takeshita, Amit Vainsencher, Theodore White, Nathan Wiebe, Z. Jamie Yao, Ping Yeh, and Adam Zalcman. Hartree-fock on a superconducting qubit quantum computer. *Science*, 369(6507):1084–1089, 2020.

[96] Gaurav Gyawali and Michael J. Lawler. Adaptive variational preparation of the fermi-hubbard eigenstates. *Phys. Rev. A*, 105:012413, Jan 2022.

[97] Naoki Yamamoto. On the natural gradient for variational quantum eigensolver, 2019.

[98] James Stokes, Josh Izaac, Nathan Killoran, and Giuseppe Carleo. Quantum natural gradient. *Quantum*, 4:269, may 2020.

[99] Jinglei Zhang, Ryan Ferguson, Stefan Kühn, Jan F. Haase, C. M. Wilson, Karl Jansen, and Christine A. Muschik. Simulating gauge theories with variational quantum eigensolvers in superconducting microwave cavities, 2021.

[100] R. R. Ferguson, L. Dellantonio, A. Al Balushi, K. Jansen, W. Dür, and C. A. Muschik. Measurement-based variational quantum eigensolver. *Phys. Rev. Lett.*, 126:220501, Jun 2021.

[101] C. Kokail, C. Maier, R. van Bijnen, T. Brydges, M. K. Joshi, P. Jurcevic, C. A. Muschik, P. Silvi, R. Blatt, C. F. Roos, and P. Zoller. Self-verifying variational quantum simulation of lattice models. *Nature*, 569(7756):355–360, may 2019.

[102] Yasar Y. Atas, Jinglei Zhang, Randy Lewis, Amin Jahanpour, Jan F. Haase, and Christine A. Muschik. SU(2) hadrons on a quantum computer via a variational approach. *Nature Communications*, 12(1), nov 2021.

[103] Cornelius Lanczos. An iteration method for the solution of the eigenvalue problem of linear differential and integral operators. 1950.

[104] Torsten V. Zache, Maarten Van Damme, Jad C. Halimeh, Philipp Hauke, and Debasish Banerjee. Toward the continuum limit of a $(1+1)$D quantum link schwinger model. *Phys. Rev. D*, 106:L091502, Nov 2022.

[105] Yu Tong, Victor V. Albert, Jarrod R. McClean, John Preskill, and Yuan Su. Provably accurate simulation of gauge theories and bosonic systems. *Quantum*, 6:816, sep 2022.

[106] Peter I. Frazier. A tutorial on bayesian optimization, 2018.

[107] Tuyen Trung Truong. Convergence to minima for the continuous version of backtracking gradient descent, 2019.

[108] Shiro Tamiya and Hayata Yamasaki. Stochastic gradient line bayesian optimization for efficient noise-robust optimization of parameterized quantum circuits. *npj Quantum Information*, 8(1), jul 2022.

[109] Maria Schuld, Alex Bocharov, Krysta M. Svore, and Nathan Wiebe. Circuit-centric quantum classifiers. *Phys. Rev. A*, 101:032308, Mar 2020.

[110] IBM Quantum Experience. ibmq_manila v1.0.18. `https://quantum-computing.ibm.com`, 2021.

[111] Anthony Ciavarella, Natalie Klco, and Martin J. Savage. Trailhead for quantum simulation of su(3) yang-mills lattice gauge theory in the local multiplet basis. *Phys. Rev. D*, 103:094501, May 2021.

[112] Martin Lüscher. Solution of the dirac equation in lattice qcd using a domain decomposition method. *Computer Physics Communications*, 156(3):209–220, 2004.

[113] Andreas Frommer, Karsten Kahl, Stefan Krieg, Björn Leder, and Matthias Rottmann. Adaptive aggregation-based domain decomposition multigrid for the lattice wilson–dirac operator. *SIAM journal on scientific computing*, 36(4):A1581–A1608, 2014.

[114] Simon Heybrock, Balint Joo, Dhiraj D. Kalamkar, Mikhail Smelyanskiy, Karthikeyan Vaidyanathan, Tilo Wettig, and Pradeep Dubey. Lattice QCD with domain decomposition on intel&amp#x00ae xeon phi co-processors. In *SC14: International Conference for High Performance Computing, Networking, Storage and Analysis*. IEEE, nov 2014.

[115] Steven R. White. Density matrix formulation for quantum renormalization groups. *Phys. Rev. Lett.*, 69:2863–2866, Nov 1992.

[116] Bá rbara Andrade, Zohreh Davoudi, Tobias Graß, Mohammad Hafezi, Guido Pagano, and Alireza Seif. Engineering an effective three-spin hamiltonian in trapped-ion systems for applications in quantum simulation. *Quantum Science and Technology*, 7(3):034001, apr 2022.

[117] Angus Kan and Yunseong Nam. Lattice quantum chromodynamics and electrodynamics on a universal quantum computer, 2022.

[118] Alexander F. Shaw, Pavel Lougovski, Jesse R. Stryker, and Nathan Wiebe. Quantum algorithms for simulating the lattice schwinger model. *Quantum*, 4:306, aug 2020.

[119] Jesse R. Stryker. Shearing approach to gauge invariant trotterization, 2021.

[120] Zohreh Davoudi, Alexander F. Shaw, and Jesse R. Stryker. General quantum algorithms for hamiltonian simulation with applications to a non-abelian lattice gauge theory, 2023.

[121] Henry Lamm, Scott Lawrence, and Yukari Yamauchi. General methods for digital quantum simulation of gauge theories. *Phys. Rev. D*, 100:034518, Aug 2019.

[122] Simon V. Mathis, Guglielmo Mazzola, and Ivano Tavernelli. Toward scalable simulations of lattice gauge theories on quantum computers. *Phys. Rev. D*, 102:094501, Nov 2020.

[123] Torsten V. Zache, Daniel González-Cuadra, and Peter Zoller. Fermion-qudit quantum processors for simulating lattice gauge theories with matter, 2023.

[124] Daniel González-Cuadra, Torsten V. Zache, Jose Carrasco, Barbara Kraus, and Peter Zoller. Hardware efficient quantum simulation of non-abelian gauge theories with qudits on rydberg platforms. *Phys. Rev. Lett.*, 129:160501, Oct 2022.

[125] Erez Zohar and Michele Burrello. Formulation of lattice gauge theories for quantum simulations. *Phys. Rev. D*, 91:054506, Mar 2015.

[126] Erez Zohar, J. Ignacio Cirac, and Benni Reznik. Cold-atom quantum simulator for su(2) yang-mills lattice gauge theory. *Phys. Rev. Lett.*, 110:125304, Mar 2013.

[127] Erez Zohar, Alessandro Farace, Benni Reznik, and J. Ignacio Cirac. Digital lattice gauge theories. *Phys. Rev. A*, 95:023604, Feb 2017.

[128] Julian Bender, Erez Zohar, Alessandro Farace, and J Ignacio Cirac. Digital quantum simulation of lattice gauge theories in three spatial dimensions. *New Journal of Physics*, 20(9):093001, sep 2018.

[129] Erez Zohar. Quantum simulation of lattice gauge theories in more than one space dimension—requirements, challenges and methods. *Philosophical Transactions of the Royal Society A: Mathematical, Physical and Engineering Sciences*, 380(2216), dec 2021.

[130] Erez Zohar, J. Ignacio Cirac, and Benni Reznik. Quantum simulations of gauge theories with ultracold atoms: Local gauge invariance from angular-momentum conservation. *Phys. Rev. A*, 88:023617, Aug 2013.

[131] Erez Zohar, J Ignacio Cirac, and Benni Reznik. Quantum simulations of lattice gauge theories using ultracold atoms in optical lattices. *Reports on Progress in Physics*, 79(1):014401, dec 2015.

[132] Roland C. Farrell, Ivan A. Chernyshev, Sarah J. M. Powell, Nikita A. Zemlevskiy, Marc Illa, and Martin J. Savage. Preparations for quantum simulations of quantum chromodynamics in $1 + 1$ dimensions. i. axial gauge. *Phys. Rev. D*, 107:054512, Mar 2023.

[133] Yasar Y. Atas, Jan F. Haase, Jinglei Zhang, Victor Wei, Sieglinde M. L. Pfaendler, Randy Lewis, and Christine A. Muschik. Real-time evolution of SU(3) hadrons on a quantum computer, 7 2022.

[134] Roland C. Farrell, Ivan A. Chernyshev, Sarah J. M. Powell, Nikita A. Zemlevskiy, Marc Illa, and Martin J. Savage. Preparations for quantum simulations of quantum chromodynamics in $1 + 1$ dimensions. ii. single-baryon β-decay in real time. *Phys. Rev. D*, 107:054513, Mar 2023.

[135] Jonathan Wurtz, Pieter W. Claeys, and Anatoli Polkovnikov. Variational schrieffer-wolff transformations for quantum many-body dynamics. *Phys. Rev. B*, 101:014302, Jan 2020.

[136] Caroline E. P. Robin and Martin J. Savage. Quantum simulations in effective model spaces (i): Hamiltonian learning-vqe using digital quantum computers and application to the lipkin-meshkov-glick model, 2023.

[137] J. R. Schrieffer and P. A. Wolff. Relation between the anderson and kondo hamiltonians. *Phys. Rev.*, 149:491–492, Sep 1966.

[138] Sergey Bravyi, David P. DiVincenzo, and Daniel Loss. Schrieffer–wolff transformation for quantum many-body systems. *Annals of Physics*, 326(10):2793–2826, 2011.

[139] Ian Affleck, Z. Zou, T. Hsu, and P. W. Anderson. Su(2) gauge symmetry of the large-u limit of the hubbard model. *Phys. Rev. B*, 38:745–747, Jul 1988.

[140] F. Berruto, G. Grignani, G.W. Semenoff, and P. Sodano. On the correspondence between the strongly coupled 2-flavor lattice schwinger model and the heisenberg antiferromagnetic chain. *Annals of Physics*, 275(2):254–296, 1999.

[141] F. Berruto, G. Grignani, G. W. Semenoff, and P. Sodano. Quantum spin-1/2 antiferromagnetic chains and strongly coupled multiflavor schwinger models, 1999.

[142] Stanisław D. Głazek and Kenneth G. Wilson. Renormalization of hamiltonians. *Phys. Rev. D*, 48:5863–5872, Dec 1993.

[143] Franz J. Wegner. Flow equations for hamiltonians. *Nuclear Physics B - Proceedings Supplements*, 90:141–146, 2000. non-perturbative QCD and hadron phenomenology.

[144] Sergio Szpigel and Robert J. Perry. The similarity renormalization group, 2000.

[145] S. K. Bogner, R. J. Furnstahl, and R. J. Perry. Similarity renormalization group for nucleon-nucleon interactions. *Phys. Rev. C*, 75:061001, Jun 2007.

[146] H. Hergert, S.K. Bogner, T.D. Morris, A. Schwenk, and K. Tsukiyama. The in-medium similarity renormalization group: A novel ab initio method for nuclei. *Physics Reports*, 621:165–222, 2016. Memorial Volume in Honor of Gerald E. Brown.

[147] Matthew Fishman, Steven R. White, and E. Miles Stoudenmire. Codebase release 0.3 for ITensor. *SciPost Phys. Codebases*, pages 4–r0.3, 2022.

[148] Matthew Fishman, Steven R. White, and E. Miles Stoudenmire. The ITensor Software Library for Tensor Network Calculations. *SciPost Phys. Codebases*, page 4, 2022.

[149] Steven R. White. Density-matrix algorithms for quantum renormalization groups. *Phys. Rev. B*, 48:10345–10356, Oct 1993.

[150] F. Verstraete, J. J. García-Ripoll, and J. I. Cirac. Matrix product density operators: Simulation of finite-temperature and dissipative systems. *Phys. Rev. Lett.*, 93:207204, Nov 2004.

[151] IBM Quantum Experience. ibm_perth v1.2.7. `https://quantum-computing.ibm.com`, 2023.

[152] Miroslav Urbanek, Benjamin Nachman, Vincent R. Pascuzzi, Andre He, Christian W. Bauer, and Wibe A. de Jong. Mitigating depolarizing noise on quantum computers with noise-estimation circuits. *Phys. Rev. Lett.*, 127:270502, Dec 2021.

[153] Sarmed A Rahman, Randy Lewis, Emanuele Mendicelli, and Sarah Powell. Real time evolution and a traveling excitation in su(2) pure gauge theory on a quantum computer, 2022.

[154] Sarmed A Rahman, Randy Lewis, Emanuele Mendicelli, and Sarah Powell. Self-mitigating trotter circuits for su(2) lattice gauge theory on a quantum computer. *Phys. Rev. D*, 106:074502, Oct 2022.

[155] Holger Bech Nielsen and Masao Ninomiya. No-go theorum for regularizing chiral fermions. Technical report, Science Research Council, 1981.

[156] Holger Bech Nielsen and Masao Ninomiya. Absence of neutrinos on a lattice:(ii). intuitive topological proof. *Nuclear Physics B*, 193(1):173–194, 1981.

[157] Stephen R. Sharpe. Rooted staggered fermions: good, bad or ugly?, 2006.

[158] Maarten Golterman. Qcd with rooted staggered fermions, 2008.

[159] A. Bazavov, C. Bernard, J. Komijani, C. DeTar, L. Levkova, W. Freeman, Steven Gottlieb, Ran Zhou, U. M. Heller, J. E. Hetrick, J. Laiho, J. Osborn, R. L. Sugar, D. Toussaint, and R. S. Van de Water. Lattice qcd ensembles with four flavors of highly improved staggered quarks. *Phys. Rev. D*, 87:054505, Mar 2013.

[160] E. Follana, Q. Mason, C. Davies, K. Hornbostel, G. P. Lepage, J. Shigemitsu, H. Trottier, and K. Wong. Highly improved staggered quarks on the lattice with applications to charm physics. *Phys. Rev. D*, 75:054502, Mar 2007.

[161] Anna Hasenfratz and Roland Hoffmann. Validity of the rooted staggered determinant in the continuum limit. *Phys. Rev. D*, 74:014511, Jul 2006.

[162] T. Banks, S. Raby, L. Susskind, J. Kogut, D. R. T. Jones, P. N. Scharbach, and D. K. Sinclair. Strong-coupling calculations of the hadron spectrum of quantum chromodynamics. *Phys. Rev. D*, 15:1111–1127, Feb 1977.

[163] D.R.T. Jones, R.D. Kenway, J.B. Kogut, and D.K. Sinclair. Lattice gauge theory calculations using an improved strong-coupling expansion and matrix padé approximants. *Nuclear Physics B*, 158(1):102–122, 1979.

[164] David B. Kaplan and Martin J. Savage. The spin-flavor dependence of nuclear forces from large-n qcd. *Physics Letters B*, 365(1):244–251, 1996.

[165] Silas R. Beane, David B. Kaplan, Natalie Klco, and Martin J. Savage. Entanglement suppression and emergent symmetries of strong interactions. *Phys. Rev. Lett.*, 122:102001, Mar 2019.

[166] Silas R. Beane, Roland C. Farrell, and Mira Varma. Entanglement minimization in hadronic scattering with pions. *Int. J. Mod. Phys. A*, 36(30):2150205, 2021.

[167] Silas R. Beane and Roland C. Farrell. Geometry and entanglement in the scattering matrix. *Annals Phys.*, 433:168581, 2021.

[168] Dong Bai and Zhongzhou Ren. Entanglement generation in few-nucleon scattering. *Phys. Rev. C*, 106(6):064005, 2022.

[169] Qiaofeng Liu, Ian Low, and Thomas Mehen. Minimal entanglement and emergent symmetries in low-energy QCD. *Phys. Rev. C*, 107(2):025204, 2023.

[170] Ian Low and Thomas Mehen. Symmetry from entanglement suppression. *Phys. Rev. D*, 104(7):074014, 2021.

[171] David B. Kaplan, Martin J. Savage, and Mark B. Wise. A new expansion for nucleon-nucleon interactions. *Physics Letters B*, 424(3):390–396, 1998.

[172] David B. Kaplan, Martin J. Savage, and Mark B. Wise. Two-nucleon systems from effective field theory. *Nuclear Physics B*, 534(1):329–355, 1998.

[173] U. van Kolck. Effective field theory of short-range forces. *Nuclear Physics A*, 645(2):273–302, 1999.

[174] Michael C Birse, Judith A McGovern, and Keith G Richardson. A renormalisation-group treatment of two-body scattering. *Physics Letters B*, 464(3):169–176, 1999.

[175] Kanav Setia, Sergey Bravyi, Antonio Mezzacapo, and James D. Whitfield. Superfast encodings for fermionic quantum simulation. *Physical Review Research*, 1(3), oct 2019.

[176] M D Segall, Philip J D Lindan, M J Probert, C J Pickard, P J Hasnip, S J Clark, and M C Payne. First-principles simulation: ideas, illustrations and the castep code. *Journal of Physics: Condensed Matter*, 14(11):2717, mar 2002.

[177] Gabriele Giuliani and Giovanni Vignale. *Quantum theory of the electron liquid*. Cambridge university press, 2005.

[178] Ryan Babbush, Nathan Wiebe, Jarrod McClean, James McClain, Hartmut Neven, and Garnet Kin-Lic Chan. Low-depth quantum simulation of materials. *Phys. Rev. X*, 8:011044, Mar 2018.

[179] Tobias Hagge. Optimal fermionic swap networks for hubbard models, 2022.

[180] Kenneth G Wilson. New phenomena in subnuclear physics, 1977.

[181] Sidney D. Drell, Marvin Weinstein, and Shimon Yankielowicz. Strong-coupling field theories. ii. fermions and gauge fields on a lattice. *Phys. Rev. D*, 14:1627–1647, Sep 1976.

[182] Paolo Nason. The lattice schwinger model with slac fermions. *Nuclear Physics B*, 260(2):269–284, 1985.

[183] David B. Kaplan. A method for simulating chiral fermions on the lattice. *Physics Letters B*, 288(3):342–347, 1992.

[184] Herbert Neuberger. Exactly massless quarks on the lattice. *Physics Letters B*, 417(1):141–144, 1998.

[185] M Falcioni, ML Paciello, G Parisi, and B Taglienti. More about exactly massless quarks on the lattice. *Phys. Lett.*, 427(3-4):353, 1998.

[186] Luuk H. Karsten and Jan Smit. The vacuum polarization with slac lattice fermions. *Physics Letters B*, 85(1):100–102, 1979.

[187] Jeffrey M. Rabin. Perturbation theory for undoubled lattice fermions. *Phys. Rev. D*, 24:3218–3236, Dec 1981.

[188] Frank Verstraete, J. Ignacio Cirac, and José I. Latorre. Quantum circuits for strongly correlated quantum systems. *Phys. Rev. A*, 79:032316, Mar 2009.

[189] Masuo Suzuki. Fractal decomposition of exponential operators with applications to many-body theories and monte carlo simulations. *Physics Letters A*, 146(6):319–323, 1990.

[190] Andrew M. Childs, Yuan Su, Minh C. Tran, Nathan Wiebe, and Shuchen Zhu. Theory of trotter error with commutator scaling. *Phys. Rev. X*, 11:011020, Feb 2021.

[191] Andrew M. Childs, Dmitri Maslov, Yunseong Nam, Neil J. Ross, and Yuan Su. Toward the first quantum simulation with quantum speedup. *Proceedings of the National Academy of Sciences*, 115(38):9456–9461, sep 2018.

[192] Matthew B Hastings, Dave Wecker, Bela Bauer, and Matthias Troyer. Improving quantum algorithms for quantum chemistry. *Quantum Information & Computation*, 15(1-2):1–21, 2015.

[193] Jacob T. Seeley, Martin J. Richard, and Peter J. Love. The Bravyi-Kitaev transformation for quantum computation of electronic structure. *The Journal of Chemical Physics*, 137(22), 12 2012. 224109.

[194] James D. Whitfield, Jacob Biamonte, and Alá n Aspuru-Guzik. Simulation of electronic structure hamiltonians using quantum computers. *Molecular Physics*, 109(5):735–750, mar 2011.

[195] Bryan O'Gorman, William J. Huggins, Eleanor G. Rieffel, and K. Birgitta Whaley. Generalized swap networks for near-term quantum computing, 2019.

[196] Ryan Babbush, Jarrod McClean, Dave Wecker, Alán Aspuru-Guzik, and Nathan Wiebe. Chemical basis of trotter-suzuki errors in quantum chemistry simulation. *Phys. Rev. A*, 91:022311, Feb 2015.

[197] Roger A Horn and Charles R Johnson. *Matrix analysis*. Cambridge university press, 2012.

[198] Vadym Kliuchnikov, Dmitri Maslov, and Michele Mosca. Fast and efficient exact synthesis of single qubit unitaries generated by clifford and t gates. *arXiv:1206.5236*, 2012.

[199] Neil J Ross and Peter Selinger. Optimal ancilla-free clifford+ t approximation of z-rotations. *arXiv:1403.2975*, 2014.

[200] Dominic W. Berry, Craig Gidney, Mario Motta, Jarrod R. McClean, and Ryan Babbush. Qubitization of arbitrary basis quantum chemistry leveraging sparsity and low rank factorization. *Quantum*, 3:208, dec 2019.

[201] Joonho Lee, Dominic W. Berry, Craig Gidney, William J. Huggins, Jarrod R. McClean, Nathan Wiebe, and Ryan Babbush. Even more efficient quantum computations of chemistry through tensor hypercontraction. *PRX Quantum*, 2:030305, Jul 2021.

[202] B. L. Higgins, D. W. Berry, S. D. Bartlett, H. M. Wiseman, and G. J. Pryde. Entanglement-free heisenberg-limited phase estimation. *Nature*, 450(7168):393–396, nov 2007.

[203] AA Abrikosov, LD Landau, and IM Khalatnikov. On the elimination of infinities in quantum electrodynamics. In *Dokl. Akad. Nauk SSSR*, volume 95, page 497, 1954.

[204] David J.E. Callaway. Triviality pursuit: Can elementary scalar particles exist? *Physics Reports*, 167(5):241–320, 1988.

[205] M. Göckeler, R. Horsley, E. Laermann, P. Rakow, G. Schierholz, R. Sommer, and U.-J. Wiese. The continuum limit of qed. renormalization group analysis and the question of triviality. *Physics Letters B*, 251(4):567–574, 1990.

[206] D. Djukanovic, J. Gegelia, and Ulf-G. Meißner. Triviality of quantum electrodynamics revisited*. *Communications in Theoretical Physics*, 69(3):263, mar 2018.

[207] Andrew M. Childs. On the relationship between continuous- and discrete-time quantum walk. *Communications in Mathematical Physics*, 294(2):581–603, oct 2009.

[208] András Gilyén, Yuan Su, Guang Hao Low, and Nathan Wiebe. Quantum singular value transformation and beyond: exponential improvements for quantum matrix arithmetics. In *Proceedings of the 51st Annual ACM SIGACT Symposium on Theory of Computing*. ACM, jun 2019.

[209] Ryan Babbush, Craig Gidney, Dominic W. Berry, Nathan Wiebe, Jarrod McClean, Alexandru Paler, Austin Fowler, and Hartmut Neven. Encoding electronic spectra in quantum circuits with linear t complexity. *Phys. Rev. X*, 8:041015, Oct 2018.

[210] Vera von Burg, Guang Hao Low, Thomas Häner, Damian S. Steiger, Markus Reiher, Martin Roetteler, and Matthias Troyer. Quantum computing enhanced computational catalysis. *Phys. Rev. Res.*, 3:033055, Jul 2021.

[211] David Poulin, Alexei Kitaev, Damian S. Steiger, Matthew B. Hastings, and Matthias Troyer. Quantum algorithm for spectral measurement with a lower gate count. *Phys. Rev. Lett.*, 121:010501, Jul 2018.

[212] Ian D. Kivlichan, Jarrod McClean, Nathan Wiebe, Craig Gidney, Alán Aspuru-Guzik, Garnet Kin-Lic Chan, and Ryan Babbush. Quantum simulation of electronic structure with linear depth and connectivity. *Phys. Rev. Lett.*, 120:110501, Mar 2018.

[213] Markus Reiher, Nathan Wiebe, Krysta M. Svore, Dave Wecker, and Matthias Troyer. Elucidating reaction mechanisms on quantum computers. *Proceedings of the National Academy of Sciences*, 114(29):7555–7560, jul 2017.

[214] Aaron Meurer, Christopher P Smith, Mateusz Paprocki, Ondřej Čertík, Sergey B Kirpichev, Matthew Rocklin, AMiT Kumar, Sergiu Ivanov, Jason K Moore, Sartaj Singh, et al. Sympy: symbolic computing in python. *PeerJ Computer Science*, 3:e103, 2017.

[215] Ryan Babbush, Craig Gidney, Dominic W Berry, Nathan Wiebe, Jarrod McClean, Alexandru Paler, Austin Fowler, and Hartmut Neven. Encoding electronic spectra in quantum circuits with linear t complexity. *Physical Review X*, 8(4):041015, 2018.

[216] Alex Bocharov, Martin Roetteler, and Krysta M Svore. Efficient synthesis of universal repeat-until-success quantum circuits. *Physical Review Letters*, 114(8):080502, 2015.

[217] Markus Reiher and Alexander Wolf. *Relativistic quantum chemistry: the fundamental theory of molecular science*. John Wiley & Sons, 2014.

[218] Peter G Szalay, Thomas Muller, Gergely Gidofalvi, Hans Lischka, and Ron Shepard. Multiconfiguration self-consistent field and multireference configuration interaction methods and applications. *Chemical reviews*, 112(1):108–181, 2012.

[219] Hans Lischka, Ron Shepard, Franklin B Brown, and Isaiah Shavitt. New implementation of the graphical unitary group approach for multireference direct configuration interaction calculations. *International Journal of Quantum Chemistry*, 20(S15):91–100, 1981.

[220] Hang Hu, Andrew J Jenkins, Hongbin Liu, Joseph M Kasper, Michael J Frisch, and Xiaosong Li. Relativistic two-component multireference configuration interaction method with tunable correlation space. *Journal of Chemical Theory and Computation*, 16(5):2975–2984, 2020.

[221] Zhang Jiang, Kevin J. Sung, Kostyantyn Kechedzhi, Vadim N. Smelyanskiy, and Sergio Boixo. Quantum algorithms to simulate many-body physics of correlated fermions. *Phys. Rev. Appl.*, 9:044036, Apr 2018.

[222] Martin Lüscher. Volume dependence of the energy spectrum in massive quantum field theories: I. stable particle states. *Communications in Mathematical Physics*, 104:177–206, 1986.

[223] Martin Lüscher. Volume dependence of the energy spectrum in massive quantum field theories: Ii. scattering states. *Communications in Mathematical Physics*, 105:153–188, 1986.

[224] Silas R. Beane, Thomas C. Luu, Kostas Orginos, Assumpta Parreño, Martin J. Savage, Aaron Torok, and André Walker-Loud. K^+K^+ scattering length from lattice qcd. *Phys. Rev. D*, 77:094507, May 2008.

[225] Luka Leskovec, Constantia Alexandrou, Stefan Meinel, John W. Negele, Srijit Paul, Marcus Petschlies, Andrew Pochinsky, Gumaro Rendon, and Sergey Syritsyn. A lattice qcd study of the ρ resonance, 2018.

[226] R. Molina, D. Guo, A. Alexandru, M. Mai, and M. Döring. Sigma resonance parameters from a $n_f = 2$ lattice qcd simulation, 2018.

[227] C. H. Mak and David Chandler. Solving the sign problem in quantum monte carlo dynamics. *Phys. Rev. A*, 41:5709–5712, May 1990.

[228] J. H. Samson. Classical effective hamiltonians, wigner functions, and the sign problem. *Phys. Rev. B*, 51:223–233, Jan 1995.

[229] Sara Bergkvist, Patrik Henelius, and Anders Rosengren. Reduction of the sign problem using the meron-cluster approach. *Phys. Rev. E*, 68:016122, Jul 2003.

[230] Kenji Fukushima and Yoshimasa Hidaka. Model study of the sign problem in the mean-field approximation. *Phys. Rev. D*, 75:036002, Feb 2007.

[231] Gert Aarts. Can stochastic quantization evade the sign problem? the relativistic bose gas at finite chemical potential. *Phys. Rev. Lett.*, 102:131601, Apr 2009.

[232] Michael G. Endres, David B. Kaplan, Jong-Wan Lee, and Amy N. Nicholson. Noise, sign problems, and statistics. *Phys. Rev. Lett.*, 107:201601, Nov 2011.

[233] Mithat Ünsal. Theta dependence, sign problems, and topological interference. *Phys. Rev. D*, 86:105012, Nov 2012.

[234] Jeff Greensite, Joyce C. Myers, and K. Splittorff. Qcd sign problem as a total derivative. *Phys. Rev. D*, 88:031502, Aug 2013.

[235] Ali Hamed Moosavian, James R. Garrison, and Stephen P. Jordan. Site-by-site quantum state preparation algorithm for preparing vacua of fermionic lattice field theories, 2019.

[236] A. Roggero. Spectral-density estimation with the gaussian integral transform. *Phys. Rev. A*, 102:022409, Aug 2020.

[237] Patrick Rall. Quantum algorithms for estimating physical quantities using block encodings. *Phys. Rev. A*, 102:022408, Aug 2020.

[238] Rolando D Somma. Quantum eigenvalue estimation via time series analysis. *New Journal of Physics*, 21(12):123025, dec 2019.

[239] Y. Chen, A. Alexandru, S. J. Dong, T. Draper, I. Horváth, F. X. Lee, K. F. Liu, N. Mathur, C. Morningstar, M. Peardon, S. Tamhankar, B. L. Young, and J. B. Zhang. Glueball spectrum and matrix elements on anisotropic lattices. *Phys. Rev. D*, 73:014516, Jan 2006.

[240] Natalie Klco and Martin J. Savage. Minimally entangled state preparation of localized wave functions on quantum computers. *Phys. Rev. A*, 102:012612, Jul 2020.

[241] WINFRIED LEIDEMANN. The lorentz integral transform (lit) method. *International Journal of Modern Physics E*, 18(05n06):1339–1358, Jun 2009.

[242] Jonathan Richard Shewchuk et al. An introduction to the conjugate gradient method without the agonizing pain, 1994.

[243] Kübra Yeter-Aydeniz, Eugene F. Dumitrescu, Alex J. McCaskey, Ryan S. Bennink, Raphael C. Pooser, and George Siopsis. Scalar quantum field theories as a benchmark for near-term quantum computers. *Phys. Rev. A*, 99:032306, Mar 2019.

[244] Emanuel Knill, Gerardo Ortiz, and Rolando D. Somma. Optimal quantum measurements of expectation values of observables. *Phys. Rev. A*, 75:012328, Jan 2007.

[245] Sepehr Ebadi, Tout T. Wang, Harry Levine, Alexander Keesling, Giulia Semeghini, Ahmed Omran, Dolev Bluvstein, Rhine Samajdar, Hannes Pichler, Wen Wei Ho, Soonwon Choi, Subir Sachdev, Markus Greiner, Vladan Vuletić, and Mikhail D. Lukin. Quantum phases of matter on a 256-atom programmable quantum simulator. *Nature*, 595(7866):227–232, jul 2021.

[246] G. Semeghini, H. Levine, A. Keesling, S. Ebadi, T. T. Wang, D. Bluvstein, R. Verresen, H. Pichler, M. Kalinowski, R. Samajdar, A. Omran, S. Sachdev, A. Vishwanath, M. Greiner, V. Vuletić, and M. D. Lukin. Probing topological spin liquids on a programmable quantum simulator. *Science*, 374(6572):1242–1247, 2021.

[247] Dolev Bluvstein, Harry Levine, Giulia Semeghini, Tout T. Wang, Sepehr Ebadi, Marcin Kalinowski, Alexander Keesling, Nishad Maskara, Hannes Pichler, Markus Greiner, Vladan Vuletić, and Mikhail D. Lukin. A quantum processor based on coherent transport of entangled atom arrays. *Nature*, 604(7906):451–456, apr 2022.

[248] D. Porras and J. I. Cirac. Effective quantum spin systems with trapped ions. *Phys. Rev. Lett.*, 92:207901, May 2004.

[249] Tobias Graß and Maciej Lewenstein. Trapped-ion quantum simulation of tunable-range heisenberg chains. *EPJ Quantum Technology*, 1(1):8, 2014.

[250] C. Monroe, W. C. Campbell, L.-M. Duan, Z.-X. Gong, A. V. Gorshkov, P. W. Hess, R. Islam, K. Kim, N. M. Linke, G. Pagano, P. Richerme, C. Senko, and N. Y. Yao. Programmable quantum simulations of spin systems with trapped ions. *Rev. Mod. Phys.*, 93:025001, Apr 2021.

[251] Mark W Johnson, Mohammad HS Amin, Suzanne Gildert, Trevor Lanting, Firas Hamze, Neil Dickson, Richard Harris, Andrew J Berkley, Jan Johansson, Paul Bunyk, et al. Quantum annealing with manufactured spins. *Nature*, 473(7346):194–198, 2011.

[252] R. Harris, M. W. Johnson, T. Lanting, A. J. Berkley, J. Johansson, P. Bunyk, E. Tolkacheva, E. Ladizinsky, N. Ladizinsky, T. Oh, F. Cioata, I. Perminov, P. Spear, C. Enderud, C. Rich, S. Uchaikin, M. C. Thom, E. M. Chapple, J. Wang, B. Wilson, M. H. S. Amin, N. Dickson, K. Karimi, B. Macready, C. J. S. Truncik, and G. Rose. Experimental investigation of an eight-qubit unit cell in a superconducting optimization processor. *Phys. Rev. B*, 82:024511, Jul 2010.

[253] Andrew J. A. James, Robert M. Konik, and Neil J. Robinson. Nonthermal states arising from confinement in one and two dimensions. *Phys. Rev. Lett.*, 122:130603, Apr 2019.

[254] Marton Kormos, Mario Collura, Gabor Takács, and Pasquale Calabrese. Real-time confinement following a quantum quench to a non-integrable model. *Nature Physics*, 13(3):246–249, nov 2016.

[255] Philip Richerme, Zhe-Xuan Gong, Aaron Lee, Crystal Senko, Jacob Smith, Michael Foss-Feig, Spyridon Michalakis, Alexey V. Gorshkov, and Christopher Monroe. Non-local propagation of correlations in quantum systems with long-range interactions. *Nature*, 511(7508):198–201, jul 2014.

[256] P. Jurcevic, B. P. Lanyon, P. Hauke, C. Hempel, P. Zoller, R. Blatt, and C. F. Roos. Quasiparticle engineering and entanglement propagation in a quantum many-body system. *Nature*, 511(7508):202–205, jul 2014.

[257] Michael L. Wall, Arghavan Safavi-Naini, and Ana Maria Rey. Boson-mediated quantum spin simulators in transverse fields: xy model and spin-boson entanglement. *Phys. Rev. A*, 95:013602, Jan 2017.

[258] Thomas G. Kiely and J. K. Freericks. Relationship between the transverse-field ising model and the xy model via the rotating-wave approximation. *Phys. Rev. A*, 97:023611, Feb 2018.

[259] Neil J. Robinson, Isaac Pérez Castillo, and Edgar Guzmán-González. Quantum quench in a driven ising chain. *Phys. Rev. B*, 103:L140407, Apr 2021.

[260] M. Heyl, A. Polkovnikov, and S. Kehrein. Dynamical quantum phase transitions in the transverse-field ising model. *Phys. Rev. Lett.*, 110:135704, Mar 2013.

[261] C. Karrasch and D. Schuricht. Dynamical phase transitions after quenches in nonintegrable models. *Phys. Rev. B*, 87:195104, May 2013.

[262] T. Rakovszky, M. Mestyán, M. Collura, M. Kormos, and G. Takács. Hamiltonian truncation approach to quenches in the ising field theory. *Nuclear Physics B*, 911:805–845, 2016.

[263] Markus Heyl. Scaling and universality at dynamical quantum phase transitions. *Phys. Rev. Lett.*, 115:140602, Oct 2015.

[264] Tomohiro Hashizume, Ian P. McCulloch, and Jad C. Halimeh. Dynamical phase transitions in the two-dimensional transverse-field ising model. *Phys. Rev. Res.*, 4:013250, Mar 2022.

[265] Atsuki Yoshinaga, Hideaki Hakoshima, Takashi Imoto, Yuichiro Matsuzaki, and Ryusuke Hamazaki. Emergence of hilbert space fragmentation in ising models with a weak transverse field. *Phys. Rev. Lett.*, 129:090602, Aug 2022.

[266] Oliver Hart and Rahul Nandkishore. Hilbert space shattering and dynamical freezing in the quantum ising model. *Phys. Rev. B*, 106:214426, Dec 2022.

[267] Lukas M. Sieberer, Tobias Olsacher, Andreas Elben, Markus Heyl, Philipp Hauke, Fritz Haake, and Peter Zoller. Digital quantum simulation, trotter errors, and quantum chaos of the kicked top. *npj Quantum Information*, 5(1), sep 2019.

[268] Markus Heyl, Philipp Hauke, and Peter Zoller. Quantum localization bounds trotter errors in digital quantum simulation. *Science Advances*, 5(4), apr 2019.

[269] Jeremy T. Young, Sean R. Muleady, Michael A. Perlin, Adam M. Kaufman, and Ana Maria Rey. Enhancing spin squeezing using soft-core interactions. *Phys. Rev. Res.*, 5:L012033, Mar 2023.

[270] Neil J. Robinson, Andrew J. A. James, and Robert M. Konik. Signatures of rare states and thermalization in a theory with confinement. *Phys. Rev. B*, 99:195108, May 2019.

[271] Toby S. Cubitt, Ashley Montanaro, and Stephen Piddock. Universal quantum hamiltonians. *Proceedings of the National Academy of Sciences*, 115(38):9497–9502, aug 2018.

[272] N. Goldman and J. Dalibard. Periodically driven quantum systems: Effective hamiltonians and engineered gauge fields. *Phys. Rev. X*, 4:031027, Aug 2014.

[273] Jon H. Shirley. Solution of the schrödinger equation with a hamiltonian periodic in time. *Phys. Rev.*, 138:B979–B987, May 1965.

[274] L. M. K. Vandersypen and I. L. Chuang. Nmr techniques for quantum control and computation. *Rev. Mod. Phys.*, 76:1037–1069, Jan 2005.

[275] Y. Salathé, M. Mondal, M. Oppliger, J. Heinsoo, P. Kurpiers, A. Potočnik, A. Mezzacapo, U. Las Heras, L. Lamata, E. Solano, S. Filipp, and A. Wallraff. Digital quantum simulation of spin models with circuit quantum electrodynamics. *Phys. Rev. X*, 5:021027, Jun 2015.

[276] M. Aidelsburger, M. Atala, M. Lohse, J. T. Barreiro, B. Paredes, and I. Bloch. Realization of the hofstadter hamiltonian with ultracold atoms in optical lattices. *Phys. Rev. Lett.*, 111:185301, Oct 2013.

[277] N. Fläschner, B. S. Rem, M. Tarnowski, D. Vogel, D.-S. Lühmann, K. Sengstock, and C. Weitenberg. Experimental reconstruction of the berry curvature in a floquet bloch band. *Science*, 352(6289):1091–1094, 2016.

[278] F. Meinert, M. J. Mark, K. Lauber, A. J. Daley, and H.-C. Nägerl. Floquet engineering of correlated tunneling in the bose-hubbard model with ultracold atoms. *Phys. Rev. Lett.*, 116:205301, May 2016.

[279] Christian Schweizer, Fabian Grusdt, Moritz Berngruber, Luca Barbiero, Eugene Demler, Nathan Goldman, Immanuel Bloch, and Monika Aidelsburger. Floquet approach to z2 lattice gauge theories with ultracold atoms in optical lattices. *Nature Physics*, 15(11):1168–1173, sep 2019.

[280] André Eckardt. Colloquium: Atomic quantum gases in periodically driven optical lattices. *Rev. Mod. Phys.*, 89:011004, Mar 2017.

[281] Karen Wintersperger, Christoph Braun, F. Nur Ünal, André Eckardt, Marco Di Liberto, Nathan Goldman, Immanuel Bloch, and Monika Aidelsburger. Realization of an anomalous floquet topological system with ultracold atoms. *Nature Physics*, 16(10):1058–1063, jun 2020.

[282] P. Scholl, H. J. Williams, G. Bornet, F. Wallner, D. Barredo, L. Henriet, A. Signoles, C. Hainaut, T. Franz, S. Geier, A. Tebben, A. Salzinger, G. Zürn, T. Lahaye, M. Weidemüller, and A. Browaeys. Microwave engineering of programmable xxz hamiltonians in arrays of rydberg atoms. *PRX Quantum*, 3:020303, Apr 2022.

[283] A. Bermudez, L. Tagliacozzo, G. Sierra, and P. Richerme. Long-range heisenberg models in quasiperiodically driven crystals of trapped ions. *Phys. Rev. B*, 95:024431, Jan 2017.

[284] Joonhee Choi, Hengyun Zhou, Helena S. Knowles, Renate Landig, Soonwon Choi, and Mikhail D. Lukin. Robust dynamic hamiltonian engineering of many-body spin systems. *Phys. Rev. X*, 10:031002, Jul 2020.

[285] Haifeng Qiao, Yadav P. Kandel, John S. Van Dyke, Saeed Fallahi, Geoffrey C. Gardner, Michael J. Manfra, Edwin Barnes, and John M. Nichol. Floquet-enhanced spin swaps. *Nature Communications*, 12(1), apr 2021.

[286] Subhajit Sarkar and Berislav Buca. Protecting coherence from environment via stark many-body localization in a quantum-dot simulator, 2022.

[287] Dmitry Abanin, Wojciech De Roeck, Wen Wei Ho, and François Huveneers. A rigorous theory of many-body prethermalization for periodically driven and closed quantum systems. *Communications in Mathematical Physics*, 354(3):809–827, jun 2017.

[288] Dominic V. Else, Bela Bauer, and Chetan Nayak. Prethermal phases of matter protected by time-translation symmetry. *Phys. Rev. X*, 7:011026, Mar 2017.

[289] Kaoru Mizuta, Kazuaki Takasan, and Norio Kawakami. High-frequency expansion for floquet prethermal phases with emergent symmetries: Application to time crystals and floquet engineering. *Phys. Rev. B*, 100:020301, Jul 2019.

[290] Martin Claassen. Flow renormalization and emergent prethermal regimes of periodically-driven quantum systems, 2021.

[291] Kartiek Agarwal and Ivar Martin. Dynamical enhancement of symmetries in many-body systems. *Phys. Rev. Lett.*, 125:080602, Aug 2020.

[292] Jad C. Halimeh, Haifeng Lang, Julius Mildenberger, Zhang Jiang, and Philipp Hauke. Gauge-symmetry protection using single-body terms. *PRX Quantum*, 2:040311, Oct 2021.

[293] Jad C Halimeh, Haifeng Lang, and Philipp Hauke. Gauge protection in non-abelian lattice gauge theories. *New Journal of Physics*, 24(3):033015, mar 2022.

[294] Jad C. Halimeh, Lukas Homeier, Christian Schweizer, Monika Aidelsburger, Philipp Hauke, and Fabian Grusdt. Stabilizing lattice gauge theories through simplified local pseudogenerators. *Phys. Rev. Res.*, 4:033120, Aug 2022.

[295] Lorenza Viola, Emanuel Knill, and Seth Lloyd. Dynamical decoupling of open quantum systems. *Phys. Rev. Lett.*, 82:2417–2421, Mar 1999.

[296] Valentin Kasper, Torsten V. Zache, Fred Jendrzejewski, Maciej Lewenstein, and Erez Zohar. Non-abelian gauge invariance from dynamical decoupling. *Phys. Rev. D*, 107:014506, Jan 2023.

[297] Jutho Haegeman, J. Ignacio Cirac, Tobias J. Osborne, Iztok Pižorn, Henri Verschelde, and Frank Verstraete. Time-dependent variational principle for quantum lattices. *Phys. Rev. Lett.*, 107:070601, Aug 2011.

[298] Jutho Haegeman, Christian Lubich, Ivan Oseledets, Bart Vandereycken, and Frank Verstraete. Unifying time evolution and optimization with matrix product states. *Phys. Rev. B*, 94:165116, Oct 2016.

[299] Mingru Yang and Steven R. White. Time-dependent variational principle with ancillary krylov subspace. *Phys. Rev. B*, 102:094315, Sep 2020.

[300] Guifré Vidal. Efficient classical simulation of slightly entangled quantum computations. *Phys. Rev. Lett.*, 91:147902, Oct 2003.

[301] Guifré Vidal. Efficient simulation of one-dimensional quantum many-body systems. *Phys. Rev. Lett.*, 93:040502, Jul 2004.

[302] Markus Heyl. Dynamical quantum phase transitions: a review. *Reports on Progress in Physics*, 81(5):054001, apr 2018.

[303] Gonzalo A Álvarez, Ernesto P Danieli, Patricia R Levstein, and Horacio M Pastawski. Environmentally induced quantum dynamical phase transition in the spin swapping operation. *The Journal of chemical physics*, 124(19):194507, 2006.

[304] Achilleas Lazarides, Arnab Das, and Roderich Moessner. Equilibrium states of generic quantum systems subject to periodic driving. *Phys. Rev. E*, 90:012110, Jul 2014.

[305] Dmitry A. Abanin, Wojciech De Roeck, and Fran çois Huveneers. Exponentially slow heating in periodically driven many-body systems. *Phys. Rev. Lett.*, 115:256803, Dec 2015.

[306] Takashi Mori, Tomotaka Kuwahara, and Keiji Saito. Rigorous bound on energy absorption and generic relaxation in periodically driven quantum systems. *Phys. Rev. Lett.*, 116:120401, Mar 2016.

[307] Kenneth G. Wilson and J. Kogut. The renormalization group and the ϵ expansion. *Physics Reports*, 12(2):75–199, 1974.

[308] Kenneth G. Wilson. The renormalization group and critical phenomena. *Rev. Mod. Phys.*, 55:583–600, Jul 1983.

[309] John B. Kogut. An introduction to lattice gauge theory and spin systems. *Rev. Mod. Phys.*, 51:659–713, Oct 1979.

[310] S. Chandrasekharan, B. Scarlet, and U.-J. Wiese. From spin ladders to the 2d o(3) model at non-zero density. *Computer Physics Communications*, 147(1-2):388–393, aug 2002.

[311] Falk Bruckmann, Karl Jansen, and Stefan Kühn. O(3) nonlinear sigma model in $1+1$ dimensions with matrix product states. *Phys. Rev. D*, 99:074501, Apr 2019.

[312] Hersh Singh. Qubit regularized $o(n)$ nonlinear sigma models. *Phys. Rev. D*, 105:114509, Jun 2022.

[313] Hersh Singh. Large-charge conformal dimensions at the $o(n)$ wilson-fisher fixed point, 2022.

[314] Stephan Caspar and Hersh Singh. From asymptotic freedom to θ vacua: Qubit embeddings of the o(3) nonlinear σ model. *Phys. Rev. Lett.*, 129:022003, Jul 2022.

[315] Tasio Gonzalez-Raya, Rodrigo Asensio-Perea, Ana Martin, Lucas C. Céleri, Mikel Sanz, Pavel Lougovski, and Eugene F. Dumitrescu. Digital-analog quantum simulations using the cross-resonance effect. *PRX Quantum*, 2:020328, May 2021.

[316] Z.L. Mádi, B. Brutscher, T. Schulte-Herbrüggen, R. Brüschweiler, and R.R. Ernst. Time-resolved observation of spin waves in a linear chain of nuclear spins. *Chemical Physics Letters*, 268(3):300–305, 1997.

[317] C. M. Sánchez, A. K. Chattah, K. X. Wei, L. Buljubasich, P. Cappellaro, and H. M. Pastawski. Perturbation independent decay of the loschmidt echo in a many-body system. *Phys. Rev. Lett.*, 124:030601, Jan 2020.

[318] Anthony N. Ciavarella, Stephan Caspar, Hersh Singh, Martin J. Savage, and Pavel Lougovski. Floquet engineering heisenberg from ising using constant drive fields for quantum simulation, 2022.

[319] Mark Saffman, Thad G Walker, and Klaus Mølmer. Quantum information with rydberg atoms. *Rev. Mod. Phys.*, 82(3):2313, 2010.

[320] Hannes Bernien, Sylvain Schwartz, Alexander Keesling, Harry Levine, Ahmed Omran, Hannes Pichler, Soonwon Choi, Alexander S Zibrov, Manuel Endres, Markus Greiner, et al. Probing many-body dynamics on a 51-atom quantum simulator. *Nature*, 551(7682):579–584, 2017.

[321] Vincent Lienhard, Sylvain de Léséleuc, Daniel Barredo, Thierry Lahaye, Antoine Browaeys, Michael Schuler, Louis-Paul Henry, and Andreas M. Läuchli. Observing the space- and time-dependent growth of correlations in dynamically tuned synthetic ising models with antiferromagnetic interactions. *Phys. Rev. X*, 8:021070, Jun 2018.

[322] Elmer Guardado-Sanchez, Peter T. Brown, Debayan Mitra, Trithep Devakul, David A. Huse, Peter Schauß, and Waseem S. Bakr. Probing the quench dynamics of antiferromagnetic correlations in a 2d quantum ising spin system. *Phys. Rev. X*, 8:021069, Jun 2018.

[323] Hyosub Kim, YeJe Park, Kyungtae Kim, H-S Sim, and Jaewook Ahn. Detailed balance of thermalization dynamics in rydberg-atom quantum simulators. *Phy. Rev. Lett.*, 120(18):180502, 2018.

[324] Sylvain de Léséleuc, Vincent Lienhard, Pascal Scholl, Daniel Barredo, Sebastian Weber, Nicolai Lang, Hans Peter Büchler, Thierry Lahaye, and Antoine Browaeys. Observation of a symmetry-protected topological phase of interacting bosons with rydberg atoms. *Science*, 365(6455):775–780, 2019.

[325] Alexander Keesling, Ahmed Omran, Harry Levine, Hannes Bernien, Hannes Pichler, Soonwon Choi, Rhine Samajdar, Sylvain Schwartz, Pietro Silvi, Subir Sachdev, et al. Quantum kibble–zurek mechanism and critical dynamics on a programmable rydberg simulator. *Nature*, 568(7751):207–211, 2019.

[326] M Morgado and S Whitlock. Quantum simulation and computing with rydberg-interacting qubits. *AVS Quantum Sci.*, 3(2):023501, 2021.

[327] Ll Masanes, Guifré Vidal, and José Ignacio Latorre. Time-optimal hamiltonian simulation and gate synthesis using homogeneous local unitaries. *arXiv preprint quant-ph/0202042*, 2002.

[328] Bartłomiej Gardas, Jacek Dziarmaga, Wojciech H Zurek, and Michael Zwolak. Defects in quantum computers. *Sci. Rep.*, 8(1):1–10, 2018.

[329] R. Harris, Y. Sato, A. J. Berkley, M. Reis, F. Altomare, M. H. Amin, K. Boothby, P. Bunyk, C. Deng, C. Enderud, S. Huang, E. Hoskinson, M. W. Johnson, E. Ladizinsky, N. Ladizinsky, T. Lanting, R. Li, T. Medina, R. Molavi, R. Neufeld, T. Oh, I. Pavlov, I. Perminov, G. Poulin-Lamarre, C. Rich, A. Smirnov, L. Swenson, N. Tsai, M. Volkmann, J. Whittaker, and J. Yao. Phase transitions in a programmable quantum spin glass simulator. *Science*, 361(6398):162–165, 2018.

[330] Andrew D. King, Juan Carrasquilla, Jack Raymond, Isil Ozfidan, Evgeny Andriyash, Andrew Berkley, Mauricio Reis, Trevor Lanting, Richard Harris, Fabio Altomare, Kelly Boothby, Paul I. Bunyk, Colin Enderud, Alexandre Fréchette, Emile Hoskinson, Nicolas Ladizinsky, Travis Oh, Gabriel Poulin-Lamarre, Christopher Rich, Yuki Sato, Anatoly Yu. Smirnov, Loren J. Swenson, Mark H. Volkmann, Jed Whittaker, Jason Yao, Eric Ladizinsky, Mark W. Johnson, Jeremy Hilton, and Mohammad H. Amin. Observation of topological phenomena in a programmable lattice of 1,800 qubits. *Nature*, 560(7719):456–460, aug 2018.

[331] Phillip Weinberg, Marek Tylutki, Jami M. Rönkkö, Jan Westerholm, Jan A. Åström, Pekka Manninen, Päivi Törmä, and Anders W. Sandvik. Scaling and diabatic effects in quantum annealing with a d-wave device. *Phys. Rev. Lett.*, 124:090502, Mar 2020.

[332] Andrew D. King, Jack Raymond, Trevor Lanting, Sergei V. Isakov, Masoud Mohseni, Gabriel Poulin-Lamarre, Sara Ejtemaee, William Bernoudy, Isil Ozfidan, Anatoly Yu. Smirnov, Mauricio Reis, Fabio Altomare, Michael Babcock, Catia Baron, Andrew J. Berkley, Kelly Boothby, Paul I. Bunyk, Holly Christiani, Colin Enderud, Bram Evert, Richard Harris, Emile Hoskinson, Shuiyuan Huang, Kais Jooya, Ali Khodabandelou, Nicolas Ladizinsky, Ryan Li, P. Aaron Lott, Allison J. R. MacDonald, Danica Marsden, Gaelen Marsden, Teresa Medina, Reza Molavi, Richard Neufeld, Mana Norouzpour, Travis Oh, Igor Pavlov, Ilya Perminov, Thomas Prescott, Chris Rich, Yuki Sato, Benjamin Sheldan, George Sterling, Loren J. Swenson, Nicholas Tsai,

Mark H. Volkmann, Jed D. Whittaker, Warren Wilkinson, Jason Yao, Hartmut Neven, Jeremy P. Hilton, Eric Ladizinsky, Mark W. Johnson, and Mohammad H. Amin. Scaling advantage over path-integral monte carlo in quantum simulation of geometrically frustrated magnets. *Nat. Commun.*, 12(1), feb 2021.

[333] Yuki Bando, Yuki Susa, Hiroki Oshiyama, Naokazu Shibata, Masayuki Ohzeki, Fernando Javier Gómez-Ruiz, Daniel A. Lidar, Sei Suzuki, Adolfo del Campo, and Hidetoshi Nishimori. Probing the universality of topological defect formation in a quantum annealer: Kibble-zurek mechanism and beyond. *Phys. Rev. Research*, 2:033369, Sep 2020.

[334] Paul Kairys, Andrew D. King, Isil Ozfidan, Kelly Boothby, Jack Raymond, Arnab Banerjee, and Travis S. Humble. Simulating the shastry-sutherland ising model using quantum annealing. *PRX Quantum*, 1:020320, Dec 2020.

[335] T. Lanting, M. H. Amin, C. Baron, M. Babcock, J. Boschee, S. Boixo, V. N. Smelyanskiy, M. Foygel, and A. G. Petukhov. Probing environmental spin polarization with superconducting flux qubits, 2020.

[336] Kohji Nishimura, Hidetoshi Nishimori, and Helmut G. Katzgraber. Griffiths-mccoy singularity on the diluted chimera graph: Monte carlo simulations and experiments on quantum hardware. *Phys. Rev. A*, 102:042403, Oct 2020.

[337] Andrew D. King, Cristiano Nisoli, Edward D. Dahl, Gabriel Poulin-Lamarre, and Alejandro Lopez-Bezanilla. Qubit spin ice. *Science*, 373(6554):576–580, 2021.

[338] Andrew D. King, Sei Suzuki, Jack Raymond, Alex Zucca, Trevor Lanting, Fabio Altomare, Andrew J. Berkley, Sara Ejtemaee, Emile Hoskinson, Shuiyuan Huang, Eric Ladizinsky, Allison MacDonald, Gaelen Marsden, Travis Oh, Gabriel Poulin-Lamarre, Mauricio Reis, Chris Rich, Yuki Sato, Jed D. Whittaker, Jason Yao, Richard Harris, Daniel A. Lidar, Hidetoshi Nishimori, and Mohammad H. Amin. Coherent quantum annealing in a programmable 2,000 qubit Ising chain. *Nature Phys.*, 18(11):1324–1328, 2022.

[339] Marc Illa and Martin J. Savage. Basic Elements for Simulations of Standard Model Physics with Quantum Annealers: Multigrid and Clock States. *Phys. Rev. A*, 106(5):052605, 2022.

[340] Jack Y. Araz, Sebastian Schenk, and Michael Spannowsky. Toward a quantum simulation of nonlinear sigma models with a topological term. *Phys. Rev. A*, 107:032619, Mar 2023.

[341] Andrei Alexandru, Paulo F. Bedaque, Andrea Carosso, Michael J. Cervia, and Andy Sheng. Qubitization strategies for bosonic field theories. *Phys. Rev. D*, 107:034503, Feb 2023.

[342] Sudip Chakravarty, Bertrand I. Halperin, and David R. Nelson. Two-dimensional quantum heisenberg antiferromagnet at low temperatures. *Phys. Rev. B*, 39:2344–2371, Feb 1989.

[343] B. B. Beard, M. Pepe, S. Riederer, and U. J. Wiese. Efficient cluster algorithm for CP(N-1) models. *Computer Physics Communications*, 175(10):629–634, November 2006.

[344] Silas R. Beane, William Detmold, Kostas Orginos, and Martin J. Savage. Uncertainty Quantification in Lattice QCD Calculations for Nuclear Physics. *J. Phys. G*, 42(3):034022, 2015.

[345] Sergio Caracciolo, Robert G. Edwards, Andrea Pelissetto, and Alan D. Sokal. Asymptotic scaling in the two-dimensional o(3) σ model at correlation length 10^5. *Phys. Rev. Lett.*, 75:1891–1894, Sep 1995.

[346] Loïc Henriet, Lucas Beguin, Adrien Signoles, Thierry Lahaye, Antoine Browaeys, Georges-Olivier Reymond, and Christophe Jurczak. Quantum computing with neutral atoms. *Quantum*, 4:327, sep 2020.

[347] Antoine Browaeys and Thierry Lahaye. Many-body physics with individually controlled rydberg atoms. *Nature Physics*, 16(2):132–142, jan 2020.

[348] Pascal Scholl, Michael Schuler, Hannah J. Williams, Alexander A. Eberharter, Daniel Barredo, Kai-Niklas Schymik, Vincent Lienhard, Louis-Paul Henry, Thomas C. Lang, Thierry Lahaye, Andreas M. Läuchli, and Antoine Browaeys. Quantum simulation of 2d antiferromagnets with hundreds of rydberg atoms. *Nature*, 595(7866):233–238, jul 2021.

[349] Anthony N. Ciavarella, Stephan Caspar, Marc Illa, and Martin J. Savage. State preparation in the heisenberg model through adiabatic spiraling. *Quantum*, 7:970, apr 2023.

[350] A. Omran, H. Levine, A. Keesling, G. Semeghini, T. T. Wang, S. Ebadi, H. Bernien, A. S. Zibrov, H. Pichler, S. Choi, J. Cui, M. Rossignolo, P. Rembold, S. Montangero, T. Calarco, M. Endres, M. Greiner, V. Vuletić , and M. D. Lukin. Generation and manipulation of schrödinger cat states in rydberg atom arrays. *Science*, 365(6453):570–574, aug 2019.

[351] TM Graham, Y Song, J Scott, C Poole, L Phuttitarn, K Jooya, P Eichler, X Jiang, A Marra, B Grinkemeyer, et al. Demonstration of multi-qubit entanglement and algorithms on a programmable neutral atom quantum computer. *arXiv preprint arXiv:2112.14589*, 2021.

[352] P. Huft, Y. Song, T. M. Graham, K. Jooya, S. Deshpande, C. Fang, M. Kats, and M. Saffman. Simple, passive design for large optical trap arrays for single atoms. *Phys. Rev. A*, 105:063111, Jun 2022.

[353] R. D. Peccei and Helen R. Quinn. CP conservation in the presence of pseudoparticles. *Phys. Rev. Lett.*, 38:1440–1443, Jun 1977.

[354] F. Wilczek. Problem of strong p and t invariance in the presence of instantons. *Phys. Rev. Lett.*, 40:279–282, Jan 1978.

[355] T. V. Zache, N. Mueller, J. T. Schneider, F. Jendrzejewski, J. Berges, and P. Hauke. Dynamical Topological Transitions in the Massive Schwinger Model with a θ Term. *Phys. Rev. Lett.*, 122(5):050403, 2019.

[356] Niklas Mueller, Joseph A. Carolan, Andrew Connelly, Zohreh Davoudi, Eugene F. Dumitrescu, and Kübra Yeter-Aydeniz. Quantum computation of dynamical quantum phase transitions and entanglement tomography in a lattice gauge theory, 2022.

[357] D. Barredo, V. Lienhard, P. Scholl, S. de Lé séleuc, T. Boulier, A. Browaeys, and T. Lahaye. Three-dimensional trapping of individual rydberg atoms in ponderomotive bottle beam traps. *Physical Review Letters*, 124(2), jan 2020.

[358] S.A. Chin, O.S. Van Roosmalen, E.A. Umland, and S.E. Koonin. Exact Ground State Properties of the SU(2) Hamiltonian Lattice Gauge Theory. *Phys. Rev. D*, 31:3201–3212, 1985.

[359] J. Piekarewicz, M.R. Zirnbauer, and S.E. Koonin. SU(2) Lattice Gauge Theory in the Electric Field Representation. *Int. J. Mod. Phys. A*, 3:409–433, 1988.

[360] Hariharan Narayanan. On the complexity of computing kostka numbers and littlewood-richardson coefficients. *Journal of Algebraic Combinatorics*, 24(3):347–354, Nov 2006.

[361] Arne Alex, Matthias Kalus, Alan Huckleberry, and Jan von Delft. A Numerical algorithm for the explicit calculation of SU(N) and SL(N,C) Clebsch-Gordan coefficients. *J. Math. Phys.*, 52:023507, 2011.

[362] Suguru Endo, Iori Kurata, and Yuya O. Nakagawa. Calculation of the green's function on near-term quantum computers. *Phys. Rev. Res.*, 2:033281, Aug 2020.